Iranica Journal of Energy & Environment 5 (1): 01-07, 2014
ISSN 2079-2115
IJEE an Official Peer Reviewed Journal of Babol Noshirvani University of Technology
DOI: 10.5829/idosi.ijee.2014.05.01.01

BUT

Batch Fermentation of Bioethanol from the Residues of *Elaeis guineensis*: Optimization and Kinetics Evaluation

[1,2]*Mohd Dinie Muhaimin Samsudin and* [1]*Mashitah Mat Don*

[1]School of Chemical Engineering, Universiti Sains Malaysia Engineering Campus,
14300 Nibong Tebal, Pulau Pinang, Malaysia
[2]Faculty of Petroleum and Renewable Energy Engineering,
Universiti Teknologi Malaysia, 81310 UTM Johor Bahru, Johor, Malaysia

(Received: December 14, 2013 , 2013; Accepted in Revised Form: February 18, 2014)

Abstract: Bioethanol was produced by *Saccharomyces cerevisiae* using oil palm trunk (OPT) sap supplemented with palm oil mill effluent (POME) in a shake flask culture. Four variables namely OPT sap to POME ratio, inoculum size, pH and incubation time were chosen to investigate their effects on production of bioethanol using One -Factor -at -a -Time (OFAT) method. The optimum process conditions were found to be at OPT sap to POME ratio of 30:20 and inoculum size of 4% v/v. The fermentation process exhibited better result in slightly basic media. The bioethanol concentration at the optimum condition was 12.52 g/l which equal to bioethanol yield of 44% g/g after four days of fermentation. It was found that the cell growth followed a sigmoidal trend. Logistic model, Luedeking-Piret model and Luedeking-Piret-like model were chosen and validated to describe the behavior of dry weight of the biomass, bioethanol production and glucose consumption, respectively. All selected models fitted well to experimental data, proven by high R^2 values (>0.9) and low RMSE values.

Keyword: Oil palm trunk sap · Palm oil mill effluent · Bioethanol fermentation · One-Factor-at-a-Time (OFAT) method · Logistic model · Luedeking-Piret model

INTRODUCTION

The worldwide production of palm oil (*Elaeis guineensis*) is rapidly increasing since past decades. In production of palm oil, palm oil mill effluent (POME) is generated in the mill at final stage of the process. For each tonne of crude palm oil (CPO) produced, an average of 0.9 - 1.5 m^3 POME is generated [1]. POME is a colloidal suspension with high biological oxygen demand (BOD), as well as chemical oxygen demand (COD). Currently, ponding system is the most common method used for the treatment of POME. However, this system gave negative effect on environment due to high green house gas emission [2]; thus, leads to secondary pollution. On the other hand, the economic life of oil palm is only about 25 years and be replanted after then [3]. During replanting, a large quantity of felled trunks is generated. Most of Oil Palm Trunk (OPT) were left abandoned or used as mulch[4]. However, there was an interesting discovery on OPT sap where it actually contained relatively high sugar content [5]. Since high glucose level is detected in OPT, it has a great potential to be used as a feedstock for the production of bioethanol.

Bioethanol is the main and most efficient biofuel; it is considered as raw material with wide range of applications. The great advantage of bioethanol is that can be produced from various feedstock including corn, sugar beet, sugarcane, red seaweed part, etc[6]. In environmental point of view, bioethanol may contribute to decrease air pollution and reduce carbon dioxide accumulation[7]. To date, *Saccharomyces cerevisiae* yeast is still regarded as the most potential microorganism for bioethanol fermentation due its robustness [8].

Kinetics models are very important in design and control of the microbial processes [9]. In this study, three

---

Corresponding Author: Mashitah Mat Don, School of Chemical Engineering, UniversitiSains Malaysia Engineering Campus, 14300 NibongTebal, Pulau Pinang, Malaysia. E-mail: chmashitah@eng.usm.my.

unstructured models were selected and validated to describe the behavior of bioethanol production from OPT sap. However, OPT sap contained high sugar content and might cause high osmotic stress on yeast cells. Therefore, OPT sap was diluted with POME to the desired glucose concentration. In the cultured media, POME served as a source of supplementary nutrients. Based on the One-Factor-at-a-Time (OFAT) method, the effects of different culture conditions on production of bioethanol were investigated.

MATERIALS AND METHODS

Chemicals: Sodium hydrochloride, sulphuric acid, acetonitrile, phenol, sodium sulfite, glucose, ethanol and sodium hydroxide were purchased from Merck (Darmstadt, Germany). Dinitrosalicylic acid was purchased from Sigma-Aldrich. All the chemicals were of analytical grade.

Preparation of Oil Palm Trunk Sap and Palm Oil Mill Effluent: OPTs were obtained from Felda Trolak, Perak, Malaysia. The trunks were squeezed at Forest Research Institute of Malaysia, Kepong, Kuala Lumpur using a hydraulic squeezer to obtain OPT sap; while, POME was collected from Serting Hilir Palm Oil Mill, Negeri Sembilan. Due to fast degradation, OPT sap and POME were stored in a freezer at -20°C. Prior use OPT sap and POME were defrosted to room temperature when needed.

Inoculum Preparation: Yeast (*S. cerevisiae*) used was an ordinary baking yeast (Mauri-pan Instant Yeast, AbMauri) purchased at a local sundry stall. Inoculum was prepared by mixing 10 g of yeast with 100 ml of sterile deionised water. The mixture was then vortexed for 30 s so that the mixture was well mixed and the yeast cells were evenly distributed.

Bioethanol Fermentation: Bioethanol fermentations were run in 250 ml cotton plugged shake flasks. The substrate (100 ml) was prepared with OPT sap and POME in a ratio of 50:0, 40:10, 30:20, 20:30, 10:40 and 0:50. Inoculum size (0, 1, 2, 3, 4, 5 and 6% w/v), pH (4.2, 5.0, 6.0, 7.0 and 8.0) and incubation time (1, 2, 3, 4, 5, 6 and 7 days) were also chosen as the process variables. The pH of the mixture was adjusted by adding 2 M sodium hydroxide and 0.5 M sulphuric acid solutions by use of a glass-electrode pH meter (Mettler Toledo Delta 320). Samples were harvested and analysed for biomass, glucose and bioethanol concentration.

Analytical Method: Total nitrogen was measured by the use of an elemental analyzer. The COD level was measured according to Eaton *et al*. [10]. Dry weight of the samples or biomass was analysed by drying in an oven at 110 °C until a constant weight was achieved.

DNS analysis was carried out to determine sugar concentration using method described by Das *et al*. [11] with slight modifications. A 3 ml DNS reagent solution (Dinitrosalicylic acid: 10 g, Phenol: 2 g, Sodium Sulfite: 0.5 g, Sodium hydroxide: 10 g, deionised water: 1 liter) was added to 3 ml of sample in a capped test tube. The sample was then heated to 90°C for 15 minutes to develop a red-brown color. A 1 ml of 40% w/v potassium sodium tartrate solution was then added to the sample to stabilize the color. After cooling to room temperature in a cold water bath, the absorbance was measured with a spectrophotometer (Human Corporation X-Ma 1200V) at wavelength 575 nm.

Bioethanol was measured by High Performance Liquid Chromatography (HPLC) (Perkin Elmer Series 200) equipped with autosampler and programmable multi-wavelength detector set at 210 nm. A 10 ml of sample was injected into a column (Kromasil 100Å - NH_2 column) with 80% acetonitrile and 20% deionised water as the mobile phase at a flow rate of 0.6 ml/min at 22°C.

Statistical Analysis: The yield of bioethanol was calculated and expressed as percentage by Equation (1).

$$Yield\ of\ ethanol\left(\%g/g\right)=\frac{bio\ ethanol\left(g/l\right)}{initial\ glu\cos e\left(g/l\right)}100\% \quad (1)$$

Selected Model and Model Parameters Estimation: Kinetics of the yeast growth was validated by the logistic equation which was associated with substrate independent condition. Luedeking-Piret equation was chosen for the kinetic of product formation, while a Luedeking-Piret-like equation was selected to model the glucose consumption of the culture. Derivations and profound discussions on these equations had been done by Elibol and Mavituna [9]. Experimental results were analyzed using the linearized equations of the selected kinetic models as summarized in Table 1.

Table 1: Selected kinetic models and their respective linear forms

Cell growth	Logistic Model	$\frac{dX}{dt} = \mu_m\left(1 - \frac{X}{X_m}\right)X$	(2)
	Integration from t=0, X=X$_o$	$X = \left(\frac{X_o e^{\mu_m t}}{1 - (X_o/X_m)(1 - e^{\mu_m t})}\right)$	(3)
	Linear form	$ln\left(\frac{X}{X_m - X}\right) = \mu_m t - ln\left(\frac{X_m}{X_o} - 1\right)$	(4)
Bioethanol production	Luedeking-Piret Model	$\frac{dP}{dt} = \alpha\frac{dX}{dt} + \beta X$	(5)
	Linear form	$[P - \beta B(t)] = \alpha A(t)$	(6)
	in which,	$\beta = \frac{(dP/dt)_{stationary}}{X_m}$	(7)
		$A(t) = X_o\left(\frac{e^{\mu_m t}}{(1 - (X_o/X_m)(1 - e^{\mu_m t}))} - 1\right)$	(8)
		$B(t) = \frac{X_m}{\mu_m} ln\left(1 - \left(\frac{X_o}{X_m}\right)(1 - e^{\mu_m t})\right)$	(9)
Glucose consumption	Luedeking-Piret-like Model	$-\frac{dS}{dt} = \gamma\frac{dX}{dt} + \delta X$	(10)
	Linear form	$S_o - S - \delta D(t) = \gamma C(t)$	(11)
	in which,	$\delta = \frac{-(dS/dt)_{stationary}}{X_m}$	(12)
		$C(t) = X_o\left(\frac{e^{\mu_m t}}{(1 - (X_o/X_m)(1 - e^{\mu_m t}))} - 1\right)$	(13)
		$D(t) = \frac{X_m}{\mu_m} ln\left(1 - \left(\frac{X_o}{X_m}\right)(1 - e^{\mu_m t})\right)$	(14)

Model Fitting and Validation: Polymath 5.1 (CACHE Corpn. USA) was used for data analyzing. Statistical coefficient and statistical error parameters were determined using a non-linear regression (Levenberg-Marquardt method).

RESULTS AND DISCUSSION

Characteristics of Oil Palm Trunk Sap and Palm Oil Mill Effluent: The characteristics of OPT sap and POME are summarized in Table 2. OPT sap contained higher glucose content (49.12 g/l) as compared to POME (3.04 g/l). Both of them are acidic condition. POME contained low total soluble solid content. The total nitrogen contained in POME was higher as compared to OPT sap. Compared to the literature, glucose concentration in our OPT sap was slightly lower but the total nitrogen value in POME was in the range that was previously reported [12-15]. This could be due to different types of oil palm tree species, palm oil mill process, analytical techniques used and the method of OPT sap squeezing process.

Effect of Oil Palm Trunk Sap to Palm Oil Mill Effluent Ratio: Table 3 shows the effect of OPT sap to POME ratio on production of bioethanol by *S. cerevisiae*. The highest bioethanol yield was found to be 3.08% when the OPT to POME ratio was 30:20. An increase in volume of OPT sap in the substrate increased the concentration of glucose and subsequently improved the conversion of glucose to bioethanol. However, the conversion of glucose to bioethanol started to decline beyond the initial glucose concentration of 27.94 g/l. This could be due to osmotic stress and consequently caused the yeast to loss its viability and thus reduced the rate of fermentation [16].

In order to maintain the cell growth and survive in the adverse and fluctuating conditions, the yeast cells were equipped with certain mechanisms to identify the changes and build up appropriate responses accordingly [17]. The ability of the cells to survive in higher glucose concentration depends on its osmoregulation system where the cellular water content and tugor pressure were regulated [18].

Inoculum Size: Microorganisms perform at their highest efficiencies if the right proportion of the substrate were provided. Table 4 presents the effect of inoculum size on conversion of glucose to bioethanol. A linear relationship was observed between the inoculum size with the yield of bioethanol up to the size of 4.0% (v/v). Beyond this level, the yield of bioethanol produced started to decrease.

Table 2:The characteristics of OPT sap and POME

	OPT Sap			POME		
	Present study	Lokesh *et al.* [12]	Yamada *et al.* [13]	Present study	Wong *et al.* [14]	Ahmad *et al.* [15]
pH	4.2	acidic	-	4.1	4.15 - 4.45	4.7
Concentration of glucose (g/l)	49.12 ± 0.04	55.4 ± 1.53	93.0 - 111.8	3.04 ± 0.03	-	-
COD (mg/l)	15000 ± 500	-	-	48600 ± 500	45500 - 65000	50000
Total soluble solid (°Brix)	5.10 ± 0.05	-	-	4.00 ± 0.05	-	-
Total solid (mg/l)	35163± 610	-	30000	37173 ± 573	33790 - 37230	40500
Total nitrogen, TN (mg/l)	648	-	-	718	500 - 800	750

Values are means ± standard deviations (n=3)

Table 3: Effect of OPT sap to POME ratio

	Glucose concentration				
OPT sap :POME ratio	Initial (g/l)	Final (g/l)	Percentage of consumption (%)	Bioethanol production (g/l)	Percentage of bioethanol yield (%)
50:00	44.72 ± 0.04	42.70 ± 0.14	4.51 ± 0.31	1.00 ± 0.07	2.24 ± 0.16
40:10	36.32 ± 0.03	34.18 ± 0.10	5.91 ± 0.28	1.06 ± 0.05	2.92 ± 0.13
30:20	27.94 ± 0.03	26.22 ± 0.07	6.16 ± 0.25	0.86 ± 0.03	3.08 ± 0.12
20:30	19.54 ± 0.03	18.56 ± 0.06	5.01 ± 0.31	0.48 ± 0.03	2.46 ± 0.15
10:40	11.16 ± 0.04	10.70 ± 0.03	4.17 ± 0.27	0.22 ± 0.01	1.97 ± 0.13
00:50	2.76 ± 0.03	2.66 ± 0.01	3.71 ± 0.36	0.04 ± 0.05	1.44 ± 0.18

Values are means ± standard deviations (n=3)

Table 4: Effect of inoculum size

	Glucose concentration				
Inoculum Size (%v/v)	Initial (g/l)	Final (g/l)	Percentage of consumption (%)	Bioethanol production (g/l)	Percentage of bioethanol yield (%)
0.0	30.72 ± 0.03	30.71 ± 0.01	0.03 ± 0.02	0.00	0.00
1.0	30.12 ± 0.02	29.40 ± 0.15	2.40 ± 0.49	0.36 ± 0.07	1.20 ± 0.23
2.0	29.54 ± 0.01	28.32 ± 0.13	4.17 ± 0.44	0.60 ± 0.06	2.03 ± 0.20
3.0	28.98 ± 0.01	27.36 ± 0.10	5.64 ± 0.35	0.80 ± 0.05	2.76 ± 0.17
4.0	28.46 ± 0.03	26.70 ± 0.13	6.18 ± 0.46	0.88 ± 0.06	3.09 ± 0.21
5.0	27.94 ± 0.01	26.22 ± 0.12	6.16 ± 0.43	0.86 ± 0.06	3.08 ± 0.21
6.0	27.44 ± 0.03	25.76 ± 0.11	6.12 ± 0.40	0.84 ± 0.05	3.06 ± 0.18

Values are means ± standard deviations (n=3)

Inoculum size is a vital parameter that imposed significant influenced on fermentation process. Prolonged lag phase was observed in the fermentation process with a smal volume of inoculum [19] and may lead to stuck fermentation process [20]. High level of inoculum size could accelerate the fermentation process and resulted in high bioethanol yield and production of glycerol [19, 20]. Therefore, fermentation with high inoculum size will enhance the production of bioethanol with suitable fermentation time [19]. In present study, the most optimum inoculum size was found to be at 4.0 % (v/v), where the increment of inoculum size after this point no longer resulted in positive impact on production of bioethanol. This happened possibly due to stress related to high cell density. However, it is still remained unclear in what type of stress is encountered by the yeast when it was exposed to high cell density [21]. The most possible factor is depletion of essential nutrient in the culture media.

Effect of pH: Table 5 shows the effect of pH on conversion of glucose to bioethanol. The production of bioethanol improved with an increase in pH values. From the results, the most optimum pH for fermentation process in this study was 8.0. Any increase in pH value more than that resulted in negative impact on fermentation productivity.

pH exhibited a great impact on the activities of microorganism. It was crucial to carry out the fermentation process at optimum pH condition so as to obtain the highest yield. The intracellular pH of *S. cerevisiae* is

Table 5:Effect of initial pH

Initial pH (g/l)	Glucose concentration Initial (g/l)	Final (g/l)	Percentage of consumption (%)	Bioethanol production (g/l)	Percentage of bioethanol yield (%)
4.2	28.46 ± 0.02	26.72 ± 0.13	6.09 ± 0.46	0.86 ± 0.07	3.02 ± 0.23
5.0	28.46 ± 0.02	26.72 ± 0.14	6.09 ± 0.49	0.88 ± 0.07	3.09 ± 0.25
6.0	28.46 ± 0.02	26.62 ± 0.14	6.44 ± 0.49	0.90 ± 0.05	3.16 ± 0.22
7.0	28.46 ± 0.02	26.64 ± 0.15	6.35 ± 0.52	0.90 ± 0.06	3.16 ± 0.22
8.0	28.46 ± 0.02	26.24 ± 0.15	7.78 ± 0.52	1.10 ± 0.06	3.87 ± 0.25
9.0	28.46 ± 0.02	26.26 ± 0.13	7.69 ± 0.46	1.08 ± 0.05	3.80 ± 0.23

Values are means ± standard deviations (n=3)

Table 6:Parameter values used

Parameter	Estimated from	Estimated Value	Simulated Value
S_o	Experimental data	28.46	31.82
μ_m	Slope of Equation (4)	0.7572	0.2302
X_o	Intercept of Equation (4)	43.68	41.66
X_m	Experimental data	45.03	46.21
α	Intercept of Equation (6)	1.6880	2.7808
β	Equation (7)	0.0087	0.0170
γ	Intercept of Equation (11)	7.2619	9.4479
δ	Equation (12)	0.0124	-0.0008

Table 7: Statistical error parameters

Parameter	Cell Growth	Product Formation	Glucose Consumption
R^2	0.904	0.905	0.918
RMSE	0.135	0.617	1.159

almost neutral. Intracellular diffusion and dissociation of weak acids through the plasma membrane are possible. In order to maintain the intracellular pH at neutral, cells utilized their metabolic energy to pump out the surplus H^+ ions. For that reason, the fermentation performance would be affected by the concentration of undissociated forms of weak acids [21]. In present study, higher amount of bioethanol was produced at the initial pH value of 8.0 compared to that of pH 7.0. This was due to decrease in pH value as the fermentation process was progressing as bioethanol is acidic. However, if a pH controlled system was applied, by maintaining the pH value at 7.0, it was possible to obtain better result than the pH at 8.0. From this study, it could be concluded that the bioethanol fermentation should be conducted with the medium of slightly basic if there was no pH control.

Incubation Time: The effect of incubation time on the bioethanol production is shown in Figure 1. A positive correlation was found between the incubation time and bioethanol produced as well as dry weight of the biomass. Cell growth followed the classical sigmoidal growth trend. The concentration of bioethanol and biomass exponentially increased with the extension of time, while a declining trend was observed in glucose concentration particularly within the range of 0-4 days. Though, improvement in the yield was observed when the incubation time was longer than 4 days, the differences were not significant. The bioethanol yield at 4 days was 12.52 g/l which equal to 0.44 g of bioethanol produced per g glucose supplied.

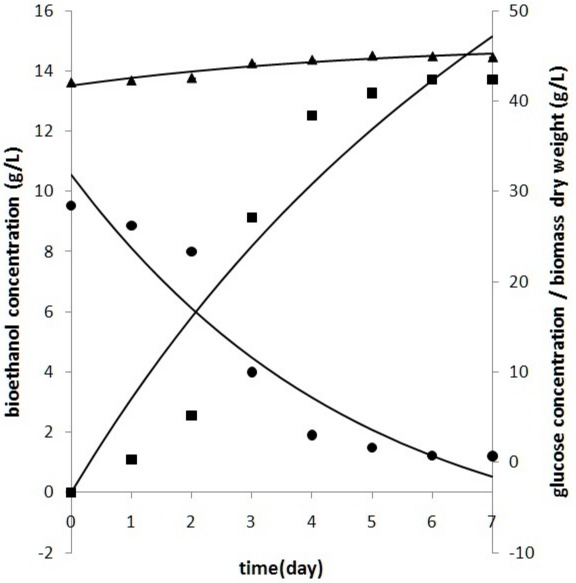

Fig. 1: Comparison of simulated value and experimental value (● Glucose concentration; □Bioethanol concentration; Δ Biomass dry weight) (dots: experimental values; line: simulated values)

Logistic model was chosen to describe the trend of cell growth, Luedeking-Piret model was selected to describe the bioethanol production; while the kinetic of glucose consumption was modeled using Luedeking-Piret-like model as suggested by Elibol and Mavituna [9]. Table 6 shows the estimated and simulated values of variables involved in these models. While, the statistical analyses of all models are presented in Table 7.

The results showed that all selected models were adequate in describing the experimental data, as evidenced by high R^2 values which were more than 0.9 for all cases. Besides, low RMSE values were also obtained for all models. This indicated that the experimental and simulated values were in agreement and close to each other.

CONCLUSIONS

Four variables were chosen to investigate their effects on production of bioethanol by *S. cerevisiae*. The yield of bioethanol increased with an increase in OPT sap to POME volume up to the ratio of 30:20 and thereafter decreased. Increase in inoculum size during the fermentation process could also lead to enhancement of bioethanol yield. Nevertheless, beyond the inoculum size of 4% v/v, no significance improvement in yield was observed. Also, it was [illegible] resulted in high yiel[illegible] The production of bio[illegible]anol increased with an extension of incubation time, [illegible]cially in the first 4 days. The bioethanol yield at [illegible]mum condition was 12.52 g/l; which was equal to bi[illegible]anol yield of 0.44 g/g. It is often very difficult to obtai[illegible] complete understanding of what is actually going on [illegible] particular fermentation system. The presented model [illegible] this present study provided a good description on [illegible]iations of biomass, bioethanol and glucose concen[illegible]ions in a batch fermentation process.

ACKN[illegible]VLEDGEMENT

The authors w[illegible]d like to thank Ministry of Education Malaysia [illegible]r financial support for this study under Fundar[illegible]tal Research Grant Scheme (FRGS).

Nomenclature: gluc[illegible]concentration (g 1^{-1})

t = Time (day)
X = Cell concent[illegible]on (g dry weight $(1)^{-1}$)
X_o = The initial [illegible]le inoculum size (g dry weight $(1)^{-1}$)
X_m = The maximu[illegible] (g dry weight $(1)^{-1}$)

Greek Letters:

α = Growth-associated product formation coefficient (g g^{-1}).
β = Non-growth-associated product formation coefficient (g g^{-1} day^{-1})
γ, δ = Parameters in Luedeking-Piret-like equation for glucose consumption (g S (g cells)$^{-1}$, g S (g cells)$^{-1}$ day^{-1}, respectively)
μ = Specific growth rate (day^{-1})
μ_m = Maximum specific growth rate (day^{-1})

REFERENCES

1. Kanu, I. and O. Achi, 2011. Industrial effluents and their impact on water quality of receiving rivers in Nigeria. Journal of Applied Technology in Environmental Sanitation, 1(1): 75-86.
2. Samsudin, M. and M. Don, *The Effect of* [illegible] *Conference on Environment* 2012 Penang, Malaysia. pp: 478-485.
3. Rupani, P.F., R.P. Singh, M.H. Ibrahim and N. Esa, 2010. Review of current palm oil mill effluent (POME) treatment methods: vermicomposting as a sustainable practice. World Applied Sciences Journal, 11(1): 70-81.
4. Ahmad, A., M. Loh and J. Aziz, 2007. Preparation and characterization of activated carbon from oil palm wood and its evaluation on methylene blue adsorption. Dyes and Pigments, 75(2): 263-272.
5. Chooklin, S., L. Kaewsichan and J. Kaewsrichan, 2011. Potential Utilization of Sap from Oil Palm (Elaeis guineensis) for Lactic Acid Production by Lactobacillus casei. Journal of Sustainable Energy & Environment, 2(3): 99-104.
6. Hii, S., T. Ding and L. Ong, 2010. Comparative Evaluation of Pretreatment Strategies on Enzymatic Saccharification of Hylocereus polyrhizus's Pericarps for Bioethanol Production. Iranica Journal of Energy & Environment 1(4): 275-279.
7. Subbaiah, G.V., K.R. Gopal and S.A. Hussain, 2010. The Effect of Biodiesel and Bioethanol Blended [illegible] Engine. Iranica Journal of Energy & Environment, 1(3): 211-221.
8. Hunag, W.H., G.S. Shieh and F.S. Wang, 2012. Optimization of fed-batch fermentation using mixture of sugars to produce ethanol. Journal of the Taiwan Institute of Chemical Engineers, 43(1): 1-8.

9. Elibol, M. and F. Mavituna, 1999. A kinetic model for actinorhodin production by *Streptomyces coelicolor* A3 (2). Process biochemistry, 34(6): 625-631.
10. Eaton, A. and M. Franson, 2005. Standard methods for the examination of water and wastewater.APHA & AWWA, American Public Health Association, pp: 21.
11. Das, B.K., S.S. Gauri and J. Bhattacharya, 2013. Sweetmeat waste fractions as suitable organic carbon source for biological sulfate reduction. International Biodeterioration & Biodegradation, 82: 215-223.
12. Lokesh, B.E., Z.A.A. Hamid, T. Arai, A. Kosugi, Y. Murata, R. Hashim, O. Sulaiman, Y. Mori and K. Sudesh, 2012. Potential of oil palm trunk sap as a novel inexpensive renewable carbon feedstock for polyhydroxyalkanoate biosynthesis and as a bacterial growth medium. Clean∈_“Soil, Air, Water, 40(3): 310-317.
13. Yamada, H., R. Tanaka, O. Sulaiman, R. Hashim, Z. Hamid, M. Yahya, A. Kosugi, T. Arai, Y. Murata and S. Nirasawa, 2010. Old oil palm trunk: a promising source of sugars for bioethanol production. Biomass and Bioenergy, 34(11): 1608-1613.
14. Wong, Y.S., M.O.A. Kadir and T.T. Teng, 2009. Biological kinetics evaluation of anaerobic stabilization pond treatment of palm oil mill effluent. Bioresource Technology, 100(21): 4969-4975.
15. Ahmad, A.L., I. Suzylawati and B. Subhash, 2003. Water recycling from palm oil mill effluent (POME) using membrane technology. Desalination, 157(1): 87-95.
16. Zhao, X. and F. Bai, 2009. Mechanisms of yeast stress tolerance and its manipulation for efficient fuel ethanol production. Journal of Biotechnology, 144(1): 23-30.
17. Logothetis, S., G. Walker and E.T. Nerantzis, 2007. Effect of salt hyperosmotic stress on yeast cell viability. Zbornik Matice Srpske Za Prirodne Nauke, (113): 271-284.
18. Karlgren, S., N. Pettersson, B. Nordlander, J.C. Mathai, J.L. Brodsky, M.L. Zeidel, R.M. Bill and S. Hohmann, 2005. Conditional osmotic stress in yeast a system to study transport through aquaglyceroporins and osmostress signaling. Journal of Biological Chemistry, 280(8): 7186-7193.
19. Ding, M.Z., H.C. Tian, J.S. Cheng and Y.J. Yuan, 2009. Inoculum size-dependent interactive regulation of metabolism and stress response of *Saccharomyces cerevisiae* revealed by comparative metabolomics. Journal of Biotechnology, 144(4): 279-286.
20. Carrau, F., K. Medina, L. Farina, E. Boido and E. Dellacassa, 2010. Effect of *Saccharomyces cerevisiae* inoculum size on wine fermentation aroma compounds and its relation with assimilable nitrogen content. International Journal of Food Microbiology, 143(1): 81-85.
21. Huang, H., X. Guo, D. Li, M. Liu, J. Wu and H. Ren, 2011. Identification of crucial yeast inhibitors in bio-ethanol and improvement of fermentation at high pH and high total solids. Bioresource Technology, 102(16): 7486-7493.

Persian Abstract

DOI: 10.5829/idosi.ijee.2014.05.01.01

چکیده

بیو اتانول توسط مخمر ساکارومیسس سرویسیه از شیره روغن کنده نخل (OPT)، به همراه پساب کارخانه روغن نخل (POME) در فلاسک شیکر دار تولید شد. چهار متغیر نسبت شیره OPT به POME، میزان تلقیح، pH و زمان انکوباسیون انتخاب شدند تا اثرات آنها در تولید بیو اتانول با استفاده از روش یک فاکتور در یک زمان (OFAT) مورد بررسی قرار گیرد. شرایط بهینه فرآیند برای نسبت شیره OPT به POME برابر ۳۰:۲۰ و میزان تلقیح ۴٪ حجمی تعیین شد. فرآیند تخمیر در محیط کشت اصلی نتیجه بهتری به نمایش گذاشته است. غلظت بیو اتانول در شرایط بهینه g/l ۱۲.۵۲ و بازده ۴۴٪ گرم/گرم بود که پس از چهار روز تخمیر بدست آمد. همچنین مشخص گردید که منحنی رشد سلول‌ها از یک روند S شکل پیروی می‌کند. برای توضیح رفتار وزن خشک سلولی، تولید بیو اتانول و مصرف گلوکز، مدل لوجستیک، مدل لودکینگ-پیرت و مدل شبه لودکینگ-پیرت انتخاب و مورد استفاده قرار گرفت. همه مدل‌های انتخاب شده به خوبی داده‌های تجربی را برازش نموده است ک ($R^2 > 0.9$) و مقادیر کم RMSE این ادعا را اثبات می‌کند.

Iranica Journal of Energy & Environment 5 (1): 08-12, 2014
ISSN 2079-2115
IJEE an Official Peer Reviewed Journal of Babol Noshirvani University of Technology
DOI: 10.5829/idosi.ijee.2014.05.01.02

BUT

Non-Structured Kinetic Model for the Cell Growth of *Saccharomyces cerevisiae* in a Batch Culture

[1]*Fatemeh Ardestani* and [2]*Shiva Shafiei*

[1]Department of Chemical Engineering, Qaemshahr Branch, Islamic Azad University, Qaemshahr, Iran
[2]Department of Chemical Engineering, Shahrood Branch, Islamic Azad University, Shahrood, Iran

(Received: July 10, 2013; Accepted in Revised Form: February 18, 2014)

Abstract: *Saccharomyces cerevisiae* is known as the most widely used eukaryotic microorganism for biological studies. In present study, cell growth profile of *Saccharomyces cerevisiae* in a batch submerged culture was evaluated with three different non-structured kinetic models. Fitness assessment of experimental data on cell growth by models was performed using the curve-fitting tool in Excel and Mat-lab software. Obtained results showed Verhulst kinetic model with R^2 equal to 0.97 was the most appropriate to describe the biomass growth rate of *Saccharomyces cerevisiae*. Maximum specific cell growth rate by Verhulst model was 0.59 h^{-1}. Other kinetic constants were also determined for all the studied models.

Key words: Cell growth · Verhulst model · Non-structured kinetic models · *Saccharomyces cerevisiae*

INTRODUCTION

The most well-known and commercially significant yeasts are the related species and strains of *Saccharomyces cerevisiae* [1]. *S. cerevisiae* is budding yeast known as a baker yeast or brewer yeast [2, 3]. Aeration is an essential factor for *S. cerevisiae* fermentation even though yeast has the ability to grow under anaerobic conditions [4]. However, *S. cerevisiae* is rather exceptional yeast since it is one of the few organisms that are able to grow anaerobic [5]. The maximum specific growth rate (μ_{max}) of *S. cerevisiae* is quite similar under aerobic and anaerobic conditions [6]. It utilizes sucrose, glucose, fructose and maltose as carbon sources to produce alcohol under anaerobic conditions [7]. *S. cerevisiae* is glucose sensitive yeast, also termed Crabtree-positive, exhibiting aerobic ethanol production in the presence of excess glucose [8, 9]. Based on a developed mathematical model for the aerobic growth of *S. cerevisiae* in batch and continuous culture, transport into and out of the mitochondrion was of the major importance in the overall metabolism of *S. cerevisiae* and was subject to long term adaptation [10]. In glucose-grown batch cultures of *S. cerevisiae*, ethanol is produced under aerobic conditions and the rate of alcoholic fermentation is barely influenced by a change to anaerobic conditions [11]. Kinetic parameters of fungi like *S. cerevisiae* may vary significantly according to culture conditions, such as oxygen and fermentation media [12]. In previous researches, nutrient uptake kinetics of filamentous microorganisms such as *Aspergillus* and *Penicillium* strains were investigated [13-19]. But, these studies were less reported for non filamentous fungi or yeast such as *S. cerevisiae*.

In this article, biomass growth rate of the *S. cerevisiae* and its fitness with three different kinetic models was assessed. This investigation was conducted with experimental data of glucose and biomass concentration in batch culture medium by three kinetic equations Monod, Moser and Verhulst. In each case, kinetic parameters were determined; the shape of statistical parameters and the fitness of the yeast growth behavior with the stated equation was evaluated using Mat Lab software.

Corresponding Author: Fatemeh Ardestani, Department of Chemical Engineering, Qaemshahr Branch, Islamic Azad University, Qaemshahr, Iran. Tel: +98-1232253216-19, E-mail: fatemh@yahoo.com.

MATERIALS AND METHODS

Preparation of Stock Culture and Cell Suspension: The stock culture of *S. cerevisiae* was prepared on potato dextrose agar (PDA) slants. In order to prepare inoculums, yeast cells were transferred to PDA plates and incubated at 27°C for 3 days. Cell growth was observed after 5 hours on the surface of plates. Then, the cultures were transferred to a refrigerator at 4°C.

Fermentation process was performed in a laboratory shake flask as a batch submerged culture. In order to use yeast cells in the fermentation process, fresh cultures of these cells were prepared on plates contained of PDA. Linear cultivate of cells was conducted on the surface of the plates in appropriate condition under laminar flow hood and near the flame. Cultivated plates were incubated at 27°C for three days. After appear the white colonies of *S. cerevisiae* that fully covered the plate surface, the cell suspension was prepared with sterile distilled water which was used as inoculums for fermentation process.

Culture Preparation: The main culture media for batch fermentation process in 250 mL shake flasks was composed of (g. L^{-1}) glucose, 20; $MnSO_4$, 0.1; KH_2PO_4, 0.5; ammonium sulfate, 1; yeast extract, 2; and (mg. L^{-1}) $ZnSO_4$, 0.28; $FeSO_4$, 6.57; $CuSO_4$, 1.65; $MnSO_4$ 1.02. The medium pH was adjusted on 5.5 using a solution of 2 M of NaOH or 2N HCl. Then, the medium was autoclaved at 121°C for 15 min. Each of the culture components was separately autoclaved and after reach to the ambient temperature, was combined with each other under the laminar flow hood at sterile conditions.

Batch Submerged Fermentation: A 0.5 mL of spore suspension was inoculated to 100 mL prepared and sterilized medium presented in each shake flask and the flasks were put in an incubator shaker at 27°C with 200 rpm agitation speed for 30 hours. At this period, cell growth was visible with the turbidity of the medium.

Sampling and Sample Preparation: Sampling from flasks was continuously performed at two hours time intervals. At each step, 10 mL of contained broth of a shake flask was taken by a sterile syringe next to flame under laminar flow hood as a sample. Then, the sampled flask was returned to incubator shaker to extend fermentation process.

Table 1: Kinetic equation of investigated models for fitting the growth rate of *S. cerevisiae*

Model	Equation
Monod	$\mu \equiv \mu_{\max} \dfrac{S}{K_s + S}$
Moser	$\mu = \mu_{\max} \dfrac{S^n}{k_s + S^n}$
Verhulst	$\mu = \mu_{\max} \left[1 - \dfrac{X}{X_m}\right]$

Analytical Methods: A colorimetric method by a 1% di-nitro salicylic acid solution with 0.5 g. L^{-1} Na_2SO_4, 10 g. L^{-1} NaOH and 2 g. L^{-1} phenols was used to determine glucose concentration. In this method, a spectrophotometer (Unico 2100, USA) at a wavelength of 540 nm was used. Cell dry weight was measured using a turbidity measurement method by spectrophotometer. Cell dry weight and glucose measurements were repeated three times for each sample.

Kinetic Models: Equation of each Kinetic model examined in this study is listed in Table 1. Monod and Moser kinetic models are two unstructured growth models that are substrate concentration dependent. Verhulst kinetic model is an unstructured model depends on biomass concentration. In equations and relations of kinetic models, μ and μ_{max} in terms of 1/h are the specific growth rate and the maximum specific growth rate of yeast, respectively. Where, S is limiting substrate (glucose) concentration in term of g. L^{-1}, K_s is the semi-saturated coefficient in term of g. L^{-1} and X_m is the maximum biomass concentration in term of g. L^{-1}.

RESULTS AND DISCUSSION

The incubation time of the fermentation process was prolonged for 30 hours. *S. cerevisiae* growth in the shake flasks was observed for approximately 3 hours after inoculation as medium turbidity. At 23 hours of incubation, cell dry weight was reached to its maximum value and then yeast growth was entered to the stationary phase. The stationary phase of *S. cerevisiae* was happened in the time interval of 24 to 27 hours of incubation. After 27 hours, the cell population gradually entered to death phase, of course it cannot be realized by its appearance because it does not change a lot. The only remarkable issue in death phase was its un-favorite smell. During the fermentative process of *S. cerevisiae* in shake flask, required samples have been taken at appropriate time intervals and were prepared for next assessments.

Table 2: Experimental data on cell growth and nutrient utilization and calculated values for specific growth rate in exponential growth phase

Time (h)	X (g. L^{-1})	S_{ave}(g.L^{-1})	μ(1/h)
7	1.6484	9.35	0.633081
9	3.096	7.55	0.527105
11	6.06358	5.9	0.479353
13	8.783	4.495	0.420534
15	12.402	3.295	0.379198
17	14.7285	2.13	0.337307
19	16.09855	1.16	0.300703
21	17.4169	0.54	0.271664
23	18.3992	0.265	0.247241

The majority of glucose in the medium was consumed in the first 13 hours of process which consisted of lag and a part of exponential growth phases of yeast. With the beginning of the stationary phase, the change profile of glucose concentration in the medium was reduced significantly and glucose concentration almost reached near to zero until the end of fermentation process. In all kinetic investigation cases, experimental data on glucose concentration and cell dry weight were used to determine an appropriate kinetic model for *S. cerevisiae* growth in batch culture.

The kinetic constants and parameters (X_{max}, K_s, μ_{max}) were determined based on the curve fitting method. The values of specific growth rate (μ) was calculated according to the cell dry weight as biomass concentration (X) and glucose concentration as limiting substrate concentration (S) during the exponential growth phase. Experimental and calculated values are presented in Table 2. Based on the experimental data, X_0 and t_0 were considered 0.13 g. L^{-1} and 3 hours, respectively.

Investigation on curve fitting of cell growth with Monod model did not show acceptable fitness (Fig. 1). Based on the software analysis, μ_{max} and K_s with Monod kinetic model were evaluated as 0.377 h^{-1} and 0.157 g. L^{-1}, respectively. Also, in this case, R^2 was fitted on 0.81 that it does not seem so desirable. According to the results, Monod kinetic model is not seemed to be a suitable model to express the kinetic behavior of this strain.

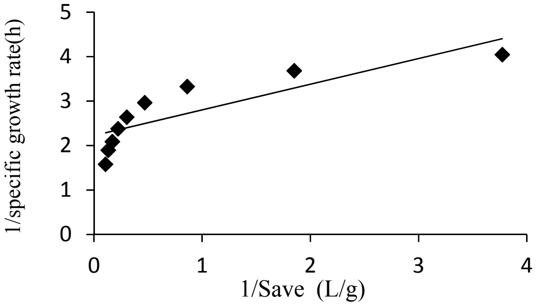

Fig. 1: The Lineweaver-Burk linear plot to fitting the experimental data on substrate utilization and cell growth to Monod kinetic model

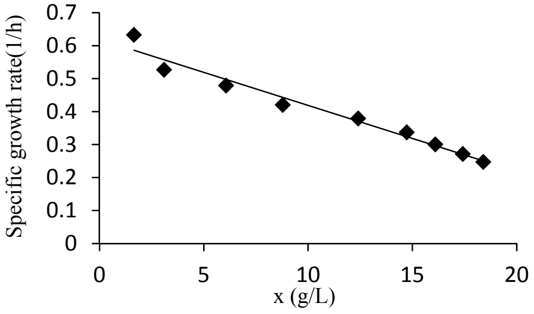

Fig. 2: The Lineweaver-Burk power plot to fitting the experimental data on substrate utilization and cell growth to Moser kinetic model

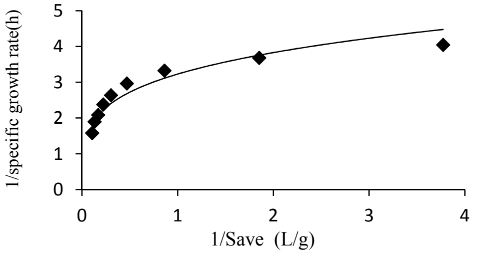

Fig. 3: The linear plot to fitting the experimental data on substrate utilization and cell growth to Verhulst kinetic model

Investigation on curve fitting of cell growth with Moser model have shown that despite suitable R^2 and μ_{max}, the behavior of this yeast does not have acceptable consistency with the described model due to illogical K_s (Fig. 2). In this case, R^2 and μ_{max} were obtained 0.97 and 0.502 h^{-1}, respectively. R^2 with Moser is more than Monod that demonstrated the better fitness of the experimental data of *S. cerevisiae* growth and substrate utilization with the theoretical base of the Moser kinetic Model. Also, in Moser case, a greater μ_{max} was obtained in comparison to the Monod. But, the obtained K_s with the Moser kinetic model was not satisfactory.

As can be seen in Figure 3, to evaluate kinetic behavior fitness of *S. cerevisiae* with Verhulst model, linear curve fitting method was used on μ based on X curve. Results showed that the experimental data of the cell growth and substrate consumption in batch submerged culture did not have a good fitness with Verhulst model by the regression of 0.97. In this regard, the maximum specific growth rate (μ_{max}) and the maximum biomass concentration (X_m), was 0.59 h^{-1} and 32.43 g. L^{-1}, respectively.

Table 3: A comparison survey of kinetic parameters of *S. cerevisiae* growth and substrate utilization with three different kinetic models

Kinetic model	RMSE	SSE	R^2	K_s (g. L^{-1})	μ_{max} (h^{-1})	X_m (g. L^{-1})
Monod	0.5721	3.273	0.81	0.157	0.377	-
Moser	0.2361	0.502	0.97	1.003	0.502	-
Verhulst	0.1103	0.121	0.97	-	0.593	32.43

Table 3 represents a comparison of the kinetic parameters obtained by fitting the kinetic models examined in this study.

CONCLUSION

This is the first report on the cell growth and substrate utilization kinetic of *S. cerevisiae* with respect to Monod, Moser and Verhulst kinetic models. The experimental data on cell growth and nutrient utilization in submerged batch fermentation process were interpreted using Monod, Moser and Verhulst kinetic models as unstructured models based on substrate concentration (Monod and Moser models) and biomass concentration (Verhulst model). Based on the results, the Verhulst kinetic model was the most appropriate to describe the biomass growth rate of *S. cerevisiae*. Maximum specific cell growth rate by Verhulst model was 0.59 h^{-1}.

REFERENCES

1. Schneiter, R., 2004. Genetic molecular and cell biology of yeast 2004: Yeast Genetics.
2. Najafpour, G., H. Younesi and K. Syahidah Ku Ismail, 2004. Ethanol fermentation in an immobilized cell reactor using *Saccharomyces cerevisiae.* Bioresource Technology, 92(3): 251-260.
3. Rajagopalan, G. and C. Krishnan, 2008. α-Amylase production from catabolite derepressed *Bacillus subtilis* KCC103 utilizing sugarcane bagasse hydrolysate. Bioresource Technol., 99(8): 3044-3050.
4. Bigelis, R., 1985. Primary metabolism and industrial fermentations in gene manipulations in fungi 1985: Academic Press.
5. Amore, G., T. Panchal and R. I, 1988. factors that influence the ethanol tolerance of brewer's yeast strains during high gravity worth fermentation. Tech Master Brew Assoc., 25: 47-53.
6. Cardona, C.A., O.J. Sanchez and L.F. Gutierrez, 2010. Process synthesis for fuel ethanol production. Taylor and Francis Group, www.Crcnetbase.com.
7. Visser, W., W.A. Scheffers, W.H. Batenbu Cardona, C.O.J. Sαnchez and L.F. Gutiérrez, 2010. Process synthesis for fuel ethanol production. Florida. Taylor and Francis Group, www.Crcnetbase.com. rg-van der Vegte and J.P. van Dijken, 1990. Oxygen requirements of yeasts. Applied and environmental microbiology, 56(12): 3785-3792.
8. De Kock, S., J. Du Preez and S. Kilian, 2001. The effect of growth factors on anoxic chemostat cultures of two S*accharomyces cerevisiae* strains. Biotechnology Letters, 23(12): 957-962.
9. Lievense, J. and H. Lim, 1982. Growth and dynamics of *saccharomyces cerevisiae*. Annu. Rep. Ferment. Processes; (United States), pp: 5.
10. Barford, J. and R. Hall, 1981. A mathematical model for the aerobic growth of Saccharomyces cerevisiae with a saturated respiratory capacity. Biotechnology and Bioengineering, 23(8): 1735-1762.
11. Verduyn, C., T.P. Zomerdijk, J.P. van Dijken and W.A. Scheffers, 1984. Continuous measurement of ethanol production by aerobic yeast suspensions with an enzyme electrode. Applied microbiology and Biotechnology, 19(3): 181-185.
12. Koutinas, A., R. Wang, I. Kookos and C. Webb, 2003. Kinetic parameters of *Aspergillus awamori* in submerged cultivations on whole wheat flour under oxygen limiting conditions. Biochemical Engineering Journal, 16(1): 23-34.
13. Seki, K., M. Thullner and P. Baveye, 2004. Nutrient uptake kinetics of filamentous microorganisms: Comparison of cubic, exponential and Monod models. Annals of Microbiology, 54: 181-188.
14. Altiok, D., F. Tokatli and S. Harsa, 2004. Kinetic modelling of lactic acid production from whey. Izmir Institute of Technology. Turkey.
15. Ardestani, F., 2011. Investigation of the Nutrient Uptake and Cell Growth Kinetics with Monod and Moser Models for *Penicillium brevicompactum* ATCC 16024 in Batch Bioreactor. culture, Iranica Journal of Energy and Environment (IJEE), 2(2): 117-121.

16. Firozjaee, T.T., G.D. Najafpour, M. Khavarpour, Z. Bakhshi, R. Pishgar and N. Mousavi, 2011. Phenol Biodegradation Kinetics in an Anaerobic Batch Reactor. in Reston, VA: ASCE Proceedings of the World Environmental and Water Resources Congress; May 22. 26, 2011, Palm Springs, *California| d 20110000*. American Society of Civil Engineers.
17. Ardestani, F., 2012. Survey of the Nutrient Utilization and Cell Growth Kinetic with Verhulst, Contois and Exponential Models for *Penicillium brevicompactum* ATCC 16024 in Batch Bioreactor. World Applied Sciences Journal, 16 (1): 135-140.
18. Pishgar, R., G. Najafpour, B.N. Neya, N. Mousavi and Z. Bakhshi, 2011. Anaerobic biodegradation of phenol: Comparative study of free and immobilized growth. Iranica Journal of Energy and Environment (IJEE), 2(4): 348-355.
19. Khorrami, M., G. Najafpour, H. Younesi and G. Amini, 2011. Growth kinetics and demineralization of shrimp shell using *Lactobacillus plantarum* PTCC 1058 on various carbon sources. Iran J. Ener. Environ., 2: 320-5.

Persian Abstract

DOI: 10.5829/idosi.ijee.2014.05.01.2

چکیده

ساکارومایسس سرویسیه به عنوان پرکاربردترین میکروارگانیسم یوکاریوتی در مطالعات زیستی شناخته شده است. در تحقیق حاضر پروفیل رشد *ساکارومایسس سرویسیه* در یک محیط کشت غوطه ور ناپیوسته با سه مدل سینتیکی غیر ساختاری متفاوت مورد بررسی قرار گرفته است. بررسی برازش داده های آزمایشگاهی رشد سلول با سه مدل سینتیکی با استفاده از ابزار برازش منحنی در نرم افزارهای اکسل و مت لب انجام شده است. نتایج حاصله نشان داده که مدل سینتیکی ورهالست با رگرسیون ۰/۹۷ مناسب ترین مدل برای بیان رفتار سینتیکی رشد *ساکارومایسس سرویسیه* بوده است. بیشینه شدت رشد ویژه سلول بر اساس این مدل برابر با ۰/۵۹ بر ساعت بوده است. سایر پارامترهای سینتیکی نیز برای هر سه مدل مورد بررسی تعیین گردیده است.

Iranica Journal of Energy & Environment 5 (1): 13-17, 2014
ISSN 2079-2115
IJEE an Official Peer Reviewed Journal of Babol Noshirvani University of Technology
DOI: 10.5829/idosi.ijee.2014.05.01.03

BUT

Numerical and Experimental Analysis of a Spiral Horizontal Axis Wind Turbine

[1]Muhammad Abid, [1]Khasan S. Karimov and [2]Hafiz A. Wajid

[1]Faculty of Mechanical Engineering,
GIK Institute of Engineering Sciences and Technology, Topi, KPK, Pakistan
[2]Department of Mathematics,
COMSATS Institute of Information Technology, Lahore, Pakistan

(Received: January 6, 2014; Accepted in Revised Form: March 13, 2014)

Abstract: This paper presents results of design, analysis, manufacturing and testing of a spiral horizontal axis wind turbine. In first step, modeling and computational fluid dynamic (CFD) analysis was performed. Helix blades angle for spiral rotors of outer and inner diameter of 0.85 and 0.45m, respectively was optimized. In the second step, as per optimized spiral rotor dimensions, a prototype was manufactured. Experiments were carried out for torque and power calculations; obtained results are discussed.

Key words: Wind turbine · Numerical and experimental analysis · Spiral horizontal axis · Torque and power calculations

INTRODUCTION

Power generation by suitable biodiesel for the gas turbine is considered as green energy [1]. It has been reported that even ocean wave energy assisted by wind power produced significant power by point absorber wave energy convertors [2]. In fact power generated by wind turbines is an environmental friendly method of producing electrical energy. The rotors are designed using aerodynamic principles with the purpose of extracting some of the kinetic energy from the wind by developing rotational forces on the rotor, when placed in sufficiently strong wind. There is significant potential for power generation from wind in Pakistan. The coastal regions of Sindh and Baluchistan offer ideal locations for wind farms. There is also impressive potential across the northern border of the provinces of Punjab and Khyber Pukhtoonkhwa. Generation of electricity through wind is not something new. India, the fifth in line of countries in the world for the generation of electricity, is producing more than 13,000 MW of electricity by utilizing wind turbines. It is not only manufacturing these turbines but exporting them toother countries. Once a wind turbine is installed, it would produce energy for 25-30 years free of cost as no other fuel is used except wind through this mode of production. Due to increase in population and technological trends, there is a growing need for energy. At present, Pakistan alone there is an estimated power shortage of approximately 4000 MW (18%) [3]. Energy shortage is a real crisis in the developing world; such deficiency is increasing as the price fuel increasing. Therefore, more funds are invested in research on renewable energy and it is rapidly becoming one of the important research areas of today.

This paper provides analysis and development of a working spiral airfoil wind turbine (SWT) to produce electricity. It is drag type device which takes advantage of the air flow produced around smooth spiral shaped blades. Preliminary analysis and testing has revealed that this device starts up at a very low speed when compared to other horizontal axis wind turbines (HAWT). It also offers better performance at low wind speeds when compared to other turbines of comparable dimensions. In SWT air is directed parallel to the horizontal axis of the turbine. When flowing air comes in contact with the rotors, it imparts a force and hence a moment which produces rotational motion about the turbine axis. The surface of the rotors is kept smooth to minimize the

---

Corresponding Author: Muhammad Abid, Faculty of Mechanical Engineering, GIK Institute of Engineering Sciences & Technology, Topi, KPK, Pakistan. E-mail: abid@giki.edu.pk.

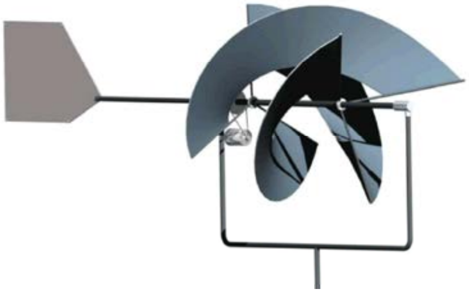

Fig. 1: The 3D Spiral Wind Turbine Model

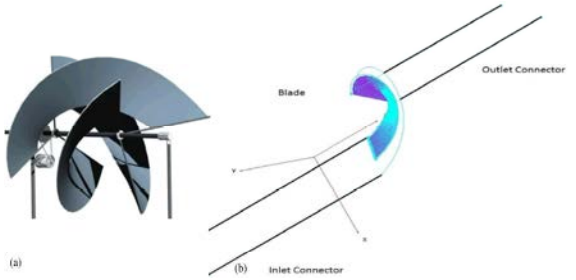

Fig. 2: (a) Model of spiral blade, (b) Extension of Inlet and Outlet Domains

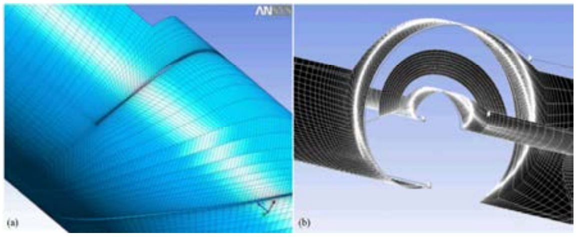

Fig. 3: (a) Meshing at 50% blade span wise location, (b) Meshing of the inlet and outlet domains

effects of turbulence. Fig. 1 shows design of a SWT which is an emerging concept with a higher efficiency as compared to a conventional three bladed propeller type wind turbine, low start-up speed, low cost of manufacturing and easy to assemble [4].

Modelling and Meshing of the Blades: The dimensions of the SWT were selected based on the availability of testing in the wind tunnel lab; i.e. blade outer radius = 0.85m, blade inner radius= 0.45m,length of the blade collar = 0.8m and helix Angle (between leading and trailing edge of blade) = 200 degree.The blades are modeled using Pro-Engineer software [5] as shown in Fig. 2a.

Turbo-Grid [6], a module of ANSYS CFX [7] required hub and shroud clearance of SWT. Therefore, a domain of influence around the blades of SWTis defined in terms of extrapolated dimensionsfor the inner diameter (0.3m), outer diameter(1.5m) and a span wise blade length (0.2m).After converting the geometric model to a combination of grid points, the inlet and outlet domains are specified in Gridgen[8]. Two "2 point connectors" are made starting from the vertex of the inlet blade side to specified points along the axis of rotation and the same procedure is carried out for the outlet side as shown in Fig. 2b.

Table 1: Mesh Sensitivity Analysis

	Baseline	Coarse	Fine
Nodes	458419	269739	636961
Elements	428124	248040	600928
Max. Face Angle	162.56	157.29	158.80
Min. Face Angle	12.44	12.57	13.62
Percent Error	0	1.62	1.09

ANSYS TURBOGRID Ver.12.1 was used to generate a structured mesh for the entire flow domain with 428124 quadrilateral mesh elements. In order to capture the flow separation effects in a suitable manor,H/J/C/L Grid method was used which also included an O-Grid around the blade, resulting in increased mesh sensitivity around the blade. Fig. 3a shows mesh elements at 50% span wise location of the blade with concentrated mesh near the blade. Fig. 3b depicts the meshing of the inlet and outlet domains. A mesh sensitivity analysis was also carried out in order to assess the validity of the numerical simulation, using three different mesh configurations which are summarized in Table 1.

Boundary Conditions: For CFD Analysis, a single blade was modeled and periodic boundary condition was applied to the model along withentire rotor. The rotor was placed in a rotating fluid domain with stationary inlet and outlet. Air at 25ºC was the fluid. The morphology of the domain was set as continuous. A reference pressure of 1atm was specified for the entire domain. Heat transfer effects were neglected by specifying the entire domain as an isothermal zone. The inlet boundary condition for the mass and momentum equations was specified as normal speed. A constant static pressure boundary condition was applied at the outlet and blade which was set as a no slip wall. Based on the limitations of the K-å turbulence model for not accurately predicting the flow separation effects at wall faces, shear stress transport (SST) Turbulence model was used to capture desired manor the flow separation effects on the face of the blades [7].

RESULTS AND DISCUSSION

Performance coefficient defines the performance of a wind turbine and is expressed with the variation in tip speed ratio (TSR). The TSR is defined as a ratio of the velocity of wind blowing from the rotor blade against the wind velocity at the tip of the blade and is a non-dimensional figure and can be derived as per equation 1.

$$\mathrm{TSR}\ (\lambda) = R\Omega/v \qquad (1)$$

In reality, the rotational speed of the rotor blade changes according to the speed of wind blowing into the system.But, if this fact is taken into account in the numerical analysis, the actual wind velocity change in blade rotation speed, which differs depending on the wind velocity, must be obtained through an experiment. This can be quite inconvenient. Therefore, this study fixes the wind velocity by using the non-dimensional number of TSR and changes only the blade rotation speed. This approach resembles Reynolds similarity principle. Even if the wind velocity is fixed, as long as only one variable among the other variables such as the blade's radius (R) and rotational speed (Ω) is adjusted and all other conditions are identical; there is no problem in the numerical analysis [9]. The calculation conditions were set as follows: the velocity of air coming normal to the inlet was set at 5 m/s. The rotational speed of the blade was varied from 30 rpm to 140 rpm and TSR was observed in the range of 0.18 to 0.87. The torque on each blade was calculated using the torque function available in ANSYS-CFX 12.1. Power is obtained by the product of the total torque acting on all the blades with the rotational speed. Performance coefficient for a wind turbine is defined as the ratio of the extracted power from the wind to the total power available in the airstream at a fixed wind speed. Ten case studies were performed and the results are summarized in Table 2. The maximum Performance Coefficient (C_p) of 0.488 is obtained as per equation 2 at a wind speed of 5 m/s and a rotational speed of 100rpm. As the Betz limit places a limit on the maximum performance coefficient for a wind turbine to be 0.593 [10]. Hence, these results indicate a high efficiency in comparison with other wind turbine designs.

$$C_p = \frac{Power\ Extracted\ \ from\ wind}{\frac{1}{2}\rho A V^3} \qquad (2)$$

Table 2: Effect of varying rotational speed on TSR and performance coefficient

	Inlet Velocity (m/s)	RPM	TSR	C_p
Case 1	5	30	0.1885	0.2577
Case 2	5	40	0.2513	0.3195
Case 3	5	50	0.3141	0.3729
Case 4	5	60	0.3770	0.4152
Case 5	5	70	0.4398	0.4503
Case 6	5	80	0.5026	0.469
Case 7	5	90	0.5655	0.4824
Case 8	5	100	0.6283	0.4877
Case 9	5	120	0.7540	0.4806
Case 10	5	140	0.8796	0.4588

Where, ρ = Density of air, A = Cross Section Area, V = Wind speed

Pressure difference between the front and back sides of the blade ranging from -75 to 85 Pa at the fixed wind speed (5 m/s) produced resultant force on the blades which is resulting in the rotational motion of the shaft [Fig. 4a] [11]. Fig. 4 billustrates swirling airflow on the downstream of the rotor.

Fabrication and Assembly of Blades for Testing: Based on Pugh and Weighted index method, fiber glass material was selected. Based on the CFD analysis and optimized helix angles and size of the SWT blades; spray lay-up an open-molding composites fabrication process where resin and fiber layers (reinforcements) are sprayed onto a reusable mold was used.A triangular-shaped structure was designed to hold the axial loads and the weight of the turbine itself with shaft held together by bearings at each end. A pulley made of Teflon material was also attached to the shaft for testing purpose. Final assembly and testing arrangement is shown in Fig. 5.

A digital anemometer was used to measure the wind velocity at inlet of wind turbine. Different values of air speed were taken. First reading was taken at the center of wind tunnel and then moving radially outward. Average value was taken as final air speed. The fan speed of the wind tunnel was changed in order to achieve different wind velocities at the exit. First the startup speed of the turbine was calculated, it was that speed at which the turbine starts to rotate (without any load). This was found out to be 0.85 m/s. The shaft torque and power were determined at different inlet air velocities ranging from 1.7 ~ 8.5 m/s and the RPM of shaft was determined at that specific wind speed using a tachometer. Further experiments were performed to measure the torque and shaft power produced at different wind velocities. SWT was placed 4ftaway from the wind tunnel so that air profile

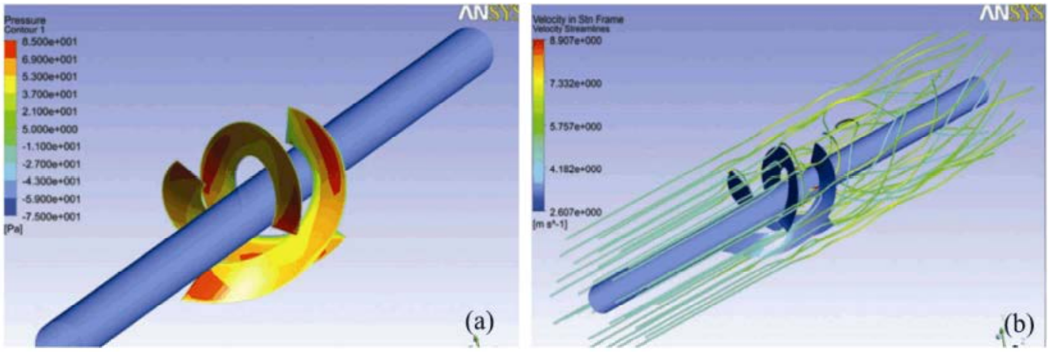

Fig. 4: (a) Pressure distribution on the blade surface, (b) Velocity streamlines at the inlet and outlet blade surface

Fig. 5: Final assembly and testing arrangement

Table 3: Results obtained for optimum distance

Air Speed m/s	Distance ft.	RPM	ω rad/s	Force N	Torque Nm	Power Experimental Watts	C_p
8.5	1.0	128	13.41	35	2.8	37.54	0.16
8.5	1.5	135	14.14	37.8	3.02	42.76	0.19
8.5	2.0	143	14.98	39.5	3.16	47.33	0.21
8.5	2.5	150	15.71	41.4	3.31	52.04	0.23
8.5	3.0	161	16.87	43.7	3.49	58.96	0.26
8.5	3.5	175	18.33	46.3	3.70	67.90	0.30
8.5	4.0	184	19.28	48	3.84	74.02	0.33
8.5	4.5	180	18.86	46.9	3.75	70.75	0.31
8.5	5.0	172	18.02	45.8	3.66	66.02	0.29
8.5	5.5	165	17.29	44.2	3.53	61.12	0.27
8.5	6.0	157	16.45	42.7	3.41	56.18	0.25

can be nearly uniform and back pressure of wind striking the rear wall could not be able to affect the RPM and at the stated distance maximum power coefficient (C_p) was achieved. Results are summarized in Table 3. Experimental power (Watts) was calculated by torques obtained in the Table using equation 3.

Power Experimental (W) = Torque (N.m) xω (rad/s) = Torque (N.m) x RPM x $2\pi/60$ (3)

Fig. 6: Wind tunnel used for experiments

The wind tunnel used for experiments is shown in Fig. 6.

CONCLUSIONS

CFD analysis provided optimized helix angles for the spirals of the horizontal axis wind turbine with given inner and outer rotor diameters. The maximum performance coefficient (C_p) of 0.488 is obtained at a wind speed of 5 m/s and a rotational speed of 100rpm. As per optimized spiral rotor dimensions, a prototype were manufactured and experiments were performed. A start up speed of 0.85 m/s, maximum power of 74 watts at air velocity of 8.5 m/s was determined.

ACKNOWLEDGEMENTS

Authors are thankful to FahadSarwar, M. Junaid Khalid, M. UsmanIftikhar, Munam Bilal Tariq, M. Rehman, M. A. Asad, A. M. Qaisrani, K. Mahmood and M. S. Z. Malik for their assistances and contributions in performing the experimental studies.

REFERENCES

1. Gupta, K., A. Rehman and R. Sarviya, 2010. Evaluation of soya bio-diesel as a gas turbine fuel. Iranica Journal of Energy and Environment, 1(3): 205-210.
2. Nazari, M., H. Ghassemi, M. Ghiasi and M. Sayehbani, 2013. Design of the Point Absorber Wave Energy Converter for Assaluyeh Port.
3. <http://www.pakistantoday.com.pk/2011/04/power-shortfall-set-to-cross-4000mw/>
4. Parker, D.B. *Wind turbine blade assembly and apparatus*, 2009, Google Patents.
5. http://www.ptc.com/products/creo-elements-pro/.
6. <http://www.ansys.com/products/turbogrid.asp>.
7. <http://www.ansys.com>.
8. http://www.pointwise.com/<http://www.pointwise.com/>
9. Kim, B., J. Kim, K. Kikuyama, V. Rooij and Y. Lee. 3-D numerical predictions of horizontal axis wind turbine power characteristics of the scales delft university T40/500 model. in The fifth JSME-KSME fluids engineering conference, Japan. 2002.
10. Hartwanger, D. and A. Horvat, 3D Modeling of a wind turbine using CFD. in NAFEMS Conference. 2008.
11. Amano, R. and R. Malloy, 2009. CFD analysis on aerodynamic design optimization of wind turbine rotor blades. World Academy of Science, Engineering and Technology, 60: 71-75.

Persian Abstract

DOI: 10.5829/idosi.ijee.2014.05.01.03

چکیده

این مقاله نتایج حاصل از طراحی، تجزیه و تحلیل، ساخت و تست یک توربین بادی با محور افقی مارپیچی را ارائه می‌نماید. در مرحله اول، مدل‌سازی و آنالیز CFD انجام شده است. زاویه پره‌ها برای روتور مارپیچ با قطر خارجی و داخلی به ترتیب ۰.۸۵ و ۰.۴۵ متر بهینه‌سازی شده است. در مرحله دوم، برای بهینه‌سازی ابعاد روتور مارپیچ، یک نمونه اولیه ساخته شد. به منظور محاسبه گشتاور و قدرت، آزمایشاتی انجام شد؛ نتایج به دست آمده مورد بحث و بررسی قرارگرفت.

Iranica Journal of Energy & Environment 5 (1): 18-25, 2014
ISSN 2079-2115
IJEE an Official Peer Reviewed Journal of Babol Noshirvani University of Technology
DOI: 10.5829/idosi.ijee.2014.05.01.04

BUT

Enrichment of Olive Oil with Alpha Linolenic Acid Catalyzed by Lipase Mediated Trans-Esterification

[1]Banin Rupani, [2]Ramchandra Gadre, [1]Kisan Kodam and [3]Ghasem D. Najafpour

[1]Department of Chemistry, University of Pune, Pune 411007, Maharashtra, India
[2] Chemical Engineering and Process Development Division,
National Chemical Laboratory, Pune 411008, Maharashtra, India
[3]Biotechnology Research Lab., Faculty of Chemical Engineering,
Noshirvani University of Technology, Babol, Iran

(Received: December 3, 2013; Accepted in Revised Form: February 28, 2014)

Abstract: Consumption of Polyunsaturated fatty acid omega-3 is the most recommended fatty acids which have a health benefits for brain, kidney and eye. The conversion of plant-derived omega-3 (n-3) α-linolenic acid (ALA, 18:3n-3) to long-chain eicosapentaenoic acid (EPA, 20:5n-3) and docosahexaenoic acid (DHA, 22:6n-3) can enhance ALA sufficient diets in compare to ALA deficient diets. Alpha-linolenic acid (ALA) was extracted and enriched from flax seed oil. Commercial lipases *Candida rugosa*, *Pseudomonas cepacea and P. fluorescens* were used for transesterification of ALA enriched from flax seed oil into olive oil TAG back bone. Gas chromatography of olive oil showed it contained high amounts of oleic acid (C18:1, n-9), linoleic acid (C18:2, n-6) and palmitic acid (C18:0) with 0% of ALA. Among the commercial lipase *C. rugosa* has more preference to ALA and 27% of ALA was incorporated to TAG back bone of olive oil. In 24 hours reaction time, the ALA concentration in TAG of olive has increased to 26% while oleic acid decreased to 60% and palmitic acid decreased from 25 to 7%. The highest incorporation of ALA into olive oil (29%) occurred for ALA: olive oil mole ratio (1:2). There was a decline in incorporation of ALA in olive oil backbone with an increase in the amount of water. ALA incorporation of 25% occurred with 100 µl water while without water it was 27%; it decreased to 15% with 1 ml of water.

Key words: Lipase · α-linolenic acid · Enriched olive oil · Polyunsaturated fatty acid · Transesterification

INTRODUCTION

Alpha-linolenic acid (ALA) is a series of n-3 polyunsaturated fatty acid (PUFA), which was found mainly in vegetable oil such as flaxseed oil, walnut oil, rapeseed oil and perilla oil [1]. Omega-3 fatty acids, docosahexaenoic acid (DHA) and eicosapentaenoic acid (EPA) and ALA are associated with health benefits [2, 3]. Consumption of appropriate amounts and proportions of these fatty acids are essential. Long -chain n-3 PUFAs such as DHA can be converted from the precursor α-linolenic acid (LNA, 18:3n-3), via delta-6 desaturase (D6D), delta-5 desaturase (D5D) and elongases, although the conversion is limited. Therefore, mammals obtain DHA [4] either as DHA itself or the precursor LNA. Also obtained from intermediates between LNA and DHA, like eicosapentaenoic acid (EPA, 20:5n-3) [5]. It has been reported that adequate intake of only LNA is sufficient to maintain normal brain DHA concentration [4].

Flax seed oil contains large amount of ω-3polyunsaturated fatty acid which can delay PUFA oxidation. ALA is partitioned to chylomicron TAG and very little to phospholipids after absorption [6]. It has recently been reported that ALA can be metabolized with emphasis on inter conversion as well as the oxidation and carbon recycling [4]. The conversion of the plant-derived omega-3 (n-3) α-linolenic acid (ALA, 18:3n-3) to the long-chain eicosapentaenoic acid (EPA, 20:5n-3) and docosahexaenoic acid (DHA, 22:6n-3) can increase ALA sufficient diets in compare to ALA deficient diets [7].

Corresponding Author: Ghasem D. Najafpour, Biotechnology Research Lab., Faculty of Chemical Engineering, Noshirvani University of Technology, Babol, Iran. E-mail: najafpour@nit.ac.ir.

Enzymatic enrichment of PUFA has shown great potential in production of high quality nutrients in mild process conditions (e.g. neutral pH and low temperatures).

Olive oil is enriched in mono-unsaturated fatty acids (MUFA), specially oleic acid (C:18 n:1). It is a desirable substrate for transesterification because a diet rich in olive oil has been shown to reduce plasma low-density lipoprotein cholesterol (LDL), while leaving high-density lipoprotein cholesterol (HDL) unchanged [8]. Since high concentration of LDL causes high risk for coronary heart disease, it is recommended to reduce intake of dietary saturated fatty acids (SFAs) and increase the consumption of PUFA and MUFA [9]. According to Indian Council of Medical Research, the desirable proportions of saturated acid, oleic acid and PUFA in the dietary fats should be in proportion of about 1:1:1 [10]. Recently, many efforts have been carried out in transesterification or inter-esterification reactions to modify and enrich the content of n-3 PUFA in vegetable oil, melonseed oil, borage oil and evening primrose oil with implementation of biocatalysts such as lipases [11, 12].

The use of lipases for olive oil enrichment in presence of ALA enriched from flax seed oil can be a novel idea. In this study, preparation of ω-3 PUFA enriched acyl-glycerol from olive oil via enzymatic transesterification was conducted using three commercial lipases. The purpose of present work was to evaluate effects of several parameters such as temperature, reaction time, ratio of ALA with olive oil and water content on ω-3 PUFA enrichment of olive oil with specific lipase.

MATERIALS AND METHODS

Chemicals: Lipases of *Candida rugosa* (lipase 1, Cat EU029c)*, Pseudomonas cepacea* (lipase 4, Cat EU088C) *and P. fluorescens* (lipase 21, Cat EU084) were purchased from Euoropa Bioproducts (Cambridge, UK). Fatty acid methyl ester mixture (Supelco 37 FAME Cat 47885-U), methyl linoleniate, triolein, 1, 2 di-olein, 1,3 di-olein, 1 mono-olein, 2 mono-olein and para-nitrophenyl palmitate (pNPP) were purchased from Sigma. All the solvents of HPLC grade or AR grade and thin layer chromatography plates (TLC, Silica gel_{60}, aluminum support) were purchased from Merck, Mumbai, India. Flax seeds and olive oil were locally purchased.

Preparation of Olive Oil Fatty Acid Methyl Ester: Fatty acid methyl esters derived from olive oil were prepared by mixing one gram of purified TAG with 3N methanolic KOH at 60°C for 3h. Unreacted TAG was extracted by hexane, while adding 3N methanolic HCl acidify the mixture and extracted fatty acids in hexane. The recovered fatty acids were subjected to esterification reaction by addition of 3N methanolic HCl and hexane at 60°C, left over night. Then FAME were extracted 3 times in hexane and dried over Na_2SO_4 and filtered through normal Whatman filter paper and evaporated under vacuum, FAMEs were analyzed by Gas chromatography (Chemito-1000). The GC was equipped with FID detector, capillary column (30m length, 0.25mm ID, 0.25µm film thickness, Supelco Company). Nitrogen gas was used as carrier gas with flow rate of 0.8ml/min. The detail of GC settings are stated in our previous published work [13].

Transesterification Reaction: A small scale transesterification reaction was conducted in 50 ml round bottom capped flask. According to author previous work [13], α-linolenic acid (ALA) which is used in transesterification reaction was enriched up to 80% by urea complexation method. The reaction mixture contained olive oil (0.4g) with enriched α-linolenic acid (ALA) (0.1g) from flax seed oil were incubated at 35°C, in stirring condition with individual free lipase sources (300U) for 24h, in 5ml hexane. The reaction was terminated by adding anhydrous sodium sulfate to the reaction mixture and filtration was carried out was through filter paper to remove the enzyme. Hexane was removed under vacuum, the reaction mixture was loaded on 10 cm Alumina column and individual components of TAG and FA were eluted with 150 ml hexane: diethyl ether as mobile phase to separate the TAG from fatty acids. Five ml fractions were collected and analyzed by TLC for absence of fatty acids. The pure TAG fractions were collected, the solvent was evaporated and purified TAGs were collected. To 10 µl of the concentrated TAG sample 1 ml methanolic HCl and 1 ml hexane were added, the mixture was transferred to reaction tubes and subjected to esterification reaction for FAME preparation with stirring condition at 60°C. The FAME produced was analyzed for determination of fatty acid components of TAG by GC as described earlier.

Effect of Different Ratio of Olive Oil: Ala on Transesterification Reaction: Transesterification reactions were performed in the same condition as described above using different ratios of ALA: olive oil as 1:2, 1:4, 1:8 to optimize the effect of the ratio of oil and α-linolenic acid on transesterification.

Effect of Incubation Time on Transesterification Reaction: Transesterification reactions were performed for different time intervals like 1, 3, 6, 12 and 24 h in the same condition as described above and the product were analyzed for FAME content in TAG by GC.

Effect of Water Content on Transesterification Reaction: The transesterification reactions were performed with different quantities of water for instance 100, 250, 500 and 1000 µl in a reaction volume of 6ml, before addition of the enzyme to determine the effect of water activity on transesterification reaction. The fatty acid compositions of the TAGs purified from the reaction mixture by column chromatography were determined by GC analysis of FAME as described earlier.

RESULT AND DISCUSSION

Some vegetable oils have only limited applications in food products when they are used in their native form. They are often chemically or physically modified in order to enhance their quality. The quality of fat is determined by its value and chemistry of fat and also human requirements encourages modifying the fat to counter changing functional and nutritional challenges. Enzymatic interesterification is an efficient way of controlling the melting characteristics of edible oils and fats. This is performed by controlling the degree of conversion and reaction. No aggressive chemicals are used in the process and "trans" fats are not formed as in other production methods. Lipase mediated hydrolysis and synthesis are preferred techniques because of their well-known specificity and milder reaction conditions. Table 1 shows α-linolenic acid contents of some vegetable sources [14, 15]. Low amount (1.2%) of long chain fatty acids (C20-C22) was found in safflower oil. Linoleic acid content of poppy and safflower oil has 74% of it [16]. α-linolenic acid content of Perilla, linseed and flaxseed oil was more than 50%.

Table 1: α-Linolenic acid content of vegetable oils

Oil	α-Linolenic acid content (g/100 g of oil)
Perilla	54-65
Linseed	50-54
Flaxseed	53
Cohni	5.9-14.5
Canola	9-11
Wheat germ	6-9
Soybean	6.8
Modified canola	22–44

Enrichment of ALA by Urea Complexation: As discussed in our early stage of the work [13] urea complexation was found to be a suitable technique for enrichment of ALA from the fatty acid mixture. The GC analysis of the free fatty acids after urea complexation showed that the ratio of ALA enhanced to 82 %. It was also found that the ratio of 4:1 (urea: fatty acids) is the best for the enrichment of ALA [13]. This was presumably because of the removal of fatty acids like linoleic and palmitic acids by complexation and crystallization of the urea-fatty acid crystals. The technique of urea crystallization is specific and used for enrichment of ALA from the mixture of other fatty acids [17]. Also urea being highly water-soluble it was possible to separate ALA from urea by simple extraction, subsequently.

Fatty Acid Composition of Olive Oil: Olive oil is used as a substrate for enrichment with ALA. It contained high amounts of oleic acid (C18:1, n-9), linoleic acid (C18:2, n-6) and palmitic acid (C18:0) as shown in Fig. 1. It is found that it contains 70% monounsaturated fatty acid, 9% n-6 polyunsaturated fatty acid and it is a suitable source to provide a glycerol backbone and enriched with n-3 Polyunsaturated fatty acids.

Effect of Different Enzyme on Incorporation of ALA in to Olive Oil: Transesterification of olive oil with ALA was performed with enrichment of ALA in TAG backbone of olive oil was up to 27% by lipase from *C. rugosa* (Table 2) and GC chromatogram has confirmed the incorporation of ALA in to TAG back bone (Fig. 2). According to the results the degree of incorporation of ALA by commercial enzymes were *C. rugosa*> *P. fluorescens* > *P. cepacea.*

Table 2: Incorporation of ALA into olive oil back bone by different enzyme sources

	Palmitic acid %	Oleic acid %	Linoleic acid %	α-linolenic acid %
Olive oil	18.28	71.81	9.90	-00.01
Candida rugosa	10.79	52.29	9.79	27.13
Pseudomonas cepacea	22.87	57.27	6.79	13.07
Pseudomonas fluorescens	14.24	57.08	7.19	21.49

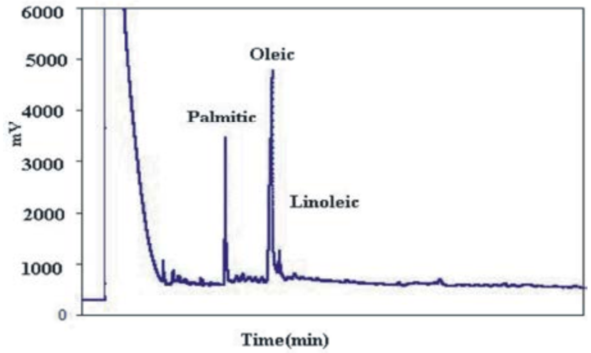

Fig. 1: GC chromatogram of olive oil fatty acids

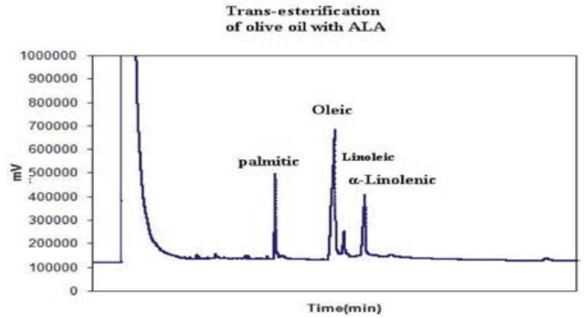

Fig. 2: GC chromatogram of Trans-esterified olive oil with ALA

It showed that free lipases can distinguish between PUFA and other fatty acids. Also, lipase shows less hydrolytic activity towards ester bonds of PUFAs that makes it more suitable for concentrating ALA. It was reported that lipase has been utilized for the recovery of EPA and DHA from marine oils and γ-linolenic acid from borage seed oil [8]. DHA-rich triglycerides were prepared from fish oil with lipases obtained from *C. rugosa* and *Chromo-bacterium viscosum* [18]. Lipase purified from *P. fluorescens* HU380 was used to concentrate EPA and DHA from oils [19]. About 19.6% incorporation of EPA and DHA in to hazelnut oil was reported by Can and Ozcelik [5]. All of these reports show that our free lipase from *C. rugosa* has a better effect on transesterification reaction which has incorporated 27% ALA into olive oil back bone.

Structured lipids containing EPA and DHA acids were synthesized in a batch reactor by lipase-catalyzed acidolysis of fish oil with caprylic acid. The following free lipases (Lipase AP, *A. niger* ; Lipase P, *Pseudomonas sp*.; Lipase A Y, *C. rugosa*; Lipase AK, *P. fluorescens*; Lipase F, *Rhizopus oryzae*; Lipase D, *R. delemar*) were used for esterification reaction. [20]. According to Tsao-Jen Lin and ShinWan Chen [21] after 6h reaction time, the degree of n-3 PUFA incorporation attained with various lipases was in order of *M. miehei* > *C. rugosa* > *C. Antarctica* > *Pseudomonas sp* and the 1,3-specific lipase from *M. miehei* resulted highest degree of incorporation 56% of PUFA. Senanyake and Shahidi [22] have reported the degree of DHA incorporation into borage oil in hexane at ambient temperature was in order of *C. antarctica* >*Pseudomonas sp*.> *M. miehei* > *C. rugosa*.

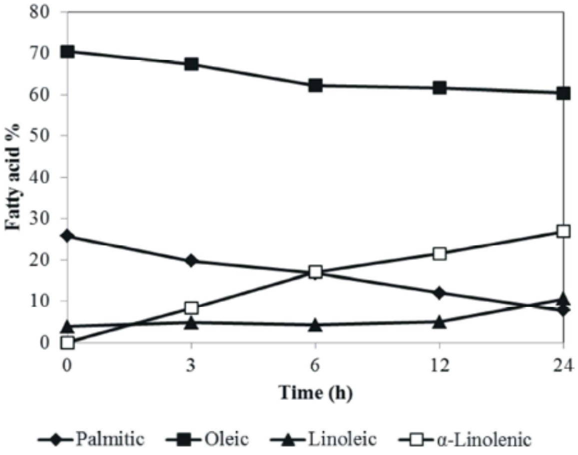

Fig. 3: Effect of time on incorporation of ALA in to TAG of olive oil

Effect of Time on ALA Incorporation in to Olive Oil: The dependence of reaction rate of transesterification with respect to time was investigated at 35°C in presence of 300U lipase. When the reaction time increased the ALA incorporation has increased and oleic acid concentration decreased from TAG back bone. The fatty acid compositions of TAG before and after transesterification are shown in Fig. 3. After transesterification for 6h ALA increased from zero to 17% and the content of oleic acid decreased from 70 to 62%, as the esterification progressed more ALA was consumed and incorporated in TAG back bone. In 24 hours of reaction time, the ALA concentration in TAG of olive has increased up to 26% while oleic acid decreased to 60% and palmitic acid decreased from 25 to 7%. In similar studies the optimal reaction time changed depending on enzyme and substrate used [22]. Incorporation of DHA into borage oil by *C. antarctica* lipase was increased as the incubation time increased to 24 h [22, 23], whereas Akoh and Moussata [24] have reported 40 h as the optimal reaction time for the incorporation of EPA and capric acid into borage oil. In addition, Can and Ozcelik [5] have reported 30-40h for incorporation of EPA and DHA in hazelnut oil,

Table 3: Effect of incorporation of ALA in TAG back bone by ratio of ALA: olive oil

Ratio of ALA: olive oil	Incorporated ALA in TAG back bone %
1:2	29
1:4	27
1:8	25

the C18-C20 acyl chain lengthened n-3 PUFAs (EPA and LA) in the triglyceride mixture were found to increase proportionally with the progress of hydrolysis up to 6 h [25].

In a similar study, Rao *et al.* [26] have used RSM to optimize reaction conditions in the modification of coconut oil TAG by lipase-catalyzed acidolysis in hexane to incorporate n-3 or n-6 PUFA. It was found that maximal incorporation of n-3 PUFA occurred at a 1:4 molar ratio of TAG/FFA when incubation carried out for 34 h at 54°C.

Effect of Ratio of ALA: Olive Oil for Enrichment of Olive Oil with ALA: Effect of ratio of ALA: olive oil on the level of incorporation of ALA in olive oil was examined at 35°C for 24 h. When the concentration of olive oil was increased from 1:4 to 1:8 (ALA: olive oil), the incorporation of ALA did not change significantly. The highest incorporation of ALA into olive oil (29%) occurred when a mole ratio of ALA: olive oil (1:2) was employed while the incorporation rate at 1:4 and 1:8 ratio were rather similar, 27 and 25%, respectively (Table 3).

This indicated that the incorporation of a foreign fatty acid into triacylglycerol is limited to replacement of one fatty acid molecule on TAG by polyunsaturated fatty acid irrespective of the concentrations and time of reaction. This is an interesting finding that requires deeper and further studies. In enzymatic enrichment of PUFA in oil, ratios can be adjusted according to the desired amount of fatty acid in product. In present study, the incorporation of ALA into olive oil increased by increasing the molar ratio of ALA: olive oil. Other investigators have also reported that the incorporation of n-3 fatty acid into seed oil raises by increasing the substrate molar ratio [11, 22]. Also, it has been stated that incorporation rate can be improved by choosing high substrate molar ratios while reducing the reaction time, but Jennings and Akoh [27] have pointed out a significant modification in large scale, using excess amounts of n-3 fatty acid had resulted in lipase inhibition and decreased in product yield while removing excess fatty acids. Fajardo *et al.* [28] have reported the incorporation of EPA into palm oil relatively enhanced (27.6%) in small volume of reaction (21.5%) at the mole ratio of 1:3.

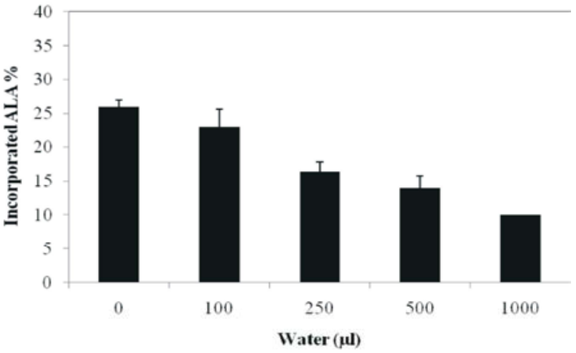

Fig. 4: Effect of water on ALA incorporation

However, there were no significant changes in terms of percentage of incorporation of DHA. Increasing the mole ratio of EPAX EE (fish oil concentrate high in n-3 PUFA) from 3 to 4 has increased the incorporation of both EPA and DHA by 11.3 and 6.5%, respectively; compared to when small quantities of the reactants used. When the mole ratio was further increased from 4 to 5, the percentage of incorporation slightly decreased. This may be due to the effect of mass transfer limitations on product yield, or the reaction may have reached to an equilibrium state. As the reactant quantities increased it has reflected on mass transfer of the reactants to the enzymes. Other researchers have shown that as the high mole ratio reflected on decrease of the reaction time; that has improved the reaction rate and resulted in less acyl migration.

Effect of Water Content on Incorporation of ALA in to Olive Oil Back Bone: The ability of lipase to catalyze reactions in organic solvents has been investigated. It is of common knowledge that the rate of enzyme catalyzed reactions in such systems strongly depend both on the amount of water present in the system and on the nature of the organic solvent used [29]. Catalytic activity and stability of enzymes are markedly influenced by hydration levels [30]. Often higher hydration levels are known to result in collection of enzyme leading to reduce yields [31]. Each enzyme displays different levels of water content profile for maximal activity [32]. A small variation in water activity can have a significant influence on the catalytic activity and selectivity of lipase. It is known that some water is necessary for catalytic activity and the precise level of water is important for equilibrium of a reaction. The transesterification reaction was performed in presence of 0 to 1000 μl water. There was a decline in incorporation of ALA in olive oil backbone with an increase in the amount of water. Fig 4 shows ALA incorporation of 25% occurred at 100 µl water while without water it was 27% and it decreased to 15% with 1 ml of water. That is indicating the change in ALA incorporation rate is because of the shifting of the transesterification reaction to hydrolysis rather than synthesis, in presence of excess water.

It was reported that the incorporation of C10:0 into rice bran oil with increasing amounts of water (0-12%) for the solvent-free reactions indicates that the water content of the unmodified rice bran oil was 0.07% [27]. The influence of water content on the synthesis of butyl butyrate by transesterification reaction (alcoholysis) using lipases from different sources was reported [33], which indicated a direct relationship between water and reaction rate. Maximum esterification yield (92%) was obtained with *C. rugosa* lipase when compared to the yields from other lipases (*R. oryzae*, 45%; *Mucor javanicus*, 84%; *A. niger*, 56% and *Penicillium roqueforti*, 67%). It indicates that at higher water content the reaction equilibrium in favor of the hydrolysis and equilibrium shifts to synthetic mode when operated at low water levels.

CONCLUSION

The lipase mediated transesterification of ALA to olive oil TAG back bone was demonstrated as a suitable technique for enrichment of n-3 PUFA into olive oil which can be modified for other edible oils as well. Free lipase from *C. rugosa* identified as a good source of lipase for transestrification of ALA with olive oil and enriched olive oil with 27% of ALA. Use of the enriched olive oil with omega-3 can give a new kind of edible oil which prevents high cholesterol and heart problems. With the above promising results, it is recommended that in future work, the use of transesterification may require more investigation with different sources of seed oil which contain PUFA to prepare nutritional supplements.

REFERENCES

1. Seong, J. and Y.O. Song, 2012. Perilla oil rich in α-linolenic acid inhibits neuronal apoptosis and the expression of inflammation-mediator protein in apoE KO mice. Biocatalysis and Agricultural Biotechnology, 1(2): 167-173.
2. Tapiero, H., G. Nguyen Ba, P. Couvreur and K. Tew, 2002. Polyunsaturated fatty acids (PUFA) and eicosanoids in human health and pathologies. Biomedicine & Pharmacotherapy, 56(5): 215-222.
3. Horrocks, L.A. and Y.K. Yeo, 1999. Health benefits of docosahexaenoic acid (DHA). Pharmacological Research, 40(3): 211-225.
4. Barcelo-Coblijn, G. and E.J. Murphy, 2009. Alpha-linolenic acid and its conversion to longer chain n-3 fatty acids: Benefits for human health and a role in maintaining tissue n- 3 fatty acid levels. Progress in lipid research, 48(6): 355-374.
5. Can, A. and B. Ozcelik, 2005. Enrichment of hazelnut oil with long-chain n-3 PUFA by lipase-catalyzed acidolysis: Optimization by response surface methodology. Journal of the American Oil Chemists' Society, 82(1): 27-32.
6. Chen, Q. and A. Nilsson, 1994. Interconversion of alpha-linolenic acid in rat intestinal mucosa: studies in vivo and in isolated villus and crypt cells. Journal of lipid research, 35(4): 601-609.
7. Gibson, R., M. Neumann, E. Lien, K. Boyd and W. Tu, 2013. Docosahexaenoic acid synthesis from alpha-linolenic acid is inhibited by diets high in polyunsaturated fatty acids. Prostaglandins, Leukotrienes and Essential Fatty Acids, 88(1): 139-146.
8. Mensink, R. and M. Katan, 1987. Effect of monounsaturated fatty acids versus complex carbohydrates on high-density lipoproteins in healthy men and women. The Lancet, 329(8525): 122-125.
9. La Rosa, J., D. Hunninghake, D. Bush, M. Criqui, G. Getz, A. Gotto Jr, S. Grundy, L. Rakita, R. Robertson and M. Weisfeldt, 1990. The cholesterol facts. A summary of the evidence relating dietary fats, serum cholesterol and coronary heart disease. A joint statement by the American Heart Association and the National Heart, Lung and Blood Institute. The Task Force on Cholesterol Issues, American Heart Association. Circulation, 81(5): 1721-1733.
10. Singh, R.B., M.A. Niaz, S.S. Rastogi, S. Bajaj, Z. Gaoli and Z. Shoumin, 1998. Current zinc intake and risk of diabetes and coronary artery disease and factors associated with insulin resistance in rural and urban populations of North India. Journal of the American college of Nutrition, 17(6): 564-570.
11. Akoh, C.C., B.H. Jennings and D.A. Lillard, 1996. Enzymatic modification of evening primrose oil: Incorporation of n-3 polyunsaturated fatty acids. Journal of the American Oil Chemists Society, 73(8): 1059-1062.
12. Huang, K.H. and C.C. Akoh, 1994. Lipase-catalyzed incorporation of n- 3 polyunsaturated fatty acids into vegetable oils. Journal of the American Oil Chemists' Society, 71(11): 1277-1280.

13. Rupani, B., K. Kodam, R. Gadre, G.D. Najafpour, 2012. Lipase-mediated hydrolysis of flax seed oil for selective enrichment of *a*-linolenic acid. European Journal of Lipid Science and Technology, 114: 1246-1253.
14. Leaf, A., 2006. Prevention of sudden cardiac death by n-3 polyunsaturated fatty acids. Fundamental and Clinical Pharmacology, 20(6): 525-538.
15. Whelan, J. and C. Rust, 2006. Innovative dietary sources of n-3 fatty acids. Annual Review of Nutrition, 26: 75-103.
16. Bozan, B. and F. Temelli, 2008. Chemical composition and oxidative stability of flax, safflower and poppy seed and seed oils. Bioresource Technology, 99(14): 6354-6359.
17. Namal Senanayake, S. and F. Shahidi, 2002. Lipase-catalyzed incorporation of docosahexaenoic acid (DHA) into borage oil: optimization using response surface methodology. Food Chemistry, 77(1): 115-123.
18. Tanaka, Y., J. Hirano and T. Funada, 1992. Concentration of docosahexaenoic acid in glyceride by hydrolysis of fish oil withcandida cylindracea lipase. Journal of the American Oil Chemists Society, 69(12): 1210-1214.
19. Kojima, Y., E. Sakuradani and S. Shimizu, 2006. Acidolysis and glyceride synthesis reactions using fatty acids with two Pseudomonas lipases having different substrate specificities. Journal of bioscience and bioengineering, 102(3): 179-183.
20. Zhou, D., X. Xu, H. Mu, C.E. Hoy and J. Adler-Nissen, 2000. Lipase-catalyzed production of structured lipids via acidolysis of fish oil with caprylic acikd. Journal of Food Lipids, 7(4): 263-274.
21. Lin, T.J. and S.W. Chen, 2008. Enrichment of n-3 polyunsaturated fatty acids into acylglycerols of borage oil via lipase-catalyzed reactions under supercritical conditions. Chemical Engineering Journal, 141(1): 318-326.
22. Senanayake, S.N. and F. Shahidi, 1999. Enzymatic incorporation of docosahexaenoic acid into borage oil. Journal of the American Oil Chemists' Society, 76(9): 1009-1015.
23. Senanayake, S.N. and F. Shahidi, 2002. Structured lipids via lipase-catalyzed incorporation of eicosapentaenoic acid into borage (Borago officinalis L.) and evening primrose (Oenothera biennis L.) oils. Journal of agricultural and food chemistry, 50(3): 477-483.
24. Akoh, C.C. and C.O. Moussata, 1998. Lipase-catalyzed modification of borage oil: incorporation of capric and eicosapentaenoic acids to form structured lipids. Journal of the American Oil Chemists' Society, 75(6): 697-701.
25. Chakraborty, K. and R.P. Raj, 2009. Selective enrichment of n-3 polyunsaturated fatty acids with C18–C20 acyl chain length from sardine oil using Pseudomonas fluorescens MTCC 2421 lipase. Food Chemistry, 114: 142-150.
26. Rao, R., B. Manohar, K. Sambaiah and B.R. Lokesh, 2002. Enzymatic acidolysis in hexane to produce n-3 or n-6 FA-enriched structured lipids from coconut oil: Optimization of reactions by response surface methodology. Journal of the American Oil Chemists' Society, 79(9): 885-890.
27. Jennings, B.H. and C.C. Akoh, 2000. Lipase-catalyzed modification of rice bran oil to incorporate capric acid. Journal of agricultural and food chemistry, 48(9): 4439-4443.
28. Fajardo, A.R., C.C. Akoh and O. Lai, 2003. Lipase-catalyzed incorporation of n- 3 PUFA into palm oil. Journal of the American Oil Chemists' Society, 80(12): 1197-1200.
29. Van Erp, S., E. Kamenskaya and Y.L. Khmelnitsky, 1991. The effect of water content and nature of organic solvent on enzyme activity in low-water media. A quantitative description. European journal of biochemistry/FEBS, 202(2): 379.
30. Zaks, A. and A.M. Klibanov, 1988. Enzymatic catalysis in nonaqueous solvents. Journal of Biological Chemistry, 263(7): 3194-3201.
31. Jeong, J. and S. Lee, 1997. Enzymatic esterification reaction in organic media with continuous water stripping: effect of water content on reactor performance and enzyme agglomeration. Biotechnology techniques, 11(12): 853-858.
32. Svensson, I., E. Wehtje, P. Adlercreutz and B. Mattiasson, 1994. Effects of water activity on reaction rates and equilibrium positions in enzymatic esterifications. Biotechnology and bioengineering, 44(5): 549-556.
33. Chowdary, G. and S. Prapulla, 2002. The influence of water activity on the lipase catalyzed synthesis of butyl butyrate by transesterification. Process Biochemistry, 38(3): 393-397.

Persian Abstract

DOI: 10.5829/idosi.ijee.2014.05.01.04

چکیده

استفاده از اسیدهای چرب حاوی امگا ۳ برای سلامت مغز، کلیه و چشم توصیه شده است. تبدیل امگا ۳، اسید آلفا لینولنیک گیاهی (ALA) به اسید چرب زنجیر بلند ۲۰ کربنی غیر اشباع ایکوسپنتانوئیک و اسید دکوساهگزانوئیک صورت می گیرد و کیفیت رژیمی روغن با کمبود ALA را بهبود بخشد. لیپاز تجاری کاندیدا روگوسا، سودوموناس کپاکا و سودوموناس فلوروسانس موجب ترانس استریفیکاسیون روغن پنبه دانه غنی از ALA به روغن پایه TAG زیتونی می گردد. نتایج کروماتوگرافی نشان می دهد که روغن زیتون حاوی اسید اولئیک (C18:1, n-9)، لینولنیک (C18:2, n-6) و پالمتیک (C18:0) و ۰٪ ALA می باشد. در میان لیپازهای تجاری کاندیدا روگوسا برتری بیشتری برای تبدیل ALA دارد که موجب تبدیل ۲۷٪ ALA به پایه TAG روغن زیتون شده است. در زمان واکنش ۲۴ ساعت غلظت ALA روغن پایه TAG زیتون به میزان ۲۶٪ افزایش داده است و میزان اسید اولئیک به ۶۰٪ و پالمتیک از ۲۵ به ۵٪ کاهش داده است. بیشترین تبدیل ALA به روغن زیتون ۲۹٪ بوده که نسبت کسر مولی ALA به روغن زیتون (۱:۲) بوده است. با افزایش میزان آب در روغن زیتون میزان به کارگیری ALA کاهش یافته است. تبدیل ALA با ۱۰۰ μl ۲۵٪ بوده در حالیکه با افزایش آب به میزان ۱ میلی لیتر میزان بکارگیری ALA به ۱۵٪ کاهش یافته است.

Iranica Journal of Energy & Environment 5 (1): 26-33, 2014
ISSN 2079-2115
IJEE an Official Peer Reviewed Journal of Babol Noshirvani University of Technology
DOI: 10.5829/idosi.ijee.2014.05.01.05

New Vegetal Biopolymeric Flocculant: A Degradation and Flocculation Study

Y.C. Ho, I. Norli, Abbas F.M. Alkarkhi and N. Morad

School of Industrial Technology, Universiti Sains Malaysia, 11800 Minden, Penang, Malaysia

(Received: February 12, 2014; Accepted in Revised Form: March 17, 2014)

Abstract: Polyacrylamide (PAM) is known to pose a hazard to human health. A newly explored plant-based flocculant, malva nut gum (MNG) is hypothesized to treat water and as a green material. This study investigates the biodegradation, thermal degradation and photodegradation of MNG and its flocculation capability. The results show MNG has a high biodegradation rate and low oxygen consumption rate. MNG biodegraded at Day-17, whilst, PAM did not show completion of biodegradation by the end of the experiment. Thermal degradation analysis shows MNG has a few decomposition stages and ash content. The photodegradation analysis shows photochemical changes in the structure of MNG and PAM. Factorial experiments show pH, concentration of cation and the concentration of MNG were the influential factors in coagulation-flocculation process. Optimization study observed 97% turbidity reduction at pH 5.77, the concentration of cation at 0.05 mM and the concentration of MNG at 0.42 mg/L. Conclusively, MNG operates effectively at near neutral pH and at low concentration. Such results strongly suggest that MNG is a suitable candidate, which could be used to replace PAM, as flocculant in water treatment.

Abbreviation: Malva nut gum (MNG) · Polyacrylamide (PAM) · Response surface methodology (RSM)

Key words: Biopolymeric flocculant · Malva nut gum · Degradation · Response surface methodology · Turbid water treatment

INTRODUCTION

Previous studies revealed that there are some environmental and health concerns of using alum salts and polyacrylamide in water and wastewater treatment, i.e. Alzheimer's disease, the residual and the derivatives of PAM i.e. its monomers, other reactants and reaction by-products [1] are neurotoxic and carcinogenic. Therefore, natural polysaccharide extracted from plants or animals are workable alternatives to synthetic polyelectrolytes like PAM. This is due to degradable properties, no risk to human health and has a wide effective dosage range for flocculation of various colloidal suspensions. Moreover, the need for readily degradable and environmental-friendly materials in water treatment process is essential. Owing to this fact, plant-based coagulant and flocculant have received increasing attention from worldwide researchers recently. The aims in this study include (i) prepare a new plant-based flocculant, (ii) study the degradation properties by biodegradation, thermal degradation and photo degradation, (iii) investigate the significant factors i.e. pH, concentration of cation, concentration of polymer and its interaction in screening process and (iv) optimize the maximum turbidity reduction using response surface methodology (RSM). The findings bring significant impact on the use of green material in water treatment plants which may increase the economic contribution to the native grown country.

The selected potential plant-based flocculant is extracted from malva nut. Malva nut is the seed of the *Scaphium scaphigerum* tree. The properties of malva nut gum (MNG) contains the key properties as a flocculant where it has high molecular weight [2] and contains properties of uronic acid [3]. These properties influence bridging or adsorption process during flocculation. It is noteworthy that the molecular weight and intrinsic viscosity of MNG are much higher than most polysaccharide gums that are currently available on the market, i.e. guar gum, locust bean gum and pectin [4].

Corresponding Author: I. Norli, School of Industrial Technology, Universiti Sains Malaysia, 11800 Minden, Penang, Malaysia. Tel: +604-6532824, Fax: +604-6573678.

Malva nuts are cheap, easily available on the market and their interesting properties could establish it to become a new renewable, sustainable and degradable flocculant.

Biodegradation study is based upon the degradation of polymers in environment in presence of microorganism. The rate of biodegradation depends on many factors such as the environment (including surrounding temperature), population of microorganism and etc. [5]. However, biodegradation requires a long period to determine the degradability, thus, thermal degradation becomes an important method to investigate [6]. It is a fast, sensitive, uniform and reproducible technique. Another useful photodegradation is a degradation method is oxidative degradation where depolymerization occurs in presence of ultraviolet (UV). The action of UV radiation reduces the molar mass and changes the structure of polymer. This method is a convenient, time saving and cost efficient. It may replace the expensive and time consuming enzymatic or chemical methods that are being currently used [7].

MATERIALS AND METHODS

Preparation of MNG: Simplified extraction process was performed in accordance to Somboonpanyakul *et al*. [4]. The dried malva nut was treated with ethanol at 85°C for 1 hour. Subsequently, the pH of the slurry was adjusted to pH 4.5 and filtered through a silk-screen filter cloth prior to precipitation with 95% ethanol for 1 hour. The gummy portion was washed with the ethanol twice. Lastly, the gum was air dried.

Biodegradation Study: Biodegradation study was carried out in accordance to Norli *et al*. [8]. Microcrystalline cellulose was used as a reference test. Inoculum solution was obtained by vermin-compost waste extraction. Often, before day 5, it is the adaptation of the inoculum to the test substance. Typically, degradation occurs between day 5-12 and ends at day 15 in an activated sludge system in a water treatment plant [9]. In this study, the experiment has a duration of 18 days with an extension of 3 days for further observation.

Thermal Degradation Study: The decomposition of MNG was performed by using thermogravimetric analysis (TGA). This study was carried out using Mettler Toledo, TGA/SDTA851e OMNIC. The weight of the samples used ranged from 10–12 mg. The heating rate was 20°C/min from 30 to 800°C under oxygen atmosphere at 30 mL/min. The decomposition temperature of polymer and ash volume produced were attained at the end of the analysis.

Photodegradation Study: Photodegradation was carried out by exposing the sample to natural environment and natural solar UV for 30 days in the month of August (2012). The weather was sunny, average temperature at around 23 to 32°C and accompanied with isolated rain for about 3 days. The degradation was examined using FTIR. This method was modified from dos Santos *et al*. [10] where the sample was exposed to natural solar light instead of artificial UV light. FTIR spectra were obtained using FTIR in mid infrared region (4000-400 cm^{-1}) to determine the functional group of the flocculants by conventional method using potassium bromide (KBr) pallet [11]. The sample pallet was analyzed using Perkin Elmer, System 2000 FTIR.

Turbid Water Treatment: Jar test is used for the coagulation-flocculation process. Kaolin suspension is prepared to simulate turbid wastewater. The initial turbidity is around 400 NTU. In this study, ferric chloride was chosen as cation that acts as a coagulant. From here onwards, it is noted as Fe. The mixing procedures were performed with rapid mixing at 150 rpm for 3 minutes and subsequently, slow mixing at 30 rpm for 20 minutes. Then, it was left standing still for 5 minutes. A 10 mL of supernatant was withdrawn and continued with a turbidity examination using HACH Turbidimeter 2100Q.

Assay of Turbidity Reduction: The capability of flocculant is measured in the ability to reduce turbidity in synthetic wastewater. The experimental procedure was carried out according to Standard Methods, Method 2130 B [12]. Percentage of turbidity reduction was calculated as in Eq. (1):

$$\text{Turbidity reduction, \%} = A\text{-}A0\,/A \qquad (1)$$

where,

- A_0 was turbidity of the control sample before treatment, NTU
- A was turbidity of the sample after treatment, NTU

Design of Experiment: The screening of factors determines influential factors to the process within the design boundary. Therefore, a screening experiment was carried out to select significant factors. Two-level full factorial designs were used with three variables or factors (2^3 factorial design), namely, pH, concentration of cation and concentration of flocculant which are denoted as factors A, B, C, respectively. The design boundary for pH is between 3 and 9, concentration of cation is between

0.01 mM to 0.1 mM and lastly, concentration of MNG is between 0.05 to 0.5 mg/L. Optimization experiment was carried out using face-centred design and turbidity reduction was the response output. Design Expert statistical software was used for the analysis.

RESULTS AND DISCUSSION

Biodegradation Study: The biodegradation study was carried out to analyze the biodegradability of MNG and PAM. Fig. 1 shows the degradation of reference test (using microcrystalline), MNG and PAM.

Previous study on pectin (another emerging green flocculant) was degraded at day 14 [8]. As illustrated in Fig. 1, reference sample completed degradation process at day 10. MNG requires less oxygen throughout biodegradation process and completed degradation process at day 17. However, PAM showed drastic consumption of oxygen and did not exhibit any behaviour for the completion of biodegradation at the end of experiment. Furthermore, the amount of oxygen required for PAM degradation is much higher than microcrystalline cellulose and MNG. During degradation process, microorganisms use the substances as food and to grow and at the same time consume oxygen available. Conclusively, natural polysaccharide has better biodegradation capability than PAM.

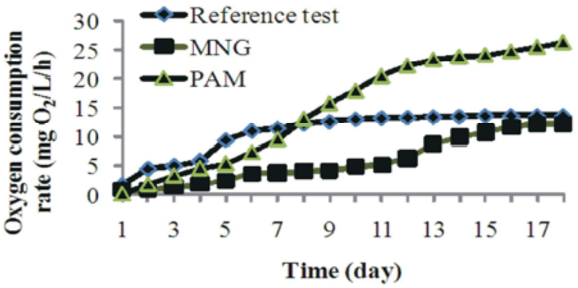

Fig. 1: Oxygen consumption by microorganisms to degrade MNG, PAM and reference test (microcrystalline cellulose)

Thermal-degradation Study: Decomposition study investigates the fate of polymer and emissions to air during degradation in the environment thermally. During thermal degradation, the weight loss is mainly due to the oxidation process whereby the molecular bonds of a polymer are attacked by oxygen molecules and broken down [13]. The TGA curve of MNG illustrated in Fig 2.

The TGA result is in accordance with DSC result where there is a degradation step at an onset temperature of 33°C. Nonetheless, the analysis is set to end at 300°C which is the limit of the instrument. Therefore, TGA is carried out to determine further thermal degradation behaviour.

The curve consists of four sections: (1) a weight loss of 18.5% from 29.63°C to 213.38°C, (2) tremendous weight loss of 41.12% from 213.38°C to 337.48°C, (3) weight loss of 10.42% from 337.48°C to 531.89°C, (4) weight loss 21.43% from 531.89°C to 799.12°C. The decomposition of MNG is completed at temperature 800°C where only 8.53% residue was left.

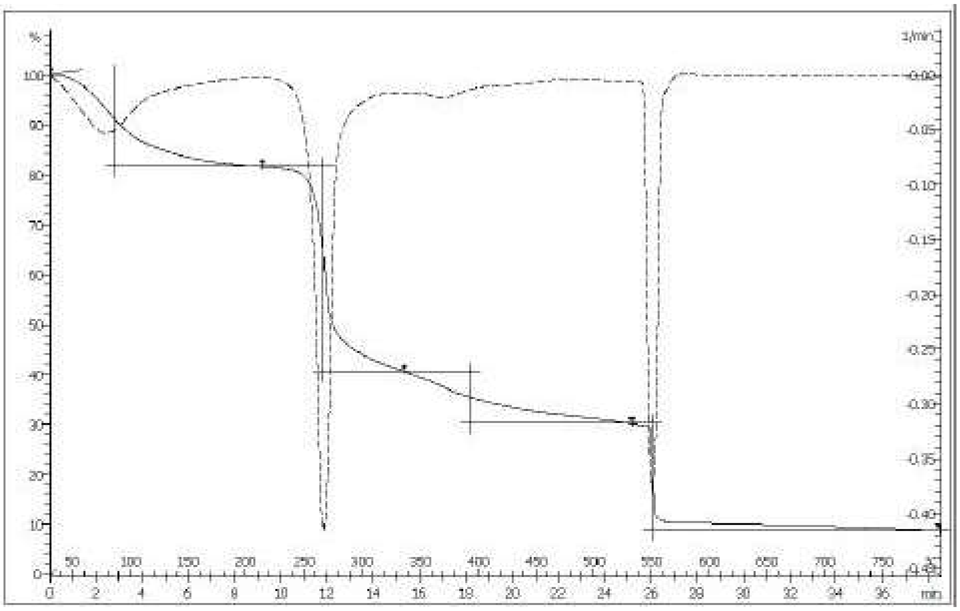

Fig. 2: Thermogravimetry curve for MNG.

Table 1: FTIR wavelength of MNG for photodegradation

0th day, cm^{-1}	15th day, cm-1	30th day, cm^{-1}	Remark
3422	3444	3444	
2936	2924	2925	
2360	2361	2360	
2341	2340	2340	
1617	1624	1623	
1420	1420	1420	
1240	1230	1230	
1148	-	-	Ester stretching
1096	-	-	C-C vibration
1038	1039	1035	
896	897	897	
820	819	819	
669	-	-	C-OH stretching

Table 2: FTIR wavelength of PAM for photodegradation

0th Day, cm^{-1}	15th Day, cm^{-1}	30th Day, cm^{-1}	Remark
3443	3450	3448	
2923	2923	-	C-H stretching
2360	2360	2360	
2340	2339	2339	
1624	1651	1635	
1455	1457	1458	
1409	-	-	C-N stretching
1033	1030	-	C-O stretching vibration
866	849	848	
686	-	-	C-H bending
668	669	669	
653	653	654	

Section 1 of degradation occurs due to depolymerization of simple bonds and desorption of physically absorbed water and water volatilization. Sections 2 and 3 degradation involves complex depolymerization and side group/substituent reaction. The degradation rate is the fastest at Section 2 whereby the weight lost is 41%. This would be the major constituent of MNG. Large numbers of carbon chains and the main chain of the biopolymeric flocculant have been broken down and released CO_2. At Section 3, there is side group degradation or reaction occurred. Therefore, it decomposes at a higher level and left only 29% residue. Finally, the formation of ash happens at Section 4 at 531.89°C and the analysis ends at 799.12°C.

MNG has fewer complex degradation processes and ash content as compared to PAM in previous study conducted [14]. During the degradation process, PAM released CO_2 and NH_3. Ammonia gas in the air causes air pollution, acidification in the ecosystem and respiratory distress to humans. It can be concluded that MNG is easier to degrade thermally and a better material for pollution prevention as compared to PAM.

Photo-degradation: Previous photodegradation studies on cassava and corn starches was conducted to examine the stability of chemical structure in the biopolymer, the result showed both polymers depolymerized with the absence of breakage of the C-C bond [15]. Thus, photodegradation study of MNG and PAM was carried out.

Photodegradation of MNG: The absorption peak of MNG determined by FTIR technique for 30 days of exposure under natural sunlight is depicted in Table 1. The result shows MNG degraded ester, C-C bonds and C-OH bonds in 15 days.

Photodegradation is a process whereby degradation initiated by absorption of light quanta i.e. ultra violet and visible light. The degradation process involves breaking of the main valence bond in the backbones of the chain or inside groups. Ester, C-C bonds and C-OH bonds are vulnerable under solar light (UV and infra-red) as most commonly chemical bonds broken down are C-C in aliphatic compounds (77-83 kcal/mol) and C-O in aliphatic ethers (76-79 kcal/mol). The break down mechanism is closely related to environmental factors under natural solar exposure. MNG reacts chemically with the atmospheric oxygen and water vapor and UV photons in the sun light. These photochemical changes in the polymer structure causes deterioration in cross-linking and chains scission [16]. Furthermore, the increase in temperature leads to acceleration of deleterious chemical reactions and can speed up the diffusion of low molecular weight components [17].

Photodegradation of PAM: Similarly, FTIR technique used to observe the changes in structure of polymer. PAM shows absorption peaks as indicated in Table 2.

The influence of light and other abiotic factors such as water, oxygen, occluded monomer, additives and other impurities cause sunlight-induced oxidation. Under these conditions, weak bond strength could be broken down. With the presence of UV, the structure in PAM underwent photochemical changes and break bonds for C-H (83 kcal/mol), C-N (73 kcal/mol) and C-O (86 kcal/mol) on day 30. The loss of these bonds in PAM is assigned as a primary alcoholic group. As a conclusion, UV broke down single bond both in MNG and PAM with energy around 70-90 kcal/mol during photodegradation.

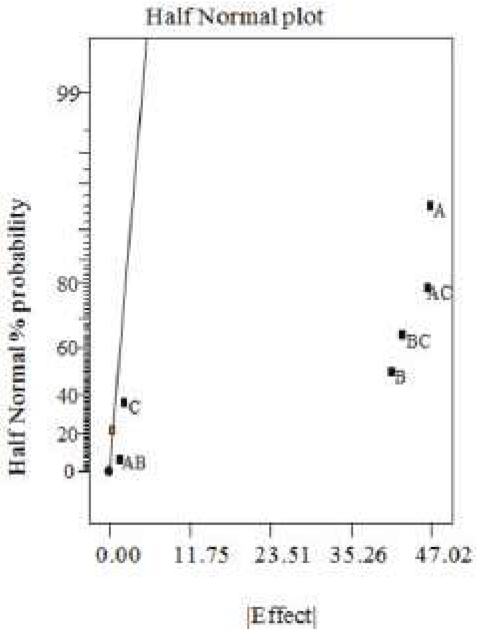

Fig. 3: Half normal plot

Design of Experiment: Screening experiment was carried out to identify the influential factors for turbidity reduction where pH, concentration of cation and concentration of MNG denoted for A, B and C, respectively (Fig. 3). Furthermore, results from screening experiment revealed significant factors are factor A (pH), B (concentration of Fe), C (concentration of MNG) and the interaction between AB (pH and concentration of Fe) and AC (pH and concentration of MNG) contributed to the coagulation-flocculation process.

Interaction between pH and concentration of Fe: pH influences all the hydrolysis equilibria resulted by addition of the metal cation. When Fe was added into water, hydrolysis reaction takes place. It leads to the formation of various hydrolyzed species as cation. The metal hydroxides have very large surface areas and positive charges. The interaction between pH and cation occurred due to the electrical potential gradient on the particle surface. The electrical potential difference between particle surface and the bulk solution greatly depends on the concentration of potential ionic constituents of the solid particle such as hydrogen (H^+) and hydroxyl (OH^-) ions. Often, at low pH and low concentration of coagulant, charge neutralization predominant the flocculation process; at high pH and high concentration of coagulant, sweep-floc mechanism may involve in flocculation process.

Interaction between pH and concentration of MNG: It has been noted that a lower concentration of polymers is not enough to bridge particles. Hence, optimum concentration of polymers is preferred for coagulation and flocculation process. At low pH, high concentration of H^+ in water could enhance the bridging mechanism in the presence of acids to form hydrogen-bonding and hydrophobic interactions. The presence of hydrophobic interaction reduces the electrostatic repulsion and promotes attachment on surface of particle. Subsequently, it leads to linking and binding during flocculation. Hence, the concentrations of hydrogen and hydroxyl ions play an important role in flocculation process.

Moreover, MNG has oxygen-containing functional groups, such as, OH^- (hydroxyl group), $-COO^-$ (carboxyl groups) and primary amide (NH_2) which contains carbonyl (C=O) and ester (N-C) group. These groups increase hydrogen bonding between surface of particle and MNG. During flocculation, the biopolymeric flocculants expose the electrolyte groups such as negatively charged carboxyl group (COO^-) and hydroxyl group (OH^-). Then, the chain stretched due to electrostatic repulsion and provides a more effective surface for the kaolin particles to attach. Likewise to polyacrylamide (PAM), it agglomerates the particles via hydrogen bonding with the presence of amide as its functional group [19]. With the presence of H^+ and OH^- in water, primary amide functional groups in polymers can be extended to produce loops and tails, which lead to the formation of flocs.

Unlike other synthetic coagulants that are widely used in industry, the flocculation mechanism of using MNG as flocculant remains unknown. More than one in four typical flocculation mechanisms could occur in the presence of polymers during flocculation [18]. Based on the properties in MNG, the flocculating mechanism (with the presence of Fe and MNG) is proposed to occur as the following sequence: (1) destabilization of particle by Fe (overcome repulsive electrostatic interaction and neutralize the surface charge), (2) adsorption onto neutralized surface (from MNG functional groups). (3) polymer bridging (MNG extends loops and tails onto surface of particles). Fig. 4 shows the bridging mechanism of adsorption of functional group on neutralized surface of particles. Here, possible flocculation mechanism that may relate to binding and bridging process using MNG is proposed.

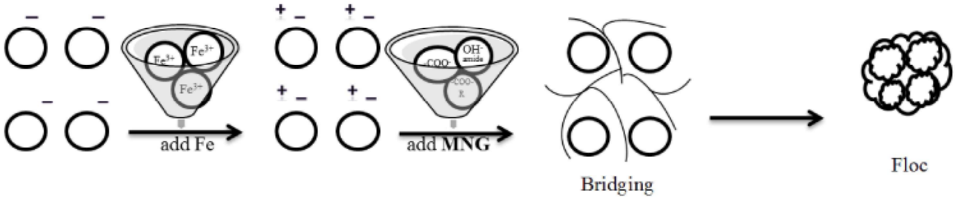

Fig. 4: MNG adsorption on neutralized surface of particle

Table 3: The results of analysis of variance (ANOVA) for turbidity reduction of MNG

Turbidity reduction

Source	Sum of squares	Degrees of freedom	Mean square	F-value	P-value
Model	8857.24	9	984.14	25.26	< 0.0001
pH	3398.86	1	3398.86	87.23	< 0.0001
Concentration of Fe	1198.15	1	1198.15	30.75	< 0.0002
Concentration of MNG	742.35	1	742.35	19.05	< 0.0014
pH×pH	588.97	1	588.97	15.12	< 0.0030
Concentration of Fe × Concentration of Fe	62.95	1	62.95	1.62	< 0.2325
Concentration of MNG× Concentration of MNG	124.72	1	124.72	3.20	< 0.1039
pH× Concentration of Fe	535.63	1	535.63	13.75	< 0.0041
pH× Concentration of MNG	148.44	1	148.44	3.81	< 0.0795
Concentration of Fe × Concentration of MNG	216.94	1	216.94	5.57	< 0.0400
Residual	389.63	10	38.96		
Total	9246.88	19			

Optimization: Based on optimization result, the linear effect, contribution of quadratic effect over the linear effect and the interaction terms were significant (P value <0.10) as shown in ANOVA table (Table 3).

It showed the behavior of each variable in the presence of other variables. A second-order model was built and adequately fitted the experimental data. The second-order regression model obtained for turbidity reduction is satisfied since the values of the coefficient of determination (R^2) is 0.9579 which is high and close to 1. This indicates that 95.79% of MNG to the total variation was explained by the model and only 4.21% was unexplained. The behaviour of turbidity reduction to optimize the process by finding the best settings of the three variables that maximize the turbidity reduction is described with a model built (Eq. 2).

$$\text{Turbidity reduction} = 96.31 - 18.44\,x_1 + 10.95\,x_2 + 8.62\,x_3 - 14.63\,x_1^2 - 4.78\,x_2^2 - 6.73\,x_3^2 + 8.18\,x_1 x_2 + 4.31\,x_1 x_3 - 5.21\,x_2 x_3 \qquad (2)$$

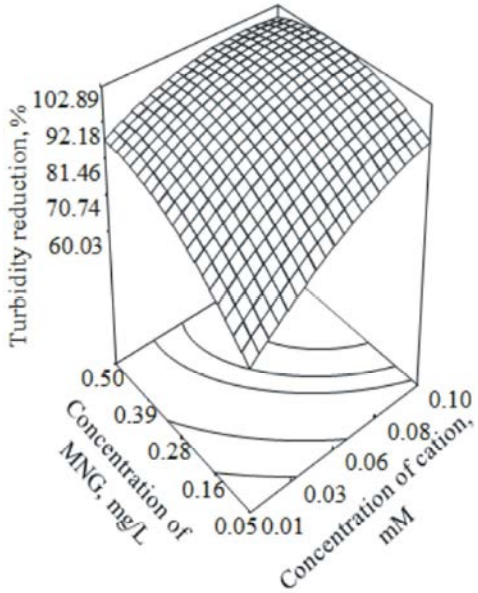

Fig. 5: 3-D optimization plot for MNG

A 3-D optimization plot is shown in Fig. 5 to illustrate the second order quadratic curve. Optimization setting revealed that maximum turbidity reduction (99%) when using MNG as biopolymeric flocculant was achieved at pH 5.77, concentration of cation at 0.05 mM and concentration of MNG at 0.42 mg/L. As compared to PAM in previous study [19_ENREF_19], at the 0.05 mM concentration of Fe, the optimal condition for PAM is around pH 8.84 and concentration of PAM required

7.77 mg/L. Therefore, MNG performs better as a flocculant than PAM where it works well at pH near to neutral and requires lower amount of flocculant. Furthermore, less amount of MNG added into water treatment reduces the operating cost. As for PAM, it contains harmful monomers whereby they bring negative impacts to environment and human health. Higher concentration of chemicals added to water may possibly induce secondary pollution and has higher operating cost. From this finding, it can be concluded that, MNG is preferable over PAM as a flocculant in water treatment.

Validation: A confirmation experiment was carried out with turbidity reduction from the optimization results in order to validate the developed model. The results of the selected combinations of pH, cation concentration and flocculant concentration display a 98.54% turbidity reduction.

CONCLUSIONS

The degradation and flocculation study of MNG were presented. MNG requires 17 days to biodegrade whereas PAM shows continuous degradation trend. Next, thermal degradation result revealed that MNG shows fewer residues and stages than PAM when heated and releases only CO_2. Thirdly, the photodegradation under natural solar exposure shows single bonds chemical structures broken by UV. When using MNG as flocculant in water treatment, the result shows 99% turbidity reduction with pH closer to neutral and lower concentration of flocculant required. In the context of operating a wastewater treatment plant, using MNG is an economically friendly and environmental sound material than that of PAM.

ACKNOWLEDGEMENT

Authors are thankful to Ministry of Higher Education for the provided funding with grant number: 203/PTEKIND/6411167 and facilities were provided by USM.

REFERENCE

1. Özacar, M. and İ.A. Şengil, 2003. Evaluation of tannin biopolymer as a coagulant aid for coagulation of colloidal particles. Colloids and Surfaces A: Physicochemical and Engineering Aspects, 229: 85-96.
2. Wu, J.Y. and H.F. Ye, 2007. Characterization and flocculating properties of an extracellular biopolymer produced from a Bacillus subtilis DYU1 isolate. Process Biochemistry, 42: 1114-1123.
3. Salehizadeh, H. and S. Shojaosadati, 2001. Extracellular biopolymeric flocculants: recent trends and biotechnological importance. Biotechnology advances, 19: 371-385.
4. Somboonpanyakul, P., Q. Wang, W. Cui, S. Barbut and P. Jantawat, 2006. Malva nut gum. (Part I): Extraction and physicochemical characterization. Carbohydrate Polymers, 64: 247-253.
5. Raymond, J.W., T.N. Rogers, D.R. Shonnard and A.A. Kline, 2001. A review of structure-based biodegradation estimation methods. Journal of hazardous materials, 84: 189-215.
6. Kim, M., 2003. Evaluation of degradability of hydroxypropylated potato starch/polyethylene blend films. Carbohydrate Polymers, 54: 173-181.
7. Yue, W., P. Yao and Y. Wei, 2009. Influence of ultraviolet-irradiated oxygen on depolymerization of chitosan. Polym. Degrad. Stab., 94: 851-858.
8. Norli, I., Y.C. Ho, K. Fischer, M. Kranert and A. Boley, 2011. Biodegradability Assessment of Bio- flocculant via Anaerobic and Aerobic Test, in: International Conference on Environment Science and Engineering (ICESE), Bali, Indonesia.
9. Pagga, U., 1997. Testing biodegradability with standardized methods. Chemosphere, 35: 2953-2972.
10. Dos Santos, K. And J.C. Suarez, 2005. Photo-degradation of synthetic and natural polyisoprenes at specific UV radiations. Polymer degradation and stability, 90: 34-43.
11. Philias, J.M. and B. Marsan, 1999. FTIR spectroscopic study and thermal and electrical properties of polymer electrolytes containing a cesium thiolate/disulfide redox couple. Electrochimica Acta, 44: 2351-2363.
12. Andrew, D.E. and H.F. Mary Ann, 2005. Standard methods for the examination of water and wastewater, American Public Health Association, New York.
13. Wong, A.Y. and F. Lam, 2002. Study of selected thermal characteristics of polypropylene/ polyethylene binary blends using DSC and TGA. Polymer testing, 21: 691-696.
14. Ho, Y.C., I. Norli, F.M.A. Abbas and N. Morad, 2010a. Reuse of Fruit Waste as Biopolymeric Flocculant and Optimizing Turbidity Reduction: Comparison Study with Industrial Flocculant. Journal of Environmental Engineering, 136: 1267-1276.

15. Bertolini, A.C., C. Mestres, J. Raffi, A. Buléon, D. Lerner and P. Colonna, 2001. Photodegradation of cassava and corn starches. Journal of agricultural and food chemistry, 49: 675-682.
16. Sionkowska, A., A. Planecka, J. Kozlowska, J. Skopinska-Wisniewska and P. Los, 2011. Weathering of chitosan films in the presence of low-and high-molecular weight additives. Carbohydrate Polymers, 84: 900-906.
17. Berdahl, P., H. Akbari, R. Levinson and W.A. Miller, 2008. Weathering of roofing materials–an overview. Construction and Building Materials, 22: 423-433.
18. Runkana, V., P. Somasundaran and P. Kapur, 2006. A population balance model for flocculation of colloidal suspensions by polymer bridging. Chemical engineering science, 61: 182-191.
19. Ho, Y.C., I. Norli, F.M.A. Abbas and N. Morad, 2010b. Characterization of biopolymeric flocculant (pectin) and organic synthetic flocculant (PAM): A comparative study on treatment and optimization in kaolin suspension. Bioresource Technology, 101: 1166-1174.

Persian Abstract

DOI: 10.5829/idosi.ijee.2014.05.01.05

چکیده

پلی آکریل آمید به عنوان یک خطر جدی برای سلامت انسان شناخته شده است. به تازگی یک لخته‌ساز با پایه گیاهی جدید (MNG) برای تیمار آب و به عنوان یک ماده سبز مورد بررسی قرار گرفته است. این تحقیق به بررسی تجزیه بیولوژیکی، تخریب حرارتی و تخریب نوری MNG و توانایی لخته‌سازی آن می‌پردازد. نتایج نشان می‌دهد MNG میزان تجزیه زیستی بالا و نرخ مصرف اکسیژن پایینی دارد. MNG در روز هفدهم تجزیه زیستی شد، در حالیکه PAM در پایان آزمایش به طور کامل تجزیه زیستی نشد. آنالیز تخریب حرارتی نشان داد که تعداد مراحل تجزیه MNG زیاد نیست و مقداری خاکستر نیز برجای می‌ماند. آنالیز تخریب نوری تغییرات شیمیایی در ساختار MNG و PAM را نشان داد. آزمایشات فاکتوریل نشان داد pH ، غلظت کاتیون و غلظت MNG عوامل مؤثر در فرایند انعقاد و لخته‌سازی می‌باشد. مطالعات بهینه‌سازی نشان داد در pH برابر ۵.۷۷، غلظت کاتیون ۰.۰۵ میلی مولار و غلظتMNG ۰.۴۲ میلی گرم بر لیتر کدورت ۹۷٪ کاهش پیدا کرده است. لذا، عملکرد موثر MNG در pH نزدیک خنثی و در غلظت کم است. این نتایج قویاً پیشنهاد می‌کند که MNG یک نامزد مناسب است که می‌تواند به جای PAM، به عنوان لخته‌ساز در تصفیه آب مورد استفاده قرار گیرد.

Iranica Journal of Energy & Environment 5 (1): 34-41, 2014
ISSN 2079-2115
IJEE an Official Peer Reviewed Journal of Babol Noshirvani University of Technology
DOI: 10.5829/idosi.ijee.2014.05.01.06

BUT

Fuzzy/State-Feedback Control of a Non-Inverting Buck-Boost Converter for Fuel Cell Electric Vehicles

Amin Hajizadeh

Department of Electrical Engineering, Shahrood University of Technology, Shahrood, Iran

(Received: January 15, 2014; Accepted in Revised Form: March 8, 2014)

Abstract: This paper presents an intelligent state feedback controller of a non-inverting buck-boost converter for fuel cell power sources. The proposed control strategy uses fuzzy logic control and state feedback control in order to combine advantages of both controllers. Fuel cell DC/DC converters often have to be able to both step-up and step-down the input voltage and provide a high efficiency in the whole range of output power. Non-inverting buck-boost converters provide both step-up and step-down characteristics. In this paper a state-space average model of converter is obtained and the effect of using a state feedback controller in order to stabilize and regulate the output voltage has been proposed. The use of intelligent state feedback controller allows choosing the proper pole placement of system and using inductor current as a feedback provides a fast dynamic response. Simulation results showed the capability of proposed control strategy during different conditions in fuel cell electric vehicles.

Key words: Fuzzy control · State feedback control · DC-DC converter · Fuel Cell · Electric Vehicle

INTRODUCTION

Due to wide variation of fuel cell output voltage, it is often necessary either to step-up or step-down the fuel cell voltage. Fuel cells have a high efficiency at low output current and it is therefore advantageous to operate them at a low power level; e.g. when charging the batteries in a fuel cell hybrid electric vehicle application, in order to save fuel. However, during periods with high power demands it is necessary to operate them at rated power [1, 2]. As fuel cells are operated in a wide variation of power, it is important that the DC/DC converters not only have a high efficiency at nominal power, but also in the whole power range [3, 4]. Several topologies are capable of both step-up and step down the fuel cell voltage [5]. Due to its simplicity, low component stress and high efficiency it is chosen to use the non-inverting buck-boost converter [6]. In this paper expression of the non-inverting buck-boost converter is therefore derived when parasitic losses are taken into account. Recently in literature, some studies have been developed for controlling of this type of DC-DC converter [4, 7]. Mostly, classic and state feedback control strategies have been designed for non-inverting buck-boost converter. The "min" disadvantage of these control strategies is that they work on fixed operating point. Meanwhile if the input voltage of converter or load current change, the designed controller could not operate well. Also, the disadvantages of conventional buck-boost converters are right half plane (RHP) zeros which restrict the controller response [8, 9]. Hence, a control strategy should be developed in order to tolerate of these limitations. For this purpose, in this paper hybrid fuzzy/ state feedback controller is developed for non-inverting buck-boost converter. This controller technique has the advantages of more robustness and faster dynamics compared to PI or PID conventional controllers.

Based on above justifications, the feasibility of the non-inverting buck-boost converter for fuel cell applications is investigated. This paper is organized as follows. The single inductor non-inverting buck-boost converter is proposed. In section II, a state space average model of converter is obtained and in the next part (section III) hybrid fuzzy/ state feedback controller is designed.

Corresponding Author: Amin Hajizadeh, Department of Electrical Engineering, Shahrood University of Technology, Shahrood, Iran. E-mail: aminhajizadeh@shahroodut.ac.ir

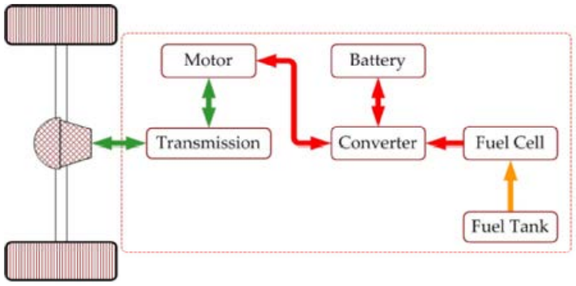

Fig. 1: Schematic block diagram of Fuel Cell and supportive controlling units

Dynamic Model of Fuel Cell Electric Vehicle: The model in a Fuel Cell Electric Vehicle (FCEV) is an important issue that needs to be carefully addressed. The electric components of a FCEV used in this paper comprise a battery bank, Non-inverting buck-boost DC/DC converter, while the electrochemical component is a Fuel Cell system (FC). The mathematical models describing the dynamic behavior of each of these components are given as follow [10]. Fig. 1 illustrates the supportive controlling units of fuel cell system in an electric vehicle.

Fuel Cell Model: Fuel cells are static energy conversion devices that convert the chemical energy of fuel directly into electrical energy. They show great promise to be an important power source of the future due to their number of advantages, such as high efficiency, zero or low emission (of pollutant gases) and flexible modular structure. The model of Polymer Exchange Membrane Fuel Cell (PEMFC) power plant used in this study is based on the dynamic PEMFC stack model developed and validated in literature [4]. The performance of FCs is affected by several operating variables, as discussed in the following. Decreasing the current density increases the cell voltage, thereby increasing the FC efficiency. One of the important operating variables is the reactant utilization or direct uptake of the energy yield restored in the fuel molecules, U_f, referring to the fraction of the total fuel (or oxidant) introduced into a FC that reacts electrochemically:

$$U_f = \frac{q_{H_2}^{in} - q_{H_2}^{out}}{q_{H_2}^{in}} = \frac{q_{H_2}^{r}}{q_{H_2}^{in}} \tag{1}$$

Where q_{H2} is the hydrogen molar flow.

High utilizations are considered desirable (particularly in smaller systems) because they minimize the required fuel and oxidant flow, for a minimum fuel cost and compressor load and size. However, utilizations that are pushed too high result in significant voltage drops. The PEMFC consists of hundreds of cells connected in series and parallel. Fuel and air are passed through the cells. By regulating the molar flow rate, the amount of fuel fed into the fuel cell stacks is adjusted and the output real power of the fuel cell system is controlled. The Nernst's equation and Ohm's law determine the average voltage magnitude of the fuel cell stack [11]. The following equations model the voltage of the fuel cell stack:

$$V_{fc} = N_0(E_0 + \frac{RT}{2F}(\ln(\frac{P_{H_2}P_{O_2}^{0.5}}{P_{H_2O}})) - rI_{f0} \tag{2}$$

Where, N_0 is the number of cells connected in series; E_0 is voltage associated with the reaction free energy; R is the universal gas constant; T is the absolute temperature; I_{f0} is the current of the fuel cell stack; F is the Faraday's constant. r is internal resistance of fuel cell. P_{H2}, P_{H2O}, P_{O2} are hydrogen, water and oxygen pressures which determined by the following differential equations [1, 11]:

$$\begin{aligned} \dot{P}_{H_2} &= -\frac{1}{t_{H_2}}(P_{H_2} + \frac{1}{K_{H_2}}(q_{H_2}^{in} - 2K_r I_{fc})) \\ \dot{P}_{H_2O} &= -\frac{1}{t_{H_2O}}(P_{H_2O} + \frac{2}{K_{H_2O}}K_r I_{fc})) \\ \dot{P}_{O_2} &= -\frac{1}{t_{O_2}}(P_{O_2} + \frac{1}{K_{O_2}}(q_{O_2}^{in} - K_r I_{fc})) \end{aligned} \tag{3}$$

Where, $q_{H_2}^{in}$ and $q_{O_2}^{in}$ are the molar flow of hydrogen and oxygen;

K_r constant is defined by the relation between the rate of reactant hydrogen and the fuel cell current

$$q_{H_2}^{r} = \frac{N_0 I}{2F} = 2K_r I \tag{4}$$

Non-Inverting Buck-Boost Converters: The circuit diagram of non-inverting buck-boost is shown in Fig. 2. The converter consists of one inductor, one output capacitor, two MOSFET switches and two diodes. A non-inverting buck-boost converter consists of two cascade buck and boost converter which can work in three different mode. When the output voltage is higher than the input; it can work in boost region, as the input voltage decrease; it works in buck-boost mode when input voltage is within the range of output. Finally, if the output voltage is much lower than inputs it is in buck region [3].

If S_1 is on and the duty cycle of S_2 is controlled the converter operates like a boost converter and if S_2 is off and duty cycle of S1 is controlled the converter is like a

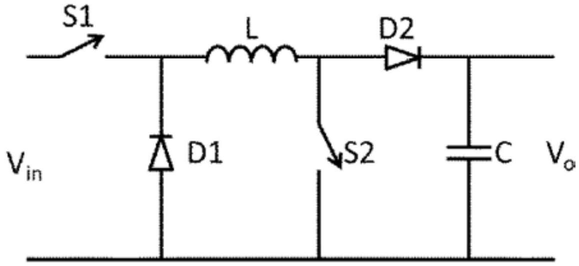

Fig. 2: Non-inverting Buck-Boost Converter topology

buck with a forward diode voltage drop. In the steady state the relation between the input and output voltage is obtained by the following formula:

$$\frac{V_O}{V_{in}} = \frac{D_1}{(1-D_2)}\begin{cases} D_1 + D_2 > 1 \to Boost \\ D_1 + D_2 < 1 \to Buck \end{cases} \tag{5}$$

Which D_1 is the duty cycle of buck switch and D_2 is the duty cycle of boost switch. In order to avoid short circuit of the input with the inductor, D_1 is always greater than D_2.

In order to determine the state space model of switching converters we need to consider the circuit in different conditions based on the allowable switching scheme. In this converter there are three different situations stated as follows.

- Both S_1 and S_2 is on ($0<t<D_2T$)
- S_1 is on and S_2 is off ($D_2T<t<D_1T$)
- Both switches are off

$$(a)\ \begin{cases} \dfrac{dv_C}{dt} = \dfrac{1}{C}\left(-\dfrac{v_C}{R}\right) \\ \dfrac{di_L}{dt} = \dfrac{1}{L}(v_{in}) \end{cases} \qquad 0 < t < D_2T$$

$$(b)\ \begin{cases} \dfrac{dv_C}{dt} = \dfrac{1}{C}\left(i_L - \dfrac{v_C}{R}\right) \\ \dfrac{di_L}{dt} = \dfrac{1}{L}(v_{in} - v_C) \end{cases} \qquad D_2T < t < D_1T$$

$$(c)\ \begin{cases} \dfrac{dv_C}{dt} = \dfrac{1}{C}\left(i_L - \dfrac{v_C}{R}\right) \\ \dfrac{di_L}{dt} = \dfrac{1}{L}(-v_C) \end{cases} \qquad D_1T < t < T$$

Where i_L is the inductor current, v_c is the capacitor voltage, v_{in} is the input voltage of converter and R is the load resistance. The uppercase variables are equilibrium of converter [3-5].

With the combination of these three equations and linearization around equilibrium operating point the average state space model of converter is obtained.

Table 1: The DC-DC converter parameters

L	100uH
C	1000uF
v_{in}	5V
R	12V
Fs	1 Ω
	50kHz

In order to simplify the model suppose that the converter always operates in buck-boost region and duty cycle of S1 and S2 are equal. The simplified state space average model will be obtained [6]:

$$\begin{pmatrix} \dfrac{d\hat{v}_C}{dt} \\ \dfrac{d\hat{i}_L}{dt} \end{pmatrix} = \begin{pmatrix} -\dfrac{1}{RC} & \dfrac{(1-D)}{C} \\ -\dfrac{(1-D)}{L} & 0 \end{pmatrix}\begin{pmatrix} \hat{v}_C \\ \hat{i}_L \end{pmatrix} + \begin{pmatrix} -\dfrac{I_L}{C} \\ \dfrac{V_{in}+V_c}{L} \end{pmatrix}\hat{d} + \begin{pmatrix} 0 \\ \dfrac{D}{L} \end{pmatrix}\hat{v}_{in} \tag{6}$$

State Feedback Control Design: Before designing state feedback controller it is needed to choose a proper operating point for converter. The converter parameters are shown in Table 1.

With the above component data the state space model of converter in the form of $\dot{X} = AX + BU + \Gamma W$ will be:

$$\begin{pmatrix} \dfrac{d\hat{v}_C}{dt} \\ \dfrac{d\hat{i}_L}{dt} \end{pmatrix} = \begin{pmatrix} -1667 & 294 \\ -2941 & 0 \end{pmatrix}\begin{pmatrix} \hat{v}_C \\ \hat{i}_L \end{pmatrix} + \begin{pmatrix} -48000 \\ 170000 \end{pmatrix}\hat{d} + \begin{pmatrix} 0 \\ 7059 \end{pmatrix}\hat{v}_{in} \tag{7}$$

Where U is input vector of system and W is disturbance vector. First step of designing state feedback controller is checking the controllability of the system [12]. By foundation of the controllability matrix (V), it is shown that it is full rank and the determinant of V is not zero so the system is controllable.

$$V = \begin{bmatrix} A & AB \end{bmatrix} = \begin{bmatrix} 0 & 1.3*10^8 \\ 7059 & 1.41*10^8 \end{bmatrix} \tag{8}$$

With this data parameters the two poles of system are at S_1=-833+413i and S_2=-833-413i. Then the open loop system is stable, but according to the time response it has to be compensated. The step response of closed loop system to a step change in the input voltage is shown in Fig. 3. Where k_1= 0.1 is the gain of the capacitor's voltage feedback and k_2=0.05 is the gain of inductor current feedback. Hence, the control signal is calculated by following equation:

$$U = -KX(t) = \begin{bmatrix} -k_1 \\ -k_2 \end{bmatrix}^T \cdot \begin{pmatrix} \hat{v}_C \\ \hat{i}_L \end{pmatrix} \tag{9}$$

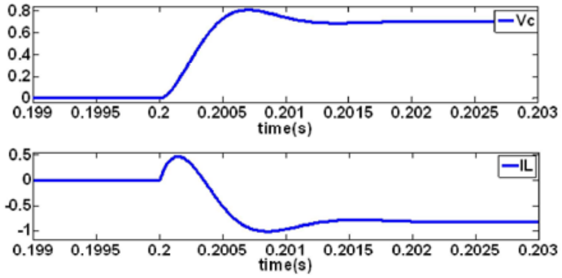

Fig. 3: Step response of system with state feedback controller

As it is shown if Fig. 3, the state feedback the whole system is stable but it is desired with a step change in the input voltage the output voltage remain constant and v_c should be near zero after the step change but the inductor current will converge to a new vaue.

Using state feedback controller by itself cannot regulate the output voltage but it has improved stability and time response so, it is needed to add an integrator term to the voltage controller loop. The step response of system with the new controller to a step change in the input voltage is shown in Fig. 4. It shows that with a proper integrator gain the output voltage remains constant while the input has changed and the inductor current will decrease as the input voltage increase.

With a state feedback controller and a voltage regulator not only the system is stable but also it has a fast and correct step response. A step change in the input voltage will force the output to rise but it reaches zero after a settling time.

Hybrid Fuzzy/ State-Feedback Control Strategy: In fuel cell power generation systems, the output voltage of fuel cell changes during the different load currents. In fact, the operating point conditions of DC-DC converter are not constant. So, it is important to design a flexible control strategy for DC-DC converter to operate under different conditions. Hence, in this paper, a robust self-tuning fuzzy control structure has been developed [13]. The block diagram of the hybrid fuzzy/ state feedback controller is shown in Fig. 5.

Use of the scaling factors (SFs) G_e, $G_{\Delta e}$, the quantities e and Δe are converted to normalized e_N and Δe_N. These normalized quantities e_N and Δe_N are crisp in nature and therefore need to be first converted to their corresponding fuzzy variables. After fuzzification, the fuzzified inputs are given to the fuzzy inference mechanism which, depending on the given fuzzy rule base, gives the normalized incremental change in control output (Δu_N). The output Δu_N is converted into actual incremental change in control output (Δu) by using the scaling factor Gu. For the implementation the fuzzy inference engine, the "min" operator for connecting multiple antecedents in a rule, the "min" implication operator and the "max" aggregation operator have been used [13]. Actually, the output Δu_N from the inference mechanism is fuzzy in nature, hence, to determine the crisp output, the defuzzification stage is applied. The centroid defuzzification scheme has been used here for obtaining the output Δu. Finally, the actual value of the controller output (u) is computed by the following expression:

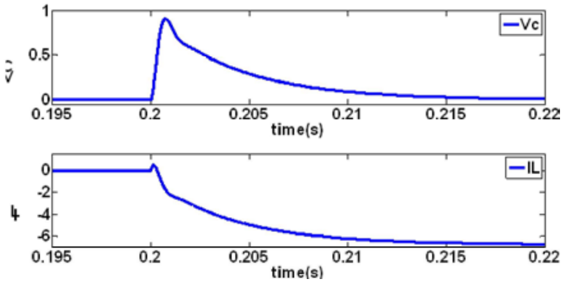

Fig. 4: Step response with state feedback controller and output voltage reugulator

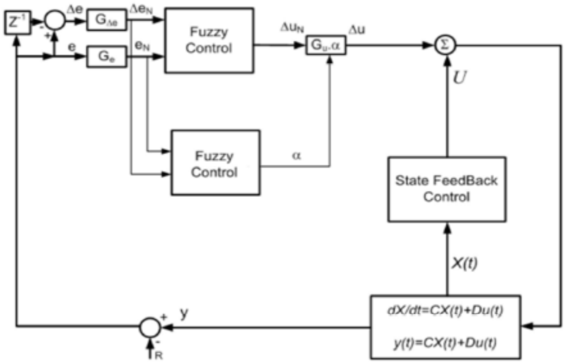

Fig. 5: Block diagram of the hybrid fuzzy/ state feedback controller

$$u(k) = u(k-1) + \Delta u(k) \tag{10}$$

The relationships between the SFs and the input and output variables of the self-tuning FLC are as follow:

$$\begin{aligned} e_N &= G_e.e \\ \Delta e_N &= G_{\Delta e}.\Delta e \\ \Delta u &= (\alpha.G_u).\Delta u_N \end{aligned} \tag{11}$$

In this scheme, the FLC is tuned on-line (while the controller is in operation) by dynamically adjusting its output scale factor by a gain updating factor (α). The value of α is determined from a rule base defined on e and Δe which are derived from the knowledge of control engineering. Generally, selection of suitable values for G_e, $G_{\Delta e}$ and Gu are made based on the knowledge about the process to be controlled and sometimes through trial and error to achieve the best possible control performance.

Each fuzzy control rule in the controller rule base is of the form:

"If *e* is *E* and Δ*e* is Δ*E*, then Δ*u* is Δ*U*"

where *E*, Δ*E* and Δ*U* are the fuzzy sets corresponding to error, change in error and the incremental change in the control output, respectively. In this work, for both the inputs (*e* and Δ*e*) and the output (Δ*u*), seven fuzzy subsets have been used. These are: PB (positive big), PM (positive medium), PS (positive small), ZE (zero), NS (negative small), NM (negative medium) and NB (negative big). For each of these fuzzy sets, triangular membership function (MF) has been used.

From this figure it is observed that the triangles are symmetric with equal base having 50% overlap with neighboring MFs. As each of the two inputs has seven fuzzy sets, there are altogether 49 control rules in the FLC. The rule base for computing the output Δ*u* is shown in Table 2 which is a widely used rule base designed with a two dimensional phase plane. The control rules in Table 3 are built based on the characteristics of the step response.

Moreover, the gain updating factor (α) is calculated using fuzzy rules of the form:

If e is E and Δ*e* is ΔE then α is α.

From Fig. 6 it is observed that the value of α is computed from the normalized values of *e* and Δ*e* by a fuzzy rule base. The membership functions used for *e* and Δ*e* are exactly the same as those used in FLC. Moreover, the same fuzzy operators also been used in this case. The membership functions for the factor α are defined in the domain (0, 1). As each of the two inputs (*e* and Δ*e*) to the fuzzy rule base (corresponding to α) has seven fuzzified variables, the rule base has 49 rules for computing the value of α. Table 4 shows the rule base for computing α. This rule base is designed to improve the control performance under large disturbances such as three-phase short circuit on the transmission lines, a sudden loss of generating unit or a large loss of load, etc. For example, immediately after a large disturbance, *e* may be small but Δ*e* will be sufficiently large (they will be of same sign) and, for this case, α is supposed to be large to increase the gain. Therefore, under these circumstances, the appropriate rules are "IF *e* is PS and Δ*e* is PM THEN ^{2} is B" or "IF *e* is NS andΔ*e* is NM THEN α is B". On the other hand, for steady state conditions (i.e. *e*≈0 and Δ*e*≈0), controller gain should be very small (e.g. IF *e* is ZE and Δ*e* is ZE THEN α is ZE) to avoid chattering problem around the set point. Further justification for using the rule base in Table 3 found in literature [9].

Table 2: Rule base for computing the output Δ*u*

Δe/e	NB	NM	NS	ZE	PS	PM	PB
NB	NB	NB	NB	NM	NS	NS	ZE
NM	NB	NM	NM	NM	NS	ZE	PS
NS	NB	NM	NS	NS	ZE	PS	PM
ZE	NB	NM	NS	ZE	PS	PM	PB
PS	NM	NS	ZE	PS	PS	PM	PB
PM	NS	ZE	PS	PM	PM	PM	PB
PB	ZE	PS	PS	PM	PB	PB	PB

Table 3: Rule base for computing the output a

Δe/e	NB	NM	NS	ZE	PS	PM	PB
NB	VB	VB	B	SB	S	S	ZE
NM	VB	VB	B	B	MB	S	VS
NS	VB	VB	B	VB	VS	S	VS
ZE	S	SB	MB	ZE	MB	SB	S
S	VS	S	VS	VB	B	MB	VB
PM	VS	S	MB	B	B	VB	VB
*PB	ZE	S	SB	B	VB	VB	VB

Simulation of Results and Validation: In order to verify the mathematical model of fuel cell, converter and controller the whole system has been simulated in MATLAB software environment. It is supposed that fuel cell is supplied 5KW of active power. Moreover, it is assumed that the output voltage of DC-DC converter should be regulated at 100V under different load current conditions. For analyzing fuel cell power generation system with designed control strategy, three cases for simulation conducted that described as continue.

Control of fuel cell power system under different load conditions: For this purpose, load current changes as shown in Fig. 6. In Figs. 6 and 7 variations of fuel cell current and voltage are presented. As shown, the fuel cell voltage varies during current variations. So it needs to regulate this voltage under different loading conditions.

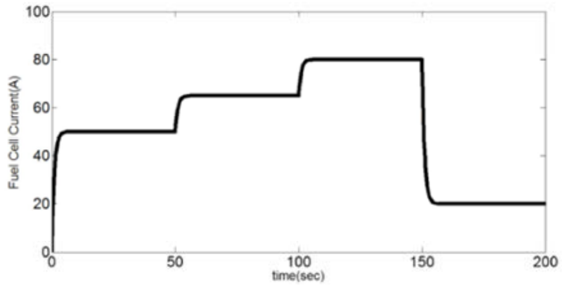

Fig. 6: Fuel cell current variations

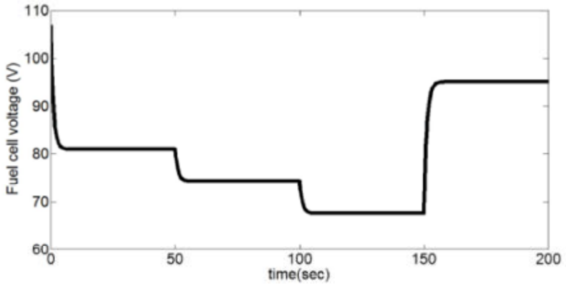

Fig. 7: Fuel cell voltage variations

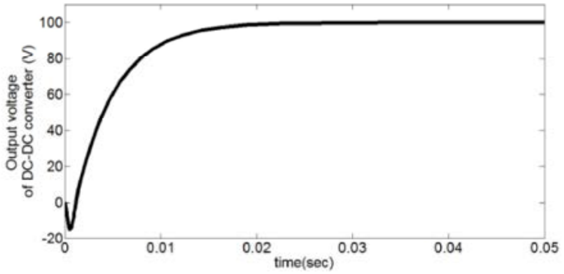

Fig. 8: Output voltage of DC-DC converter

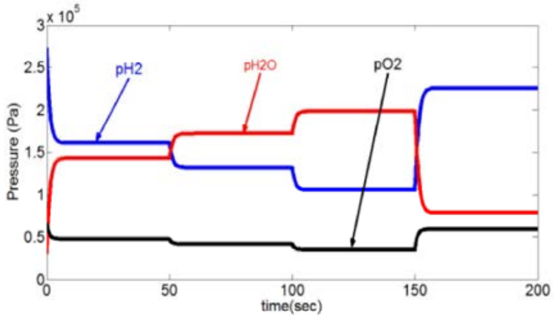

Fig. 9: Variation of hydrogen, oxygen and water pressures

Moreover, the output voltage of DC-DC converter is illustrated in Fig. 8. As it is shown, this voltage is controlled very fast under variations of fuel cell voltage. Because of non-minimum phase characteristic of DC-DC converter, there is undershoot at the fist time of simulation.

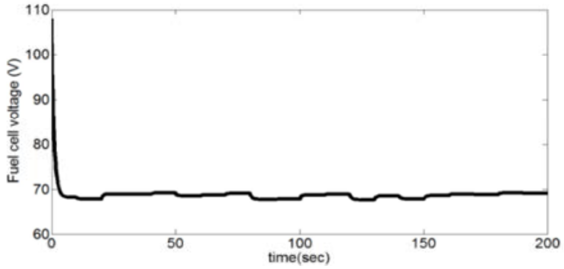

Fig. 10: Perturbed fuel cell voltage

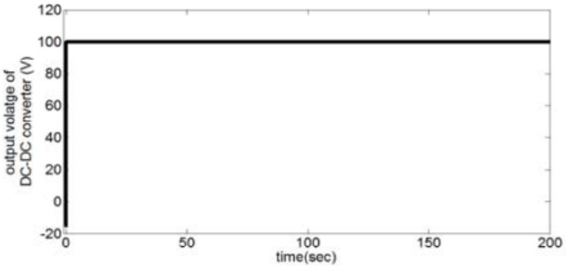

Fig. 11: Regulated output voltage of DC-DC converter

In order to show the dynamics of fuel cell during simulation, the variation of hydrogen, oxygen and water pressures are shown in Fig. 9.

In order to show the robustness of the hybrid fuzzy/state feedback control, a disturbance is added to input hydrogen fuel flow in order to perturb fuel cell voltage as shown in Fig. 10. In this case, supposed that the fuel cell current is constant (80A), but there are variations in voltage of fuel cell. In this case, output voltage of DC-DC converter is presented in Fig. 11.

Implementation of Proposed Control Strategy in Fuel Cell Hybrid Vehicle: According to the presented results, it is achieved that the proposed control strategy is very suitable for fuel cell power generation system. In fact, by this control strategy the output voltage of fuel cell is regulated under different loading conditions and existing disturbances which may occur in fuel cell stack. Moreover, this control strategy is proper for fuel cell hybrid vehicle during requested power from duty cycle. For this purpose, a simulation of results is conducted based on research work in literature [1, 10]. The requested power from fuel cell stack during standard driving cycle of ECE [14] has been implemented to show the response of DC-DC converter. In Fig. 12 variations of fuel cell current and voltage are illustrated.

In this condition, regulated voltage of DC-DC converter is presented in Fig. 13.

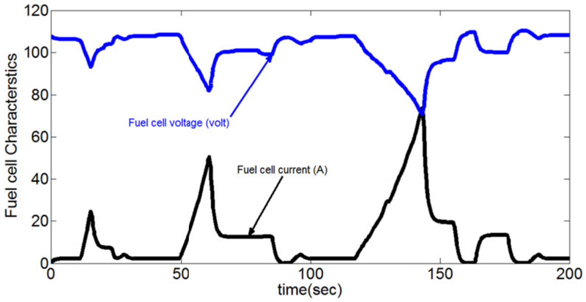

Fig. 12: Variations of fuel cell current and voltage in fuel cell hybrid vehicle

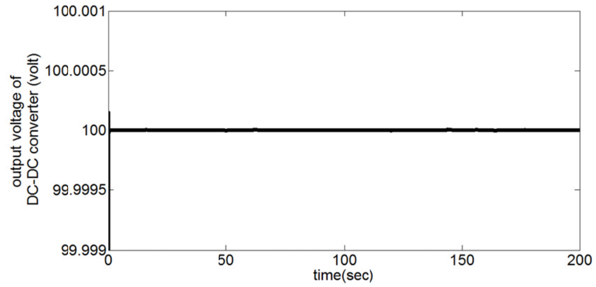

Fig. 13: Output voltage of DC-DC converter in fuel cell hybrid vehicle

CONCLUSION

A non-inverting buck boost with a hybrid fuzzy/ state feedback control method was introduced in this paper. It shows that using hybrid fuzzy/state feedback controller improves the system response. In fact, state feedback controller is designed based on fixed operating point of DC-DC converter. Fuzzy controller regulates the response of dynamic system when operating point of DC-DC converter changes which makes during input voltage or load current variation Moreover, a current sensor and a voltage sensor must be added in order to measure the system states. An external voltage controller was designed in order regulate the output voltage during any disturbances in the input voltage or output load. Comparing the output characteristics of a state space feedback to a conventional PI controller it has been shown that state space feedback controller has a better dynamic response but the steady state response are as the same.

REFERENCES

1. Hajizadeh, A., 2011. Intelligent Control Strategy of Fuel Cell Hybrid Vehicles. Journal of Intelligent Systems in Electrical Engineering, 2(2): 55-66.
2. Schaltz, E., P.O. Rasmussen and A. Khaligh. Non-inverting buck-boost converter for fuel cell applications. in Industrial Electronics, 2008. IECON 2008. 34th Annual Conference of IEEE. 2008. IEEE.
3. Shiau, J.K. and C.J. Cheng, 2010. Design of a non-inverting synchronous buck-boost DC/DC power converter with moderate power level. Robotics and Computer-Integrated Manufacturing, 26(3): 263-267.
4. Lee, Y.J., A. Khaligh and A. Emadi, 2009. A compensation technique for smooth transitions in a noninverting buckâ_“boost converter. Power Electronics, IEEE Transactions on, 24(4): 1002-1015.
5. Sahu, B. and G.A. RincÃ³n-Mora, 2004. A low voltage, dynamic, noninverting, synchronous buck-boost converter for portable applications. Power Electronics, IEEE Transactions on, 19(2): 443-452.
6. Gaboriault, M. and A. Notman, A high efficiency, noninverting, buck-boost DC-DC converter. in Applied Power Electronics Conference and Exposition, 2004. APEC'04. Nineteenth Annual IEEE. 2004. IEEE.
7. Dehghani, H., A. Abedini and M. Tavakoli Bina, Advanced non-inverting step up/down converter with LQR control technique. in Power Electronics, Drive Systems and Technologies Conference (-PEDSTC), 2013 4th. 2013. IEEE.
8. Erickson, R., 1997. Fundamentals of power electronics. 1997. Massachusetts: Kluwer Academic.
9. Calvente, J., L. Martinez-Salamero, P. Garces and A. Romero, 2003. Zero dynamics-based design of damping networks for switching converters. Aerospace and Electronic Systems, IEEE Transactions on, 39(4): 1292-1303.
10. Hajizadeh, A. and M.A. Golkar. Control of hybrid fuel cell/battery distributed power generation system with voltage sag ride-through capability. in Power and Energy Conference, 2008. PECon 2008. IEEE 2nd International. 2008. IEEE.
11. Padulles, J., G. Ault and J. McDonald, 2000. An integrated SOFC plant dynamic model for power systems simulation. Journal of Power Sources, 86(1): 495-500.
12. Chen, C.T., Linear system theory and design1995: Oxford University Press, Inc.
13. Mudi, R.K. and N.R. Pal, 1999. A robust self-tuning scheme for PI-and PD-type fuzzy controllers. Fuzzy Systems, IEEE Transactions on, 7(1): 2-16.
14. Golden, C., 2009. National Renewable Energy Laboratory. Richland, WA: Pacific Northwest National Laboratory.

Persian Abstract

DOI: 10.5829/idosi.ijee.2014.05.01.06

چکیده

در این مقاله یک روش کنترل فیدبک حالت هوشمند برای مبدلهای افزاینده-کاهنده غیر معکوس به منظور اتصال به منابع تولید توان پیل سوختی ارائه می شود. روش کنترل پیشنهادی ترکیبی از یک کنترل کننده فازی و کنترل فیدبک حالت می باشد که باعث می شود از ویژگیهای هر دو بتوان استفاده کرد. مبدلهای DC-DC مرتبط به پیلهای سوختی در خودورهای برقی نیاز دارند تا براساس نیاز عملکردی در آنها بتوانند ولتاژ را افزایش و کاهش دهند. لذا مبدلهای افزاینده= کاهنده غیر معکوس انتخاب مناسبی برای این کاربرد می باشد. در این مقاله ابتدا مدل میانگین غیر خطی مبدل استفاده می شود. سپس در یک نقطه کار مشخص، کنترل کننده فیدبک حالت به منظور پایدار سازی و تنظیم ولتاژ خروجی در نقطه کار طراحی می گردد. سپس سعی می گردد تا با یک کنترل کننده فازی تغییرات نقطه کار در ولتاژ خروجی را کنترل نمود. نتایج شبیه سازی براساس پیاده سازی این مبدل در خودورهای برقی پیل سوختی نشان می دهد که کنترل کننده طراحی شده قادر است تا تحت شرایط عملکردی مختلف، سیستم مورد نظر را درستی کنترل نماید.

Iranica Journal of Energy & Environment 5 (1): 42-50, 2014
ISSN 2079-2115
IJEE an Official Peer Reviewed Journal of Babol Noshirvani University of Technology
DOI: 10.5829/idosi.ijee.2014.05.01.07

BUT

Conversion Efficiencies of Urea –SCR System for Mahua Methyl Ester Fuelled DI Diesel Engine

[1]A. Veeresh Babu, [2]Rajnish K. Calay and [3]P.V. Rao

[1]Department of Mechanical Engineering, NIT Warangal, India
[2]Energy Technology, Narvik University College, Narvik, Norway
[3]Mechanical Engineering, Kakatiya Institute of Technology and Science, Warangal, India

(Received: January 15, 2013; Accepted in Revised Form: March 14, 2014)

Abstract: Stringent emission regulations on diesel-powered vehicles and some of biodiesel emissions have led to development of new technologies to reduce emission of nitrogen oxides (NO_X). Out of the choices available, Selective Catalytic Reduction (SCR) has shown to be the most promising exhaust after-treatment system for reducing oxides of nitrogen in the near term in-use applications. SCRs use the ammonia containing compound urea, as a reducing agent. This paper describes an experimental investigation of Urea-SCR,which has been designed for comparing efficiency of the SCR system for diesel and biodiesel. For this study, a SCR exhaust system was tested on a steady state, direct injection Kirloskar single cylinder diesel engine. Mahua Methyl Ester (MME) oil has used as a biodiesel. From the experimentation, it was concluded that the conversion efficiencies were higher for diesel comparable to biodiesel. The analysis also shows the Urea SCR system has a maximum of 93.4% NO_X conversion efficiency of diesel fuel. For biodiesel, maximum NO_X conversion efficiency of Urea-SCR was approximately 49%. This experimentation also revealed that the Urea-SCR system hasan excellent HC conversion efficiency at all engine loads and using both fuels.

Key words: Selective Catalytic Reduction System · DI Engine · Mahua Oil · Biodiesel · CO_2 · NO_X

INTRODUCTION

Diesel engine is an internal combustion engine, uses compression to ignite the hydrocarbon fuel (i.e. Diesel) to start the combustion and to convert the chemical energy into useful work. Therefore, environmental concerns attributable to polluting gases, i.e. oxides of nitrogen (NO_X), oxides of carbon (CO and CO_2) and unburnt hydrocarbon (HC) are associated with the use of diesel engines. However, diesel engine offers higher thermal efficiency and durability in comparison with a petrol engine that makes it as a better choice for many applications; automobiles, particularly in heavy-duty vehicles, locomotives, ships, farm machinery, generators for backup power, etc. Despite their advantages over petrol engines, diesel engines has specific concerns relates to soot, smoke and particulate matter released by diesel fuel. Thus, investigations have been underway to explore the role of diesel derived from renewable sources into diesel engines. Diesel derived from different vegetable oils, oil from bio-waste, algae, etc., is being tested in diesel engines by many researchers. In fact, Rudolph diesel who invented the diesel engine tested the engine using peanut oil over 100 years ago and its use continued within the agricultural community as fuel for tractors, pumping water and other agricultural machinery.

Vegetable oils are triglycerides (glycerin esters) of fatty acids. Alcohol esters of fatty acids prepared by the transesterfication of the glycerides, wherein linear, mono-hydroxyl alcohols react with vegetable oils in the presence of a catalyst to produce alcohol esters of vegetable oils and glycerin as a by-product. This transesterfication reaction is affected by the molar ratio of glycerides of alcohol, catalyst used, reaction temperature, reaction time and free fatty acids and water content of oils or fats [1].

Corresponding Author: A. Veeresh Babu, Department of Mechanical Engineering, NIT Warangal, India.

As an alternate fuel, vegetable oil is renewable and contains lesser sulfur to petroleum diesel. The combustion of vegetable oil produces negligible sulfur dioxide emissions and much lesser toxic emissions. In principle, vegetable oils are carbon neutral because the carbon dioxide (CO_2) released by combustion is absorbed back for photosynthesis by the plant source. Vegetable oil is biodegradable, safe to store and transport and does not cause other environmental or health problems. Several vegetable oils are of edible, such as rapeseed oil, sunflower oil, cottonseed oil, palm oil, olive oil etc. that have resulted in fuel versus food debate. In addition, various non-edible oils such as Jatropha, Mahua, Karanja oils that are available potentially used as alternate fuels for diesel engines. However, the choice mainly depends upon the climate and soil conditions and availability, thus different nations are looking into different vegetable oils for diesel fuels. For example, soybean oil in the United States, rapeseed and sunflower oils in Europe, palm oil in the Southeast Asia (mainly Malaysia and Indonesia) and coconut oil in Philippines are being believed possible substitutes for diesel fuel [2].

This paper presents experimental results of performance of Mahua Methyl Ester (MME) in a diesel engine, obtained from the two species of the genus Madhucaindica and MadhucaLongifoliafound in India. The aim of the research was to investigate the performance of MME in the engine and to investigate the emissions. For this Mahua oil wastransesterifiedwith Methanol in the presence of Sodium Hydroxide (NaOH) catalyst as per the standards established for maximum yield of biodiesel. Different after-treatment techniques for control exhaust emissions searched. Selective catalyst reduction (SCR) is a commonly used in lean burn engines for reducingNO_xemissions. The experiments are also being conducted to study the performance of the SCR with MME.

Background Literature

Mahua Oil: The two species Madhucaindica and Madhucalongifolia are closely related and no distinction is available in the trade of their seed or oil. The drying and de-cortification yield 70% kernel on the weight of seed. The kernel of seed contains about 50% oil. The oil yield in an expeller is nearly 34-37%. The fresh oil from properly stored seed is yellow in color. The properties of Mahua oil and of MME are as shown in Table 1. MME oil has a lower calorific value but higher density, indicating that the calorific value of MME oil on a volumetric basis approaches the volumetric calorific value of diesel fuel. The Mahua oil Cetane number increases with flash and fire point [3-5].

Table 1: Properties of Mahua oil [5][4]

Properties	Diesel	Mahua oil	MME
Kinematic viscosity at 40°C (CST)	3.05	39.45	5.8
Density (kg/m^3)	850	924	916
Flash point (°C)	56	230	129
Fire point (°C)	63	246	141
Net calorific value (KJ/kg)	42800	37614	39400

Many researchers have tested the use of Mahua oil in diesel engines. Sukumar Puhan *et al.* [6] conducted experiments on performance and emission study of MahuaOil Ethyl Ester with the some modification of pressure and injection timing of the fuel injection. It is concluded reductions of Carbon monoxide (CO), Hydrocarbons (HC) and oxides of nitrogen to nearly 58, 63 and 12%, respectively. Similarly, Raheman and Ghadge [7, 8] conducted experiments to study the performance of Mahua for various blend ratios, various compression ratios and ignition timing. It is reported that similar performance, efficiency could also be achieved on par with Diesel by B100 (pure biodiesel) with increased compression ratio and advancing injection from 30 to 40° before the top dead center (TDC) of the engine.

Catalytic Converters: Reduction in NOx emissions from compression-ignition engines has previously been addressed by the addition of exhaust gas to incoming air charge, known as exhaust gas recirculation (EGR). Recently, the two techniques suggested for the reduction ofNOx emissions under lean exhaust conditions - Selective Catalytic Reduction (SCR) and the lean NOx trap or NOxadsorber. Instead of precious metal-containing NOx adsorbers, manufacturers almost selected base-metal SCR systems that use a reagent such as ammonia (AdBlue) to reduce the NO_X into nitrogen. Ammonia supplied to the catalyst by the injection of urea and water into the exhaust pipe, which then undergoes thermal decomposition and hydrolysis into Ammonia.

Oxidation catalytic converter owes to the oxidation of some of the contents of exhaust fumes, in particular carbon monoxide and un-burnt hydrocarbons. Generally, used in diesel engines because of the exhaust gases contain a large quantity of oxygen generated by lean-burn combustion. This catalytic converter however, does not allow the treatment of NOx gases and soot usually present in diesel exhaust fumes. It may therefore

Table 2: Status of Emission Control Devices Research, Development and Demonstration [8, 7]

Emission Control Device	Description	Typical / Expected No_x Efficiency	Typical / Expected PM Efficiency	Status
NOxAdsorber	Adsorbs NO and oxygen during lean operation, uses CO and HC from periodic rich operation to convert to N_2	>80%	30%	In development: available in 2007
Diesel Particulate Filter	Collects particles in diesel exhaust	None	80 to 90%	Verified for some heavy duty engines model year and duty cycles in CA
Oxidation Catalyst	Oxidizes HC and CO in exhaust	None	20 to 30%	In commercial use in bus engines; not verified for non-bus heavy-duty vehicles
Selective Catalytic Reduction Catalyst	Converts NOxto N_2 and O_2 in presence of ammonia, or ammonia carrying agent (e.g., urea)	>80%	30%	In development/ demonstration; Available 2005 – 2007. Requires reductant dispensing and storing infrastructure
Non-thermal plasma	High energy electrons convert exhaust Pollutants to inert species	>65%	30%	In demonstration phase for light – duty only; in development for heavy-duty applications

necessary to associate the oxidation catalytic converter to catalytic reduction kind and if required, a particulate filter to guarantee an efficient and more thorough treatment and meet regulations in force.

Selective Catalytic Reduction (SCR) is a promising technology with the potential to achieve large NO_X and some PM reductions. SCR has been used to control stationary source NO_X emissions for over twenty years. It is at present demonstrated in mobile diesel applications, both in Europe and in the United States [9, 10]. Table 2 describes the status of Research, Development and Demonstration of emission control devices.

SCR used in lean-burn combustion engine typically, diesel engine to reduce NO_X. For compression-ignition (i.e., diesel engines), the more commonly used catalytic converter is the Diesel Oxidation Catalyst (DOC).

This catalyst uses O_2 (oxygen) in the exhaust gas stream to convert CO to CO_2 and HC (hydrocarbons) to H_2O (water) and CO_2. These converters often operate virtually at 90% efficiency; eliminating diesel odor and helping to reduce visible particulates (soot). These catalysts are not active in NO_X reduction because any reduce presents should react first with the high concentration of O_2 in diesel exhaust gas.

The LEV II and EURO V legislation in 2007/2008 require a highconversion level of nitrogen oxides to meet the emission levels for diesel Sport Utility Vehicles (SUVs) and trucks. Almost all the light–duty diesel vehicles of US and European trucks have the catalytic systems to meet the new federal emissions regulation since 2010[11]. Another example of successful implementation of SCR to meet the emissions requirements in 50 states in the US is for Passat's 2.0-liter TDI Clean Diesel in-line four-cylinder engine [12, 20].

Researchers are also conducting experiments on the SCR using the biodiesel and biodiesel blends. A reduction of $NO_X$of 73% was achieved with Soybean biodiesel when ethanol –SCR application on Ag/Al_2O_3 catalyst [13]. However, to reduce the total hydrocarbons (THC) and CO the set-up had modified with two catalytic systems with a small increase in NO_Xemissions. Similarly, SCR with urea as a reducing agent was also beinginvestigated for many years and today is the well-establishedtechnique for stationary diesel engines. The addition of external injection of a reducing agent (urea or ammonia) breaks up the NO_X into nitrogen and water.

Studies on road emissions of buses with urea - SCR and EGR + DPF using diesel and biodiesel reveals better performance with urea – SCR than EGR + DPF [13-15]. The degree of EGR is greater and during rapid accelerations, the degree of EGR is less, with a weaker control of NOx. In this sense, the SCR + Urea performs better than EGR + DPF. Additionally, reported that as the biodiesel mix increases, NOx also increases owing to the presence of an increase in oxygen content. However, unburned hydrocarbon (HC) and the particulate matter (PM) levels are remained low and no significant differences observed for the B20 and B100 in comparison to the reference diesel fuel [11, 15, 16].

It is one of the most promising ways to reduce NO_X emissions from diesel engines. Several studies have reported that urea-SCR systems affect more when coupled with an oxidation catalyst upstream to convert some of the NO to NO_2. This promotes NOx reduction through the fast-SCR reaction path on the SCR catalyst [11, 15,17-19].

A urea-SCR plays a significant role not only in the abatement of NOx but also results in the improvement of the performance enhancement of the engine.

Fig. 1: Principle of SCR

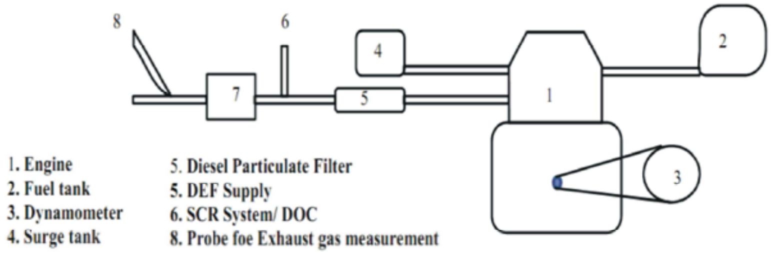

Fig. 2: Experimental Set-up

These advantages include increased fuel economy, efficient power and torque production over a long life, Enhanced durability and reliability resulting in longer service intervals and optimized power potential of the engine.

The compact urea-SCR can reduce NOx pollutants by over 70% of the European transient cycle (ETC) and European steady-statecycle(ESC)[15, 20]. Miller*etal*.[16] have reported on the cold US transient cycle that the reductions of NOx and PM with a urea-SCR catalyst are 55.6 and 22.2%, respectively. While reduction of NOx and PM on the hot US transient cycle are 70.5 and 25%, respectively. Heavy-duty trucks alone, SCR can reduce NO_X emissions up to 90%, hydrocarbons and carbon monoxide by 50-90% and PM emissions by 30-50% with reliable and proven capabilities. Figure 1 shows the principle of the SCR system with the components. There are 3 main components of the SCR system;

- Diesel exhaust fluid (DEF)
- A solution of urea and purified water
- Hot exhaust and catalytic converter

Diesel Exhaust Fluid (DEF) is a crucial component of SCR technology. It is a 32.5% strength urea- 67.5% water solution. It is non-toxic, non-polluting and non-flammable with an odor similar to that of ammonia. DEF is nonetheless safe to handle and store, posing no serious risk to humans, animals, equipment or the environment with proper handling. DEF will begin to freeze to a slushy consistency at – 11°C. SCR designed to heat the DEF storage tank, providing lines that reduce the melting time. If DEF freezes when the vehicle was shut down, ignition and normal operation of the vehicle will not be inhibited, the SCR heating system quickly returns the DEF to liquid form without upsetting the vehicle's operation even if the vehicle is operated in such a way that is runs out of DEF, the vehicle will not shut down. However, additional methods (yet to be determined) are to be encouraged to enable the operator to refill the DEF tank. Depending on vehicle operation, DEF consumption is approximately 2 to 4% of fuel consumption. Therefore, the tank must sized according to usage requirements and generally allowing 2-3 fuel refills before needed to replenish the DEF tank.

In the following sections, we present the results of an experimental study of testing the Urea-SCR uses Mahua Methyl Ester oil with the objectives of studying the combined performance of the SCR and MME.

Experimental Set-up: A Kirloskar 5 HP single cylinder DI engine has used for the experiment. Fig. 2 shows the experimental setup with SCR, Diesel Particulate Filter (DPF) and the dosing location. Tables 3 and 4 respectively show specifications of the engine used and the dosing details of DEF as specified by the supplier.

For benchmarking, the experiment had conducted first with diesel as a fuel and without the attachment of the catalytic converter. Subsequently, the experiments being conducted using a catalytic converter and a catalytic converter with SCR using diesel then followed by Mahua Methyl Ester fuel. Measurements of Fuel consumption of the both fuels usage and exhaust

Table 3: Dosing Module Specifications

Dosing quantity	2.4 liter/min.
Dosing pressure	1.8 bars
Atomization	≤ 400 µm
Operating voltage	12 V
Injection line between supply module & dosing Module	3805 mm

Table 4: Specifications of Kirloskar Engine

Make	Kirloskar AVI
Bore	80 mm
Stroke	110 mm
Number of cylinders	1
Compression ratio	16.5
Engine speed	1500 RPM
Power	5 HP/3.7 W
Cooling system	Water cooled

emissions with the scheme of attachments discussed above recorded in each case once the engine comes to steady condition. For the consistency of measurements at every load the average of three trials are considered.

A D.C. Shunt dynamometer is used for the loading the engine and the experiment was restricted to 80% full load only with an apprehension of engine failure. For the exhaust gas measurements NETEL make of MGA – II is used.

RESULTS AND DISCUSSION

Figs. 3 and 4 show the performance curves of the engine. As seen from these figures the Specific Fuel Consumption (SFC) of Mahua Methyl Ester (MME) was higher than diesel at 20, 40 and 60% of full load. However, SFC at 80% of full load for MME is lower than that for diesel. This is because of the high density of MME, results in good performance and low fuel consumption of MME at high loads.

The brake thermal efficiency (BTE) of MME was higher than that of diesel fuel (Fig. 4). A value of higher than 21.8% was observed with MME at 80% of full load.

The exhaust gas emissions either with or without after-treatment attachments and the conversion efficiencies of the attachments at different loads are shown in Figs. 5 to 8.

CO Emissions: Figs. 5a and 5b show the CO concentration variation at various loads on the engine. The CO concentration is higher with the MME fuel in comparison to diesel at no loads and 20% of full load and it is less in comparison with diesel at other loads including 80% of full load [6, 20]. Nearly a reduction of 28.4% at 80% of full load was observed.

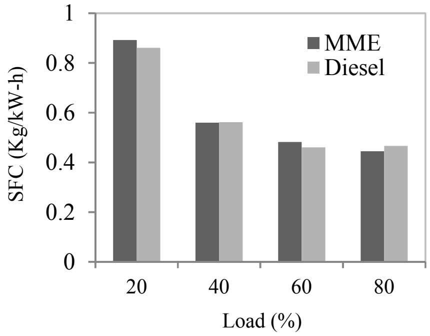

Fig. 3: Variation of SFC with load

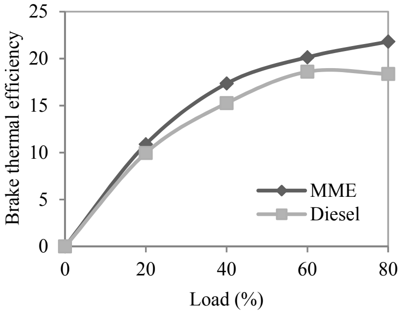

Fig. 4: Variation of $\eta_{thermal}$ with load

With the attachment of a catalytic converter (CAT) alone, the CO of MME is relatively higher than the CO of diesel initially and it is approaching diesel for the higher loads. The average conversion efficiency of CAT is 78.1% and with the addition of SCR 83.85% of CO observed in diesel fuel operation (Fig. 5c). That means it gives an act of possible oxidation in SCR too in the diesel operation.

Fig. 5c Shows the conversion efficiencies of the attachments when intended for the after-treatment of exhaust gases. The conversion efficiency of oxidation of CO with diesel is superior to that of Mahua Methyl Ester. The average conversion efficiencies of 48.7% with CAT and 73% with the addition of SCR are achieved at MME operation. The reasons for the improvement in the conversion efficiency with SCR attachment is further oxidation and the self-oxygen content present in the fuel.

Oxides of Nitrogen (Nox): TheNOx emissions from diesel is more that of the MME nearly 349 PPM more at 80% full load as it is shown in Figs. 6a and 6b[6]. This is because of the average temperature of combustion prevailed. This is also one of the reasons for the declined efficiency for the after-treatment attachments of MME as a fuel (Fig. 6c). The average efficiencies for diesel with CAT alone, with the addition of SCR and MME with CAT, with addition SCR are 87.6, 71.5, 21.2 and 33.7%, respectively.

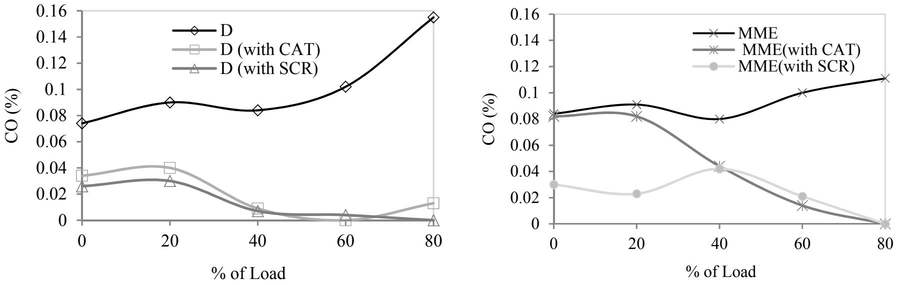

a) Diesel with different attachments b) MME with different attachments

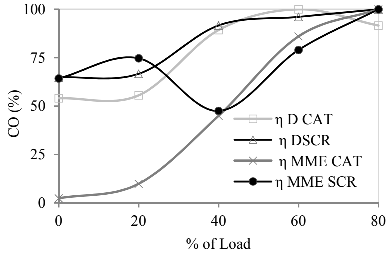

c) Conversion efficiencies of CAT and SCR with Diesel and MME

Fig. 5: Variation of CO with the load when fuelled with diesel and MME with and without attachments and the conversion efficiencies of attachments

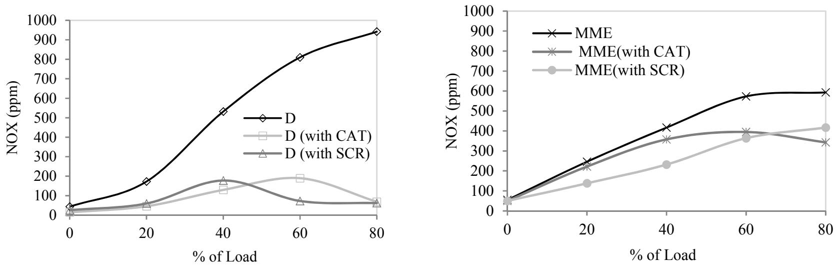

a) Diesel with different attachments b) MME with different attachments

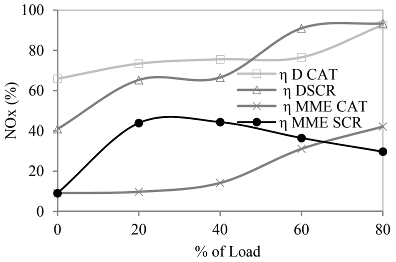

c) Conversion efficiencies of CAT and SCR with Diesel and MME

Fig. 6: Variation of NO_x with the load when fuelled with diesel and MME with and without attachments and the conversion efficiencies of attachments

Unburned Hydrocarbon (HC): Though, the HC emissions are relatively high with diesel the conversion efficiencies of the attachments did effectively in bringing down the HC (Figs. 7a to 7c). Originally, with MME and without attachments the HC emissions are lesser than diesel [6, 5]. The conversion efficiency of either with diesel or MME with the either CAT alone or CAT with SCR is above 60% at 80% full load operation [14].

Carbon Dioxide (CO_2): CO_2 emissions are almost same for diesel and diesel with SCR at near full load operations (Figs. 8a, 8b). There is a maximum of 2.3% difference of CO_2 emissions between diesel and MME at near full load operation and without any attachments. Fig. 8c reveals maximum oxidation of CO to CO_2 is taking place in the catalytic converter. The maximum conversion efficiencies of CO_2 observed with CAT alone and addition of SCR in diesel fuel operation were 54.8 and 19.6%, respectively.

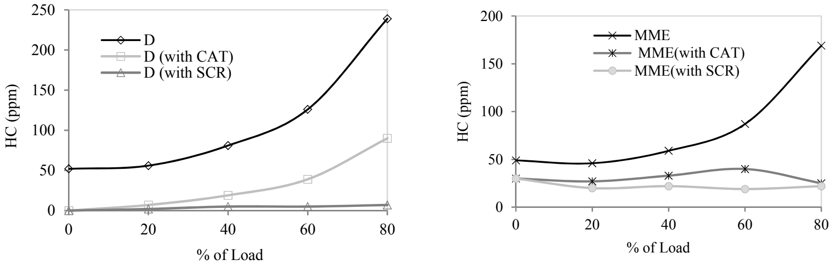

a) Diesel with different attachments b) MME with different attachments

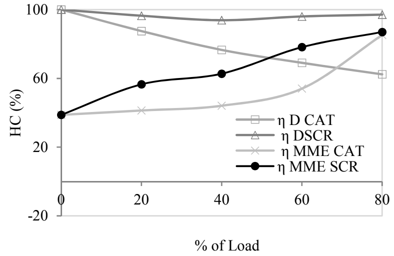

c) Conversion efficiencies of CAT and SCR with Diesel and MME

Fig. 7: Variation of HC with the load when fuelled with diesel and MME with and without attachments and the conversion efficiencies of attachments

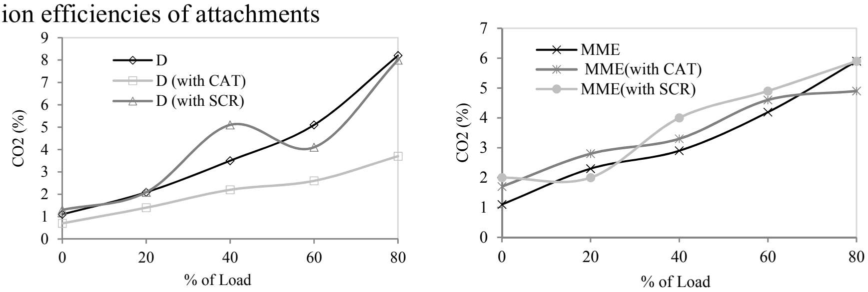

a) Diesel with different attachments b) MME with different attachments

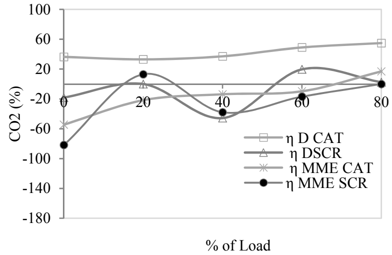

c) Conversion efficiencies of CAT and SCR with Diesel and MME

Fig. 8: Variation of CO_2 with the load when fuelled with diesel and MME with and without attachments and the conversion efficiencies of attachments

CONCLUSIONS

The study demonstrated the use of MME for the SCR designed for diesel engine operation. It is observed that the SCR performing well during diesel operations. Following are the conclusions made.

- MME consists of oxygen also as an element in its composition. Therefore, much reduced CO emissions and less HC emissions observed. Furthermore, it also attributed for the complete combustion of MME.
- The average surface temperature is lower in case of MME fuel burn. Therefore, less NO_X emissions recorded.
- The efficiency of CAT and SCR depends on the temperature of the operation. Hence, there is declining in the conversion efficiency of the after treatment attachments with the MME fuel operation.

REFERENCES

1. Ma, F. and M.A. Hanna, 1999. Biodiesel production: a review. Bioresource Technology, 70(1): 1-15.
2. Srivastava, A. and R. Prasad, 2000. Triglycerides-based diesel fuels. Renewable and Sustainable Energy Reviews, 4(2): 111-133.
3. Godiganur, S., C. Suryanarayana Murthy and R.P. Reddy, 2009. 6BTA 5.9 G2-1 Cummins engine performance and emission tests using methyl ester mahua (*Madhuca indica*) oil/diesel blends. Renewable Energy, 34(10): 2172-2177.
4. Lenin, A.H., R. Ravi and K. Thyagarajan, 2013. Performance characteristics of a diesel engine using mahua biodiesel as alternate fuel. Iranica Journal of Energy and Environment, 4(2): 136-141.
5. Solaimuthu, C. and P. Govindarajan, 2012. Effect of injection timing on performance, combustion and emission characteristics of diesel engine using mahua oil methyl ester as fuel. Journal of Scientific & Industrial Research, 71: 69-74.
6. Puhan, S., N. Vedaraman, G. Sankaranarayanan and B.V.B. Ram, 2005. Performance and emission study of Mahua oil (Madhuca indica oil) ethyl ester in a 4-stroke natural aspirated direct injection diesel engine. Renewable Energy, 30(8): 1269-1278.
7. Raheman, H. and S. Ghadge, 2007. Performance of compression ignition engine with mahua (*Madhuca indica*) biodiesel. Fuel, 86(16): 2568-2573.
8. Raheman, H. and S. Ghadge, 2008. Performance of diesel engine with biodiesel at varying compression ratio and ignition timing. Fuel, 87(12): 2659-2666.
9. Fable, S., F. Kamakate and S. Venkatesh, 2012. A sub-contractor report on Selective Catalytic Reduction Urea Infrastructure Study. NREL, NREL/SR-540-32689.
10. Fable, S., F. Kamakate, S. Venkatesh and A. Little, 2002. Selective Catalytic Reduction Urea Inferastructure Study. National Renewable Energy Laboratory, NREL/SR-540-32689.
11. Subbaiah, G.V., K.R. Gopal and S.A. Hussain, 2010. The Effect of Biodiesel and Bioethanol Blended Diesel Fuel on the Performance and Emission Characteristics of a Direct Injection Diesel Engine. Iranica Journal of Energy and Environment, 1(3): 211-221.
12. Shi, X., Y. Yu, H. He, S. Shuai, H. Dong and R. Li, 2008. Combination of biodiesel-ethanol-diesel fuel blend and SCR catalyst assembly to reduce emissions from a heavy-duty diesel engine. Journal of Environmental Sciences, 20(2): 177-182.
13. Lopez, J.M., F. Jimenez, F. Aparicio and N. Flores, 2009. On-road emissions from urban buses with SCR+ Urea and EGR+ DPF systems using diesel and biodiesel. Transportation Research Part D: Transport and Environment, 14(1): 1-5.
14. Sluder, C.S., J.M. Storey, S.A. Lewis and L.A. Lewis, 2005. Low temperature urea decomposition and SCR performance. SAE Paper, 1: 1858.
15. Hums, E., S. Liebsch and H. Zellbeck, 2004. Improvement on PM reduction using a catalyst based on $V_2O_5/WO_3/TiO_2$. Industrial & Engineering Chemistry Research, 43(25): 8001-8013.
16. Miller, W., J. Klein, R. Mueller and W. Doelling, 2000. The development of urea-SCR technology for US heavy duty trucks. Training, 2012: 09-05.
17. Gupta, K., A. Rehman and R. Sarviya, 2010. Evaluation of soya bio-diesel as a gas turbine fuel. Iranica Journal of Energy and Environment, 1(3): 205-210.
18. Rao, P.V., B.A. Rao and D. Radhakrishna, 2012. Experimental Analysis of DI Diesel Engine Performance with. Iranica Journal of Energy and Environment, 3(2): 109-117
19. Karnwal, A., N. Kumar, M. Hasan, R. Chaudhary, A.N. Siddiquee and Z.A. Khan, 2010. Production of biodiesel from thumba oil: optimization of process parameters. Iranica Journal of Energy and Environment, 1(4): 352-358.
20. V.W., P., 2012. TDI Clean Diesel Vehicle Travels 1626 Miles on One Tank of Fuel with SCR system standard.<http: / / scitechdaily. Com/vw-PASSAT-tdi-clean-diesel-vehicle-travels-1626-miles-on-one-tank-of-fuel/>.

Abbreviations, Acronyms, Notatiuons/Legends:

B20	:	20% biodiesel + 80% diesel
B100	:	Pure biodiesel
BTE	:	Brake Thermal Efficiency
CAT	:	Catalytic Converter
CO	:	Carbon monoxide
CO_2	:	Carbon dioxide
D	:	Diesel fuel
D (with CAT)	:	Diesel with Catalytic Converter
D (with SCR)	:	Diesel with Selective Catalytic Reduction system
DEF	:	Diesel Exhaust Fluid
DI	:	Direct Injection
DOC	:	Diesel Oxidation Catalyst
DPF	:	Diesel Particulate Filter
EGR	:	Exhaust Gas Recirculation
ESC	:	European Steady state Cycle
ETC	:	European Transient Cycle
HC	:	Hydrocarbons
LEV	:	Low Emission Vehicle
MME	:	Mahua Methyl Ester
MME (with CAT)	:	Mahua Methyl Ester with Catalytic Converter
MME (with SCR)	:	Mahua Methyl Ester with Selective Catalytic Reduction system
NAOH	:	Sodium Hydroxide
NO	:	Nitric oxide
NO_2	:	Nitrogen dioxide
NO_x	:	Oxides of Nitrogen
PM	:	Particulate Matter
ppm	:	Parts per million
O_2	:	Oxygen
SCR	:	Selective Catalytic Reduction
sfc	:	Specific fuel consumption
SUV	:	Sports Utility Vehicle
TDI	:	Turbocharged Direct Injection
η D CAT	:	Conversion efficiency of diesel with Catalytic Converter
η DSCR	:	Conversion efficiency of diesel with Selective Catalytic Reduction system
η MME CAT	:	Conversion efficiency of Mahua Methyl Ester with Catalytic Converter
η MME SCR	:	Conversion efficiency of Mahua Methyl Ester with Selective Catalytic Reduction system

Persian Abstract

DOI: 10.5829/idosi.ijee.2014.05.01.07

چکیده

قوانین سختگیرانه برای کاهش انتشار اکسیدهای نیتروژن (NO_X) منتشره از وسایل نقلیه دیزلی و همچنین تولید گازهای گلخانه ای بیودیزل منجر به توسعه فن آوری های جدید شده است. برای کاهش اکسیدهای نیتروژن استفاده از کاتالیست کاهشی (SCR) در مجرای گازهای خروجی (وسایل نقلیه) ، در برنامه های کوتاه مدت قابل استفاده می باشد. SCRs، ترکیبی از آمونیاک حاوی اوره را به عنوان یک عامل کاهنده استفاده می کند. در این مقاله یک تحقیق تجربی با استفاده از ترکیب اوره-SCR، برای مقایسه کارایی SCR بین سیستم دیزل و بیودیزل طراحی شده است. برای این مطالعه، از یک سیستم اگزوز SCR در حالت پایدار استفاده شده، که با تزریق مستقیم Kirloskar در موتور دیزل تک سیلندر مورد آزمایش قرار گرفته است. از روغن Mahua متیل استر (MME) به عنوان بیودیزل استفاده شده است. آزمایش ها، نشان داد که بازده تبدیل در سیستم دیزل در مقایسه با بیودیزل بالاتر بود. همچنین تحلیل دادها نشان می دهد که سیستم اوره-SCR ، حداکثر راندمان تبدیل ۹۳.۴٪ NO_X را در سوخت دیزل دارد. برای سیستم بیودیزل، حداکثر بازده تبدیل NO_X با استفاده از اوره-SCR حدود ۴۹٪ بوده است. این آزمایش همچنین نشان داد که سیستم اوره-SCR دارای راندمان تبدیل HC بسیار عالی در تمام بارهای موتور و با استفاده از هر دو نوع سوخت می باشد.

Iranica Journal of Energy & Environment 5 (1): 51-58, 2014
ISSN 2079-2115
IJEE an Official Peer Reviewed Journal of Babol Noshirvani University of Technology
DOI: 10.5829/idosi.ijee.2014.05.01.08

BUT

Dust Level Forecasting and its Interaction with Gaseous Pollutants Using Artificial Neural Network: A Case Study for Kermanshah, Iran

[1]A.A. Zinatizadeh, [2]M. Pirsaheb, [3]A.R. Kurdian,
[1]S. Zinadini, [4]A. Dezfoulinejad, [4]F. Yavari and [2]Z. Atafar

[1]Department of Applied Chemistry,
Faculty of Chemistry, Razi University, Kermanshah, Iran
[2]Health Research Center (KHRC), Kermanshah University of Medical Science, Iran
[3]Faculty of Chemical Engineering,
Sahand University of technology, Sahand New Town, East Azerbaijan, Iran
[4]Department of Environment, Kermanshah, Iran

(Received: January 24, 2014; Accepted in Revised Form: March 8, 2014)

Abstract: An artificial neural network (ANN) was used to forecast natural airborne dust as well as five gaseous air pollutants concentration by using a combination of daily mean meteorological measurements and dust storm occurrence at a regulatory monitoring site in Kermanshah, Iran for the period of 2007-2011. We used local meteorological measurementsand air quality data collected from three previous days as independent variables and the daily pollutants records as the dependent variables (response). Neural networks could be used to develop rapid air quality warning systems based on a network of automated monitoring stations. Robustness of constructed ANN acknowledged and the effects of variation of input parameters were investigated. As a result, dust had a decreasing impact on the gaseous pollutants level. The prediction tests showed that the ANN models used in this study have the high potential of forecasting dust storm occurrence in the region studied by using conventional meteorological variables.

Key words: Artificial neural network · Dust · Gaseous pollutants · Forecasting model

INTRODUCTION

Recent frequent occurrence of airborne ambient particulate matter inthe west of Iran has generated considerable public and academic interests and become a well-recognized problem in environmental sciences. The occurrence of dusty weather events is influenced by geological and climatic variations as well as human activities. The main sources of these dust storms are arid deserts of neighbor countries such as Iraq and Kuwait. In the time of dry climate condition, strong winds prevail in these areas, lifting large quantities of dust particles into the atmosphere and generating dust storms. Then these fine particulates can be transferred to Iran with a little reduction in concentration. These events lead to reduction of visibility, the deposition pof trace elements and the direct impact on human health via inhalation and require drastic measures such as the closing of the schools and factories and the restriction of vehicular traffic. The forecasting of such phenomena with up to two days in advance would allow taking more efficient countermeasures to safeguard citizens' health and even premature deaths among sensitive groups such as asthmatics and elderly people[1, 2].Over the past years, the health impact of airborne particulate matter (PM) has become a very topical subject. In the environmental sciences a lot of research effort goes towards the understanding of the PM phenomenon and the ability to forecast ambient PM concentrations[3]. A wide variety of operational warning systems based on empirical, causal, statistical and hybrid models have been developed in order to start preventive action before and during episodes [4].

Deterministic photochemical air quality models are commonly used for regulatory management and planning of urban air sheds. These models are complex, computer

---

Corresponding Author: A.A. Zinatizadeh, Department of Applied Chemistry,
Faculty of Chemistry, Razi University, Kermanshah, Iran.

intensive and hence are prohibitively expensive for routine air quality predictions. Stochastic methods are becoming increasingly popular as an alternative, which relegate decision making to artificial intelligence based on neural networks (NN) that are made of artificial neurons or 'nodes' capable of 'learning through training' via historic data [5]. Recently, several researchers started to check the capability of artificial neural network techniques to forecast airborne particulate matter concentrations. They conclude that a NN can be a useful tool to predict PM, although the accuracy they could reach is limited [6-8].

Niskaand coworkers [9] described evolving the neural network model for forecasting air pollution time series. They used a parallel genetic algorithm (GA) for selecting the inputs and designing the high-level architecture of a multi-layer perceptron model for forecasting hourly concentrations of nitrogen dioxide at a busy urban traffic station in Helsinki. Although their models were acceptable in low dust concentration, in all the cases, maximum fitness values of evaluated models were in of order 0.11.

A neural network forecast for daily average particulate matter concentrations in Belgium is developed by Jef and his co-workers [3]. The most important input variable found was the boundary layer height. The model based on this parameter serves to monitor the daily average threshold of 100 ìg/m³. Entering the other input parameters into the model increased the model accuracy [3]. Also, application of artificial neural networks to the prediction of dust storms in Northwest China, using a combination of daily mean meteorological measurements and dust storm occurrence was investigated [10]. The prediction tests showed that the ANN model used in this study has the potential of forecasting dust storm occurrence in Northwest of China by using conventional meteorological variables [10].

A neural network was used to predict particulate matter concentration at a regulatory monitoring site in Phoenix, Arizona. Its development, efficacy as a predictive tool and performance vis-à-vis a commonly used regulatory photochemical model are described by Fernando and his co-wrokers [5]. It was concluded that Neural Networks are much easier, quicker and economical to implement without compromising the accuracy of predictions. Neural Networks can be used to develop rapid air quality warning systems based on a network of automated monitoring stations.

In this study, relationship betweenthe local meteorological measurementsand air quality data collected from three previous days as independent variablesandthe daily pollutants records as the dependent variables was modeled by ANN approach. Filtering and the principle component analysis (PCA) methods are used to refine and reduce the data and number of input variables for introducing to the ANN model. Robustness of constructed ANN investigates and the effects of variation of input parameters are explored. Dust interaction on the other gaseous pollutants was also investigated.

MATERIALS AND METHODS

Artificial Neural Network (ANN): Artificial neural network (ANN) is a group of uncomplicated processing elements arranged in parallel layers, which are internally connected. Artificial neural networks are composed of simple elements operating in parallel layers which are internally connected. The singularity of ANN comes from its capability to be trained and generate interrelationships between observed input and output data without impracticalassumptions. ANN's architecture, activation or transfer function and training algorithm can group into different categories [11, 12]. The selection of the network architecture depends on task to be done specifying the neuron characteristics, network topology and learning algorithm [13]. The multi-layer feed forward back propagation is the simplest feed-forward network. In a standard architecture, neurons are grouped into different layers such as input, output and hidden layers. Fig. 1 shows a simple multilayer perceptron (MLP) model with input layer, one hidden layer containing three hidden neurons and one output layer. Another important factor in ANN design is the type of the transfer functions [14, 15]. A transfer function produces scalar neuron output according to weight, bias and neurons input. Hagen and Demuth [16]reported several transfer functions. The 'S' shape log-sigmoid transfer function as:

$$f(x) = \frac{1}{1+e^{-x}} \tag{1}$$

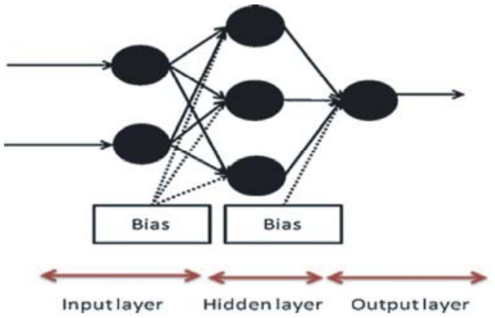

Fig 1: MLP with one hidden layer

is commonly used in multilayer networks that are trained using the back propagation algorithm. Algorithm training is a procedure determining the weights and biases of a network [16]. Such function which its derivatives could be expressed in term of a function may save training time because there is no need to repeat estimation of the derivatives [16].

Training algorithm is a procedure for determining the weights and biases of a network [16]. Due to the convergence speed and the performance of network, the Levenberg-Marquardt training method may be selected as a proper training algorithm. This is preferred compared to the other training techniques such as resilient back propagation, scaled conjugate gradient, variable learning rate back propagation and BFGS quasi-Newton. This is in agreement with the literature [17].

Data Collection: The data used in this study are the meteorological measurements and six air quality parameters collected from 2007 to 2011 in Kermanshah, Iran. Temperature (average, minimum and maximum), pressure, rain precipitation, sunny hours, snowing days, cloudiness value (at 6:30’, 12:30’ and 18:30’), relative humidity (at 6:30’,12:30’ and 18:30’), wind speed and direction were used as independent variables. Air quality data collected from three previous days including O_3, NO_2, NO_x, Dust, SO_2 and CO were also used as dependent variables and input for ANN. However, concentrations of O_3, NO_2, NO_x, Dust, SO_2 and CO on the fourth day were selected to be forecasted. Finally, 48 input vectors were prepared to introduce to ANN.

Modeling: To avoid the numerical overflow due to very large or very small weights, input data were normalized according to the following equation:

$$y = \frac{X - X_{mean}}{X_{std}} \tag{2}$$

where X_{mean} is mean value for each row of X and X_{std} is standard deviation for each row of X. The generated data via simulation were changed into the real values and were compared with the experimental results. In pollution prediction, the dimension of the input vectors is large due to high number of parameters affecting the pollution process. For the current case, a technique such as principle component analysis (PCA) is required to reduce the variables. In PCA redundancy in the initial number of variables is reduced and variables with the highest variance are grouped into the main components [18].

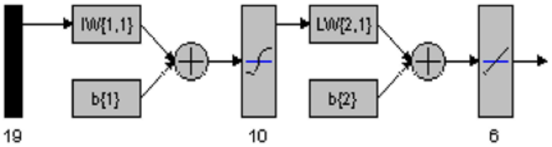

Fig 2: The structure of designed ANN

The preprocessing including filtering, normalization and PCA stages were performed before modeling which lead to the reduction of the number of variables to 19.

The schematic of system structure is depicted in Fig. 2. Filtering process used a moving average filter which the spanfor the moving average was 5. The main idea behind PCA is to derive a linear function consisting of several elements, for each of the vector variables. The variance of the linear function is maximized. The rows in PCA with contribution to total variation less than maximum fraction of variance are removed. Here maximum fraction of variance was considered 0.001.The input vector was used for ANNs to find an appropriate MLP architecture for predicting concentrations of O_3, NO_2, NO_x, Dust, SO_2 and CO on the fourth day. Model’s performance can be evaluated through different criteria. In this study root mean square error and R-square were selected for evaluation purposes. The root mean square error, RMSE, was calculated by:

$$RMSE = \sqrt{\frac{1}{N}\sum_{i=1}^{N}(a_i - t_i)^2} \tag{3}$$

where t_i is the real value from the field measurements, a_i is the predicted value by model and N is the number of data points. The R-square ranges from 0 to 1. A value closer to 1 indicates high model precision, i.e. a greater proportion of variance is accounted for by the model.

Through a trial- and error method, MLP neural network with one hidden layer were employed as the optimal network structure. The hidden layer consists of 10 neurons. They were used to transform the input data into the desired responses (concentrations of pollutants on the fourth day). With the aid of the hidden layer, any input-output map may be virtually approximated. The well-trained neural network can be used for prediction. Experimental data were divided into three sets for developing model in a random way, 1024 data (60%) for training, 340 data (20%) for validation and 340 data (20%) for querying. The training data were applied for learning process and the validation data were used for checking the over fitting, whereas the querying data were utilized for testing the model predictability. For the latter, the employed data were not a part of training and validation processes. In fact, validation set controls the over fitting problem during training of ANN. When the modeling error of training set decreases, the error of validation set is also decreased, otherwise the algorithm will stop.

RESULTS AND DISCUSSIONS

Kermanshah Air Quality: In the recent years, Kermanshah region has exposed dust phenomenon originated from westneighbor countries. Figures 3a-d summarize air quality of Kermanshah at 4 classes (non-standard, warning, emergency and critical) designated based on PSI (Table 1) in a 6.5-year period of monitoring. As presented in Fig. 3a, the urban air quality has been recorded as non-standard owing to dust phenomenon. This trend has been remarkably increased from 2008 on. Similar trend found for the other conditions (warning, emergency and critical) but with less values. The statistics given for emergency and critical conditions (Figs. 3c and d) are significant, implying that the events origin is being developed. Therefore, forecasting the dust occurrence along with its level and sustainability would be of importance in order to minimize the adverse impact of the event.

Modeling Results: Table 2 presents R-square and RMSE for the pollutants measured and RMSE for training, validation and test data. As shown in that table, the determination coefficient (R^2) was obtained to be in the range of 0.979 (for dust) to 0.992 (for O_3). The model shows enough accuracy for prediction of the pollutants concentrationon the day 4. The pollutants concentrationon 4th day (real and predicted values) versus timefor the monitoring duration (5 years) are presented in Figs. 4a-f, respectively for O_3, NO_2, NO_x, Dust, SO_2 and CO. The figures indicateavery good agreement between the actual and model data. In order to check the robustness of the ANN developed model, around 20% of the total data were utilized for predictability test of the model.

As can be seen in the figures, almost similar trend found forthe pollutants concentration measured. In overall, at high dust levels, the gaseous pollutantsremained at low levels. This correlation could be explained by the interactions between dust and gaseous pollutants.

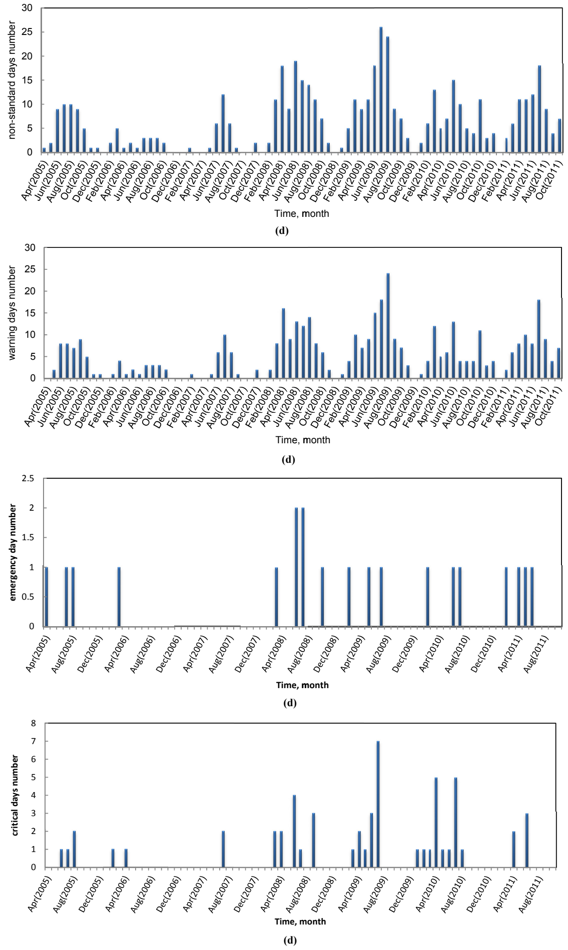

Fig. 3: Kermanshah air quality in 2005-2011

Table 1: Air quality classification based on PSI

PSI calculated based on Dust concentration (µg/m³)	Types of days
PSI≥100	Non-standard condition
100<PSI<250	Warning condition
250≤PSI<350	Emergency condition
PSI≥350	Critical condition

Table 2: Performance evaluation of ANN.

	O_3 (ppb)	NO_2 (ppb)	
NO_x(ppb)	Dust (µg/m³)	SO_2 (ppb)	CO
(ppm)			
R-Square	0.9923	0.9902	
0.9861	0.9797	0.9871	
0.9846			
RMSE	1.1743	1.3102	
2.7938	9.5671	1.5044	
0.1017			
RMSE	Train	Validation	
Test	4.1025	4.3333	
4.2416			

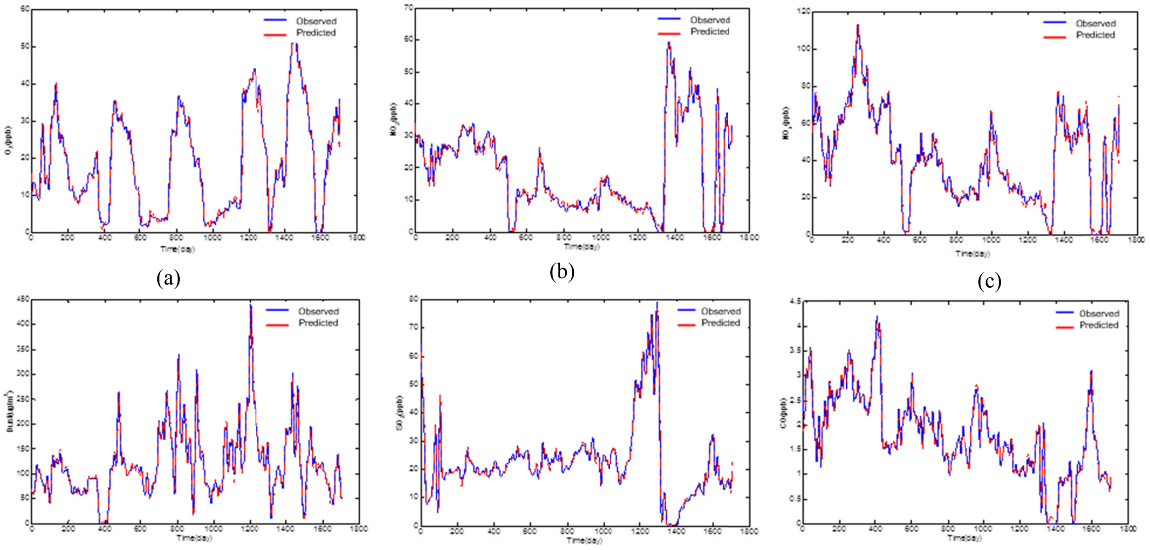

(a) (b) (c)

(d) (e) (f)

Fig. 4: ANN simulation results for (a) O_3, (b)NO_2, (c) NO_x, (d) Dust, (e) SO_2 and (f) CO, Kermanshah, Iran-2006-2011.

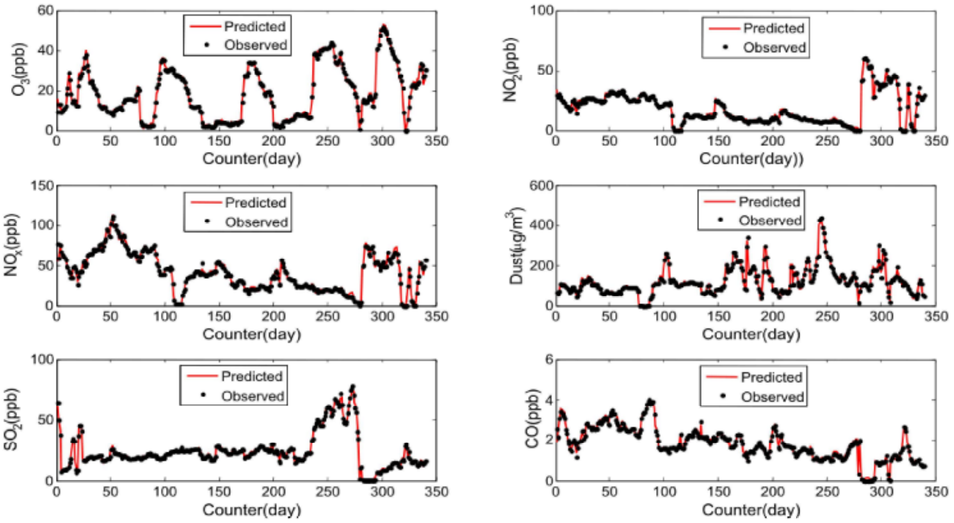

Fig. 5: Comparison between observed and ANN predicted data for test data set.

Fig. 5 illustrates a comparison for testing set between the experimental results and the ANN model prediction for the pollutants monitored. There is a high agreement between model prediction and the experimental data for the test data set, which were not used during model development.

In a research work carried out by Fernando and coworkers [5], they used ANN for air quality prediction. They found reasonable agreement between the calculated and observed values. Hooyberghs and coworkers [3] used neural network tool to forecast the daily average PM_{10} concentrations in Belgium. The most important input variable found was the boundary layer height. By extending the model with other input parameters they were able to increase the performance only slightly.

Wang and his coworkers [19] examined relationships between the formation and the movement of the dust storms in East Asia by numerical simulation and synoptic analysis of dust emission and transport. The simulated results are verified by observations and satellite images. It is found that the dust model has considerable skill in the prediction of Asian dust storms, but dust concentrations in regions of rainfall are generally overestimated as wet deposition was not considered in the model. An integrated dust storm modeling system was also developed by Sun and coworkers [20], for the prediction of dust storms. The system coupled a wind erosion scheme, a dust transportation model with a geographic information database. The system could be

Table 3: List of mean value of climate parameter and pollutant gases

Temperature							
Average	Maximum	Minimum	Pressure	Rain precipitation		Sunny Hours	
16.4	24.6	7.8	868.3	1		7.8	
Snowing days			Cloudiness Value			Relative Humidity %	
Snowing	Rainy	6.5	12.5	18.5	6.5	12.5	18.5
0	0	2	3	3	85	10	12
Wind (00-3:30)		Wind (03-6:30)		Wind (06-9:30)		Wind (09-12:30)	
Direction	Speed	Direction	Speed	Direction	Speed	Direction	Speed
Constant	0	Constant	0	Constant	0	SW	4
Wind(12-15:30)		Wind(15-18:30)		Wind(18-21:30)		Wind(21-00:30)	
Direction	Speed	Direction	Speed	Direction	Speed	Direction	Speed
W	4	W	4	W	4	Constant	0
O_3(ppb)	NO_2(ppb)	No_x(ppb)		Dust(µg/m^3)		SO_2(ppb)	CO (ppm)
18.6	18.8	41.2		121.4		22.8	1.8

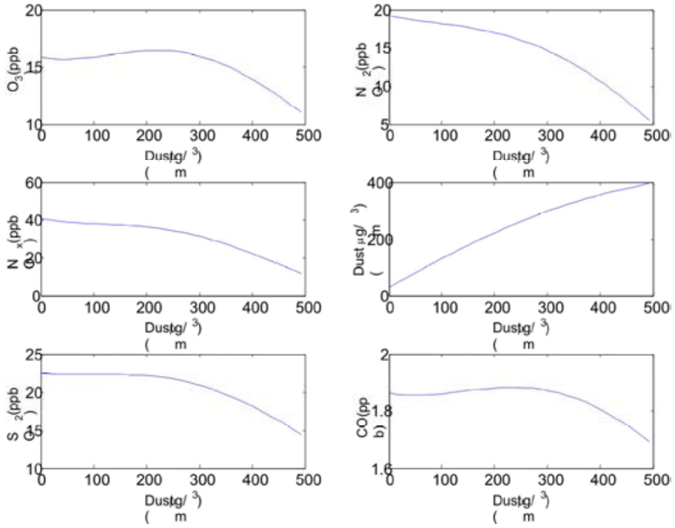

Fig. 6: Effects of increasing dust value on the gaseous pollutants at constant values of the other variables presented in Table 3.

used for the prediction of dust emission rate and dust concentration associated with individual dust storm events.

Interaction of Dust with the Gaseous Pollutants: In order to study dust interaction with the gaseous pollutants, all mean values of input data were evaluated. The values are listed in Table 3. In this table, metrological parameters includingtemperature, pressure, rain precipitation, sunny hours, snowing days, cloudiness value, relative humidity and direction and speed of wind during day and night (every 210 min) were selected to be studied. It must be noted that the pollutants data measured in three continuous days were also selected for the investigation.

The effect of increasing in dust on the pollutants measured is shown in Fig. 6. In this stage, the pollutantsvalues are the predicted values by ANN. Dust had a decreasing impact on the gaseous pollutants. As shown in the figure, increase in dust up to 400 µg/m^3, caused about 60 % decrease in the gaseous pollutants. It might be due to adsorption of the gaseous pollutants on the dust particles. This may be attributed to physical and chemical interaction of gases with functional groups of dust surface.Generally, The atmospheric chemical composition is affected by the interaction mechanisms among gases and particulate matter through a wide range of chemical reactions that can occur with the aid of particulate matter (e.g. particles act as reacting or absorbing surfaces) or be influenced by the presence of

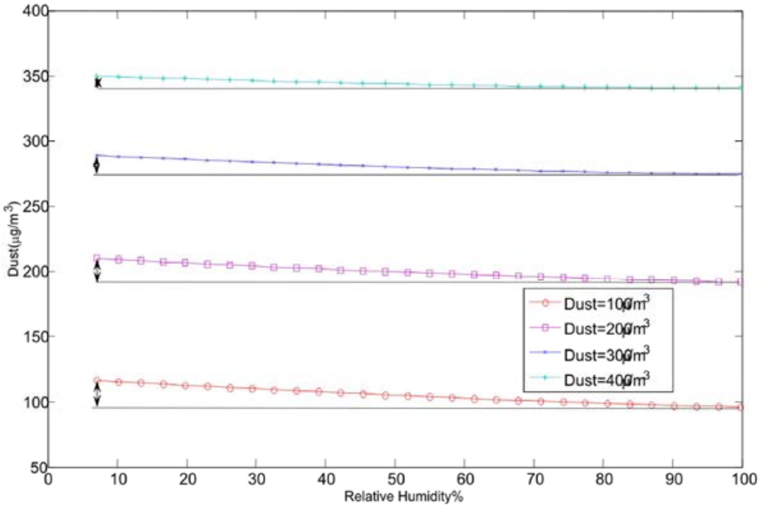

Fig. 7: Effects of relative humidity on dust at different initial values

particulate matter in the atmosphere (photochemical reactions). Physical and chemical processes are also bonded in an interactive way that often leads to the influence of the radiation budget, cloud physics and the warming or cooling of the lower atmospheric levels [18].

Another important parameter affecting the gaseous pollutants is relative humidity (RH) which has a controlling effect on reduction of dust pollution. In order to assess the effect of RH on dust levels, RH varied from 0 to 100 % at four different dust levels (100, 200, 300 and 400 μg/m^3). Fig. 7 represents the effect of RH on dust. The concentration of dust ispredicted by ANN. In this figure, this reduction is approaching to a constant value which means that relative humidity can only reduce a limited value of dust particles.Originally, humidity affect such that some dust particles coagulate and settle on the ground. As a result, it could be inferred that sensitivity of dust to relative humidity decreases with an increase in initial dust value.

Spellman [21] predicted surface ozone concentration using surface meteorological variable as predictors by a multi-layer perception neural network for five locations in the United Kingdom. He concluded that the relationship between weather and ozone is highly complex and non-linear in his studies.

CONCLUSION

Neural network model was useful and applicable for forecasting dust levels few days before dust storm occurrence as a reliable warning system for given sites. Selection of the variables by stepwise regression as the inputs of ANN model was a feasible methodology. The ANN model prediction showed a very good agreement with the actual data. The dust occurrence had a decreasing impact (up to 60 %) on the gaseous pollutants in the urban areas. Relative humidity (RH) and dust level also showed an interactive effect, a decrease in RH by increasing in dust and vice versa.

REFERENCES

1. Pope III, C.A., D.W. Dockery, J.D. Spengler and M.E. Raizenne, 1991. Respiratory health and PM10 pollution: a daily time series analysis. American Review of Respiratory Disease, 144(3): 668-674.
2. Tiitanen, P., K. Timonen, J. J Ruskanen, A. Mirme and J. Pekkanen, 1999. Fine particulate air pollution, resuspended road dust and respiratory health among symptomatic children. European Respiratory Journal, 13(2): 266-273.
3. Jef, H., M. Clemensa, D. Gerwinb, F. Fransb and B. Olivierc, 2005. A neural network forecast for daily average PM10 concentrations in Belgium. Atmospheric Environment, 39(18): 3279-3289.
4. Schlink, U., S. Dorling, E. Pelikan, G. Nunnari, G. Cawley, H. Junninen, A. Greig, R. Foxall, K. Eben and T. Chatterton, 2003. A rigorous inter-comparison of ground-level ozone predictions. Atmospheric Environment, 37(23): 3237-3253.
5. Fernando, H.J.S., M.C. Mammarella, G. Grandoni, P. Fedele, R.D. Marco, R. Dimitrova and P. Hyde, 2012. Forecasting PM10 in metropolitan areas: Efficacy of neural networks. Environmental Pollution, 163: 62-67.

6. Kukkonen, J., L. Partanen, A. Karppinen, J. Ruuskanen, H. Junninen, M. Kolehmainen, H. Niska, S. Dorling, T. Chatterton and R. Foxall, 2003. Extensive evaluation of neural network models for the prediction of NO_2 and PM_{10} concentrations, compared with a deterministic modelling system and measurements in central Helsinki. Atmospheric Environment, 37(32): 4539-4550.
7. Lu, W., W. Wang, X. Wang, Z. Xu and A. Leung, 2003. Using improved neural network model to analyze RSP, NOx and NO_2 levels in urban air in Mong Kok, Hong Kong. Environmental monitoring and assessment, 87(3): 235-254.
8. Ordieres, J., E. Vergara, R. Capuz and R. Salazar, 2005. Neural network prediction model for fine particulate matter ($PM_{2.5}$) on the US-Mexico border in El Paso (Texas) and Ciudad Juárez (Chihuahua). Environmental Modelling & Software, 20(5): 547-559.
9. Niska, H., T. Hiltunen, A. Karppinen, J. Ruuskanen and M. Kolehmainen, 2004. Evolving the neural network model for forecasting air pollution time series. Engineering Applications of Artificial Intelligence, 17(2): 159-167.
10. Huang, M., G. Peng, J. Zhang and S. Zhang, 2006. Application of artificial neural networks to the prediction of dust storms in Northwest China. Global and Planetary change, 52(1): 216-224.
11. Chen, H. and A.S. Kim, 2006. Prediction of permeate flux decline in crossflow membrane filtration of colloidal suspension: a radial basis function neural network approach. Desalination, 192(1): 415-428.
12. Sahoo, G.B. and C. Ray, 2006. Predicting flux decline in crossflow membranes using artificial neural networks and genetic algorithms. Journal of membrane science, 283(1): 147-157.
13. Zhao, Y., J.S. Taylor and S. Chellam, 2005. Predicting RO/NF water quality by modified solution diffusion model and artificial neural networks. Journal of membrane science, 263(1): 38-46.
14. Rai, P., G. Majumdar, S. DasGupta and S. De, 2005. Modeling the performance of batch ultrafiltration of synthetic fruit juice and mosambi juice using artificial neural network. Journal of food engineering, 71(3): 273-281.
15. Shokrian, M., M. Sadrzadeh and T. Mohammadi, 2010. C_3H_8 separation from CH_4 and H_2 using a synthesized PDMS membrane: Experimental and neural network modeling. Journal of Membrane Science, 346(1): 59-70.
16. Hagan, M.T., H.B. Demuth and M.H. Beale, 1996. Neural network design: Pws Pub. Boston.
17. Al-Abri, M. and N. Hilal, 2008. Artificial neural network simulation of combined humic substance coagulation and membrane filtration. Chemical Engineering Journal, 141(1): 27-34.
18. Astitha, M. and G. Kallos, 2009. Gas-phase and aerosol chemistry interactions in South Europe and the Mediterranean region. Environmental fluid mechanics, 9(1): 3-22.
19. Wang, W. and Z. Fang, 2006. Numerical simulation and synoptic analysis of dust emission and transport in East Asia. Global and planetary change, 52(1): 57-70.
20. Sun, J., L. Zhao, S. Zhao and R. Zhang, 2006. An integrated dust storm prediction system suitable for East Asia and its simulation results. Global and Planetary Change, 52(1): 71-87.
21. Spellman, G., 1999. An application of artificial neural networks to the prediction of surface ozone concentrations in the United Kingdom. Applied Geography, 19(2): 123-136.

Persian Abstract

DOI: 10.5829/idosi.ijee.2014.05.01.08

چکیده

پیش گویی گرد وغبار با منشاء طبیعی و همچنین غلظت پنج آلاینده گازی با استفاده از اطلاعات جمع آوری شده از متوسط روزانه پارامترهای هواشناسی و پدیده گرد وغبار در ایستگاه پایش هوای کرمانشاه-ایران در دوره ۲۰۰۷-۲۰۱۱ با بهره گیری از یک شبکه هوش مصنوعی انجام شد. برداشت های هواشناسی محلی و داده های کیفیت هوای مربوط به سه روز گذشته بعنوان متغیرهای مستقل و اطلاعات روزانه از آلاینده ها بعنوان پاسخ استفاده شدند. به منظور ایجاد سیستم های هشدار دهنده بر مبنای اطلاعات ایستگاههای پایش، شبکه عصبی می تواند استفاده شود. اطمینان پذیری شبکه عصبی مصنوعی ارایه شده تایید شد و اثرات تغییر پارامترهای ورودی مورد بررسی قرار گرفت. بعنوان نتیجه گیری، گرد و غبار اثر کاهشی بر غلظت آلاینده های گازی نشان داد. آزمایشات مربوط به پیش بینی نشان داد که مدلهای شبکه عصبی استفاده شده در این مطالعه، قابلیت بالایی در پیشگویی رخدادهای گرد و غبار در منطقه مورد مطالعه دارند.

Iranica Journal of Energy & Environment 5 (1): 59-66, 2014
ISSN 2079-2115
IJEE an Official Peer Reviewed Journal of Babol Noshirvani University of Technology
DOI: 10.5829/idosi.ijee.2014.05.01.09

BUT

Xylanase, Laccase and Manganese Peroxidase Production from White Rot Fungi

[1,2]Rabia Saleem, [1]Mohsin Khurshid and [2]Safia Ahmed

[1]Department of Biosciences, University of Wah, Wah Cantt, Pakistan
[2]Department of Microbiology, Faculty of Biological Sciences,
Quaid-i-Azam University, Islamabad, Pakistan

(Received: January 8, 2014; Accepted in Revised Form: March 14, 2014)

Abstract: Xylanase, laccase and manganese peroxidase (MnP) were produced and optimized by three strains of white rot fungi *Phanerochaete sordida* MRL3, *Lentinus pigrinus* MRL6 and *Poliporus caliatus* MRL7. These strains were initially isolated from wood decaying samples and then screened on minimal salt media,xylanase activities for the above strains were 55, 77.4 and 64.8 IU/mL, respectively. In addition, laccase activities were 80.65, 112.91 and 101.61 U/L, respectively. The activities forMnP were 123, 182.6 and 106.6 U/L, respectively. The maximum xylanase activity was observed at pH: 5.0, 30°C after 216 hours of incubation period. The maximum activities were 272.7, 278.52 and 292.8 IU/mL and the total protein was 1.24, 1.2 and 1.16 mg/mL, respectively. The maximum laccase activity was observed after 192-216 hours of incubation period, at pH: 5.0 on 30°C, the activities were 483.9, 516.4 and 459.67 U/L and the total protein 1.03, 1.2 and 1 mg/ml, respectively. The MnP activities were observed after 192-216 hours, at pH: 5.0 on 30°C, the activities were 588.66, 645.16 and 585.27 U/L and the total protein 1, 1.1 and 0.96 mg/mL, respectively.

Key words: Enzyme Production · White Rot Fungi · Hemicelluloses · Xylan · Lignin

INTRODUCTION

Lignocellulosic materials are widespread in nature and xylan is a polysaccharide found in hemicellulosic fraction of lignocellulose. Xylan is a potential significant resource for renewable biomass, which can be utilized as a substrate for the preparation of many products such as fuels, solvents and pharmaceuticals. On the other hand, xylanases are needed for making use of hemicelluloses. For most bioconversion processes, xylan must first be converted to xylose or xylo-oligosaccharides. There are several applications of xylanases in industry [1]. Xylanases are used in the prebleaching of kraft pulp to reduce the use of harsh chemicals in the subsequent chemical bleaching stages. The enzymatic treatments improve the chemical liberation of lignin by hydrolysing residual xylan. This reduces the need for chlorine-based bleaching chemicals, which is beneficial for the environment [2]. Currently, the major applications of xylanases are in pulp and paper, feed and baking industries [3].

Lignin, a complex and heterogeneous aromatic biopolymer in woody and herbaceous plants, is one of the most abundant naturalpolymers on earth. White rot fungi are primarily responsible forinitiating the depolymerization of lignin in wood [4]. The extracellular lignolytic enzyme system of white rotfungi has been studied extensively in recent years. Lignin peroxidase,manganese peroxidase (MnP) and laccase are associated with thedegradation of lignin. Several attempts to bleach hardwood kraftpulp by means of enzyme treatment have been reported. Arbeloa *et al.* [5] have showed that treatment of unbleached kraft pulp withlignin peroxidase facilitated subsequent chemical bleaching.

Many efforts have been made to utilize enzymes for the degradation of lignin in the pulp and paper industry. One enzyme known to play a major role in natural delignification is laccase (benzenediol: oxygen oxidoreductase) [6]. The enzyme was first identified in the sap of the Japanese lacquer tree *Rhusvernicifera* [7] Among the large blue copper containing enzymes, laccase is the most widely distributed [8] and

Corresponding Author: Mohsin Khurshid, Department of Biosciences, University of Wah, WahCantt, Pakistan.
Tel: +92-3334301513.

occurs in various plants and fungi [9]. In the fungi, *Deutromycetes, Ascomycetes* and a wide range of *Basidiomycetes* are known producers of laccases, which are particularly abundant in many lignin-degrading white-rot fungi.

MATERIALS AND METHODS

Microorganism: Five strains of white rot fungi were used initially in this research project supplied byMicobiology laboratory Quaid-i-Azam University, Islamabad; known as *Phanerochaete chrysosporium* MRL1, *Phanerochaete sordida* MRL3, *Sterium hirsutum* MRL4, *Lentinus pigrinus* MRL 6 and *Poliporus caliatus* MRL7.

Culture Refreshment: Five strains of white rot fungi were refreshed thrice time on Malt-extract agar pH: 5.

Screening of Laccase, Manganese Peroxidase and Xylanase: The initial screening minimal salt medium (Yeast extract: 10g, Citric acid: 0.25g, Ammonium sulphate: 5g, K_2HPO_4: 0.26g, $MgSO_4.7H_2O$: 0.5g, $CaCl_2.2H_2O$: 0.02g and Streptomycin: 0.03g/L) with 2% wheat straw was used for detecting the ability of the white rot fungi strains to produce laccases, Mn-peroxidases and xylanases was used according to method developed in the literature [10] with some modifications.

Measurement of Xylanase, Laccase and Manganese Peroxidase Activities: Activity of xylanase was determined by the method described by Tuncer, *et al.* [11] against birchwoodxylan. Laccase activity was measured by using 5mM 2, 6-dimethoxy phenol (DMP) as substrate in 100mM sodium tartarate buffer pH: 4.5. Laccase activity was measured according the method stated in literature [10]. Manganese peroxidase (MnP) was assayed by using 2,6-Dimethoxy phenol (DMP) as substrate. MnP activity was measured by the method discussed in the literature [12].

Media Used for Xylanase, Laccase and MnP Production: Kim media was used for the production of xylanase against three strains of white rot fungi, (Proteous-peptone: 0.5g, Urea: 0.3g, KH_2PO_4: 0.2g, $CaCl_2$: 0.3g, Tween-80: 0.2, $(NH_4)_2SO_4$: 1.4g, $MgSO_47H_2O$: 0.3g, $FeSO_4$: 0.05g, $ZnSO_47H_2O$: 0.014g, $CoCl_2$: 0.02g and $MnSO_4$: 0.016g/L) described in the literature [13] whichwas used with some modification for growth and enzyme production according the method stated in literature [14]. For laccase production media (Soy meal: 30g, Maltose and 15g, Mycological Peptone: 15g/L) discussed in the literature [15] was used for growth and enzyme production, against three strains of white rot fungi. Medium described by [15] was used for MnP production with some modification for growth and enzyme production (Soy meal: 15g, Maltose: Mycological Peptone: 6g and Wheat straw: 8g/L).

Inoculum Preparation: 50mL medium was dispensed into 250mL conical flask. Medium was given steam autoclaving for 15 minutes at 121°C and 15 psi. The inoculum was allowed to grow at 30°C on orbital shaker (120rev/min) for 3-5 days.

Growth Conditions: 1 liter flask was filled with 225mL medium of (pH: 5). Inoculum at 10% (v/v) level was transferred to each growth flask and put into incubator on 30°C at speed 120 rev/min for 7-9 days. Initial and final pH was between 5 and 6.8.

pH Optimization for the Maximum Production of Xylanase, Laccase and MnP: pH of the liquid medium in each flask containing 100mL of medium was adjusted to pH values of 3.0, 4.0, 5.0, 6.0 and 7.0. Sample taken after every 24 hours was analyzed for enzyme activities. Final pH of samples was also noted.

Incubation Period for the Maximum Production of Xylanase, Laccase and MnP: Production of extracellular enzymes was carried out at a range of temperatures 25, 30 and 37°C. Production medium was incubated at different temperatures. Samples were collected and assayed for enzyme activities and dry cell weight was also estimated.

Time Optimization for the Maximum Production of Xylanase, Laccase and MnP: Three strains of white-rot fungi *Phanerochaete sordida* MRL3, *Lentinus pigrinus* MRL 6 and *Poliporus caliatus* MRL7 were incubated at optimum pH and temperature for 1½ week. Samples were collected after every 24 h assayed for enzyme activities and dry cell weight was also estimated.

Large scale production of these enzymes: After optimization, these enzymes were produced in 3liters flasks for biobleaching purpose. 110mL of Malt-extract media was prepared in 500mL flasks and with three strains of white rot fungi, the inoculum was allowed to grow at 120 revolutions/minutes on 30°C for 4-5day. 1100mL of production media of these three enzymes were prepared in 3 liters flasks and inoculated with 10% inoculum size and incubated on 30°C in orbital shaker for 7-9 days. Assayed for enzyme activities and protein was also estimated.

RESULTS

Initially 5 strains of white rot fungi were screened for xylanase, laccase and MnP activities on minimal salt media with 2% wheat straw. *Phanerochaete sordida*MRL3, *Lentinus pigrinus*MRL6 and *Poliporus caliatus*MRL7 were screened on the basis of their activities. Xylanase activities shown by these three strains were 55.0, 77.40 and 64.83 IU/mL, respectively. Laccase activities shown by these three strains were 80.65, 112.91 and 101.61 U/L, respectively. Manganese peroxidase activities shown by these three strains were 123.0, 182.62 and 106.65 U/L, respectively.

Effect of pH on the Production of Xylanase, Laccase and MnP: It is evident from (Figures 1, 2 and 3) that maximum xylanase production was obtained after 216 hours by *P. sordida* MRL3, *L. pigrinus* MRL6 and *P. caliatus* MRL7. Activities were observed 272.74, 278.52 and 292.86 IU/mL, respectively at pH: 5.0. Maximum laccase production was observed after 216 hours at pH: 5.0. Activities were 483.9 U/L after 192 hours, 516.4 U/L after 192 hours and 459.67 U/L. Maximum MnP production was observed at pH: 5.0 after 216 hours, activities were 588.66 U/L after 216 hours, 645.16 U/L after 192 hours and 585.27 U/L. There was decrease in activity with further increase or decrease in pH.

Effect of Temperature on the Production of Xylanase, Laccase and MnP: The optimum temperature for maximum xylanase production was found by growing *Phanerochaete sordida* MRL3, *Lentinus pigrinus* MRL6 and *Poliporus caliatus* MRL7 at different temperatures i.e. 25, 30 and 37°C keeping 1% wheat straw at pH: 5.0 on rotary incubator shaker. It was found that optimum temperature for xylanase production was 30°C; maximum activity was obtained after 216 hours of incubation period. The activities were 272.74, 278.52 and 292.86 IU/mL, respectively.

Maximum laccase production was obtained after 216 hours of incubation period at 30°C; activities were 483.9 U/L after 192 hours, 516.4 U/L after 192 hours and 459.67 U/L after 216 hours, respectively.

It was observed that maximum MnP production was obtained at 30°C after 216 hours of incubation period. The activities of *Phanerochaete sordida* MRL3, *Lentinus pigrinus* MRL6 and *Poliporus caliatus* MRL7 were 588.66 U/L after 216 hours, 645.16 U/L after 192 hours and 585.27 U/L after 216 hours, respectively.

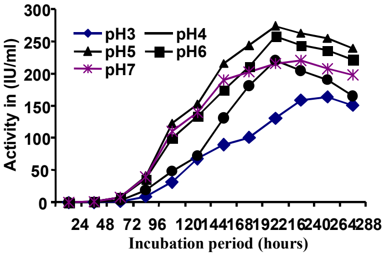

Fig. 1: Effect of pH on the specific activity of Xylanase in shake flask culture with 10% inoculum size on 30°C, in rotary shaker by *P. sordida* MRL3

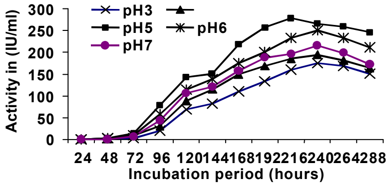

Fig. 2: Effect of pH on the specific activity of Xylanase in shake flask culture with 10% inoculum size at 30°C, in rotary shaker by *L. tigrinus*.

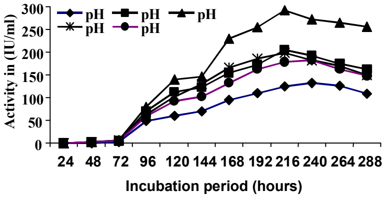

Fig. 3: Effect of pH on the specific activity of Xylanase in shake flask culture with 10% inoculum size at 30°C, in rotary shaker by *P. caliatus* MRL7.

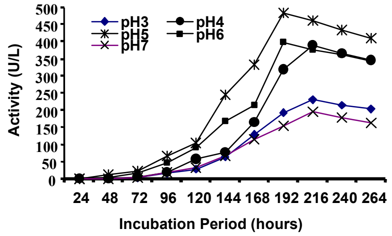

Fig. 4: Effect of pH on the specific activity of laccase in shake flask culture with 10% inoculum size at 30°C, in rotary shaker by *Phanerochaete sordida* MRL3.

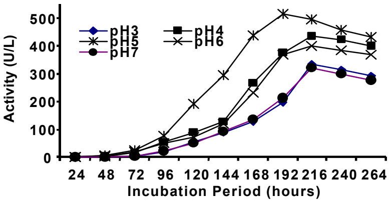

Fig. 5: Effect of pH on the specific activity of laccase in shake flask culture with 10% inoculum size at 30°C, in rotary shaker by *Lentinus pigrinus* MRL6.

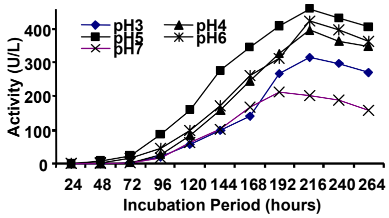

Fig. 6: Effect of pH on the specific activity of laccase in shake flask culture with 10% inoculum size at 30°C, in rotary shaker by *Poliporus caliatus* MRL7.

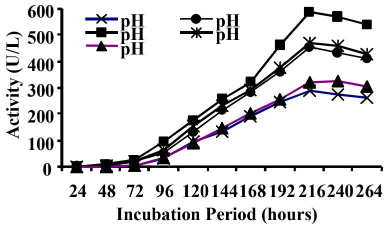

Fig. 7: Effect of pH on the specific activity of MnP in shake flask culture with 10% inoculum size at 30°C, in rotary shaker by *Phanerochaete sordida* MRL3.

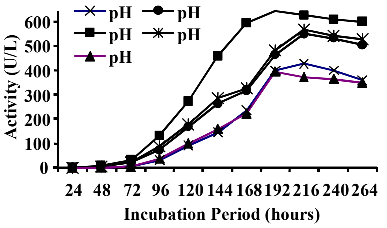

Fig. 8: Effect of pH on the specific activity of MnP in shake flask culture with 10% inoculum size at 30°C, in rotary shaker by *Lentinus pigrinus* MRL6.

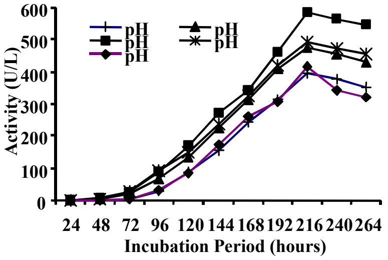

Fig. 9: Effect of pH on the specific activity of MnP in shake flask culture, with 10% inoculum size on 30°C, in rotary shaker by *Poliporus caliatus* MRL7.

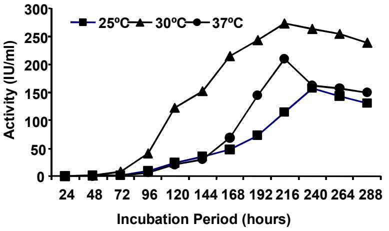

Fig. 10: Effect of Temperature on the specific activity of Xylanase at pH: 5, 10% inoculum size in rotary shaker by *P. sordida* MRL3.

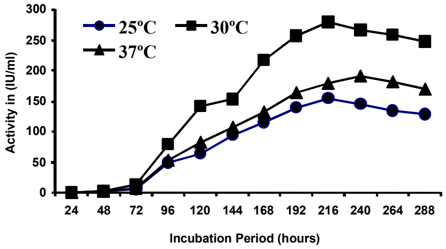

Fig. 11: Effect of Temperature on the specific activity of Xylanase in shake flask culture at pH: 5, 10% inoculum size in rotary shaker by *Lentinus pigrinus* MRL6.

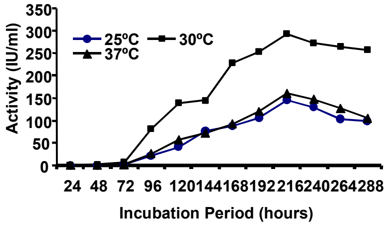

Fig. 12: Effect of Temperature on the specific activity of Xylanase at pH: 5, 10% inoculum size in rotary shaker by *Poliporus caliatus* MRL7.

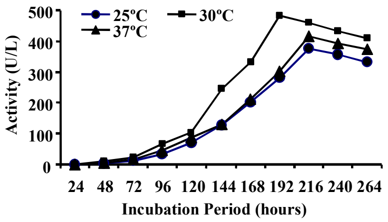

Fig. 13: Effect of Temperature on the specific activity of laccase in shake flask culture at pH: 5, 10% inoculum size in rotary shaker by *Phanerochaete sordida* MRL3.

Effect of Incubation Period on Production of Xylanase, Laccase and MnP: The maximum specific activity by *Phanerochaete sordida* MRL3 was 272.74 IU/mL and the total protein 1.24 mg/mL was observed after 216 hours of incubation period. The maximum specific activity by *Lentinus pigrinus* MRL6 was observed after 216 hours of incubation period, maximum activity was 278.52 IU/mL and the total protein was 1.2 mg/mL. The maximum specific activity by *Poliporus caliatus* MRL7 was 292.86 IU/mL and the total protein 1.16 mg/mL was observed after 216 hours of incubation period.

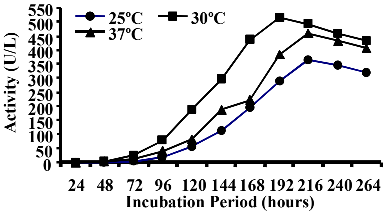

Fig. 14: Effect of Temperature on the specific activity of laccase in shake flask culture at pH: 5, 10% inoculum size in rotary shaker by *Lentinus pigrinus* MRL6.

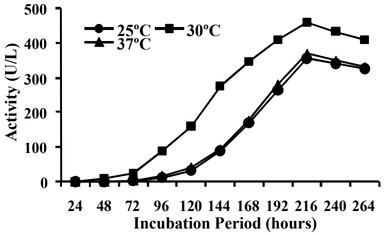

Fig. 15: Effect of Temperature on the specific activity of laccase in shake flask culture at pH: 5, 10% inoculum size in rotary shaker by *Poliporus caliatus* MRL7

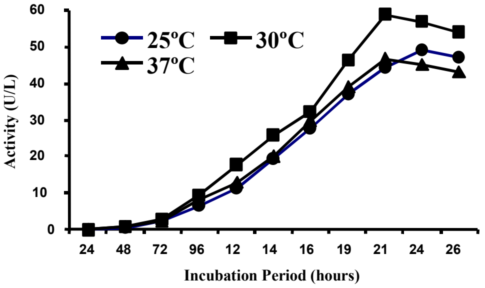

Fig. 16: Effect of Temperature on the specific activity of MnP in shake flask culture at pH: 5, 10% inoculum size in rotary shaker by *Phanerocheate sordida* MRL3.

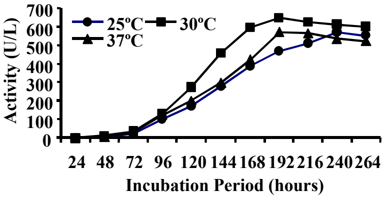

Fig. 17: Effect of Temperature on the specific activity of MnP in shake flask culture at pH: 5, 10% inoculum size in rotary shaker by *Lentinus pigrinus* MRL6.

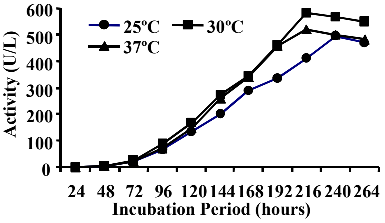

Fig. 18: Effect of Temperature on the specific activity of MnP in shake flask at pH: 5, 10% inoculum size in rotary shaker by *Poliporus caliatus* MRL7.

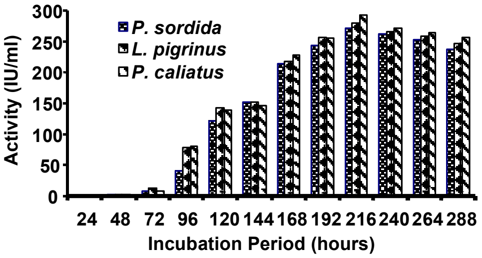

Fig. 19: Effect of Incubation period on the specific activity of Xylanase in shake flask culture at pH: 5, 10% inoculum size in rotary shaker on 30°C by *Phanerochaete sordida* MRL3, *Lentinus pigrinus* MRL6 and *Poliporus caliatus* MRL7.

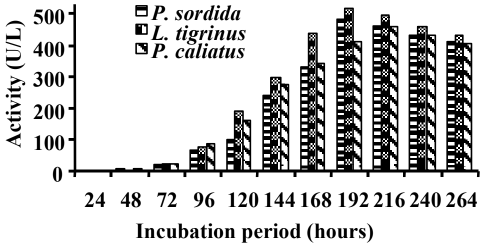

Fig. 20: Effect of Incubation period on the specific activity of laccase in shake flask culture at pH: 5, 10% inoculum size in rotary shaker at 30°C by *Phanerochaete sordida*MRL3, *Lentinus pigrinus* and *Poliporus caliatus* MRL7.

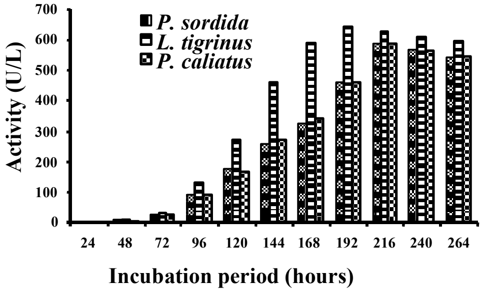

Fig. 21: Effect of Incubation period on the specific activity of MnP in shake flask culture at pH: 5, 10% inoculum size in rotary shaker on 30°C by *P. sordida* MRL3, *L. tigrinus* MRL6 and *P. caliatus* MRL7.

The maximum specific activity by *Phanerochaete sordida* MRL3 was 483.9 U/L and the total protein 1.03 mg/mL was observed after 192 hours of incubation period. The maximum specific activity by

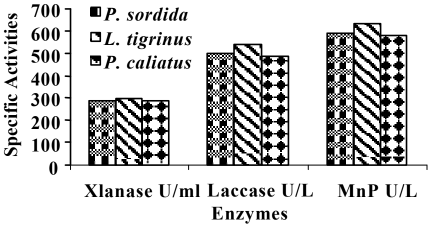

Fig. 22: Production of Xylanase, Laccase and MnP in 1liter flask at pH: 5, 10% inoculum size in rotary shaker on 30°C by *P. sordida* MRL3, *L. tigrinus* MRL6 and *P. caliatus* MRL7.

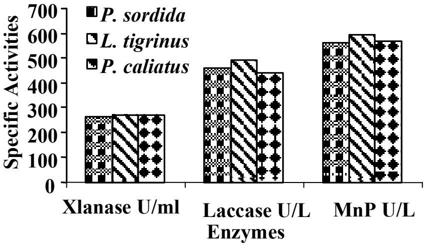

Fig. 23: Production of Xylanase, Laccase and MnP in 3liter flask at pH: 5, 10% inoculum size in rotary shaker on 30°C by *P. sordida* MRL3, *L. tigrinus* MRL6 and *P. caliatus* MRL7.

Lentinus pigrinus MRL6 was 516.4 U/L and the total protein 1.2 mg/mL was observed after 192 hours of incubation period. The maximum specific activity by *Poliporus caliatus* MRL7 was 459.67 U/L and the total protein 1 mg/mL was observed after 216 hours of incubation period.

The maximum specific activity of MnP by *Phanerochaete sordida* MRL3 was observed, 588.66 U/L and the total protein was 1 mg/mL after 216 hours of incubation period. The maximum specific activity by *Lentinus pigrinus* MRL6 was 645.16 U/L and the total protein 1.1 mg/mL was observed after 192 hours of incubation period. The maximum specific activity by *Poliporus caliatus* MRL7 was 585.27 U/L and the total protein 0.96 mg/mL was observed after 216 hours of incubation period.

Large Scale Enzymes Production: After optimization in 250mL flasks, these enzymes were produced in 1liter and 3liters flasks. Xylanase production in 1 liter flask by *P. sordida, L. tigrinus and P. caliatus*, xylanase activities were 287, 295 and 284 IU/mL, respectively. While laccase production in 1 liter flasks by these strains were 496, 540 and 490 U/L, respectively. In case of MnP activities were 586, 632 and 580 U/L, respectively.

In case of 3 liters flask production of these enzymes by *P. sordida, L. tigrinus and P. caliatus*, xylanase activities were 264, 272 and 269 IU/mL, respectively. While laccase activities were 460, 489 and 440 U/L, respectively. TheMnP activities were 560, 592 and 565 U/L, respectively.

DISCUSSION

Xylanase, laccase and manganese peroxidase were produced and optimized by three strains of white rot fungi *P. sordida* MRL3, *L. tigrinus* MRL6 and *P. caliatus* MRL7. Five strains of white rot fungi were screened on minimal salt media with 2% wheat straw for the production of xylanase, laccase and manganese peroxidase activity, these strains were initially isolated from wood decaying samples. These strains were shown high levels of xylanase, laccase and MnP activities. White rot fungi were isolated from woodlands were screened for xylanase, laccase and MnPactivies on minimal salt media, maximum strains showed activities for these enzymes [10]. Three hundred fugal strains were screened for lignin modifying enzymes, some of these strains showed maximum activities of these enzymes [16].

Maximum xylanase production was observed with Kim media, after 216 hours by *P. sordida* MRL3, *L. tigrinus* MRL6 and *P. caliatus* MRL7. A wild strain of *Aspergillus nidulans* isolated from soil produce cellulase-free xylanase activity when developed on submerged cultures using corn cob powder as the main substrate. Maximum xylanase production (220 U/mL) was obtained when the strain was developed in mineral medium supplemented with 3% (w/v) corn cob for 6 days [17].

Xylanase activity was maximally obtained at pH: 5.0 by these three strains. Xylanase was produced by *Thermomyces lanuginosus*, maximum production was observed between pH 5.5 and 9.5. In another study xylanase was produced by *Aspergillus nidulans*, with optimal activity at pH values between 5 and 6 [17].

The optimum temperature for maximum xylanase production was found 30°C. Extracellular xylanase produced by thermophilic fungus *Paecilomyces themophila,* maximum activity was observed at 50 °C [18].

Laccase was produced by *P. sordida* MRL3, *L. pigrinus* MRL6 and *P. caliatus* MRL7, maximum activity was observed with 3% soy meal, 1.5% maltose and 1.5% mycological peptone. Barley bran gave the

Table 1: Xylanase, laccase and Manganese peroxidase activity of different white rot fungi

Strains of white-rot fungi	Xylanase activity in IU/mL	Laccase activity in U/L	Manganese peroxidase activity in U/L
P. chrysosporium MRL1	20.6	11	88.57
P. sordida MRL3	55.0	80.65	123.0
S. hirsutum MRL 4	0.8	14	48.98
L. tigrinus MRL 6	77.4	112.91	182.62
P. caliatus MRL7	64.8	101.61	106.65

highest activities, a maximum value of 639U/L, which was 10 times the value attained in the cultures without lignocellulosics addition [19]. Maltose (2 g L^{-1}) and ammonium tartrate (10 g L^{-1}) were the most suitable carbon and nitrogen source for laccase production. Under optimal culture medium, the maximum laccase activity was determined to be 13.55 U mL^{-1} [20].

Optimum pH for laccase production was at pH: 5.0. When fungi were grown in a medium with pH as optimal for growth (pH: 5.0) the laccase was produced in excess [7]. Laccase produced by *T. modesta* was fully active at pH 4.0 [21].

Maximum laccase activity was observed at 30°C after 216 hrs (9 days) by these three strains. Laccase and manganese peroxidase were detected in liquid medium with ammonium phosphate, yeast extract and ammonium molybdate as nitrogen sources after 3 days of cultivation. Laccase optimal temperature was 45°C [22].

MnP production was optimized for pH, temperature and incubation time, maximum specific activity was observed by *Phanerochaete sordida* MRL3, *Lentinus pigrinus* MRL6 and *Poliporus caliatus* MRL7 at pH: 5.0 at 30 °C after 216 hrs incubation periods. Theproduction of MnP by *Pleurotus ostreatus* in different liquid cultures was investigated. The highest level of activity was observed after 8 days [23].

CONCLUSION

By screening among the white rot fungi; suitable strains were identified for production of xylanase, laccase and manganese peroxidase. Maximum active units enzymes for the desired media compositions, pH and incubation period at optimal temperature were obtained.

REFERENCES

1. Subramaniyan, S. and P. Prema, 2002. Biotechnology of microbial xylanases: enzymology, molecular biology and application. Critical Reviews in Biotechnology, 22(1): 33-64.
2. Viikari, L., M. Tenkanen and A. Suurnäkki, 2001. Biotechnology in the pulp and paper industry. Biotechnology Set, Second Edition, Wiley.
3. Beg, Q., M. Kapoor, L. Mahajan and G. Hoondal, 2001. Microbial xylanases and their industrial applications: a review. Applied Microbiology and Biotechnology, 56(3-4): 326-338.
4. Gold, M.H., H. Wariishi and K. Valli, 1989. Extracellular Peroxidases Involved in Lignin Degradation by the White Rot. Biocatalysis in Agricultural Biotechnology, 389: 127-140.
5. Arbeloa, M., J. De Leseleuc, G. Goma and J.C. Pommier, 1992. An evaluation of the potential of lignin peroxidases to improve pulps. Tappi Journal, 75(3): 215-221.
6. Call, H. and I. Mücke, 1997. History, overview and applications of mediated lignolytic systems, especially laccase-mediator-systems (Lignozym®-process). Journal of Biotechnology, 53(2): 163-202.
7. Thurston, C.F., 1994. The structure and function of fungal laccases. Microbiology, 140(1): 19-26.
8. Leontievsky, A.A., T. Vares, P. Lankinen, J.K. Shergill, N.N. Pozdnyakova, N.M. Myasoedova, N. Kalkkinen, L.A. Golovleva, R. Cammack and C.F. Thurston, 1997. Blue and yellow laccases of ligninolytic fungi. FEMS Microbiology Letters, 156(1): 9-14.
9. Bourbonnais, R., M. Paice, I. Reid, P. Lanthier and M. Yaguchi, 1995. Lignin oxidation by laccase isozymes from Trametes versicolor and role of the mediator 2, 2'-azinobis (3-ethylbenzthiazoline-6-sulfonate) in kraft lignin depolymerization. Applied and Environmental Microbiology, 61(5): 1876-1880.
10. Muzariri, C.C., J. Mapingire, J. Mazorodze and L. Mandikutse, 2001. Isolation and screening of microorganisms for potential application in remediation of effluent water from the pulp and paper industry. 2nd WARFSA/WaterNet Symposium: Integrated Water Resources Management: Theory. Practice, Cases, pp: 242-250.

11. Tuncer, M.r., A.S. Ball, A. Rob and M.T. Wilson, 1999. Optimization of extracellular lignocellulolytic enzyme production by a thermophilic actinomycete *Thermomonospora fusca*BD25. Enzyme and Microbial Technology, 25(1): 38-47.
12. Gold, M.H. and J.K. Glenn, 1988. Manganese peroxidase from *Phanerochaete chrysosporium.* Methods in Enzymology, 161: 258-264.
13. Kim, J.H., M. Hosobuchi, M. Kishimoto, T. Seki, T. Yoshida, H. Taguchi and D.D. Ryu, 1985. Cellulase production by a solid state culture system. Biotechnology and Bioengineering, 27(10): 1445-1450.
14. Rezende, M.I., A.d.M. Barbosa, A.F.D. Vasconcelos and A.S. Endo, 2002. Xylanase production by Trichoderma harzianum rifai by solid state fermentation on sugarcane bagasse. Brazilian Journal of Microbiology, 33(1): 67-72.
15. Heinzkill, M., L. Bech, T. Halkier, P. Schneider and T. Anke, 1998. Characterization of laccases and peroxidases from wood-rotting fungi (family Coprinaceae). Applied and Environmental Microbiology, 64(5): 1601-1606.
16. Dhouib, A., M. Hamza, H. Zouari, T. Mechichi, M. Labat, M. Martínez and S. Sayadi, 2005. Autochthonous fungal strains with high ligninolytic activities from Tunisian biotopes. African Journal of Biotechnology, 4(5): 431-436.
17. Reis, D., M. Costa and R.M. Peralta, 2003. Xylanase production by a wild strain of Aspergillus nidulans. Acta Scientiarum: Biol. Sci., 25: 221-225.
18. Yang, S., Q. Yan, Z. Jiang, L. Li, H. Tian and Y. Wang, 2006. High-level of xylanase production by the thermophilic *Paecilomyces themophila* J18 on wheat straw in solid-state fermentation. Bioresource Technology, 97(15): 1794-1800.
19. Lorenzo, M., D. Moldes, S. Rodrýguez Couto and A. Sanroman, 2002. Improving laccase production by employing different lignocellulosic wastes in submerged cultures of *Trametes versicolor.* Bioresource Technology, 82(2): 109-113.
20. Wang, J., J. Wu, W. Huang and R. Tan, 2006. Laccase production by *Monotospora sp.*, an endophytic fungus in *Cynodon dactylon.* Bioresource Technology, 97(5): 786-789.
21. Nyanhongo, G., J. Gomes, G. Gübitz, R. Zvauya, J. Read and W. Steiner, 2002. Production of laccase by a newly isolated strain of*Trametes modesta.* Bioresource Technology, 84(3): 259-263.
22. Cavallazzi, J.R.P., M.G.D.A. Oliveira and M.C.M. Kasuya, 2004. Laccase production by Lepista sordida. Brazilian Journal of Microbiology, 35(3): 261-263.
23. Kamitsuji, H., Y. Honda, T. Watanabe and M. Kuwahara, 2004. Production and induction of manganese peroxidase isozymes in a white-rot fungus Pleurotus ostreatus. Applied Microbiology and Biotechnology, 65(3): 287-294.

Persian Abstract

DOI: 10.5829/idosi.ijee.2014.05.01.09

چکیده

در این تحقیق، زایلاناز، laccase و پراکسیداز منگنز (MNP) توسط سه گونه از قارچ پوسیدگی سفید *Phanerochaete sordida* MRL3، *Lentinus pigrinus* MRL6 و *Poliporus caliatus* MRL7 تولید و بهینه سازی شد. در ابتدا این گونه از نمونه های چوب پوسیده جدا شد و پس از آن در محیط کشت هایی با حداقل نمک غربالگری شده اند، فعالیت های زایلاناز برای سویه های بالا ۵۵، ۷۷.۴ و ۶۴.۸ IU/mL بود. علاوه بر این، فعالیت های laccase، ۸۰.۶۵، ۱۰۱.۶۱، و ۱۱۲.۹۱ U/L می باشد. میزان فعالیت برای منیزیم اکسید ۱۲۳، ۱۸۲.۶ و ۱۰۶.۶ می باشد. حداکثر فعالیت زایلاناز در pH، ۵، و دمای ۳۰ °C بعد از ۲۱۶ ساعت از گرمخانه گذاری مشاهده شده است. حداکثر فعالیت ۲۷۲.۷، ۲۷۸.۵۲ و ۲۹۲.۸ IU/mL و پروتئین کل ۱.۲۴، ۱.۲ و ۱.۱۶ mg/mL بود. فعالیت حداکثر laccase بعد از ۱۹۲-۲۱۶ ساعت از دوره کمون، مشاهده شد در pH، ۵ و دمای ۳۰ °C ، فعالیت ۴۸۳.۹، ۵۱۶.۴ و ۴۵۹.۶۷ U/L بود و مجموع پروتئین ۱.۰۳، ۱.۲ و ۱ mg/mL بود. فعالیت های MNP بعد از ۱۹۲-۲۱۶ ساعت، در pH، ۵، و دمای ۳۰ °C مشاهده شد، فعالیت های ۵۸۸.۶۶، ۶۴۵.۱۶ و ۵۸۵.۲۷ U/L بود و مجموع پروتئین ۱، ۱.۱ و ۰.۹۶ mg/mL بود.

Iranica Journal of Energy & Environment 5 (1): 67-72, 2014
ISSN 2079-2115
IJEE an Official Peer Reviewed Journal of Babol Noshirvani University of Technology
DOI: 10.5829/idosi.ijee.2014.05.01.10

BUT

Simulation and Optimization of LNG Production Unit for Energy Conservations

Ali Tarjoman Nejad and Ali Farzi

Department of Chemical Engineering, University of Tabriz, P.O. Box: 5166616471, Tabriz, Iran

(Received: January 6, 2014; Accepted in Revised Form: March 14, 2014)

Abstract: The prospect of LNG could become a major global energy source is one of the most debated issues. The Liquefied Natural Gas (LNG) supply chain and the properties that make this fuel environmental friendly is in high demand for energy supply. In this paper, at first, the process of converting the natural gas to LNG was simulated; then, the process is optimized to archive minimum energy consumption per ton of LNG produced. Using a three stage exchanger is the best way for minimization of energy consumption in LNG production unit. Outlet pressure from the compressor and also type of refrigerant in cooling system is very effective on rate of energy conservations. The best mass fraction for refrigerants in liquefaction cycle are 0.88 for methane and 0.12 for ethane. For subcooling cycle that fraction is defined as 0.6 for methane and 0.4 for nitrogen. The optimized pressure in outlet of compressors in liquefaction cycle is 650 kPa; also, for the subcooling cycle is 1800 kPa. The amount of consumed energy was 14.91 kW per ton of produced LNG.

Key words: Natural gas · LNG · Energy optimization · Simulation · Refrigeration cycle

INTRODUCTION

For production of LNG the natural gas is cooled down to temperature of -161°C. In this case, the gas turned to an odorless and transparent liquid with density about 450 kg/m^3. The gas volume is reduced to 1/600 with liquefaction which economizes transportation of natural gas [1].

LNG is an environmental friendly fuel and this factor together with economic factors causes this fuel to be very important and be pursued [1]. LNG market in Asia, Northern America and Europe progressively developed in past decades [2]. For production of LNG, the natural gas temperature should decrease to -161 °C while the pressure has to increase to 5 bar.

Various refrigerants can be used for LNG process. The best and the most available ones are: R-22, methane, ethane and nitrogen [3]. In this work, these refrigerants have been used for the liquefaction of natural gas.

Process Description: LNG exchanger should be used for cooling natural gas temperature to -161 °C. Three stage exchangers can be used for this purpose. In first stage which is precooling stage, natural gas is cooled down to -40°C. In the second stage which is liquefaction stage, natural gas is cooled to -90 °C. Finally, in the third stage which is subcooling stage, natural gas is cooled down to -161 °C [4].

The plate-fin heat exchanger are often used to achieve such temperature. A brazed aluminium plate-fin heat exchanger consists of a block of alternating layers of corrugated fins. The layers are separated from each other by parting sheets and sealed along the edges by means of side bars and are provided with inlet and outlet ports for the streams. The block is bounded by cap sheets at top and bottom. The minimum design temperature for this heat exchanger is -269°C [4].

In general, fluids should be clean, dry and noncorrosive to aluminium. Trace impurities of H_2S, NH_3, CO_2, SO_2, NO_2, CO, Cl_2 and other acid-forming gases do

---

Corresponding Author: Ali Tarjoman Nejad, Department of chemical Engineering, University of Tabriz, P.O. Box: 5166616471, Tabriz, Iran.
Tel: +98-411-3393158, Cell: +98-937-7786511.

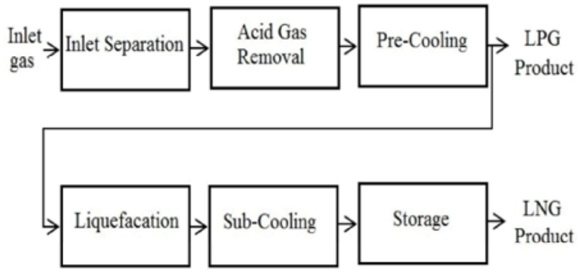

Fig. 1: The actual process flow diagram

not create corrosion problem in streams with water dew point temperatures lower than the cold-end temperature of the brazed aluminium plate-fin heat exchanger [5]. Acid gas removal is performed first to reduce carbon dioxide levels to around 50 ppm. To remove CO_2 from natural gas, amine tower can be used [6]. The process flow diagram of LNG production is shown in Fig. 1.

Precooling: In precooling stage, R-22 has been used as a refrigerant and J-T valves are also used. The J-T valve can be designed for any pressure drop.Joule-Thomson effect is made by using j-t valve. When Joule-Thomson coefficient is positive, a drop in pressure means a drop intemperature. In this situation Joule-Thomson coefficient for R-22 will be positive. So, Temperature in the cycle will decrease.

Inlet natural gas feed is in temperature of 25 °C and the pressure of 7 bar. In inital stage, the temperature is reduced to -40 °C. The temperature cannot be reduced to lower than the stated temperature using R-22. In this stage, a flash drum is used for the separation of LPG gas. In flash drum, water is separated in addition to LPG. In order to prevent freezing of water in the subsequent stages, separation of water is very important in the cryogenic process. It is curcial for water vapor content compressed gas should be reduced to lower than 1ppmv [7].

Liquefaction: In this stage, one LNG exchanger with three streams is used. Although one refrigerant can be used for cooling, but use of mixture of two refrigerants is more desired, because it guarantees more ranges for existence of two phases [8]. The first stream is a mixture of methane and ethane. This stream is a part of stage which includes a compressor, a chiller and a turbine. The second stream is a mixture of nitrogen and methane. It is cooled in the LNG exchanger for using in third exchanger i.e. subcooling stage.

In second stage, the first stream enters to the compressor for increasing its pressure, then it enters into a chiller for the reduction of its temperature. At last, it enters into a turbine and then enters LNG exchanger.

Subcooling: In the third stage, the stream enters a compressor for increasing its pressure, then it enters the first LNG exchanger of its precooling. Then, it enters a turbine and its pressure is reduced and finally it enters the second LNG exchanger. In this stage, the temperature of refrigerants stream should be -165 °C in order to reduce the temperature of natural gas to -161 °C.

Boil-off Gas (BOG) is the vapor phase in LNG tanks. The increase in BOG will lead to an increase in pressure of LNG tank, as the specific volume of gas is much larger than that of liquid form. It seems that BOG can be a serious problem for LNG storage tanks [9].

At the end of the process, LNG enters the storage tanks where 5% of LNG is evaporated. Boil-off gas is compressed to the pressure of natural gas and is recycled and added to the feed.

Simulation: ASPEN HYSYS software was used for the simulation of LNG production unit. Because, in this simulation available components are hydrocarbon and nonpolar, Peng Robinson equation of state is used for thermodynamic calculations [10]. The simulation environment for the process is shown in Fig. 2. The properties of produced LNG are summarized in Table 1.

Optimization: The effective parameters on energy consumption should be recognized for the optimization of consumed energy. The kind of refrigerant important in consumed energy. For the stages it is more desired to use the refrigerants in such a way that temperature ranges of the stages have optimal performance. It is suitable to use more than one refrigerant in the stage to increase the range of existence two phases. Two refrigerants of methane and ethane are appropriate for liquefaction stage while two refrigerants of methane and nitrogen are appropriate for subcooling stage. This choice is due to high efficiency of these refrigerants within the temperature ranges of stages. The best mass fraction of refrigerants should be specified for both cycles. The consumed energy per ton of LNG versus the mass fraction of the refrigerants for liquefaction and subcooling cycles are shown in Figs. 3 and 4.

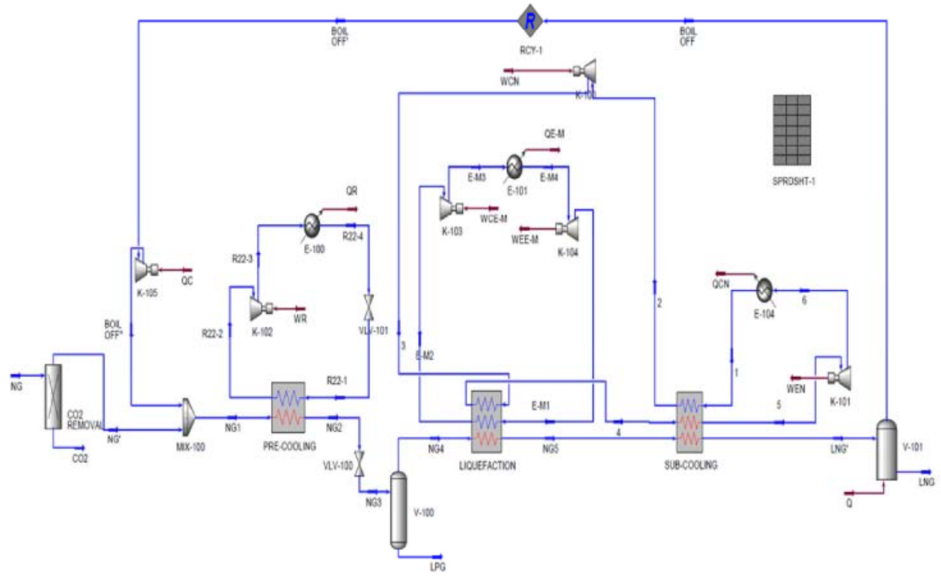

Fig. 2: LNG unit simulation enviroment

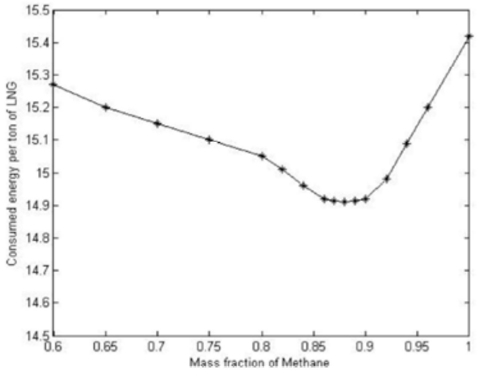

ig. 3: Consumed energy per ton of produced LNG vs the mass fraction of Methane in liquefaction cycle

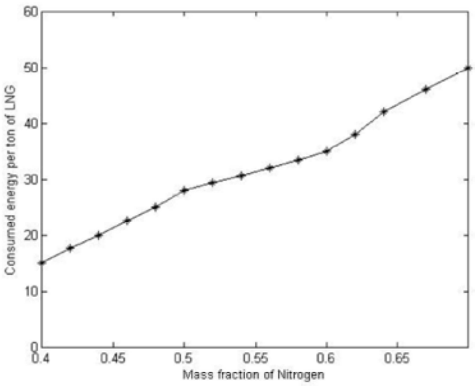

Fig. 4: Consumed energy per ton of produced LNG vs the mass fraction of Nitrogen in sub-cooling cycle

Table 1: The properties of prouduced LNG obtained by simulation

Parameters	Value
vapor phase fraction	0
Temprature (°C)	-160
Pressure (kPa)	500
mass density (kg/m^3)	458.357
mass heat capacity (kJ/kg.C)	3.192
Viscocity (cP)	0.113
Thermal conductivity (W/m.k)	0.186
Mass heat of vaporization (kCal/kg)	156.047

The results showed that the best mass fraction of refrigerants in liquefaction stage defined as 0.88 for methane and 0.12 for ethane. In subcooling stage, consumed energy decreases with decreasing of nitrogen mole fraction, but LNG exchanger can't act properly for mass fractions lower than 0.4 and temperature cross is occurred in the exchanger. Therefore, the mass fraction of nitrogen was considered to be 0.4. In Table 2 shows the mass fraction of refrigerants for liquefaction and subcooling stages.

The outlet pressure of compressor has very important effect on energy consumption. When the pressure increases, the turbine outlet temperature can be reduced, but this leads to an increase in energy consumption of compressor [11]. When the pressure is reduced, more energy in chiller is required. Therefore, the optimized pressure should be considered for the stages. In Fig. 5 depicts the consumed energy per ton of

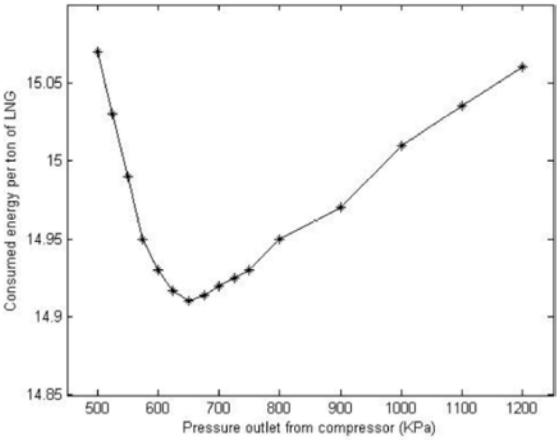

Fig. 5: Consumed energy vs the outlet pressure from compressor for liquefaction cycle

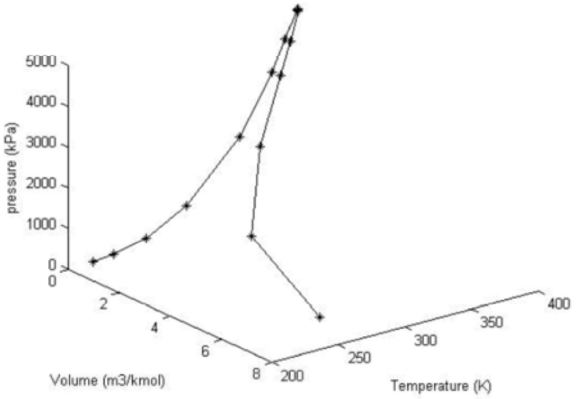

Fig. 6: PVT diagram for precooling cycle

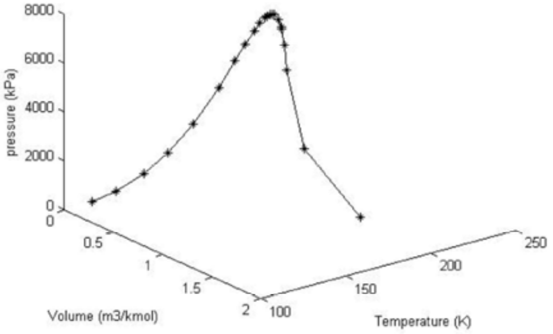

Fig. 7: PVT diagram for liquefaction cycle

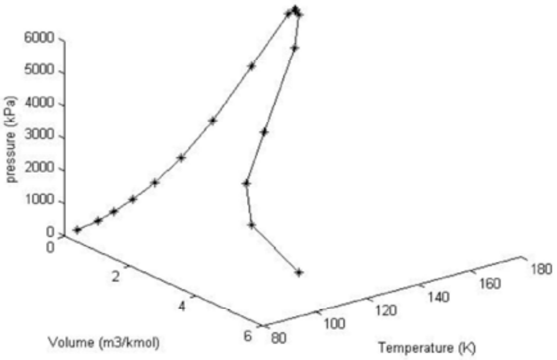

Fig. 8: PVT diagram for subcooling cycle

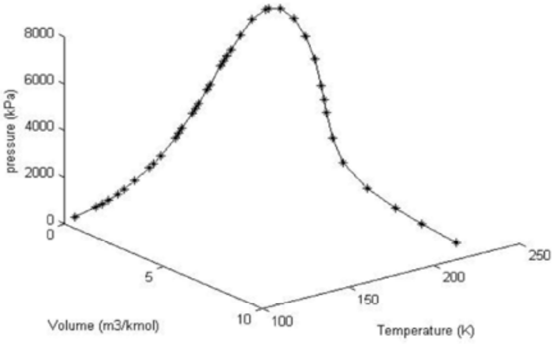

Fig. 9: PVT diagram for final LNG product

Table 2: Optimal refrigerants mass fraction obtaind by ASPEN HYSYS

Stage	Refrigerant	Mass fraction
liquefaction	Ethane	0.12
	Methane	0.88
Subcooling	Nitrogen	0.4
	Methane	0.6

Table 3: Specifications of streams in liquefaction stage

Variables	E-M1	E-M2	E-M3	E-M4
Vapor fraction	0.963	1	1	1
Temperature (°C)	-115.1	-112.7	-78.2	-103.3
Pressure (kPa)	400	390	700	700

Table 4: Specifications of streams in subcooling stage

Variables	1	2	3	4	5	6
Vapor fraction	0.345	0.999	1	1	1	1
Temperature (°C)	-165	-150.4	-71.8	-60	-74	-126.8
Pressure (kPa)	400	390	1800	1790	1780	420

produced LNG versus the outlet pressure of the compressor for liquefaction stage. The optimized pressure for this compressor is 650 kPa.

In subcooling stage, the compressor outlet pressure should be high, because of the refrigerants are needed in very low temperature. In this situation, the least possible pressure for prevention of temperature crosses in LNG exchanger and reach to the desired temperature is 1800 kPa. If the pressure increases to high value, then the consumed energy will also increase. The temperature and pressure of each of the streams in liquefaction and subcooling stages are summarized in Tables 3 and 4. At optimal conditions, amount of consumed energy per ton of LNG is 14.91 kW.

Table 5: Comparison between various designs

Design	Process	Compression Eff. %	kW/ton
Conoco Phillips	Optimized Cascade Refrigeration	100	14.1
Prico	Single Mixed Refrigeration	100	16.8
Dual TEX Cycle	Turbo-Expander	100	16.5
Kryopak EXP	Turbo-Expander	100	15.5
This work	Three stage exchanger - Mixed Refrigeration	75	14.91

In Figs. 6 to 8, PVT diagram for precooling, liquefaction and subcooling cycles are shown. According to the presented data, with the increasing number of materials in stream, two-phase region is broader. Operating Temperature cycles from the first to the third cycle is reduced. In Fig. 9, PVT diagram for final LNG product is shown. The final product is in liquid zone.

In this paper simulated design is compared with some conventional processes. This comparison is shown in Table 5. Only ConocoPhillips method has less energy consumption, but the energy consumption for this process is calculated in 100% compression efficient while in this design the efficiency is intended to 75%. So the design has lower energy consumption in real situation.

CONCLUSIONS

Using a three stage exchanger is the best arrangements for the optimization of energy consumption in LNG production unit. The outlet pressure from the compressor and the kind of refrigerants are very effective on energy consumption. Energy consumption can be reduced by obtaining the optimized pressure for the compressor and by obtaining the best mass fractioin for the refrigerants. The best mass fraction of refrigerants in the liquefaction stage is 0.88 for methane and 0.12 for ethane and for subcooling stage is 0.6 for methane and 0.4 for nitrogen. The optimal outlet pressure from the compressor in liquefaction and subcooling stages were 650 and 1800 kPa, respectively. In this optimal condition, consumed energy per ton of LNG is 14.91 kW.

REFERENCES

1. Aoki, I. and Y. Kikkawa, 1995. Technical efforts focus on cutting LNG plant costs. Oil and Gas Journal, 93(27).
2. Kikkawa, Y., M. Nakamura and S. Sugiyama, 1997. Development of liquefaction process for natural gas. Journal of Chemical Engineering of Japan, 30(4): 625-630.
3. Geist, J., 1985. Refrigeration cycles for future base-load LNG plants need a close look.Oil and Gas Journal, 83(5).
4. Habibullah, A., P. Lardi and M. Passmore, 2009. LNG conceptual design strategies. in The 88th GPA Annual Convention in San Antonio, TX. 2009.
5. ALPEMA, 2000. The standard of the brazed aluminium plate-fin heat exchanger manufacturers association. Second Edition.
6. Lorn, W. Liquefied Natural Gas, 1974, Applied Science Publishers Ltd, Barking.
7. Jamieson, D., P. Johnson and P. Redding, Targeting and achieving lower cost liquefaction plants. in Twelfth International Conference and Exhibition on Liquefied Natural Gas, Perth, Australia. 1998.
8. Haywood, R., 1990. Analysis of Engineering Cycles, 1990, Pergamon Press, Oxford.
9. Aimikhe, V., B. Kinigoma and E. Iyagba, 2013. Predicting the Produced Boil off Gas in the Moss Spherical Liquefied Natural Gas (LNG) Vessel. in *SPE Nigeria Annual International Conference and Exhibition*. 2013. Society of Petroleum Engineers.
10. Carlson, E.C., 1996. Don't gamble with physical properties for simulations. Chemical Engineering Progress, 92(10): 35-46.
11. Alabdulkarem, A., A. Mortazavi, Y. Hwang, R. Radermacher and P. Rogers, 2011. Optimization of propane pre-cooled mixed refrigerant LNG plant. Applied Thermal Engineering, 31(6): 1091-1098.

Persian Abstract

DOI: 10.5829/idosi.ijee.2014.05.01.10

چکیده

این چشم انداز که LNG می‌تواند به یکی از مهمترین منابع انرژی در جهان تبدیل شود، همواره مورد بحث بوده است. LNG سوختی سازگار با محیط زیست است، این عامل علاوه بر عوامل اقتصادی موجب می‌شود که این فرایند بسیار مورد اهمیت باشد. در این مقاله ابتدا فرایند تبدیل گاز طبیعی به LNG شبیه سازی شده و سپس فرایند برای به دست آوردن حداقل مقدار انرژی مصرف شده به ازای هرتن LNG تولیدی بهینه شده است. برای بهینه کردن مصرف انرژی در واحد بهترین روش استفاده از یک فرایند سه مرحله‌ای است. فشار خروجی کمپرسور و نوع مبرد بر میزان انرژی مصرفی بسیار موثر هستند. بهترین کسر جرمی برای مبردها در سیکل مایع سازی برابر ۰/۸۸ برای متان و ۰/۱۲ برای اتان است. در سیکل سردسازی برابر ۰/۶ برای متان و ۰/۴ برای نیتروژن است. فشار بهینه در خروجی کمپرسور در سیکل مایع سازی برابر ۶۵۰ کیلوپاسکال و برای سیکل سردسازی برابر ۱۸۰۰ کیلوپاسکال به دست آمده است. میزان انرژی مصرفی به ازای هرتن از LNG تولیدی برابر ۱۴/۹۱ کیلو وات آمده است.

Iranica Journal of Energy & Environment 5 (1): 73-77, 2014
ISSN 2079-2115
IJEE an Official Peer Reviewed Journal of Babol Noshirvani University of Technology
DOI: 10.5829/idosi.ijee.2014.05.01.11

BUT

Emissions and Performance of Diesel Engine Fueled with Waste Cooking Oil Methyl Ester Diesel Blends

[1]Sheila M. Zakiya, [1]Susan A. Roces, [1]Nathaniel P. Dugos,
[1]Michael Angelo B. Promentilla and [2]Masahiro Shioji

[1]Chemical Engineering Department, De La Salle University, 2401 Taft Ave, Manila 1004, Philippines
[2]Energy Conversion Science, Graduate School of Energy Science, Kyoto University, Kyoto 606-8501, Japan

(Received: January 14, 2014; Accepted in Revised Form: March 17, 2014)

Abstract: In this study, waste cooking oil methyl ester (WCOME) and diesel were blended in 20, 40, 60 and 80% percentage volume basis. Biodiesel and the blends were tested in 4-cylinders, 4-strokes and direct injection diesel engine to investigate the emissions and performance at engine speeds of 600-3000 rpm under idle and full load. The result was compared to the data of petroleum diesel. The experimental data showed that the emissions of biodiesel and blends were much lower than B100. In comparison, the emission of biodiesel was more than 50% lower than B100. The average reductions were 76.19% for smoke opacity; and 97.62, 90.36 and 98.69% for brake specific emission factors of BS-HC, BS- CO and BS-SO_2, respectively. The engine performances were also observed. Results showed that when WCOME were used both BHP and BMEP showed slight reductions about 8.63% compared to diesel. However, higher fuel consumption, had been indicated by the BSFC. The BSFCs of B100 were recorded to be 9.45% higher than biodiesel. The Highest BTEs were also recorded at a maximum average percentage of 19.93%.

Key words: Brake Horse Power · Brake Specific Fuel Consumption · Brake Thermal Efficiency · Brake Mean Effective Pressure · Brake Specific Hydrocarbon · Smoke Opacity

INTRODUCTION

Biodiesel is a non-toxic, biodegradable and renewable fuel that is manufactured usually from vegetable oils, recycled oils, or animal fats. Biodiesel production from vegetable oil has been extensively studied in many literature reviews [1-4]. However, the raw material costs and the availability of vegetable oil feedstocks remains a major hurdle for the biodiesel production. Ma and Hanna [5] investigated that the high cost of vegetable oils, which could be up to 70% of the total manufacturing cost, has lead to the biodiesel production becomming approximately 1.5 higher than that for diesel.

Waste Cooking Oil (WCO) is an oil-based substance consisting of animal or vegetable matter that has been used in cooking or in preparing foods and is non-edible [6]. Although, there are many studies on biodiesel production using various feedstock and different oil characterizations [7], high price and availability of virgin vegetable oil resources remain obstacles to biodiesel production. Since waste cooking oil is priced 2-3 times lower than virgin vegetable oils, using WCO as source for biodiesel can greatly reduce manufacturing cost [6].

Also, despite the optimization of biodiesel production from waste cooking oil there are still obstacles to using WCO. One major obstacle is the inadequacy of information on the side effects of having a biodiesel-fueled diesel engine and the lack of information about different tested engines, operating conditions and measurement techniques, among others.

Thus, given the need for a more convincing work in biodiesel, performances and emissions of diesel engine when fueled with waste cooking oil methyl ester (WCOME) will be addressed in this study. The study looked into how the effects of WCOME on BHP, BSFC, BTE and BMEP justified engine performance and brake specific emission factors of BS-CO, BS-HC, BS- SO_2 and smoke opacity during emission testing.

Corresponding Author: Susan A. Roces, Chemical Engineering Department, De La Salle University, 2401 Taft Ave, Manila 1004, Philippines.

This research measured the performance and emissions of the pure WCOME (B100) and several blend variations (B20, B40, B60 and B80). Determination of engine performance and analyses of brake specific emission factors were conducted. Baseline test was conducted using pure diesel (B0) to compare its performance and emissions with those of biodiesel blends.

MATERIALS AND METHODS

Materials: Biodiesel from waste cooking oil and petroleum diesel were used for the present study. Biodiesel from WCO was purchased from Eway 54, a local company in Philippines. The petroleum diesel was obtained from SHELL De La Salle University gas station.

Methodology: Four blends of diesel and waste cooking oil methyl ester on volume basis were prepared. The blends were B20, B40, B60 and B80. Blending was done using a HEIDOLPH RZR 2012 stirrer machine.

Engine tests were carried out using an Isuzu 4BC2, 3268 cc and a Nishishiba EDDY Current Dynamometer. A Vetronix PXA-1100 Gas Exhaust Analyzer was used to measure gas emissions. The analyses of the fuels were conducted in ZEXEL Calibration Center, Commonwealth Avenue in Quezon City, Philippines.

For every new fuel, the engine was operated both at idle and 100% load at various speeds. To make sure data remained accurate for every new fuel the measurements were made after the engine had run for around 5-10 minutes. This procedure made sure of the engine's stable condition for that certain blend. The tests were repeated twice for each fuel sample to ensure that all instrumentation had stabilized and get reasonable value. The average data were then used for the analysis and discussion. In conclusion, the engine performance (BHP, BSFC, BTE, BMEP), smoke opacity and brake specific emission factors (BS-HC, BS-CO, BS-SO_2) of the biodiesel blends were compared to those for 100% petroleum diesel.

RESULT AND DISCUSSIONS

Brake Horse Power: As can be seen in Fig. 1, the values of BHP for all tested fuels were very close and followed by increments with diesel fuel registering the highest BHP, followed by B20, B40, B60, B80 and B100 registering the lowest BHP. High BHPs were obtained when the engine was fueled by blends with low biodiesel content.

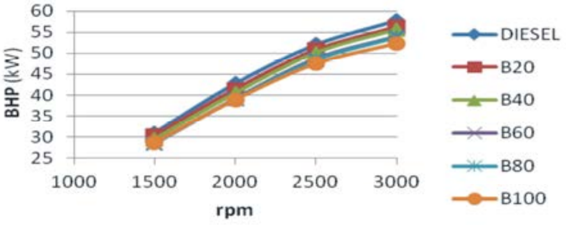

Fig. 1: Variation of Brake Horsepower with Engine Speed

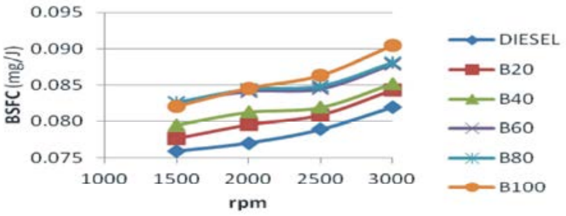

Fig. 2: Variation of Brake Specific Fuel Consumption with Engine Speed

The difference in average brake power of diesel-biodiesel and its blends was observed only by less than 10% with diesel possessed higher BHP values.

The low BHP values were attributed to low heating values [8] and resulted in lower engine power [9]. These low values could also be due to biodiesel's high density and viscosity that resulted to fuel flow problems [10]. Overall, it could be said that the BHP of WCOME and its blends in the present study resembled the BHP of diesel.

Brake Specific Fuel Consumption (BSFC): BSFC is the ratio of specific fuel consumption to the brake power, thus, lower BSFC is expected [11]. However it was found that the average BSFC of B100 was 9.45% higher than that of diesel fuel. BSFCs were lowest for diesel fuel and highest for B100. It increased proportionally with the addition of biodiesel blends. This was due to the low heating value of the blends. Diesel has a higher heating value than biodiesel. As consequence, the heating value of biodiesel blends increased linearly by addition of more diesel. The reason of higher BSFC of WCOME and its blends was because of the low heating value of WCOME and its blends compared to diesel fuel. Low heating value on the fuel means that more fuel would be required to produce the same energy and result in a high BSFC [12].

Brake Thermal Efficiency: From Fig. 3 it was observed that BTE increased with the addition of biodiesel in the blends. Among all fuels tested, the BTEs were lowest for diesel fuel and highest for B100. The average differences were 9.41, 14.08, 15.36, 16.13 and 19.93% for B20, B40, B60, B80 and B100, respectively.

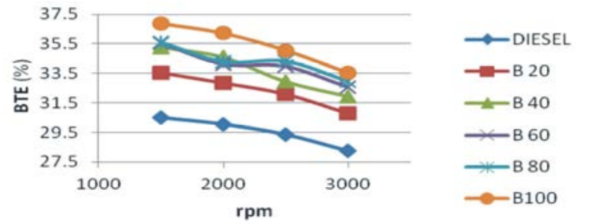

Fig. 3: Variation of Brake Thermal Efficiency with Engine Speed

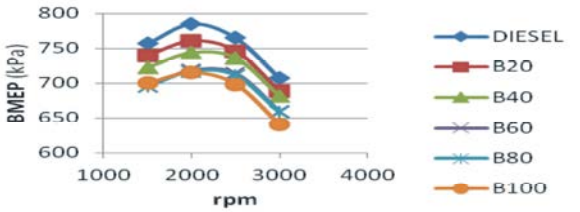

Fig. 4: Variation of Brake Mean Effective Pressure with Engine Speed

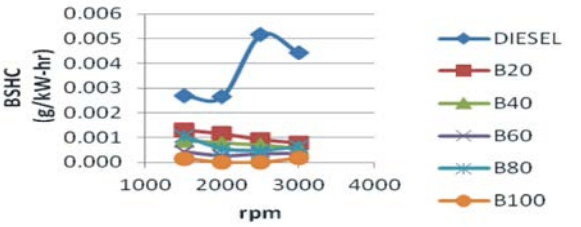

Fig. 5: Variation of Hydrocarbon with Engine Speed

A study by Murillo, et al. [13] observed that BTEs of B100 were higher than that of diesel. However, compared to diesel, the blends were found to have low BTEs. The high value of BTE when WCOME and blends was used might be due to high oxygen content of WCOME resulting in better combustion [14].

Brake Mean Effective Pressure: The BMEPs of diesel, biodiesel and biodiesel blends tested at full load are summarized in Fig. 4. For all fuels tested, the highest BMEP values were reached by diesel fuel. The percentage differences in BMEP with diesel as the base shows only less than 10% in the average drop of BMEP values. B20 was found with the minimum difference between diesel and biodiesel blends with a 2.65% average drop. Meanwhile, B100 showed the maximum average drop differences in BMEP with diesel with an 8.63%.

Brake Specific Hydrocarbon (BS-HC): The BS-HC emissions of diesel, biodiesel and its blends are shown in Fig. 5. Among the fuel tested, B100 produced the lowest BS-HC with average drop of 97.62% compared to diesel fuel. It was followed by B60, B80, B40 and B20 with 89.82, 79.17, 77.95 and 67.99%, respectively. The percentage differences in hydrocarbons emissions presented in g/kW-h with diesel as the base. In this study, average BS-HC was found to be 0.0037g/kW-h when diesel was used; while it was 0.0001g/kW-h for B100.

In the present study, BS-HC emissions tended to decrease at high engine speeds. This could be the result of high engine speeds causing an increase in inlet airflow, which triggered the atomization process that resulted in a more uniform fuel mixture [15, 16].

Brake Specific Carbon Monoxide (BS-CO): CO emissions were mostly comes from the incomplete combustion. When B100 was used, the average drop in BS-CO compared to the exhaust when diesel fuel used was 90.36%. This value has followed by the average drop for B60 at 91.67% and then by those of B80 at 89.72%, B40 at 86.61% and B20 at 76.53%. The mean BS-CO were presented in g/kW-h and showed the values of diesel fuel was 14.8536g/kW-h, followed by B20, B40, B60, B80 and B100 with 3.0262, 1.7627, 1.1389, 1.3094 and 1.1397g/kW-h, respectively.

As observed from the results, the formation of carbon monoxide in diesel fuel was the highest among the fuels tested. When engine speed increased more fuel were injected. Fortunately, there had been enough oxygen as needed for a complete combustion. When there was too much fuel. However, insufficient oxygen for complete combustion a rich condition would occur and more HC would be produced [17].

Brake Specific Sulfur Dioxide (BS-SO_2): The formation of BS-SO_2 can be observed in Fig. 7 which gives an overview of the different amounts of BS-SO_2 formed by WCOME and its blends. This average percentage difference for the blends B20, B40, B60, B80 and B100 were recorded at 30.86, 47.05, 60.24, 78.23 and 98.69%, respectively.

The emission factors of SO_2 were 0.0039, 0.0639, 0.1173, 0.1576, 0.2048 and 0.2952 g/kW-h for B100, B80, B60, B40, B20 and diesel, respectively. When B100 was used, there were hardly any SO_2 emissions found. This could be because biodiesel possessed very low sulfur content resulted in lower SO_2 emission.

Smoke Opacity: Fig. 8 shows the variation of the smoke opacity of diesel, WCOME and its blends related to engine speed. It can be observed that smoke opacity of WCOME and its blends were all lower than diesel fuel. The increments were as expected, where the fuel with higher percentage of biodiesel produced lower smoke

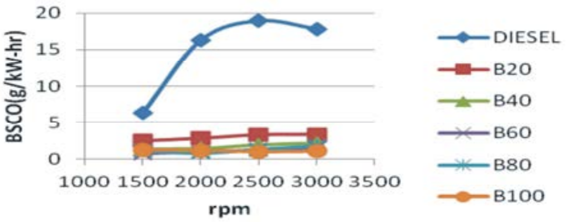

Fig. 6: Variation of Carbon Monoxide with Engine Speed

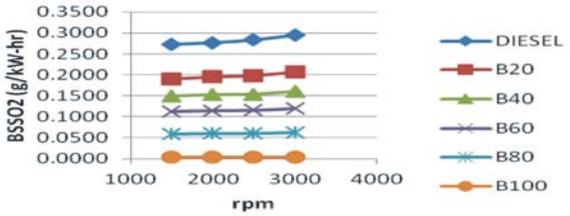

Fig. 7: Engine Emission Factors of SO_2 versus Engine Speed

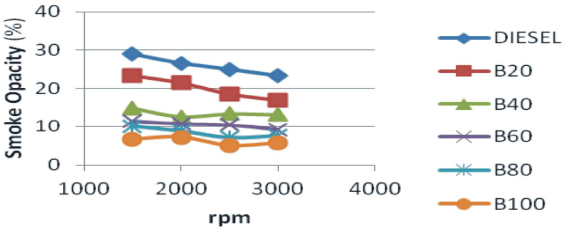

Fig. 8: Variation in Smoke Opacity Engine Speed

opacity as well. Pure biodiesel or B100 reduce smoke opacity compared to diesel fuel by 76.19%, followed by B80, B60, B40 and B20. The average reductions are 67.52, 59.71, 47.77 and 22.89% for B80, B60, B40 and B20, respectively.

The lower smoke opacity in biodiesel and its blends explained more complete combustion due to higher cetane index and oxygen content [18]. According to Canakci *et al.*, [16] since the smoke is highly dependent on oxygen and sulfur content of the fuel, no wonder that smoke opacity was found to be lower when diesel was blended with biodiesel.

At low engine speed, the percentages of smoke opacity were high and as the engine speed increased the smoke opacities decreased. At high engine speeds the air turbulence and fuel oxidation increased, resulted at low smoke production [16].

CONCLUSIONS

In the present research biodiesel from waste cooking oil methyl ester (WCOME) and its blends B20, B40, B60 and B80 were tested on a four-stroke, direct-injection diesel engine. The results have shown that WCOME and its blends can be tapped as a good substitute or petroleum diesel supplement. This can be noticed from the emissions and performance tests done in this study.

BHP and BMEP showed a slight reduction when biodiesel and diesel were used,. The maximum average drop on BHPs and BMEPs when biodiesel was used were 8.63% as compared to diesel. The increases on BTEs were observed with the maximum average percentage of 19.93%. The higher BTEs indicated higher oxygen content in the fuel and more complete combustion. However, higher fuel consumptions were also indicated by the BSFC. BSFCs of B100 were recorded to be higher by 9.45%.

The exhaust emissions were presented in g/kW-hr for BS-HC, BS-CO, BS-SO_2 and smoke opacity in BSU. The emissions factor of WCOME and its blends were found to be much lower compared to those for petroleum diesel. When B100 was used the average emission factors were 0.0001g/kW-h for HC, 1.1397g/kW-h for CO, 0.00391g/kW-h for SO_2 and for smoke opacity it was lower by 76.19% compared to diesel fuel.

ACKNOWLEDGEMENTS

The authors would like to express their gratitude for the contributions and support of AUN/SEED-net and JICA, Chemical Engineering Department of De La Salle University (Philippines), Gadjah Mada University (Indonesia) and Kyoto University (Japan).

REFERENCES

1. Phan, A.N. and T.M. Phan, 2008. Biodiesel production from waste cooking oils. Fuel, 87(17): 3490-3496.
2. Gupta, K., A. Rehman and R. Sarviya, 2010. Evaluation of soya bio-diesel as a gas turbine fuel. Iranica Journal of Energy and Environment, 1(3): 205-210.
3. Karnwal, A., N. Kumar, M. Hasan, R. Chaudhary, A.N. Siddiquee and Z.A. Khan, 2010. Production of biodiesel from thumba oil: optimization of process parameters. Iranica Journal of Energy and Environment, 1(4): 352-358.
4. Lenin, A.H., R. Ravi and K. Thyagarajan, 2013. Performance characteristics of a diesel engine using mahua biodiesel as alternate fuel. Iranica journal of energy and environment, 4(2): 136-141.
5. Ma, F. and M.A. Hanna, 1999. Biodiesel production: a review. Bioresource technology, 70(1): 1-15.

6. Zhang, Y., M. Dube, D. McLean and M. Kates, 2003. Biodiesel production from waste cooking oil: 2. Economic assessment and sensitivity analysis. Bioresource technology, 90(3): 229-240.
7. Singh, S. and D. Singh, 2010. Biodiesel production through the use of different sources and characterization of oils and their esters as the substitute of diesel: a review. Renewable and Sustainable Energy Reviews, 14(1): 200-216.
8. Aydin, H. and H. Bayindir, 2010. Performance and emission analysis of cottonseed oil methyl ester in a diesel engine. Renewable Energy, 35(3): 588-592.
9. Knothe, G., J.H. Van Gerpen and J. Krahl, 2005. The biodiesel handbook. Vol. 1.: AOCS press Champaign.
10. Subbaiah, G.V., K.R. Gopal and S.A. Hussain, 2010. The Effect of Biodiesel and Bioethanol Blended Diesel Fuel on the Performance and Emission Characteristics of a Direct Injection Diesel Engine. Iranica Journal of Energy and Environment, 1(3): 211-221.
11. Karabektas, M., 2009. The effects of turbocharger on the performance and exhaust emissions of a diesel engine fuelled with biodiesel. Renewable Energy, 34(4): 989-993.
12. Qi, D., H. Chen, L. Geng and Y. Bian, 2010. Experimental studies on the combustion characteristics and performance of a direct injection engine fueled with biodiesel/diesel blends. Energy Conversion and Management, 51(12): 2985-2992.
13. Murillo, S., J. Miguez, J. Porteiro, E. Granada and J. Moran, 2007. Performance and exhaust emissions in the use of biodiesel in outboard diesel engines. Fuel, 86(12): 1765-1771.
14. Rao, P., B. Rao and D. Radhakrishna, 2012. Experimental Analysis of DI Diesel Engine Performance with blend fuels of oxygenate additive and COME biodiesel. Iranica Journal of Energy and Environment 3(2): 109-117.
15. Enweremadu, C. and H. Rutto, 2010. Combustion, emission and engine performance characteristics of used cooking oil biodiesel-A review. Renewable and Sustainable Energy Reviews, 14(9): 2863-2873.
16. Canakci, M., A.N. Ozsezen, E. Arcaklioglu and A. Erdil, 2009. Prediction of performance and exhaust emissions of a diesel engine fueled with biodiesel produced from waste frying palm oil. Expert systems with Applications, 36(5): 9268-9280.
17. Park, S.H., J. Cha and C.S. Lee, 2012. Impact of biodiesel in bioethanol blended diesel on the engine performance and emissions characteristics in compression ignition engine. Applied Energy, 99: 334-343.
18. Chauhan, B.S., N. Kumar and H.M. Cho, 2012. A study on the performance and emission of a diesel engine fueled with Jatropha biodiesel oil and its blends. Energy, 37(1): 616-622.

Persian Abstract

DOI: 10.5829/idosi.ijee.2014.05.01.11

چکیده

در این مطالعه، از ترکیب متیل استر موجود در پسماند روغن خوراکی (WCOME) و دیزل بر اساس درصد حجمی ۲۰، ۴۰، ۶۰ و ۸۰٪ مخلوط شد. از بیودیزل و سوخت ترکیبی در یک موتور دیزل با ۴ سیلندر، ۴، ضربه ای، و تزریق مستقیم استفاده گردید و میزان تولید گازهای گلخانه ای و همچنین عملکرد سرعت موتور در ۶۰۰–۳۰۰۰ دور در دقیقه تحت بار غیر کامل و کامل مورد آزمایش قرار گرفتند. نتایج به دست امده با داده های دیزل مشتق شده از نفت مقایسه شد. داده های تجربی نشان داد که تولید گازهای گلخانه ای از بیودیزل و سوخت ترکیبی بسیار کمتر از B100 بودند. در مقایسه، انتشار بیودیزل بیش از ۵۰ درصد کمتر از B100 بود. متوسط کاهش ۷۶.۱۹٪ برای کدورت دود بودند و ۹۷.۶۲، ۹۰.۳۶، و ۹۸.۶۹٪ برای قطع عوامل انتشار خاص از BS-HC، BS-CO، و $BS\text{-}SO_2$ بود. عملکرد موتور نیز مورد بررسی قرار گرفت. . نتایج نشان داد که زمانی که WCOME مورد استفاده قرار گرفت کاهش کمی در مورد BHP و BMEP حدود ۸.۶۳ ٪ در مقایسه با دیزل نشان دادند. با این حال، مصرف سوخت بالاتر، توسط BSFC نشان داد شده است. BSFCs از B100 به ۹.۴۵ درصد بالاتر از بیودیزل ثبت شده است. بالاترین BTEs نیز در حداکثر ۱۹.۹۳٪ گزارش شده است.

Iranica Journal of Energy & Environment 5 (1): 78-86, 2014
ISSN 2079-2115
IJEE an Official Peer Reviewed Journal of Babol Noshirvani University of Technology
DOI: 10.5829/idosi.ijee.2014.05.01.12

BUT

Creation Typical Meteorological Year Data for Baghdad Province, Iraq

Ali M. AL-Salihi

Department of Atmospheric Sciences, College of Science, AL-Mustansiriyah University, Baghdad, Iraq

(Received: December 20, 2013; Accepted in Revised Form: March 8, 2014)

Abstract: Weather data can vary significantly from year to other, so there is a need to create a Typical Meteorological Year (TMY) data to represent the long-term typical weather data sets which are very important as inputs in modeling, designing and performance evaluation of energy balance calculations. In present study Finkelstein-Schafer statistical method was employed to analyze the long-term measured weather data of a 30-year period (1971-2000) for Baghdad province, which included six major meteorological parameter (Global solar Radiation, Sunshine Duration, Maximum, Minimum and Mean Temperature, Relative Humidity) Typical meteorological months from the period of considered years were selected by choosing the smallest (FS) deviation from the long-term of a TMY for Baghdad province.

Key words: Typical Meteorological Year · Finkelstein-Schafer · Meteorology · Baghdad

INTRODUCTION

Weather is the main exterior factor that governs the construction and structure of building designs, especially solar radiation, sunshine duration, air temperature and relative humidity. In order to have a suitable indoor temperature in the buildings, we need to know the energy balance of building and then we can calculate the required power for devices of heating and cooling, which are used to regulate the indoor temperature on a desired value. One year time series of meteorological variables, which serve as an input into the model of the energy balance, is needed for this purpose. Testing the energy response of a building on specific weather types usually requires the so called Typical Meteorological Year (TMY) [1].

The modern simulation software for evaluating the performance of solar energy systems requires accurate and high-resolution meteorological data series [2]. Information concerning solar irradiation and meteorological variables; such as air temperature, relative humidity, necessary for the analysis of renewable energy systems and to simulate the evaluation of heating and cooling loads in buildings and the performance of solar thermal and photovoltaic systems. The analysis of renewable solar energy systems can be carried out using multiyear hourly data that involve additional and expensive computational efforts or creating a year of representative data, called long-term average measured data series from many years of available data series. Long-term average measured data are a feasible series with the drawback that the values are averaged and do not take directly into account the extreme meteorological values reached in the year [3].

Typical Meteorological Year (TMY) which is a dataset of hourly meteorological variables throughout the year, with the advantage of representing reference rather than extreme conditions in the region. TMYs data series can simplify the work with weather data in energy studies. They also have the property of facilitating performance comparisons of different types of energy systems and installers of energy systems could use them more easily.

The need for such appropriate weather data led to development of methodologies for generating the Typical Meteorological Year. In last two decades many researchers have been made attempts to generate a climatic database for different areas around the world employing different approaches [4-18]. One of the most common methodologies for generating TMY is the one proposed by Hall [4] using the Filkenstein-Schafer (FS) statistical method [19].

Corresponding Author: Ali M. AL-Salihi, Department of Atmospheric Sciences, College of Science, AL-Mustansiriyah University, Baghdad, Iraq.

The real recorded data from past weather observations are selected for generation of representative weather data. A representative database for one-year duration is known as test reference year (TRY) or typical meteorological year (TMY). TMY or TRY consists of the months selected from the individual years and concatenated to form a complete year. Many attempts have been made to produce such weather databases for different locations around the world [15, 18].

An accurate knowledge of the meteorological data at a particular geographical location is of vital importance for the development of meteorological elements measuring devices and for estimates of their performances [20]. In this study, an attempt is made to generate a representative weather database for Baghdad province by using Filkenstein-Schafer (FS) statistical method. The TMY will created using available weather data, which recorded by the Iraqi Meteorological Organization and Seismology (IMOS) covering the period 1971 to 2000. This restriction on the length of time series is related to the availability of the data in electronic form. It is hope that in a near future the generation of a TMY will became feasible for other provinces of Iraq, especially when solar radiation records will be available.

TMY Generation Method: Thirty years of meteorological data collected by Iraqi Meteorological Organization and Seismology (IMOS) at Baghdad station were used as a data base for selecting Typical meteorological year (TMY) by using the common methodology for creating typical weather data is Filkenstein-Schafer (FS) static's [19], It were used by many researcher such as; [5, 6, 9-12, 16]. According to these static's (FS), if a number (n) of observations of a variable (X) are available and have been sorted into an increasing order $X_1, X_2 \ldots\ldots, X_n$, the Cumulative Distribution Function (CDF) of this variable is given by a function S_n (X) which is defined as flows:

$$0 \text{ for } X < X_1 \tag{1}$$

$$S_n(X) = (k-0.5)/n \text{ for } X_k < X < X_{(k+1),} \tag{1}$$
$$1 \text{ for } X > X_{(n),}$$

where Sn (X) is value of the CDF at X; n, the total number of elements; k, ranked order number (k=1, 2, 3,…..n-1). The FS by which comparison between the long-term CDF of each month and the CDF for each individual year of the month was done is given by the equation:

$$FS_x(y,m) = \frac{1}{N}\sum_{i=1}^{N}\left|CDF_m(x_i) - CDF_{y,m}(x_i)\right| \tag{2}$$

$$WS(y,m) = \frac{1}{M}\sum_{x=1}^{M} WF_x.FS_x(y,m) \tag{3}$$

$$\sum_{x=1}^{M} WF_x = 1 \tag{4}$$

where CDFm is the long term and CDFy,m is the short term cumulative distribution function of the daily index x for month m and WFx are the weighting factors, one for each daily index. N is the number of bins and M is the number of considered meteorological parameters in the present study [19]. Finally, the typical year for each month of the data set was determined on the basis, that the typical year is that of the minimum values of FS through the year.

RESULT AND DISCUSSION

The intensity of solar radiation received by the earth's surface varies from location to other owing the attenuating properties of the atmosphere and the diverse geographical characteristic of the earth surface. Generally from the daily global solar radiation data as well as sunshine duration which employed in present study illustrated in Figures 1 and 2, respectively. It is a clear that the daily solar radiation are higher from late February early September and lower from October to late January with maximum values during June (8 kwh/m^2.day). But for temperature group there are about one month and half shift between the distribution of solar radiation and air temperature group, where the mean air temperature shows higher values late April and mid September with maximum values in July (about 40°C in average) and the minimum and maximum value reaches to 28 and 48 °C, respectively. The mean temperature records are illustrated in Figures 3, 4 and 5. While, the annual behavior of relative humidity show an opposite distribution against the previously mentioned meteorological parameters (solar radiation and air temperature parameters), where the relative humidity presents lower values during May, June, July and Augustus months and higher during other months of the year as shown in Figure 6. The representative year for each month for each meteorological parameter was determined on the basis that the representative year is that concluded the smallest values of FS as presented in previous section (TMY Generation Method).

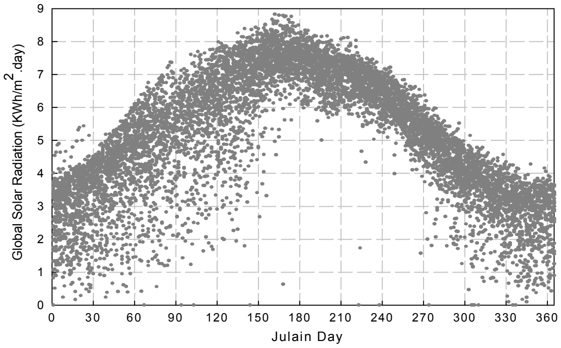

Fig. 1: Variation of long term measured daily global solar radiation data for Baghdad city

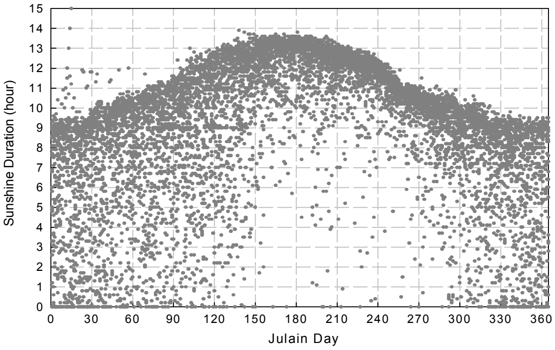

Fig. 2: Variation of long term measured sunshine duration data for Baghdad City.

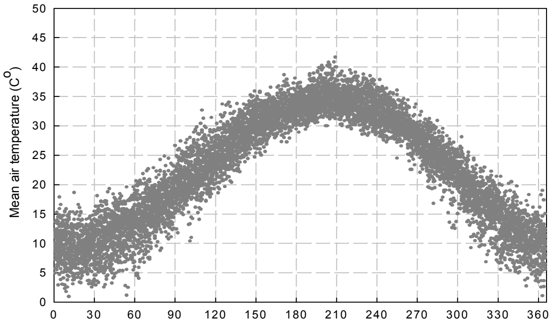

Fig. 3: Variation of long term measured mean air temperature data for Baghdad city

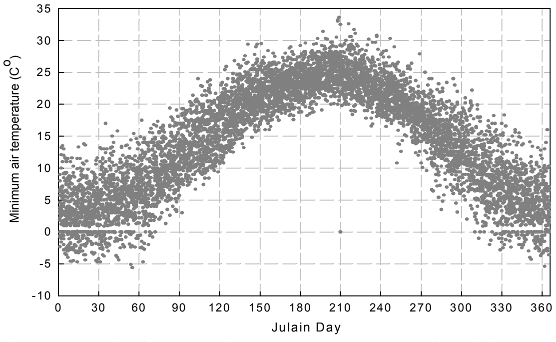

Fig. 4: Variation of long term measured minimum air temperature data for Baghdad city.

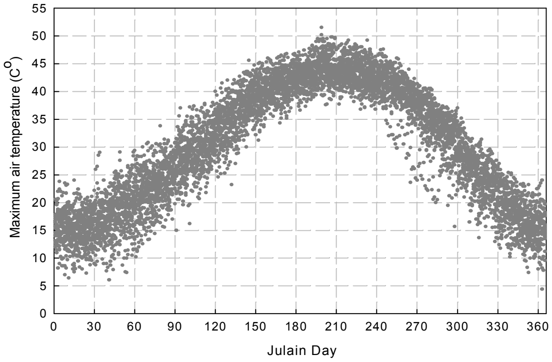

Fig. 5: Variation of long term measured maximum air temperature data for Baghdad city.

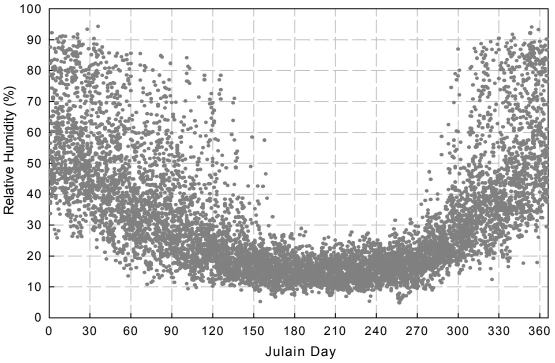

Fig. 6: Variation of long term measured relative humidity data for Baghdad city

There are six TMY resulted from different years to carry out the weighted FS for each meteorological element. Daily measured data (derived from hourly measurements) for years (1971-2000) for all the considered meteorological elements except of solar radiation the data represented by the years (1971-1987) and (1989-1999), sun shine duration (1971-1990) and (1992-2000) and relative humidity for the period (1975- 2000) are shown in Figures 1 to 6. In present study, the function FS was computed for each month of every year for all the considered data set shown in Tables 1-6.

The abdicated months for each element with lowest FS values are shown in underline in Tables 1-6 for solar radiation (kwh/m^2.day), sunshine duration (h), mean air temperature (°C), minimum air temperature (°C), Maximum air temperature (°C) and relative humidity (%), respectively. Usually the sunshine duration not concluded in TMY and replaced by solar radiation which is represented. But in our case we have a very big shortage in solar radiation measurements in most meteorological stations in Iraqi provinces and its available in a few stations in main provinces, so that we conclude this additional parameter to use it instead of solar

Table 1: Weighted sum of the FS statistics of global solar radiation for Baghdad. (The candidate months of each year are underlined)

	Month											
Year	Jan	Feb	Mar	Aprl	May	Jun	Jul	Aug	Sept	Oct	Nov	Dec
1971	0.0785	0.1012	0.0779	0.0083	0.0653	0.1071	0.0027	0.0171	0.0434	0.0942	0.0751	0.0960
1972	0.0361	0.1000	0.0442	0.0308	0.1274	0.1707	0.1224	0.1145	0.0050	0.0178	0.1365	0.1366
1973	0.1207	0.0472	0.1284	0.0649	0.1822	0.1060	0.0227	0.0036	0.0046	0.1340	0.0942	0.1704
1974	0.0957	0.1039	0.0514	0.1797	0.1863	0.007	0.0420	0.0329	0.1050	0.0548	0.1462	0.0050
1975	0.2314	0.0903	0.0175	0.1743	0.1645	0.0074	0.0368	0.1066	0.0368	0.0359	0.0691	0.0827
1976	0.0409	0.0463	0.1028	0.0458	0.1560	0.3380	0.0023	0.0390	0.0039	0.0552	0.0491	0.0580
1977	0.0829	0.0780	0.0343	0.1022	0.1161	0.0341	0.0081	0.3214	0.0080	0.0332	0.0492	0.0772
1978	0.0560	0.0353	0.1125	0.0941	0.0921	0.0145	0.0038	0.0628	0.0313	0.0054	0.1598	0.1543
1979	0.0557	0.1086	0.0812	0.0335	0.0613	0.1199	0.1507	0.1061	0.1701	0.0844	0.1177	0.1088
1980	0.1143	0.0703	0.1125	0.0668	0.1845	0.2672	0.2550	0.0547	0.2027	0.1729	0.1291	0.0508
1981	0.0962	0.1164	0.1124	0.1011	0.1039	0.2142	0.0449	0.0977	0.0053	0.0328	0.1554	0.1296
1982	0.0115	0.1065	0.0813	0.1093	0.0879	0.0354	0.0929	0.2015	0.2483	0.1405	0.1088	0.0613
1983	0.0979	0.1208	0.0692	0.0652	0.0510	0.1483	0.0853	0.0028	0.3535	0.0519	0.1247	0.1015
1984	0.0653	0.0345	0.0194	0.0630	0.1216	0.0057	0.1993	0.0474	0.0197	0.0859	0.0896	0.1194
1985	0.0558	0.0606	0.0861	0.1115	0.1356	0.0516	0.0083	0.0190	0.0065	0.1949	0.0491	0.1035
1986	0.1331	0.0698	0.0801	0.1300	0.1357	0.0941	0.0432	0.1691	0.0402	0.0545	0.1592	0.0392
1987	0.0265	0.0209	0.1145	0.0752	0.1098	0.2003	0.2280	0.2294	0.1707	0.1221	0.1057	0.0123
1989	0.0979	0.1408	0.0425	0.0868	0.1294	0.1567	0.0151	0.0398	0.0301	0.0120	0.1113	0.0471
1990	0.1263	0.0329	0.1130	0.0784	0.0802	0.0828	0.0072	0.0083	0.0596	0.1287	0.1102	0.0574
1992	0.0226	0.0007	0.0677	0.1292	0.0747	0.0012	0.0386	0.0332	0.0315	0.0169	0.1078	0.0275
1993	0.0441	0.1149	0.1092	0.0964	0.0948	0.0209	0.0505	0.0567	0.0524	0.0314	0.0524	0.0814
1994	0.0682	0.0094	0.0189	0.1350	0.0423	0.0244	0.0533	0.0384	0.0226	0.0594	0.0114	0.1002
1995	0.0697	0.1213	0.1260	0.1136	0.0596	0.1063	0.0639	0.1774	0.0853	0.1011	0.0369	0.1204
1996	0.0942	0.0558	0.0570	0.1288	0.0790	0.0669	0.1125	0.0669	0.0003	0.0318	0.1804	0.0834
1997	0.0297	0.0955	0.0195	0.0701	0.1044	0.1961	0.0212	0.0090	0.0376	0.1032	0.1319	0.1056
1998	0.0750	0.0876	0.0807	0.0392	0.0081	0.008	0.0295	0.0382	0.0445	0.0254	0.1758	0.1259
1999	0.0967	0.0771	0.0907	0.1883	0.1715	0.1615	0.0604	0.0185	0.1211	0.1318	0.0379	0.0673

Table 2: Weighted sum of the FS statistics of Sun shine duration for Baghdad. (The candidate months of each year are underlined)

	Month											
Year	Jan	Feb	Mar	Aprl	May	Jun	Jul	Aug	Sept	Oct	Nov	Dec
1971	0.1271	0.0626	0.0655	0.0654	0.0430	0.1199	0.1654	0.0055	0.0101	0.0658	0.0939	0.0115
1972	0.0847	0.1541	0.0469	0.0053	0.0446	0.1425	0.1491	0.2337	0.1114	0.1092	0.1490	0.1371
1973	0.0843	0.1088	0.1389	0.0434	0.1763	0.1108	0.0291	0.0031	0.0020	0.0989	0.1499	0.0804
1974	0.0270	0.1442	0.0379	0.0873	0.1035	0.1115	0.0427	0.0704	0.1822	0.0700	0.1407	0.0337
1975	0.0698	0.0684	0.1958	0.0529	0.0848	0.1132	0.0103	0.0564	0.0915	0.2476	0.1218	0.0214
1976	0.0381	0.0673	0.0646	0.0816	0.1350	0.1490	0.1006	0.0045	0.0877	0.1126	0.0620	0.0247
1977	0.0282	0.1079	0.0187	0.0828	0.0869	0.1237	0.0162	0.0283	0.0044	0.0938	0.1158	0.0512
1978	0.0984	0.1515	0.0591	0.1080	0.1190	0.1241	0.0008	0.0853	0.0123	0.0074	0.1516	0.1339
1979	0.1322	0.1308	0.0592	0.0102	0.0251	0.1273	0.1429	0.0928	0.1031	0.1065	0.1230	0.0881
1980	0.1224	0.0504	0.0833	0.0725	0.1838	0.1090	0.1034	0.0707	0.1493	0.1544	0.1072	0.0782
1981	0.0554	0.0968	0.1442	0.0698	0.0847	0.2437	0.1121	0.0645	0.0446	0.0888	0.1268	0.0775
1982	0.0105	0.0683	0.0878	0.0481	0.0381	0.0529	0.0204	0.0147	0.0203	0.1167	0.1378	0.0730
1983	0.1317	0.0920	0.0563	0.0720	0.0585	0.1933	0.0749	0.1360	0.2278	0.1186	0.0896	0.0832
1984	0.1230	0.0859	0.0381	0.0719	0.0747	0.1985	0.1488	0.0559	0.0150	0.0961	0.0597	0.1201
1985	0.1150	0.1533	0.0974	0.1332	0.0811	0.0980	0.0205	0.0366	0.0090	0.1393	0.1442	0.1115
1986	0.1361	0.0678	0.1253	0.0070	0.1416	0.1466	0.0534	0.0241	0.0065	0.0880	0.0690	0.0825
1987	0.0995	0.0216	0.0412	0.0343	0.0484	0.0916	0.1453	0.0778	0.1078	0.0792	0.1276	0.0560
1988	0.1349	0.0873	0.0183	0.0893	0.1095	0.0466	0.0848	0.1363	0.1412	0.0595	0.1993	0.0998
1989	0.1308	0.0877	0.0943	0.2437	0.0873	0.1400	0.0328	0.00035	0.0507	0.0897	0.1113	0.0182
1990	0.0254	0.0231	0.0764	0.0509	0.0707	0.0166	0.0173	0.0016	0.0213	0.1455	0.0474	0.0262
1992	0.0180	0.0026	0.0952	0.0778	0.0559	0.0682	0.0837	0.0968	0.0644	0.0954	0.0279	0.0654
1993	0.1958	0.1266	0.1333	0.0594	0.0124	0.0079	0.1453	0.0266	0.0431	0.1806	0.1574	0.0698
1994	0.1175	0.0701	0.0909	0.1350	0.1965	0.1247	0.2769	0.3113	0.1577	0.0700	0.0645	0.1450
1995	0.1668	0.1381	0.0651	0.0223	0.1008	0.2393	0.0607	0.0304	0.0225	0.2393	0.1753	0.1282
1996	0.0225	0.0305	0.0063	0.1217	0.0527	0.2446	0.1870	0.0190	0.0617	0.3202	0.1617	0.0015
1997	0.1040	0.2094	0.0471	0.0927	0.1025	0.2437	0.0838	0.0073	0.0911	0.0936	0.1116	0.1389
1998	0.0655	0.0763	0.0939	0.0852	0.0642	0.0307	0.0527	0.0793	0.0365	0.0857	0.1573	0.0561
1999	0.0784	0.1113	0.0374	0.1322	0.1707	0.1412	0.1505	0.0816	0.2485	0.0682	0.1201	0.0044
2000	0.0889	0.1799	0.1146	0.0159	0.1095	0.0850	0.0523	0.0535	0.1293	0.1396	0.0908	0.0420

Table 3: Weighted sum of the FS statistics of Mean air temperature for Baghdad. (The candidate months of each year are underlined)

	Month											
Year	Jan	Feb	Mar	Aprl	May	Jun	Jul	Aug	Sept	Oct	Nov	Dec
1971	0.0152	0.0048	0.0276	0.0465	0.0343	0.0177	0.0078	0.0044	0.0311	0.0523	0.0055	0.0360
1972	0.0299	0.0159	0.0207	0.0135	0.0017	0.0048	0.0120	0.0162	0.0407	0.0401	0.0820	0.0321
1973	0.0094	0.0314	0.0069	0.0016	0.0137	0.0198	0.0164	0.0083	0.0059	0.0153	0.0462	0.0156
1974	0.0373	0.0050	0.0225	0.0201	0.0471	0.0235	0.0111	0.0327	0.0189	0.0172	0.0031	0.0023
1975	0.0076	0.0137	0.0488	0.0196	0.0287	0.0134	0.0092	0.0129	0.0466	0.0236	0.0305	0.0021
1976	0.0258	0.0629	0.0354	0.0085	0.0317	0.0133	0.0373	0.0439	0.0172	0.0427	0.0499	0.0098
1977	0.0017	0.0140	0.0174	0.0515	0.0019	0.0199	0.0170	0.0804	0.0130	0.0079	0.0155	0.0245
1978	0.0132	0.0232	0.0203	0.0435	0.0052	0.0145	0.0047	0.0208	0.0371	0.0370	0.0272	0.0318
1979	0.0374	0.0485	0.0322	0.0196	0.0067	0.0101	0.0159	0.0161	0.0286	0.0255	0.0413	0.0326
1980	0.0277	0.0609	0.0013	0.0226	0.0103	0.0164	0.0326	0.0213	0.0184	0.0020	0.0351	0.0119
1981	0.0113	0.0260	0.0955	0.0013	0.0012	0.0293	0.0200	0.1595	0.0281	0.0368	0.0012	0.0051
1982	0.0295	0.0108	0.0146	0.0536	0.0108	0.0134	0.0034	0.0397	0.0033	0.0146	0.0390	0.0257
1983	0.0108	0.0360	0.0212	0.0249	0.0066	0.0076	0.0227	0.0447	0.0173	0.0384	0.0349	0.0475
1984	0.0221	0.0250	0.0227	0.0048	0.0552	0.0614	0.0019	0.0362	0.0076	0.0456	0.0372	0.0059
1985	0.0305	0.0485	0.1219	0.0219	0.0200	0.0225	0.0189	0.0110	0.0122	0.0344	0.0362	0.0151
1986	0.0427	0.0145	0.0229	0.0210	0.0166	0.0839	0.0050	0.0371	0.0073	0.0114	0.0427	0.0441
1987	0.0629	0.0293	0.0815	0.0099	0.0051	0.0009	0.1099	0.0390	0.0327	0.0136	0.0329	0.0390
1988	0.0140	0.0179	0.0246	0.0345	0.0247	0.0549	0.1415	0.2129	0.1466	0.0444	0.0148	0.0809
1989	0.0317	0.0166	0.0199	0.0466	0.0370	0.0170	0.0031	0.0504	0.0524	0.0062	0.0056	0.0420
1990	0.0019	0.0243	0.0025	0.0268	0.0555	0.0237	0.0130	0.0293	0.0079	0.0037	0.0667	0.0410
1991	0.0439	0.0213	0.0136	0.0134	0.0804	0.0290	0.0255	0.0467	0.0139	0.0429	0.0178	0.0129
1992	0.0562	0.0182	0.0417	0.0234	0.0672	0.0185	0.0232	0.0076	0.0059	0.0290	0.0879	0.0621
1993	0.0401	0.0293	0.0804	0.0274	0.0529	0.0066	0.0256	0.0131	0.0037	0.1062	0.0027	0.0293
1994	0.0214	0.0418	0.0083	0.0391	0.0080	0.0174	0.0452	0.0342	0.0366	0.0016	0.0248	0.0109
1995	0.0393	0.0707	0.0635	0.0137	0.0055	0.0452	0.0141	0.0426	0.0297	0.0561	0.0342	0.0175
1996	0.0542	0.0475	0.0444	0.0104	0.0060	0.0094	0.0254	0.0075	0.0131	0.0149	0.0415	0.0185
1997	0.0115	0.0147	0.0312	0.0081	0.0348	0.0073	0.0372	0.0038	0.0118	0.0175	0.0461	0.0352
1998	0.0404	0.0353	0.0414	0.0081	0.0100	0.0179	0.0100	0.0360	0.0181	0.0053	0.0393	0.0382
1999	0.0039	0.0356	0.0123	0.0490	0.0018	0.0368	0.0148	0.0062	0.0235	0.0121	0.1860	0.0243
2000	0.0443	0.0229	0.0196	0.0351	0.0674	0.0323	0.0605	0.0492	0.2648	0.0336	0.0244	0.0369

Table 4: Weighted sum of the FS statistics of Minimum Temperature for Baghdad. (The candidate months of each year are underlined)

	Month											
Year	Jan	Feb	Mar	Aprl	May	Jun	Jul	Aug	Sept	Oct	Nov	Dec
1971	0.8046	0.8238	0.8178	0.8244	0.8664	0.8463	0.8415	0.8565	0.8639	0.8094	0.8889	0.8260
1972	0.8859	0.8168	0.8968	0.8297	0.8502	0.8485	0.8408	0.8309	0.8799	0.8545	0.7725	0.8517
1973	0.1060	0.0167	0.0202	0.0116	0.0386	0.0110	0.0007	0.0439	0.0275	0.0007	0.0689	0.0103
1974	0.0622	0.0028	0.0858	0.0907	0.0015	0.0512	0.0081	0.0538	0.0459	0.0226	0.0714	0.0852
1975	0.0788	0.0145	0.0121	0.0232	0.0092	0.0052	0.0393	0.0139	0.0245	0.0054	0.0206	0.0583
1976	0.0579	0.0884	0.0081	0.0529	0.0001	0.0255	0.0847	0.0004	0.0061	0.0011	0.0014	0.0187
1977	0.0324	0.0326	0.0437	0.0249	0.0139	0.0384	0.0137	0.0289	0.0514	0.0424	0.0162	0.0237
1978	0.0014	0.1384	0.0809	0.0389	0.0387	0.0185	0.0433	0.0622	0.0505	0.0905	0.0905	0.0254
1979	0.0172	0.0035	0.0206	0.0163	0.0004	0.0554	0.0234	0.0303	0.0037	0.0260	0.0198	0.0851
1980	0.0717	0.0237	0.0140	0.0223	0.0127	0.0269	0.0247	0.0418	0.0038	0.0637	0.0016	0.0981
1981	0.0970	0.0068	0.0132	0.0806	0.0098	0.0770	0.0560	0.1375	0.0754	0.0503	0.0710	0.0649
1982	0.0183	0.0150	0.0181	0.0036	0.0088	0.0169	0.0315	0.0409	0.0283	0.0029	0.0064	0.0019
1983	0.0459	0.0034	0.0063	0.0643	0.0272	0.0182	0.0014	0.0013	0.0160	0.0630	0.0300	0.0192
1984	0.0596	0.0202	0.0470	0.0011	0.0619	0.1209	0.0127	0.0348	0.0607	0.0549	0.0320	0.0351
1985	0.0569	0.0112	0.0348	0.0213	0.0388	0.0310	0.0270	0.0317	0.0130	0.0115	0.0126	0.0506
1986	0.0176	0.0035	0.0051	0.0168	0.0569	0.0283	0.0233	0.0602	0.0388	0.0042	0.0525	0.0569
1987	0.0446	0.0046	0.0012	0.0325	0.0017	0.0571	0.2337	0.0061	0.0320	0.0956	0.0409	0.0809
1988	0.0861	0.0796	0.0186	0.0384	0.0629	0.0144	0.0413	0.0165	0.0464	0.0239	0.0395	0.0695
1989	0.8799	0.0956	0.0549	0.0380	0.0202	0.0414	0.0509	0.0215	0.0468	0.0034	0.0112	0.0339
1990	0.0248	0.0469	0.0268	0.0809	0.0092	0.0591	0.0003	0.1167	0.0225	0.0102	0.0102	0.0185
1991	0.0550	0.0319	0.0488	0.0151	0.0145	0.0227	0.0180	0.0415	0.0260	0.0213	0.0569	0.0247
1992	0.0222	0.0330	0.0173	0.0373	0.0176	0.0019	0.0277	0.0034	0.0024	0.0079	0.0364	0.0037
1993	0.0619	0.0418	0.0637	0.0160	0.0404	0.0298	0.0284	0.0166	0.0242	0.0431	0.0199	0.0569
1994	0.0103	0.0254	0.0058	0.0337	0.0131	0.0287	0.0097	0.0029	0.0305	0.0202	0.0392	0.0640
1995	0.0209	0.0089	0.0076	0.0005	0.0161	0.0163	0.0245	0.0574	0.0467	0.0183	0.0115	0.0015
1996	0.0746	0.0056	0.0051	0.0722	0.0878	0.0672	0.0015	0.0171	0.0197	0.0027	0.1115	0.0515
1997	0.0335	0.0359	0.0170	0.0388	0.0144	0.0478	0.0168	0.0116	0.0070	0.0380	0.0807	0.0672
1998	0.0066	0.0159	0.0289	0.0243	0.0226	0.0084	0.0472	0.0652	0.0550	0.0450	0.0915	0.0450
1999	0.0365	0.0035	0.0157	0.0634	0.0114	0.0304	0.0038	0.0339	0.0374	0.0414	0.0140	0.0314
2000	0.0340	0.0106	0.0269	0.0301	0.0266	0.0986	0.0514	0.0931	0.0551	0.0049	0.0539	0.0201

Table 5: Weighted sum of the FS statistics of Maximum Temperature for Baghdad. (The candidate months of each year are underlined)

	Month											
Year	Jan	Feb	Mar	Aprl	May	Jun	Jul	Aug	Sept	Oct	Nov	Dec
1971	0.0291	0.0136	0.0174	0.0487	0.0214	0.0706	0.0065	0.0175	0.0457	0.0042	0.0480	0.0143
1972	0.0071	0.0351	0.0383	0.0354	0.0374	0.0186	0.0289	0.0022	0.0040	0.0848	0.0884	0.0129
1973	0.0389	0.0250	0.0248	0.0088	0.0037	0.0482	0.0393	0.0247	0.0145	0.0311	0.0428	0.0077
1974	0.0057	0.0138	0.0352	0.0178	0.0422	0.0467	0.0081	0.0056	0.0086	0.0500	0.0545	0.0131
1975	0.0842	0.0511	0.0143	0.0224	0.0003	0.0690	0.0172	0.0200	0.0271	0.0660	0.1148	0.0008
1976	0.0391	0.0035	0.0140	0.0031	0.0028	0.0057	0.0375	0.0541	0.0159	0.0509	0.0919	0.0154
1977	0.0243	0.0548	0.0013	0.0193	0.0117	0.0220	0.0878	0.0356	0.0029	0.0262	0.0804	0.0300
1978	0.0338	0.0277	0.0534	0.0282	0.0213	0.0157	0.0033	0.0061	0.0855	0.0098	0.0249	0.0341
1979	0.0218	0.0139	0.0182	0.0086	0.0179	0.0021	0.0100	0.0383	0.0200	0.0338	0.0689	0.0267
1980	0.0277	0.0609	0.0004	0.0226	0.0103	0.0164	0.0326	0.0213	0.0184	0.0020	0.0351	0.0119
1981	0.0174	0.0075	0.0986	0.0068	0.0303	0.0569	0.0225	0.0984	0.0531	0.0534	0.0586	0.0619
1982	0.0427	0.0318	0.0361	0.0377	0.0182	0.0044	0.0044	0.0445	0.0204	0.0134	0.0233	0.0269
1983	0.0183	0.0072	0.0347	0.0016	0.0103	0.0108	0.0437	0.0380	0.0073	0.0177	0.0410	0.0449
1984	0.0312	0.0392	0.0522	0.0520	0.0077	0.0408	0.0369	0.0354	0.0236	0.0394	0.0267	0.0054
1985	0.0096	0.0169	0.0157	0.0291	0.0044	0.0468	0.0462	0.0282	0.0059	0.0165	0.0160	0.0511
1986	0.1240	0.0041	0.0192	0.0071	0.0102	0.0387	0.0325	0.0002	0.0334	0.0393	0.0082	0.0545
1987	0.0396	0.0158	0.0018	0.0166	0.0236	0.0279	0.0392	0.0203	0.0322	0.0134	0.0213	0.0175
1988	0.0182	0.0117	0.0073	0.0541	0.0348	0.0134	0.0233	0.0983	0.0271	0.0983	0.0241	0.0241
1989	0.0140	0.0250	0.0509	0.0482	0.0408	0.0915	0.0434	0.0315	0.0410	0.0298	0.0343	0.0455
1990	0.0406	0.0096	0.0470	0.0385	0.0305	0.0062	0.0382	0.0376	0.0142	0.0166	0.0066	0.0085
1991	0.0892	0.0110	0.0278	0.0489	0.0231	0.0496	0.0162	0.0166	0.0482	0.0226	0.0367	0.0109
1992	0.0034	0.0412	0.0566	0.0395	0.0180	0.0465	0.0142	0.0328	0.0218	0.0015	0.0606	0.0326
1993	0.0375	0.0534	0.0383	0.0656	0.0273	0.0069	0.0448	0.0313	0.0109	0.1324	0.0823	0.0025
1994	0.0088	0.0253	0.0123	0.0138	0.0423	0.0241	0.0201	0.0271	0.0983	0.0237	0.0136	0.0094
1995	0.0106	0.0279	0.0302	0.0116	0.0085	0.0296	0.0292	0.0104	0.0070	0.0348	0.0810	0.0338
1996	0.0061	0.0031	0.0193	0.0105	0.0291	0.0581	0.0125	0.0010	0.0108	0.0050	0.0420	0.0062
1997	0.0787	0.0234	0.0211	0.0329	0.0243	0.0167	0.0283	0.0094	0.0360	0.0174	0.0387	0.0326
1998	0.0098	0.0123	0.0327	0.0110	0.0515	0.0472	0.0057	0.0054	0.0221	0.0323	0.0359	0.0241
1999	0.0535	0.0351	0.0183	0.0240	0.00821	0.0061	0.0482	0.0252	0.0816	0.0419	0.0917	0.0207
2000	0.0645	0.0024	0.0101	0.0561	0.0587	0.0374	0.0736	0.1319	0.3634	0.0060	0.0861	0.0028

Table 6: Weighted sum of the FS statistics of Relative humidity for Baghdad. (The candidate months of each year are underlined)

	Month											
Year	Jan	Feb	Mar	Aprl	May	Jun	Jul	Aug	Sept	Oct	Nov	Dec
1975	0.0589	0.0078	0.0380	0.0466	0.0301	0.0451	0.0419	0.0459	0.0576	0.0107	0.0499	0.0409
1976	0.0275	0.0087	0.0108	0.0475	0.1181	0.0106	0.0083	0.0501	0.0011	0.0092	0.0357	0.1043
1977	0.0790	0.0290	0.0263	0.0046	0.0176	0.0141	0.0105	0.0596	0.0424	0.0832	0.0490	0.0404
1978	0.0553	0.0515	0.0174	0.0753	0.0158	0.0469	0.0749	0.0279	0.0450	0.0171	0.0578	0.0218
1979	0.0311	0.0147	0.0068	0.0412	0.0224	0.0125	0.0478	0.0905	0.0475	0.0512	0.0643	0.0160
1980	0.0488	0.0532	0.0634	0.0426	0.0629	0.0149	0.0081	0.0303	0.0238	0.0863	0.1087	0.0501
1981	0.0861	0.0796	0.0186	0.0384	0.0049	0.0144	0.0413	0.0069	0.0064	0.0239	0.0395	0.0695
1982	0.0563	0.0840	0.0161	0.0359	0.0354	0.0818	0.0107	0.0927	0.0244	0.1073	0.0224	0.0623
1983	0.0099	0.0288	0.0288	0.0085	0.0908	0.0363	0.0873	0.0093	0.0210	0.1179	0.0423	0.0371
1984	0.0520	0.0558	0.0138	0.0398	0.0306	0.0256	0.0315	0.0227	0.0505	0.0462	0.0292	0.0549
1985	0.0194	0.0057	0.0734	0.0481	0.0063	0.0835	0.0388	0.0739	0.0173	0.0170	0.0262	0.0098
1986	0.0089	0.0636	0.0032	0.0690	0.0422	0.0351	0.0134	0.0291	0.0179	0.0307	0.0348	0.0315
1987	0.0501	0.0181	0.0107	0.0087	0.0130	0.0490	0.0148	0.0158	0.0298	0.0841	0.0842	0.1201
1988	0.0327	0.0275	0.0359	0.0237	0.0362	0.0174	0.0073	0.0057	0.0705	0.0261	0.0491	0.0548
1989	0.0095	0.0146	0.0152	0.0298	0.1489	0.0371	0.0405	0.0084	0.0006	0.0415	0.0126	0.1169
1990	0.0566	0.0420	0.0356	0.0475	0.0344	0.0590	0.0605	0.0721	0.0402	0.0921	0.1179	0.0353
1991	0.0052	0.0307	0.0733	0.0812	0.0645	0.0341	0.0423	0.0021	0.0036	0.0750	0.0077	0.0439
1992	0.0291	0.0356	0.0657	0.0038	0.0516	0.0698	0.0605	0.0323	0.0630	0.0832	0.0275	0.0414
1993	0.0249	0.0776	0.0024	0.0290	0.0164	0.0036	0.0523	0.0031	0.0177	0.0391	0.1006	0.0160
1994	0.0154	0.0126	0.0816	0.0062	0.0536	0.0947	0.0408	0.0557	0.0460	0.0460	0.0396	0.0601
1995	0.0589	0.0078	0.0379	0.0466	0.0301	0.0451	0.0420	0.0458	0.0577	0.0107	0.0499	0.0408
1996	0.0275	0.0087	0.0108	0.0475	0.1181	0.0106	0.0083	0.0501	0.0011	0.0199	0.0357	0.1043
1997	0.0790	0.0290	0.0263	0.0079	0.0176	0.0141	0.0105	0.0596	0.0424	0.0832	0.0490	0.0404
1998	0.0553	0.0515	0.0174	0.0753	0.0158	0.0469	0.0749	0.0279	0.0450	0.0171	0.0578	0.0218
1999	0.0312	0.0147	0.0078	0.0412	0.0224	0.0126	0.0478	0.0905	0.0474	0.0512	0.0643	0.0160
2000	0.0488	0.0532	0.0634	0.0426	0.0026	0.0149	0.0081	0.0303	0.0238	0.0863	0.1087	0.0501

Table 7: The weight factors for each meteorological parameter considered in present study

Parameter	Solar Radiation	Sun Shine Duration	Mean Air Temperature	Maximum Air Temperature	Minimum Air Temperature	Relative Humidity
Weights	0.276	0.248	0.085	0.098	0.186	0.107

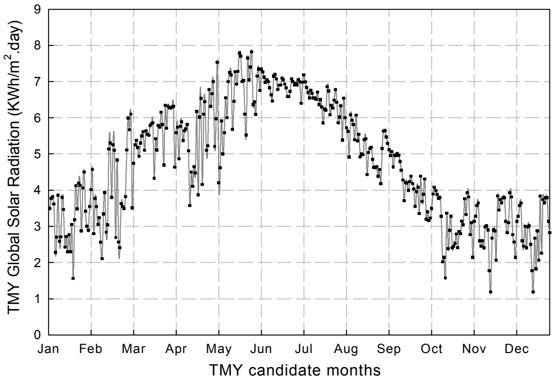

Fig. 7: Annual variation of TMY values of global solar radiation for the whole period of 27 years.

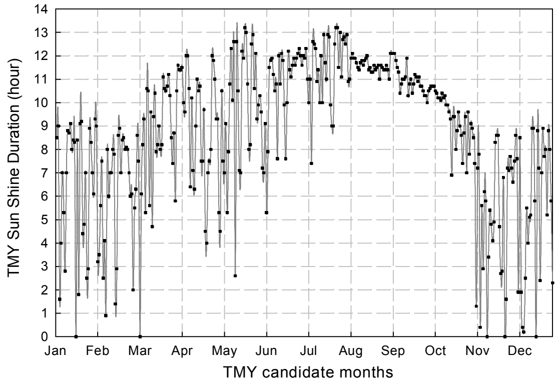

Fig. 8: Annual variation of TMY values of sunshine duration for the whole period of 29 years.

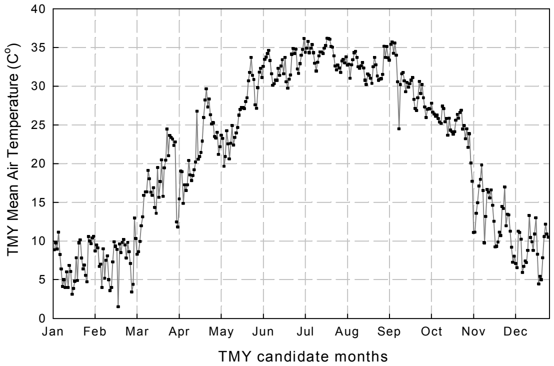

Fig. 9: Annual variation of TMY values of mean air temperature for the whole period of 30 years.

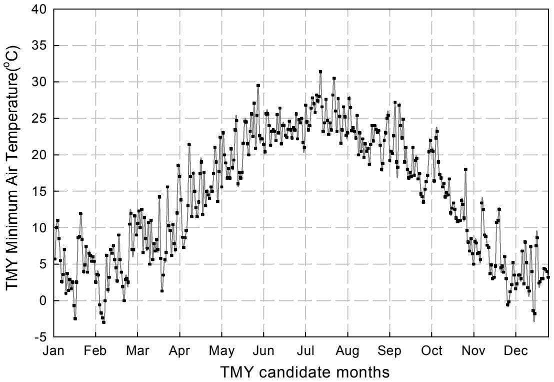

Fig. 10: Annual variation of TMY values of minimum air temperature for the whole period of 30 years.

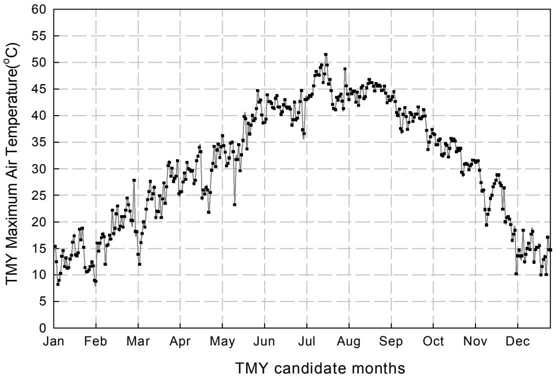

Fig. 11: Annual variation of TMY values of maximum air temperature for the whole period of 30 years.

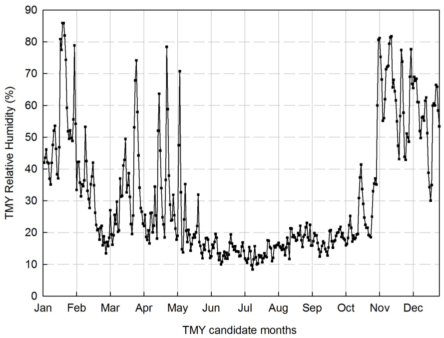

Fig. 12: Annual variation of TMY values of relative humidity for the whole period 26 years.

radiation in other stations which there are no solar radiation measurements available. The resulted TMY data for the solar radiation (kwh/m^2.day), sunshine duration (h), mean air temperature (°C), minimum air temperature (°C), Maximum air temperature (°C) and relative humidity (%) are presented in Figures 7-12, respectively.

Finally the values of month of the 30 years period where calculated to conform the weights for each meteorological elements and the results are shown in Table 7. It was seen that with TMY using Filkenstein-Schafer (FS) static's the solar radiation and sunshine duration have the heights score among the considered meteorological parameters (0.276 kwh/m^2.day for solar radiation and 0.248 h for sunshine duration) and this result indicated that the solar radiation and sunshine duration became the key parameter while the mean, minimum, maximum air temperature and relative humidity became less priority parameters.

CONCLUSION

The generation of the TMY for any location is very important for the solar energy calculation, many applications of thermal engineering and building energy analysis. In present study, a Typical Meteorological Year for six previously mentioned parameters for Baghdad province using at least 26 years measured data and presented throughout year in a graphical form, the solar radiation and sunshine duration play the dominant role in the general situation of the weather.

It is expected that the presented TMY data set for Baghdad will be useful to the designers of solar energy systems, Architects, Urban planning specialist and energy experts.

REFERENCES

1. Ecevit, A., B. Akinoglu and B. Aksoy, 2002. Generation of a typical meteorological year using sunshine duration data. Energy, 27(10): 947-954.
2. Crawley, D.B. and Y.J. Huang, 1997. Does it matter which weather data you use in energy simulations. User News, 18(1): 2-12.
3. Rahman, I.A. and J. Dewsbury, 2007. Selection of typical weather data (test reference years) for Subang, Malaysia. Building and Environment, 42(10): 3636-3641.
4. Hall, I.J., R.R. Prairie, H.E. Anderson and E.C. Boes, 1978. Generation of Typical Meteorological Years for 26 SOLMET stations. Sandia Laboratories Report, Albuquerque, New Mexico,. SAND, pp: 78-1601.
5. Pissimanis, D., G. Karras, V. Notaridou and K. Gavra, 1988. The generation of a “typical meteorological year” for the city of Athens. Solar Energy, 40(5): 405-411.
6. Said, S. and H. Kadry, 1994. Generation of representative weather-year data for Saudi Arabia. Applied Energy, 48(2): 131-136.
7. Al-Hinai, H. and S. Al-Alawi, 1995. Typical solar radiation data for Oman. Applied Energy, 52(2): 153-163.
8. Petrakis, M., S. Lykoudis and P. Kassomenos, 1996. A software tool for the creation of a typical meteorological year. Environmental Software, 11(4): 221-227.
9. Petrakis, M., H. Kambezidis, S. Lykoudis, A. Adamopoulos, P. Kassomenos, I. Michaelides, S. Kalogirou, G. Roditis, I. Chrysis and A. Hadjigianni, 1998. Generation of a “typical meteorological year” for Nicosia, Cyprus. Renewable Energy, 13(3): 381-388.
10. Argiriou, A., S. Lykoudis, S. Kontoyiannidis, C.A. Balaras, D. Asimakopoulos, M. Petrakis and P. Kassomenos, 1999. Comparison of methodologies for TMY generation using 20 years data for Athens, Greece. Solar Energy, 66(1): 33-45.
11. Bulut, H., 2003. Generation of typical solar radiation data for Istanbul, Turkey. International Journal of Energy Research, 27(9): 847-855.
12. Kalogirou, S.A., 2003. Generation of typical meteorological year (TMY-2) for Nicosia, Cyprus. Renewable Energy, 28(15): 2317-2334.
13. Bulut, H., 2004. Typical solar radiation year for southeastern Anatolia. Renewable Energy, 29(9): 1477-1488.
14. Skeiker, K., 2004. Generation of a typical meteorological year for Damascus zone using the Filkenstein–Schafer statistical method. Energy Conversion and Management, 45(1): 99-112.
15. Bilbao, J., A. Miguel, J.A. Franco and A. Ayuso, 2004. Test Reference Year Generation and Evaluation Methods in the Continental Mediterranean Area. Journal of Applied Meteorology, 43(2): 390-400.
16. Zhang, Q., 2006. Development of the typical meteorological database for Chinese locations. Energy and Buildings, 38(11): 1320-1326.
17. Skeiker, K., 2007. Comparison of methodologies for TMY generation using 10 years data for Damascus, Syria. Energy conversion and Management, 48(7): 2090-2102.
18. Chaiyapinunt, S. and K. Mangkornsaksit, 2001. Standard meteorological data for Bangkok. Journal of Energy Heat and Mass Transfer, 23(1): 23-38.
19. Finkelstein, J.M. and R.E. Schafer, 1971. Improved goodness-of-fit tests. Biometrika, 58(3): 641-645.
20. Townsend, T.U., 1989. A method for estimating the long-term performance of direct-coupled photovoltaic systems, 1989, UNIVERSITY OF WISCONSIN.

Persian Abstract

DOI: 10.5829/idosi.ijee.2014.05.01.12

چکیده

اطلاعات هواشناسی سال به سال در حال تغییر می باشد، بنابر این ایجاد اطلاعات یک سال هواسنجی نوعی (TMY) برای نمایش مجموع اطلاعات هواشناسی بلند مدت ضروری می باشد که بعنوان ورودی در مدلسازی، طراحی و ارزیابی عملکرد و محاسبات موازنه انرژی بسیار مهم می باشد. در مطالعه حاضر روش آماری فینکلشتاین-شافر برای آنالیز اطلاعات هواشناسی جمع آوری شده در یک دوره ۳۰ ساله (۲۰۰۰-۱۹۷۱) برای استان بغداد به کار گرفته شد، که شامل ۶ پارامتر هواسنجی اساسی (تشعشع خورشیدی جهانی، مدت تابش آفتاب، حداکثر، حداقل و میانگین دما، رطوبت نسبی) می باشد. ماههای هواسنجی نوعی از دوره سالهای در نظر گرفته شده با استفاده از کمترین انحراف (FS) نسبت به بلند مدت یک TMY برای استان بغداد انتخاب شدند.

Iranica Journal of Energy & Environment 5 (1): 87-93, 2014
ISSN 2079-2115
IJEE an Official Peer Reviewed Journal of Babol Noshirvani University of Technology
DOI: 10.5829/idosi.ijee.2014.05.01.13

BUT

Physical Properties of Silver Doped ZnSe Thin Films for Photovoltaic Applications

[1]Nazar Abbas Shah, [2]Mussart Abbas, [2]Waqar Adil Syed and [1]Waqar Mahmood

[1]Thin Films Technology (TFT) Research Laboratory, Department of Physics,
COMSATS Institute of Information Technology, Islamabad 40000 Pakistan
[2]International Islamic University, Islamabad 40000 Pakistan

(Received: December 23, 2013; Accepted in Revised Form: March8, 2014)

Abstract: Closed space sublimation (CSS) technique was used to deposit pure (99.99%) zinc selenide(ZnSe) powder on to glass substrates for fabricating the ZnSe thin films. The temperatures of source, substrate and the deposition time were optimized to deposit thin films of different thicknesses. Silver (Ag) was used as a dopant by ion exchange process in the ZnSe thin films. The structural analysis showed that as-deposited ZnSe thin films were polycrystalline having preferred orientation [111] direction. Micro structural parameters such as crystallite size, lattice parameter were determined using X-rays diffraction (XRD). Grains boundaries, roughness on surface and the grain density of the thin film samples were measured by scanning electron and atomic force microscopy before and after Ag doping.As-deposited, Ag-doped ZnSe samples before and after annealing were optically characterized by spectrophotometer in ultra violet, visible and infrared regions. The energy band gap of as-deposited ZnSe thin films for varying thicknesses were ranging from 2.62-2.67 eV which was reduced after Ag doping.The electrical properties showed that as-deposited thin films were highly resistive of the order of $10^8\Omega$-cm and after Ag immersion, it was reduced to 1Ω-cm. Deposition parameters and Ag doping influenced the structural, surface, optical and electrical properties.

Key words: ZnSe thin films · Vacuum coating · Surface morphology · Electrical properties

INTRODUCTION

Since last few decades zinc selenide (ZnSe) gained a remarkable attention due to its tuneable energy band gap. It belongs to II-VI semiconductor family. It has direct band gap transition type [1]. It is a leading material in the fabrication of solar cells [2]. The energy band gap of ZnSe at room temperature is 2.7 eV, make it suitable candidate for the window layer in the solar cells fabrication [3-5].

ZnSe had been fabricated by different approaches including thermal evaporation [6], sputtering [7], chemical bath deposition [8], pyrolysis [9] two source evaporation [10], pulsed laser deposition [11], Melt-quenching technique [12] and closed space sublimation (CSS) technique [13]. In group I, silver (Ag) increases the electrical conductivity due to acceptor dopant in II-VI materials [14]. Bismuth was used as a dopant to make low resistive P-type ZnSe thin films with complex method of doping [11]. The electrical and the optical properties are important for solar cell applications [1, 8, 10, 13]. Silver and copper (Cu) was doped by ion exchange process in II-VI semiconductor materials [10, 13].

In the present work, ZnSe thin films were sublimated using closed space technique and doped with low concentration solution containing 1 g of $Ag(NO_3)_2$ in 100 ml of distilled water at room temperature by ion exchange process.After immersion, Annealing was carried out for diffusion of Ag into the films. The prepared samples were characterized in various aspects including structural, morphological, elemental composition, optical and electrical parameters. A comparative study was carried out between as-deposited and Ag-doped ZnSe thin film samples.

Corresponding Author: Nazar Abbas Shah, Thin Films Technology (TFT) Research Laboratory,
Department of Physics COMSATS Institute of Information Technology, Islamabad 40000 Pakistan.

MATERIALS AND METHODS

Zinc selenide powder was used as a source material to deposit polycrystalline thin films on to glass slides (as substrates) under vacuum. The dimension of the glass slide was 75 mm x 25mm. Before deposition, the substrates were cleaned with isopropyl alcohol (IPA) in ultrasonic bath at 65°C for 30 minutes and dried in air. Substrate was loaded in the vacuum chamber with 25 mg source material in the cleaned graphite boat. The vacuum chamber was evacuated up to 10^{-5} mbar with the help of rotary and diffusion pumps.Two Halogen lamps were switched on for direct heating the source and substrate after attaining the desire vacuum. A1000 W lamp was applied to heat the source material and 500 W was used to heat the substrate. The distance between source and substrate was 5 mm for a good quality film. Temperature gradient was created between the source and substrate using mica sheet. A graphite slab was placed on the substrate for uniform heating. K-type thermocouple wires were use to monitor the temperatures of the source and substrate. Halogen lamps were switched on to increase the temperatures of source and substrate up to 575 and 475°C, respectively. Different deposition times were offer ranging from 01 to 05 minutes for varying thickness of films. After attaining the deposition time, the lamps were switched off and left the chamber to cool down to room temperature under vacuum to avoid contamination or oxidization.

Low concentrated (0.1/100ml) solution of Ag $(NO_3)_2$ was prepared in the distilled water. ZnSe as-deposited thin films were dipped in the solution for different times ranging from 5 minute to 40 minutes. After doping, these films were dipped in IPA and dried in a heater. Ag layer was formed on ZnSe thin film surface after immersion which was due to the ion exchange process. The doped thin films were then annealed under vacuum at 400°C for 1 hfor diffusion of Ag in to these films. Different immersed time relates to different composition of Ag into the films. Finally Ag-doped ZnSesamples were characterized by X-rays diffraction (XRD) for structural analysis, scanning electron microscope (SEM) and atomic force microscope (AFM) to analyse the surface, UV-VIS-NIR spectrophotometer to observe the optical properties and four probe method using Hall measurement apparatus for the electrical properties before and after Ag doping for various solar cells applications.

RESULTS AND DISCUSSION

X-Rays Diffraction Analysis: X-rays diffraction was used to estimate the structural properties of thin films. It is a non destructive technique which gives information about phases, crystallite size, lattice parameter, internal stress and dislocation density etc. XRD of the prepared thin film samples were characterized by spectrometer PANalytical X'Pert Pro. The operating parameters of the spectrometer were Cu-Kα line; wavelength was1.5406Å. Diffraction angle varied from 20 to 60 degrees. The XRD traces of as-deposited ZnSe thin filmswith varying thickness are shown in Fig. 1. The crystallite size can be calculated using Scherrer formula:

$$D = (0.89)\lambda / \beta\cos\theta \qquad (1)$$

where 0.89 is a constant, λ is the wavelength used, β is full width at half maximum and θ is the diffraction angle. All other parameters including dislocation density, strain etc can be obtained using Eqs. (2) and (3), respectively.

$$\varepsilon = \frac{\beta Cos\theta}{4} \qquad (2)$$

$$\delta = \frac{n}{D^2} \qquad (3)$$

Fig. 1 relates to the effect of thickness of as-deposited ZnSe thin films. The peak width of (111) and the intensity level increases gradually with the increase in film thickness. This observation may be attributed to the improvement of particle size. The intensity increases due to the orientation in the structure of thin films. Table 1 shows the variation in lattice parameters, the crystallite size, strain and dislocation density. The decrease in dislocation density, strain and the increase in crystallite size are observed as the film thickness increases. These effects are due to the improvement in crystal structure. Fig. 2 represents the XRD traces of A-doped ZnSe samples. The preferred orientation of as deposited ZnSe thin films is (111) with cubic phase as matched with the standard cards. As the thin films were doped in low concentrated silver nitrate solution at room temperature and subsequent annealing, the orientation of the (111) plane was disturbed along with the loss of texture of ZnSe thin films after immersion. The peak intensity of planes (220) and (311) were small as compared to (111) direction of as-deposited ZnSe thin films. After Ag immersion with post annealing, the peak intensity of (220) and (311) were large as the intensity level of (111) was decreased which was evident of loss of texture after Ag immersion. No AgSe compound peak was found which indicated that Ag diffused interstitially [14]. The results are in consistent with the reported literature [10, 13].

Table 1: Table Effect of thickness on micro structural parameters

Thickness (nm)	2θ (Deg.)	Lattice parameters a(A°)	Grain size D (nm)	Strain^a x 10^{-3} (lin^{-2} m^{-4})	Dislocation Density δ x10^{15} (lin m^{-2})
986	27.1627	5.686	53.8	0.673	0.346
912	27.1982	5.679	51.0	0.709	0.384
895	27.2159	5.675	48.6	0.745	0.423
880	27.3199	5.654	44.8	0.809	0.499

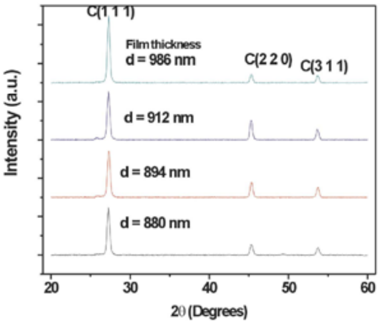

Fig. 1: X-ray diffraction patterns of as-deposited ZnSe thin films with variation in thickness

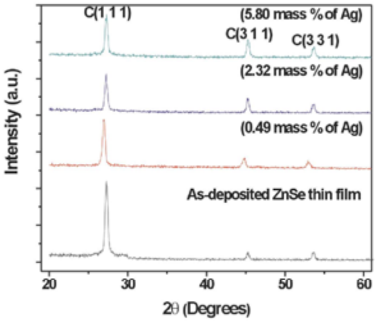

Fig. 2: X-ray diffraction patterns of as-deposited ZnSe thin film and Ag-doped ZnSe samples

Surface Morphology: The surface morphological study was carried out using scanning electron microscope. The SEM micrographs of as-deposited and Ag-doped ZnSe thin film samples are shown in Fig. 3. The average grain size of as-deposited ZnSe thin film was 250 nm which was increased up to 400 nm after Ag immersion. The increase in grain size was due to the process of coalescences, a well known phenomenon in II-VI semiconductor material [14]. Annealing temperature is most powerful toolfor Ag diffusion in ZnSe thin films also usefulin the reorientation of the structure [14]. The elemental analysis of un-doped and Ag-doped ZnSe thin film samples are carried out by energy dispersive X-rays (EDX) attached withthe SEM. Theelemental results show the atomic contents of elements, present in the ZnSe thin films. The as-deposited thin films are selenium enriched. After immersion of Ag $(NO_3)_2$ with subsequent annealing at 400°C, the elemental composition are changed. After Ag-doping, the Se composition decreased as the Ag concentration increases.

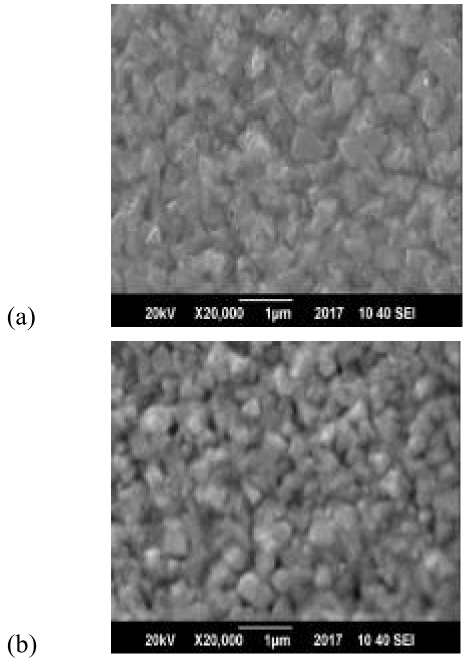

Fig. 3: Scanning electron microscope micrographs of (a) as-deposited ZnSe thin film and (b) Ag-doped ZnSe sample

Atomic Force Microscopy: Atomic force microscopeis an important tool to observe the surface morphology. It provides two and three dimensional images of the sample surface. The average roughness of the sample surface can be measured by using AFM analysis. The images of atomic force microscopy of as-deposited and Ag-doped ZnSe thin film samples are shown in Fig. 4. As the doping contents are increased, the colour of the surface is changed; dark part of the image shows the diffusion of Ag into the ZnSethin filmsamples.As the number of grain decreases, due to the diffusion of Ag impurity in ZnSe films. Thechanges on the AFM images are observed after Ag doping in ZnSethin films. Table 2 shows that the surface roughness of Ag doped ZnSe samples increases due to increase in silver composition.

Optical Analysis: The transmission spectra of as-deposited and Ag-doped ZnSe thin film samples are taken in the ultra violet (UV), visible(VIS) and infrared (IR) regions (300-2000 nm) by using UV-VIS-NIR Perkin Elmer

Table 2: Surface roughness and variation in energy band gap of ZnSe samples

Immersion time (min)	Ag (Mass %)	Roughness on the surface (nm)	Energy band gap (eV)
0	0	15	2.65±0.01
10	0.5	10	2.64±0.01
20	2.3	11	2.63±0.01
30	6	12	2.62±0.01

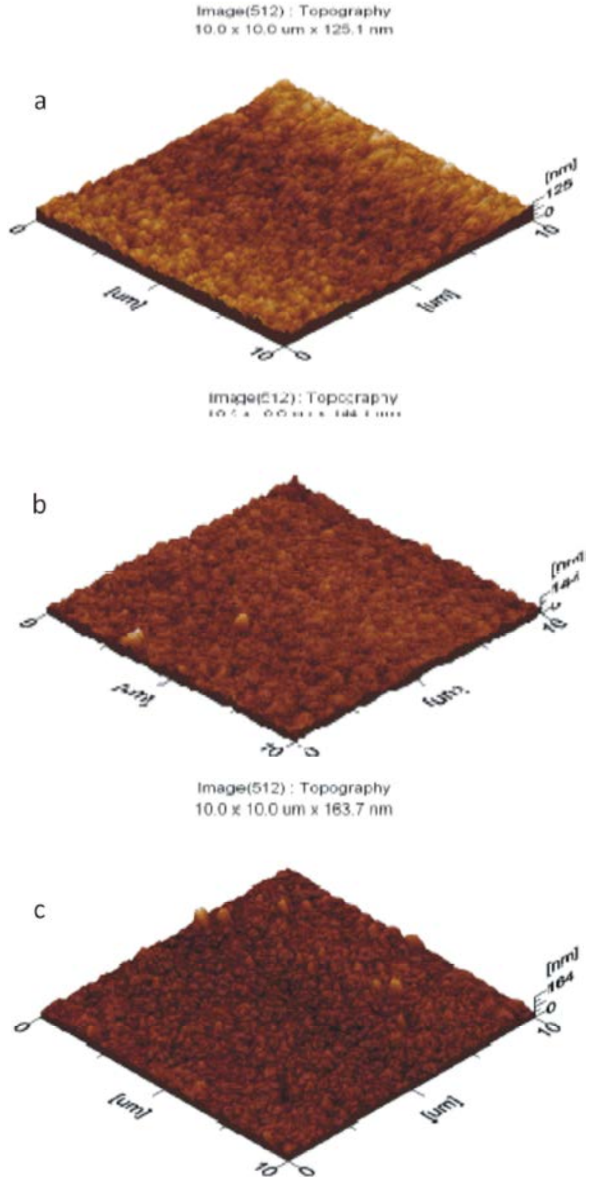

Fig. 4: Atomic force microscopy of (a) as-deposited ZnSe thin film (b) & (c) Ag-doped ZnSe sample

spectrophotometer Lambda 950 with UV Win lab software. The machine directly measures the transmission of the sample. By using the %T data,all other optical parameters can be calculated byswanpoul model [14-16]. The formula for the optical thickness is given by:

$$d = \frac{\lambda_{\max}\lambda_{\min}}{4n(\lambda_{\max} - \lambda_{\min})} \qquad (4)$$

In Eq. (4)$\lambda_{\max}$ is maximum transmission and $\lambda_{\min}$ is the consecutive minimum transmission respectively. For the calculation of refractive index n, the following relation is used:

$$n = \frac{[N + (N^2 - 4s^2)^{\frac{1}{2}}]}{2} \qquad (5)$$

and

$$N = 1 + s^2 + 4s(\frac{T_{\max} - T_{\min}}{T_{\max} * T_{\min}}) \qquad (6)$$

where T_{max} and T_{min} represents maximum and minimum transmission. 's' is the refractive index of glass. The optical energyband gap E_g is determine by thegiven relation

$$\alpha h\nu = A(h\nu - E_g)^{N/2} \qquad (7)$$

where 'A' is the constant and $h\upsilon$ is the photon energy. The absorption coefficientα is measured by the Eq. (8).

(8)

The transmission decreased with the increase of thickness, which is due to trapping of light in the sample. The transmission of light is 70 to 90 % in the visible and IR region, so the ZnSe thin films can be used as window layer material in the solar cells. The energy band gap of ZnSe thin films is 2.7 eV, which is a suitable light absorber in UV region.In Fig. 5 with increasing thickness, there are more possibilities for absorption and scattering of the light while passing through the material, which is one of the reasons of decreasing transmission. The transmission spectra of Ag-doped samples as compared toas-deposited ZnSe thin film are shown in Fig. 6. An increasing the Ag content, the transmission is decreasing due to the fact that Ag is a good reflector. By using Eq. (7) and extrapolating $(\alpha.h\upsilon)^2$ against the photon energy (hυ), the band gap of ZnSe thin films can be calculated. As-deposited ZnSe thin films has 2.66 eV, which was shrink up to 2.62 eV after Ag doping. Although there is a

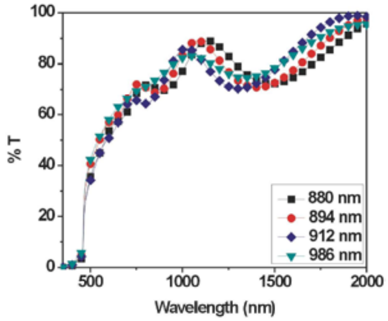

Fig. 5: Optical transmission of as-deposited ZnSe thin films of various thicknesses

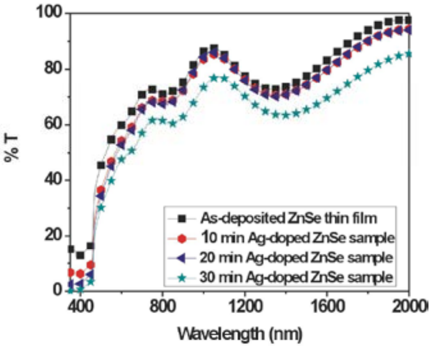

Fig. 6: Optical transmission of as-deposited ZnSe thin film and Ag-doped ZnSe samples

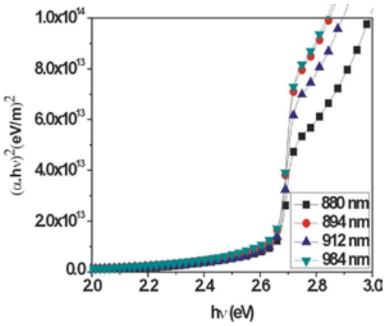

Fig. 7: Optical energy band gap as-deposited ZnSe thin films with varying thicknesses

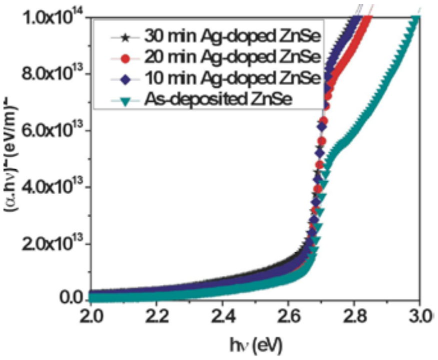

Fig. 8: Energy band gap of Ag-doped ZnSe samples with increasing Ag composition

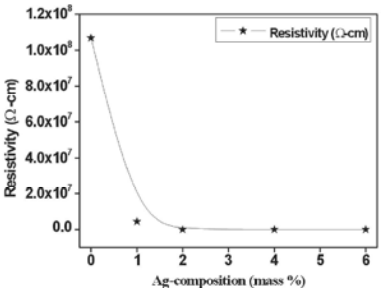

Fig. 9: Change in resistivity with the increase in Ag composition

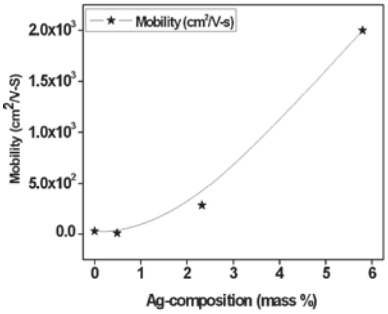

Fig. 10: Mobility variations with the increase in Ag composition

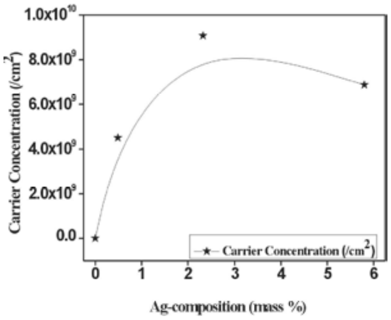

Fig. 11: Variation of carrier's concentration with the increase in Ag composition

small change in energy band gap, the decrease is related to the Ag compositions in ZnSe samples. The energy band gap was reduced due to the overlapping of energy levels which were created due to Ag doping in the ZnSe thin films. Fig. 8 shows the energy band gaps *Eg* of the Ag-doped ZnSe samples with different compositions of Ag. Table 2 shows the variation in energy band gap after Ag doping.

Electrical Measurements: Hall apparatus (Ecopia HMS 5000) was used to measure the electrical properties i.e the resistivity, sheet concentration and mobility. A1 nA current at room temperature with constant magnetic field of 0.5 Twas applied for these measurements.

Ag compositionincreases as the immersion time increased and decrease in resistivity is observed. The lowest value of resistivity 1.4 Ω-cm after Ag doping is observed. The As-deposited ZnSe thin films have the resistivity of 1.069 × 10^8Ω-cm. Decrease in resistivity with the Ag doping isof several orders of magnitude, as shown in Fig. 9. As the Ag composition increases, the value of mobility also increases as illustrated in Fig. 10. The behaviour ofcarrier's concentration with the Ag composition is checked. Carrier's concentration increases to some extent and then decreased sharply as shown in Fig. 11. This behaviour shows that Ag facilitates in ZnSe thin filmsamples due to the larger grains and less grain boundaries. The number of charge carrier increases as the Ag composition increases, confirmed by the change in mobility and resistivity. The results show the change in electrical properties due to the diffusion of Ag in the ZnSe thin film samples.

CONCLUSIONS

ZnSe thin films showed strong adherence with glass substrates. The preferred orientation was (111) with cubic phase as observed in the XRD. The width and intensity of the peaks in the patterns were proportional withthe increase in thickness. The crystallite size increased as thickness increased but a decreased in strain and dislocation density was observed. These effects were attributed to the improvement in the crystal structure. Ag doped ZnSe thin films in low concentrated $Ag(NO_3)_2$ solution and after annealing, the texture was lost. The SEM micrographs showed the average grain size 250 nm for as-deposited which was increased up to 400 nm and grain boundaries were decreased after Ag immersion. The effect might was due to the diffusion of Ag into the ZnSe thin filmsamples. The mass percentage of Ag was about 6 % after Ag immersion. AFM results confirmed the surface roughness decreased from 15 to 12 as the Ag was diffused in ZnSe thin films. Optical parameters including transmission and energy band gap showed the decreasing trend after Ag doping in ZnSe thin films. The resistivity of as-deposited ZnSe thin films was 10^8Ω-cm, which was reduced up to 1 Ω-cm after Ag diffusion. These results confirmed that Ag affects theZnSe and altered the physical properties after immersion. On the basis of these finding, the ZnSe thin films could be used as a window layer/contact in the II-VI thin filmsolar cells.

ACKNOWLEDGEMENTS

The authors are thankful to higher education commission (HEC) Pakistan for the financial supportthrough project No. 20 – 1187 / R & D / 09.We are also thankful to COMSATS Institute of information Technology (CIIT) Islamabad for providing excellent research facilities and funding through project.

REFERENCES

1. Ismail, B. and R. Gould, 1989. Structural and electronic properties of evaporated thin films of cadmium telluride. Physica Status Solidi (A), 115(1): 237-245.
2. Chopra, K.L. and S.R. Das, 1983. Why Thin Film Solar Cells? Springer.
3. Yang, C., Y. Hsieh, M. Kuo, P. Tseng, Z. Yeh, K. Chiu, J. Shen, A. Chu, W. Chou and W. Lan, 2003. Compressive strain induced heavy hole and light hole splitting of $Zn_{1-x}Cd_xSe$ epilayers grown by molecular beam epitaxy. Materials Chemistry and Physics, 78(3): 602-607.
4. Mokili, B., Y. Charreire, R. Cortes and D. Lincot, 1996. Extended X-ray absorption fine structure studies of zinc hydroxo-sulphide thin films chemically deposited from aqueous solution. Thin Solid Films, 288(1): 21-28.
5. Tripathi, L., S. Mishra and R.N. SINGH, 1993. Luminescence in ZnSe doped with Pr and (Sn, Pr) phosphors. Indian journal of Pure & Applied Physics, 31(12): 899-903.
6. Thutupalli, G. and S. Tomlin, 1976. The optical properties of thin films of cadmium and zinc selenides and tellurides. Journal of Physics D: Applied Physics, 9(11): 1639-1646.
7. Kuzel Jr, R., V. Valvoda, M. Chladek, J. Musil and J. Matous, 1995. XRD microstructural study of Zn films deposited by unbalanced magnetron sputtering. Thin Solid Films, 263(2): 150-158.
8. Rizzo, A., M. Tagliente, L. Caneve and S. Scaglione, 2000. The influence of the momentum transfer on the structural and optical properties of ZnSe thin films prepared by rf magnetron sputtering. Thin Solid Films, 368(1): 8-14.
9. Balasubramanian, A., N. Sankar, S. Ramakrishnan and K. Ramachandran, 2004. Thermal conductivity of ZnSe by molecular dynamics simulation. Crystal Research and Technology, 39(6): 558-563.

10. Ali, Z., A.K. Aqili, A. Maqsood and S. J Akhtar, 2005. Properties of Cu-doped low resistive ZnSe films deposited by two-sourced evaporation. Vacuum, 80(4): 302-309.
11. Shen, Y., N. Xu, W. Hu, X. Xu, J. Sun, Z. Ying and J. Wu, 2008. Bismuth doped ZnSe films fabricated on silicon substrates by pulsed laser deposition. Solid-State Electronics, 52(11): 1833-1836.
12. Sharma, J. and S. Tripathi, 2011. Effect of deposition pressure on structural, optical and electrical properties of zinc selenide thin films. Physica B: Condensed Matter, 406(9): 1757-1762.
13. Aqilia, A., Z. Alib and Z. Hussainb, 2012. Optical and structural properties of silver doped ZnSe thin films prepared by CSS and ion exchange process. in Proc. of SPIE Vol. 2012.
14. Shah, N.A. and W. Mahmood, 2013. Physical properties of sublimated zinc telluride thin films for solar cell applications. Thin Solid Films, 544: 307-312.
15. Shah, N., R. Sagar, W. Mahmood and W. Syed, 2012. Cu-doping effects on the physical properties of cadmium sulfide thin films. Journal of Alloys and Compounds, 512(1): 185-189.
16. Shah, N., A. Nazir, W. Mahmood, W. Syed, S. Butt, Z. Ali and A. Maqsood, 2012. Physical properties and characterization of Ag doped CdS thin films. Journal of Alloys and Compounds, 512(1): 27-32.

Persian Abstract

DOI: 10.5829/idosi.ijee.2014.05.01.13

چکیده

روش تصعید فضای بسته (CSS) برای لایه نشانی پودر سلنید روی (ZnSe) خالص (۹۹.۹۹٪) در سوبسترای شیشه ای برای ساخت فیلم های لایه نازک ZnSe استفاده شد. درجه حرارت منبع، بستر و زمان لایه نشانی برای نشاندن فیلم لایه نازک با ضخامت های مختلف بهینه سازی شد. در فیلم های لایه نازک ZnSe، نقره (Ag) در طی فرایند تبادل یونی به عنوان یک دوپه کننده استفاده شد. تجزیه و تحلیل ساختاری نشان داد که فیلم های لایه نازک ZnSe لایه نشانی شده پلی کریستالی با جهت گیری ترجیحی [۱۱۱] بودند. پارامترهای ریز ساختاری مانند اندازه کریستال و پارامتر شبکه با استفاده از پراش اشعه X (XRD) تعیین شد. مرز دانه ها، زبری روی سطح و چگالی دانه از نمونه های فیلم لایه نازک با روبش الکترونی و میکروسکوپ نیروی اتمی قبل و بعد از دوپینگ نقره اندازه گیری شد. نمونه های ZnSe نقره دوپه شده، قبل و بعد از بازپخت نوری با دستگاه اسپکتروفتومتر در ماورا بنفش، ناحیه مرئی و مادون قرمز مشخص شد. گاف انرژی فیلم های لایه نازک ZnSe لایه نشانی شده برای ضخامتهای مختلف در محدوده ۲/۶۲-۲/۶۷ eV بود که بعد از دوپه شدن Ag کاهش یافت. خواص الکتریکی نشان داد که فیلم های لایه نازک نشانده شده بسیار مقاومتی در درجه Ω-cm $۱۰^{۸}$ سانتی متر بودند، و بعد از غوطه ور شدن نقره به Ω-cm ۱کاهش یافت. پارامترهای لایه نشانی و دوپینگ نقره خواص ساختاری ، سطح، نوری و الکتریکی را تحت تاثیر قرار داد.

Iranica Journal of Energy & Environment 5 (1): 94-100, 2014
ISSN 2079-2115
IJEE an Official Peer Reviewed Journal of Babol Noshirvani University of Technology
DOI: 10.5829/idosi.ijee.2014.05.01.14

BUT

Isolation Purification and Screening of Biodegradable Polymer PHB Producing Cyanobacteria from Marine and Fresh Water Resources

K. Gopi, S. Balaji and B. Muthuvelan

School of Bio Sciences and Technology, VIT University, Vellore, India

(Received: February 12, 2014; Accepted in Revised Form: March 17, 2014)

Abstract: Fifteen cyanobacteria species were isolated from fresh water and marine water resources from different parts of Tamil Nadu, India. Based on their morphological features they were identified through microscopic observations. The isolates were then screened for PHB production using nile red staining. It was found eleven of them were capable of producing PHB in their native forms. Further, PHB quantitative analysis by HPLC showed marine *Phormidium* sp with 7.60±0.005 mg/L (7.6%) of PHB, followed by *Synechococcus* sp with 4.59±0.012 mg/L (4.5%), *Synechocystis* sp with 3.74±0.007 mg/L (3.7%) and *Anabaena* sp with 2.31±0.012 mg/L (2.3%) of fresh water isolates. Among the isolates, *Phormidium* sp (VIT-BMN3) isolated from marine environments is reporting first time for its PHB production. In addition, biodegradable polymer extracted in hot chloroform is analysed by FTIR which showed strong bands near 1725 cm^{-1}, 2977 cm^{-1} and 3437 cm^{-1} wave numbers and confirms the presence of ester carbonyl group (C=O), methylene C-H vibration and terminal OH group of PHB, respectively. Overall, nile red staining, HPLC analysis and FTIR spectrums obtained for all cultures conforms the PHB production by our isolates in their native conditions. Further studies of media optimization for increased PHB production are under the process.

Key words: *Cyanobacteria* · Poly-β-hydroxy butyrate · Biopolymers; Biodegradable

INTRODUCTION

Polyhydroxyalkanoates (PHAs) are microbial polyesters produced by various microorganisms [1] including cyanobacteria. Cyanobacteria, also known as blue-green algae are prokaryotic organisms which can carry out oxygenic photosynthesis under photoautotrophic conditions [2, 3]. PHAs are among the most investigated biodegradable polymers in recent years due to their similar chemical and physical properties to polypropylene and also some special properties like nontoxic, biocompatibility and biodegradability [4]. PHAs composition was first reported from bacteria as unknown material in the form of homopolyester of the 3-hydroxybutyric acid (PHB) [5] and the biodegradability of PHB was noticed since 1958 by Macrae, Wilkinson and others [6-8]. Today, more than 300 different microorganisms are found to synthesize and accumulate PHAs intracellular. The most well studied type of PHAs is PHB.

To reduce the production cost, it is more advantageous to use photosynthetic organisms such as plants and cyanobacteria as alternative host systems because of their minimal nutrient requirement for growth and biomass production and photoautotrophic nature [9, 10]. Recently, higher plants into which PHB synthesis genes have been introduced have been used to produce PHB from CO_2 by photosynthesis. The transformant of *Arabidopsis thaliana* harboring PHB genes in a plastid accumulated approximately 14% dry weight as PHB in its leaves [11]. Under appropriate growth conditions, PHB can be accumulated up to 85% of the cellular dry weight of *Alcaligenes eutrophus* [12] and 70-90% in recombinant *Escherichia coli* cells [13-15]. Nevertheless, the demands for plant products can be expected to increase, which certainly will require more fertile land to be used for agricultural activities. In such a scenario, using cyanobacteria to produce PHB may become more promising because the large-scale cultivation of cyanobacteria does not require fertile land [16].

Corresponding Author: B. Muthuvelan, School of Bio Sciences and Technology, VIT University, Vellore. India.
Tel: +91-9840404304.

In addition, cyanobacteria grow faster than higher plants and some can accumulate PHB under nitrogen or phosphorus limited conditions [17]. Cyanobacteria have a mechanism for storing phosphate predominantly in the form of polyphosphate and during phosphate deficiency these organisms counter the paucity of ð by breaking the polyphosphate chains [18]. Various species of cyanobacteria accumulate considerable amounts of PHB. The presence of PHB inclusion bodies in cyanobacteria was first reported by Carr in 1966 [19] following extraction of PHB from *Chloroglea fritschii* [20]. To date, the occurrence of PHB has been demonstrated for several cyanobacteria such as *Spirulina* sp, *Aphanothece* sp, *Gloeothece* sp, *Synechococcus* sp etc. Since then, the occurrence of PHB has been reported for several other species of cyanobacteria, including *Gloeocapsa* sp., *Spirulina platensis, Aphanothece* sp [21], *Synechococcus* sp [22], *Synechosystis* sp [23]. However, *Synechosystis* sp PCC6803 has only been reported so far for highest amount of PHB accumulation nearly 38% of its dry cell weight (DCW) [14]. Industrial utilization of cyanobacteria as PHB producers has the advantage of converting waste carbon dioxide, a greenhouse gas to environmental friendly plastics using the energy of sunlight. Therefore, in the current situation, searching for novel cyanobacterial species for increased PHB production has become obligatory. In the present report, 15 cyanobacterial species from different environments were isolated and screened for PHB production in their native conditions using nile red staining method followed by HPLC and FTIR analysis.

MATERIALS AND METHODS

Sample Collection: Samples were collected from both fresh water regions as well as from marine environments of different parts of Tamil Nadu which includes Trichy, Elagiri, Chennai, Mandapam, Vellore.

Isolation and Purification of Cyanobacterial Species: Cyanobacterial species were isolated and purified from different sources using basic microbial techniques primarily with serial dilution and followed by spread plating and quadrant streaking on BG11 agar plates. Bacterial and fungal contamination was avoided using antibiotics like; streptomycin and cycloheximide, each at 100 µg/mL [24]. Morphological identification of the cyanobacterial strains was performed through microscopic observations. In total 15 different strains were isolated, in which 12 strains from fresh water bodies and 3 strains are from marine environments.

Culture Conditions: The purified axenic cultures were grown in 250 mL Erlenmeyer flasks containing 100 mL of BG11 broth medium (Himedia). The medium constituents were citric acid: 0.006 g, ferric citrate: 0.006 g, EDTA: 0.001 g, Na_2CO_3: 0.02 g, $MgSO_4.7H_2O$: 0.075 g, $CaCl_2 .2H_2O$: 0.036 g, K_2HPO_4: 0.04 g, $MnCl_2 .4H_2O$: 1.81 mg, Na_2MoO_4: 0.039 mg, H_3BO_3: 2.86 mg, $CuSO_4 .5H_2O$: 0.079 mg, $Co (SO_4) .7H_2O$: 0.04 mg and $ZnSO_4 .7H_2O$: 0.222 mg/L. The pH of the culture medium was maintained at 8.0. Experimental cultures were incubated at 25±2°C, 14/10 light/dark cycle with illumination of 3000 lux under cool white fluorescent lamps. Every day the cultures were mildly shaken by hand for 10 minutes.

Screening for PHB Producing Cyanobacterial Species

Nile Red Staining: PHB accumulation in cyanobacterial isolates was observed by staining with lipophilic dye Nile red. Staining solution was prepared by dissolving 1 mg Nile red in 1 mL of dimethyl sulfoxide (DMSO). Two drops of Nile red dye solution were added to 200 µL sterile culture medium and incubated for 10 min at 55°C. Cells were then centrifuged and washed with PBS solution to remove excess of dye. Slides were prepared with stained cultures and were observed under fluorescent microscope (Olympus-BX61) at an excitation wavelength of 450–490 nm [16].

Quantification of PHB using HPLC: A modified HPLC method [19] was used to quantify the PHB produced from different cultures. From each purified samples (O.D 1-1.5@ 730 nm) 5 mL of culture was taken in 15 mL screw cap centrifuge tubes and centrifuged (MPW-351R, Poland) at 10,000 rpm for 10 minutes. The resulting pellet was dried at 80°C at overnight. The dry pellets were boiled in 1 mL of conc. H_2SO_4 at 90°C for 30 minutes. Samples were then diluted with 4 mL of 5 mM H_2SO_4 and vortexed. From this, 200 µL of sample was taken in a fresh micro centrifuge tube and further diluted 10 times with 5 mM H_2SO_4 followed by membrane filtration using 0.22 µm filters (Millipore). 50 µl of this filtered sample was then analysed by HPLC with an ROA column 78 X 300 mm (Shimadzu CBM-20A, Made in Japan). Commercially available PHB (Sigma-Aldrich) was also processed in parallel with the samples.

Extraction of poly-β-hydroxybutyrate (PHB): Cells were harvested by centrifugation at 8000 rpm for 10 min and washed with distilled water followed by overnight methanol suspension at 4°C for the removal of pigments. The pellet obtained after centrifugation was dried at 60°C for 1 h and PHB was extracted into hot chloroform using soxhlet extractor [25]. After evaporation of the solvent, PHB was obtained as a tough, translucent film which was further analyzed by FTIR spectroscopy.

Fourier-transform Infrared Spectroscopy (FT-IR) Analysis: Chloroform was evaporated from the extracted PHB and KBr pellet was prepared with PHB from different cultures and standard PHB from Sigma. A PerkinElmer spectrum GX FTIR spectrometer was used with spectral range, 4000-450 cm^{-1} to record the IR spectra.

RESULTS AND DISCUSSION

The efficient production of PHB (bioplastics) using cyanobacteria is technologically challenging. Nevertheless, it remains as an attractive approach considering the fact that the carbon source comes directly from atmospheric CO_2 for PHB synthesis [13, 26]. The present study aimed to screen novel and potential cyanobacterial species from different environments for PHB production.

Cyanobacterial Isolates and Screening for PHB Production: A total of 15 strains were isolated from different regions of Tamil Nadu. Among the strains isolated, 3 species are from marine resources while rest of them are from freshwater regions. On the basis of their morphological features observed through microscopic studies, cultures were identified in genus level as *Anabaena* sp., *Synechococcus* sp., *Synechocystis* sp., *Spirulina* sp., *Nostoc* sp., *Phormidium* sp., *Oscillatoria willei, Lyngbya* sp. and summarised them in Table 1. All species were primarily screened for PHB production using Nile red staining method and found 11 out of them are capable of producing PHB which were seen as bright orange colour inclusions under the fluorescent microscope (Fig. 1). All the positive species were named as VIT-BMN1 to VIT-BMN11.

Quantification of PHB using HPLC: Eleven cyanobacterial isolates found promising for PHB production with Nile red staining, were further taken for PHB quantification using high performance liquid chromatography by converting PHB into crotonic acid. PHB analysis relies on measuring crotonic acid which is formed by acid-catalyzed elimination during chemical depolymerization of PHB. The crotonic acid from acid digested PHB (Sigma) showed one peak with retention time of 31 min and it served as standard to calculate the PHB produced by different cyanobacterial isolates. The cultures treated with con. H_2SO_4 have also shown single peak with no change in their elution pattern with respect to retention time. Among all species, *Phormidium* sp. isolated from marine environments was found to accumulate maximum PHB of 7.606±0.005 mg/L medium followed by marine *Synechococcus* sp., fresh water cultures *Synechosystis* sp. and *Anabaena* sp. of PHB 4.599±0.012 mg/L, 3.746±0.007 mg/L and 2.314±0.012 mg/L respectively. Stal [24] has reported that *Phormidium* sp. isolated from microbial mat are found negative for PHB accumulation but in oppose to Stal's statement, findings in the present study showed marine *Phormidium* sp. with maximum PHB accumulation among all isolates. Further to enhance the PHB production, media optimization and genetic manipulation studies on this marine isolate *Phormidium* sp. could results with high yield. The amount of PHB produced by different species of marine and fresh water cyanobacterial cultures were summarised in Table 1. However, the reason for higher production is yet to discover.

Qualitative Analysis of PHB using FT-IR Spectrometry: Fourier-transform infrared spectroscopy (FT-IR) has been proved to be a powerful analytical tool for studying microorganisms and their cell components in intact form [27-30]. It has been reported that PHB is observable in FT-IR spectra [31-33]. In the present study, PHB

Table 1: Quantitative analysis of PHB produced by different isolates using HPLC

S. No	Strain No.	Species	Source	PHB mg/L
01	VIT-BMN 1	*Anabaena* sp.	Fresh water	2.30±0.012
02	VIT-BMN 2	*Synechococcus* sp.	Marine environment	4.60±0.012
03	VIT-BMN 3	*Phormidium* sp.	Marine environment	7.60±0.005
04	VIT-BMN 4	*Synechosystis* sp.	Fresh water	0.83±0.001
05	VIT-BMN 5	*Spirulina* sp.	Fresh water	1.18±0.007
06	VIT-BMN 6	*Nostoc* sp.	Fresh water	0.54±0.008
07	VIT-BMN 7	*Phormidium* sp.	Fresh water	0.90±0.004
08	VIT-BMN 8	*Synechosystis* sp.	Fresh water	3.75±0.007
09	VIT-BMN 9	*Oscillatoria willei*	Marine environment	0.42±0.007
10	VIT-BMN 10	*Lyngbya* sp.	Fresh water	0.71±0.007
11	VIT-BMN 11	*Nostoc* sp.	Fresh water	0.58±0.021

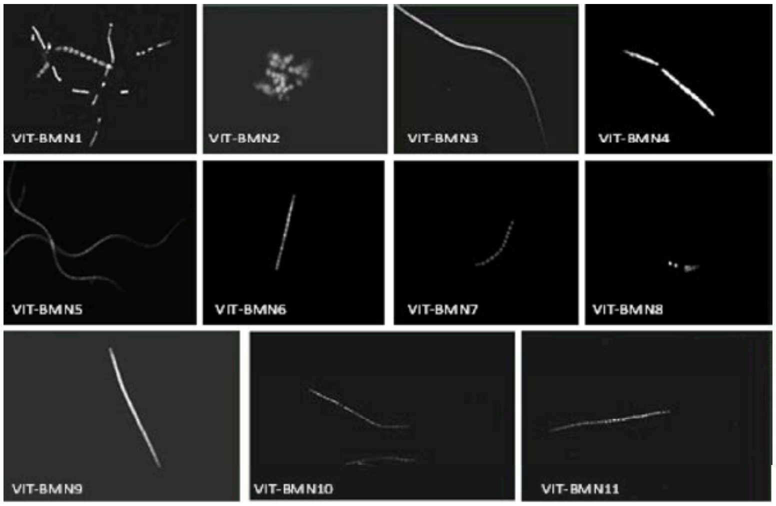

Fig. 1: Nile red staining of different Cyanobacterial isolates showing PHA granules as bright inclusions under fluorescent microscope (Olympus-BX61).

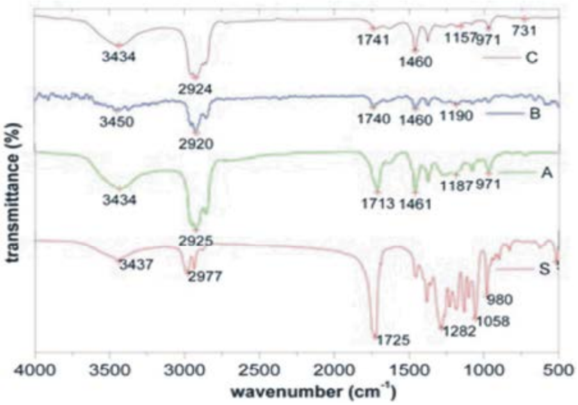

Fig. 2A: FT-IR analysis of PHB extracted from different isolates showing similarities with standard PHB obtained from sigma. (S) Standard, (A) *Anabaena* sp. (B) *Synechococcus* sp. (C) *Phormidium* sp.

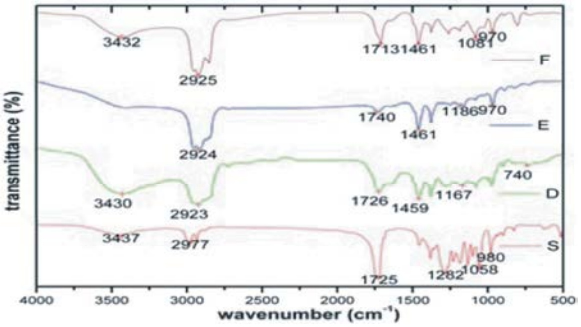

Fig. 2B: FT-IR analysis of PHB extracted from different isolates showing similarities with standard PHB obtained from sigma. (S) Standard, (D) *Synechosystis* sp. (E) *Spirulina* sp. (F) *Nostoc* sp.

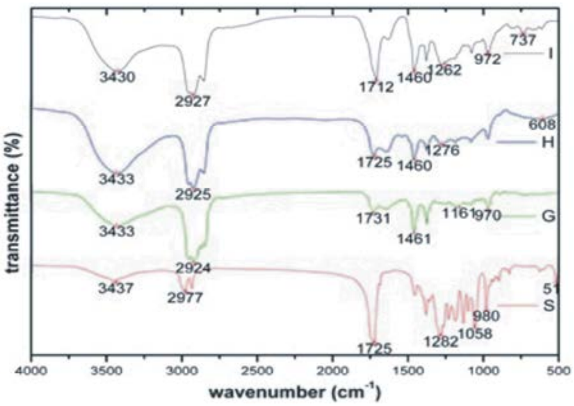

Fig. 2C: FT-IR analysis of PHB extracted from different isolates showing similarities with standard PHB obtained from sigma. (S) Standard, (G) *Phormidium* sp. (H) *Synechosystis* sp. (I) *Oscillatoria willei*.

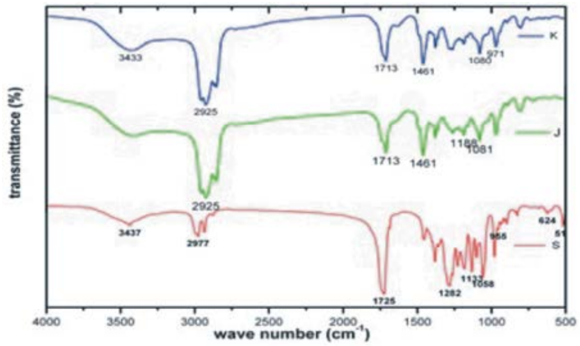

Fig. 2D: FT-IR analysis of PHB extracted from different isolates showing similarities with standard PHB obtained from sigma. (S) Standard, (J) *Lyngbya* sp. (K) *Nostoc* sp.

produced by different strains were observed by FTIR analysis. The standard PHB (sigma) showed its strong bands at 1725 cm^{-1}, 2977 cm^{-1} and 3437 cm^{-1} which corresponds to ester carbonyl group (C=O), methylene C-H vibration and its terminal OH group respectively [34-36]. Similar band patterns were observed in spectrum obtained for all extracted PHB samples of different cyanobacterial isolates and correlated to standard PHB spectrum. The spectrums obtained for standard PHB as well as extracted PHB's are given in a comparative manner in the Figs. 2A-2D.

CONCLUSIONS

At present, PHB production from photosynthetic microorganisms to produce biodegradable plastics as an alternative to conventional plastics is considered to be cost effective and eco-friendly compared to bacterial production of PHB [37, 38]. In this context, as a first report from Tamil Nadu, India this study reports 11 cyanobacterial species for PHB production in their native forms. Among the isolates *Phormidium* sp. (VIT-BMN3) is reporting first time for its PHB accumulation. The poly-β-hydroxybytyrate production of each individual was confirmed by Nile red staining method, HPLC analysis in addition with FT-IR spectrum analysis. Further studies on these isolates for improved PHB production will improve the ability to discover unexploited industrially important cyanobacteria present in the environment.

ACKNOWLEDGEMENT

The present work was financially supported by the Department of Biotechnology (DBT), Ministry of Science and Technology, New Delhi, India and is thankfully acknowledged. The authors are thankful to the management of VIT University for providing infrastructure and facilities. The authors wish to thank Dr. K.B. Ramachandran, Professor and Head, Department of Biotechnology, Indian Institute of Technology Madras for his support in HPLC studies.

REFERENCES

1. Johnson, K., R. Kleerebezem and M. Van Loosdrecht, 2010. Influence of the C/N ratio on the performance of polyhydroxybutyrate (PHB) producing sequencing batch reactors at short SRTs. Water Research, 44(7): 2141-2152.
2. Vermaas, W., 1996. Molecular genetics of the cyanobacteriumSynechocystis sp. PCC 6803: Principles and possible biotechnology applications. Journal of Applied Phycology, 8(4-5): 263-273.
3. Sestak, Z. and J. Catsky, 2003. Bibliography of Reviews and Methods of Photosynthesis-87. Photosynthetica, 41(3): 453-480.
4. Chaogang, W., H. Zhangli, L. Anping and J. Baohui, 2010. Biosynthesis of Poly- Β-Hydroxybutyrate (Phb) in the Transgenic Green Alga *Chlamydomonas Reinhardt.* Journal ofPhycology, 46(2): 396-402.
5. Lemoigne, M., 1926. Produit de deshydratation et de polymerization de l'acide β-oxybutyrique. Bulletin de la Société De Chimie Biologique, 8: 770-782.
6. Macrae, R. and J. Wilkinson, 1958. Poly-β-hyroxybutyrate metabolism in washed suspensions of Bacillus cereus and Bacillus megaterium. Journal of General Microbiology, 19(1): 210-222.
7. Baei, M.S., G. Najafpour, Z. Lasemi, F. Tabandeh, H. Younesi, H. Issazadeh and M. Khodabandeh, 2010. Optimization PHAs production from dairy industry wastewater (cheese whey) by Azohydromonas lata DSMZ 1123. Iranica Journal of Energy and Environment, 1(2): 132-136.
8. Balaji, S., G.K., Lavanya B. and B. Muthuvelan, 2012. Isolation and optimization of polyi hydroxybutyrate producing cyanobacterial strains. International Journal of Applied Biology and Pharmaceutical Technology, 3(1): 137-145.
9. Shrivastav, A., S.K. Mishra and S. Mishra, 2010. Polyhydroxyalkanoate (PHA) synthesis by *Spirulina subsalsa* from Gujarat coast of India. International Journal of Biological Macromolecules, 46(2): 255-260.
10. Srivastav, A., K.M. Sanjiv and M. Sandhya, 2013. Isolation and characterization of oxygen-evolving photosystem II particles and photosystem II core complex from the filamentous cyanobacterium Spirulina platensis. Photosynthetica, 51(4): 517-530.
11. Yang, C.F. and C.M. Lee, 2011. Enhancement of photohydrogen production using PHBC deficient mutant *Rhodopseudomonas palustris* strain M23. Bioresource Technology, 102(9): 5418-5424.
12. Liu, B.F., N.Q. Ren, J. Tang, J. Ding, W.Z. Liu, J.F. Xu, G.L. Cao, W.Q. Guo and G.J. Xie, 2010. Bio-hydrogen production by mixed culture of photo-and dark-fermentation bacteria. International Journal of Hydrogen Energy, 35(7): 2858-2862.
13. Hrabak, O., 1992. Industrial production of poly-b-hydroxybutyrate. FEMS Microbiology Review, 103: 251-256.

14. Arun, A., R.M. Murugappan, A.D.D. Ravindran, V. Veeramanikandan and S. Balaji, 2006. Utilization of various industrial wastes for the production of poly-bhydroxybutyrate (PHB) by *Alcaligeneseutrophus.* African Journal Biotechnology, 5: 1524-1527.
15. Andreessen, B., A.B. Lange, H. Robenek and A. Steinbuchel, 2010. Conversion of glycerol to poly (3-hydroxypropionate) in recombinant *Escherichia coli.* Applied and environmental Microbiology, 76(2): 622-626.
16. Anderson, A.J. and E.A. Dawes, 1990. Occurrence, metabolism, metabolic role and industrial uses of bacterial polyhydroxyalkanoates. Microbiological Reviews, 54(4): 450-472.
17. Wang, F. and S.Y. Lee, 1998. High cell density culture of metabolically engineered Escherichia coli for the production of poly (3-hydroxybutyrate) in a defined medium. Biotechnology and Bioengineering, 58(2-3): 325-328.
18. Ibrahim, M.H.A. and A. Steinbuchel, 2010. Zobellella denitrificans strain MW1, a newly isolated bacterium suitable for poly (3-hydroxybutyrate) production from glycerol. Journal of Applied Microbiology, 108: 214-225.
19. Carr, N.G., 1992. The occurrence of poly-β-hydroxybutyrate in the blue green algae *Chlorogloea fritschii.* Biochimica Biophysica Acta, 120: 308-310.
20. Fidler, S. and D. Dennis, 1992. Polyhydroxyalkanoate production in recombinant *Escherichia coli.* FEMS Microbiology Letters, 103(2): 231-235.
21. Abed, R., S. Dobretsov and K. Sudesh, 2009. Applications of cyanobacteria in biotechnology. Journal of Applied Microbiology, 106(1): 1-12.
22. Bhati, R., S. Samantaray, L. Sharma and N. Mallick, 2010. Poly-β-hydroxybutyrate accumulation in cyanobacteria under photoautotrophy. Biotechnology Journal, 5(11): 1181-1185.
23. Nawrath, C., Y. Poirier and C. Somerville, 1994. Targeting of the polyhydroxybutyrate biosynthetic pathway to the plastids of Arabidopsis thaliana results in high levels of polymer accumulation. Proceedings of the National Academy of Sciences, 91(26): 12760-12764.
24. Stal, L.J., 1992. Poly (hydroxyalkanoate) in cyanobacteria: an overview. FEMS Microbiology Letters, 103(2): 169-180.
25. Capon, R.J., R.W. Dunlop, E.L. Ghisalberti and P.R. Jefferies, 1983. Poly-3-hydroxyalkanoates from marine and freshwater cyanobacteria. Phytochemistry, 22(5): 1181-1184.
26. Penloglou, G., A. Rousso s, C. Chatzidouka s and C. Kiparissides, 2010. A combined metabolic/ poly (3-hydroxypropionate) in recombinant Escherichia coli. Applied and Environmental polymerization kinetic model on the microbial production of poly(3-hydroxybutyrate). New Biotechnology, 27: 358-367.
27. Ferris, M.J. and C. Hirsch, 1991. Method for isolation and purification of cyanobacteria. Applied and environmental Microbiology, 57(5): 1448-1452.
28. Miyake, M., M. Erata and Y. Asada, 1996. A thermophilic cyanobacterium, *Synechococcus sp*. MA19, capable of accumulating poly-β-hydroxybutyrate. Journal of Fermentation and Bioengineering, 82: 512-514.
29. Taroncher-Oldenburg, G., K. Nishina and G. Stephanopoulos, 2000. Identification and analysis of the polyhydroxyalkanoate-specific β-ketothiolase and acetoacetyl coenzyme A reductase genes in the cyanobacterium Synechocystis sp. strain PCC6803. Applied and environmental Microbiology, 66(10): 4440-4448.
30. Zhenggui, L., W. Yuanpeng, H. Ning, H. Jiale, Z. Kang, S. Wenyao, W. Haitao, Y. Weilong and L. Qingbiao, 2011. Optimization of polyhydroxybutyrate (PHB) production by excess activated sludge and microbial community analysis. Journal of Hazardous Materials, 185: 185: 8-16.
31. Karr, D.B., J.K. Waters and D.W. Emerich, 1983. Analysis of poly-β-hydroxybutyrate in Rhizobium japonicum bacteroids by ion-exclusion high-pressure liquid chromatography and UV detection. Applied and environmental Microbiology, 46(6): 1339-1344.
32. Helm, D., H. Labischinski, G. Schallehn and D. Naumann, 1991. Classification and identification of bacteria by Fourier-transform infrared spectroscopy. Journal of General Microbiology, 137(1): 69-79.
33. Yellore, V. and A. Desia, 1998. Production of poly-β-hydroxybutyrate from lactose and whey by *Methylobacterium* sp. ZP24. Letters in Applied Microbiology, 26: 391-394.
34. Naumann, D., D. Helm, H. Labischinski and P. Giesbrecht, 1991. The characterization of microorganism by Fourier-transform infrared spectroscopy (FT-IR). In: Nelson WH, editors. Modern techniques for rapid microbiological analysis. VCH, New York.

35. Naumann, D., S. Keller, D. Helm, C. Schultz and B. Schrader, 1995. FT-IR spectroscopy and FT-Raman spectroscopy are powerful analytical tools for the non-invasive characterization of intact microbial cells. Journal of Molecular Structure, 347: 399-405.
36. Helm, D. and D. Naumann, 1995. Identification of some bacterial cell components by FTIR spectroscopy. FEMS Microbiology Letters, 126(1): 75-79.
37. Nicols, P.D., J.M. Henson, J.B. Guckert, D.E. Nivens and D.C. White, 1984. Fourier transform-infrared spectroscopic methods for microbial ecology: analysis of bacteria, bacterial polymer mixtures and biofilms.. Journal of Microbialogy Letters, 4: 79-94.
38. Hong, K., S. Sun, W. Tian, G. Chen and W. Huang, 1999. A rapid method for detecting bacterial polyhydroxyalkanoates in intact cells by Fourier transform infrared spectroscopy. Applied Microbiology and Biotechnology, 51(4): 523-526.

Persian Abstract

DOI: 10.5829/idosi.ijee.2014.05.01.14

چکیده

پانزده گونه سیانو باکتری از آب شیرین و منابع آب دریایی از نقاط مختلف تامیل نادو، هند ایزوله شد. این پانزده گونه بر اساس ویژگی های مورفولوژیک و از طریق مشاهدات میکروسکوپی شناسایی شدند. سپس گونه های ایزوله شده برای تولید PHB با استفاده از رنگ آمیزی قرمز نیل غربال شدند. مشخص شد یازده گونه از آنها قادر به تولید PHB در حالت طبیعی خود بودند. علاوه بر این، تجزیه و تحلیل کمی PHB توسط HPLC، وجود گونه دریایی سودوموناس پرمیدیوم با ۷/۶ ±۰/۰۰۵ mg/L (۷/۶٪)، و وجود سودوموناس سینکوکوکوس با ۴/۵۹ ±۰/۰۱۲ mg/L (۴/۵٪)، سودوموناس سینکوسیستیس با ۳/۷۴ ±۰/۰۰۷ mg/L (۳/۷٪) و سودوموناس آنابنا با ۲/۳۱ ±۰/۰۱۲ mg/L (۲/۳٪) از آب شیرین را نشان داد. در میان گونه های ایزوله شده، گونه دریایی سودوموناس پرمیدیوم (VIT - BMN3) برای اولین بار برای تولید PHB گزارش شده است. علاوه بر این، پلیمر زیست تخریب پذیر استخراج شده در کلروفرم داغ توسط FTIR آنالیز شد که باندهای قوی نزدیک به عددهای موج ۱۷۲۵ ، ۲۹۷۷ و ۳۴۳۷ cm^{-1} را نشان داد و به ترتیب حضور گروه کربونیل استر (C = O) ، ارتعاش C-H متیلن و گروه OH ترمینال از PHB را تایید کرد. به طور کلی، رنگ آمیزی قرمز نیل، تجزیه و تحلیل HPLC و طیف FTIR به دست آمده برای تمام کشتهای میکروبی، تولید PHB از گونه های ایزوله شده را تایید کرد. مطالعات بیشتر بر روی بهینه سازی محیط کشت برای افزایش تولید PHB تحت فرآیند می باشد.